Interactions of fluorophores with complex surfaces and spectroscopic examinations of ancient manuscripts

DUCKWORTH, ANDREW,ROBERT

Interactions of Fluorophores with Complex Surfaces

&

Spectroscopic Examinations of Ancient Manuscripts

Andrew Robert Duckworth

Durham University, Department of Chemistry

September 21, 2017

Submitted for admission to the degree of
DOCTOR OF PHILOSOPHY

Declaration

The work described in this thesis was carried out at the Department of Chemistry, University of Durham, except where otherwise stated, between October 2012 and March 2016. This thesis is the sole work of the author, except where acknowledged by reference, and has not been submitted for any other degree.

Statement of Copyright

Abstract

In the first part of this thesis, it was found by fibre-optic fluorescence spectroscopy, that the greening of fabrics washed in optical brighteners is due to a reabsorption effect. The quantum yield of fluorescence of the optical brighteners OB15, OB36 and OB49 in water are 0.11, 0.08 and 0.71 respectively. Their respective fluorescence natural lifetimes are 6700 ± 109, 5971 ± 712 and 1685 ± 22 ps. In solution, the excited state of OB15 experiences more competing relaxation processes as the solvatochromic shift increases. OB49 displays the opposite trend.

A literature cellulose model surface is employed as a cotton mimic for evanescent wave fluorescence studies. Two model greases are similarly developed and used, and a third is presented for future work. These are based on surface-specific reactions with glass substrates, and the doping of a regenerated cellulose film with long chain alcohols. On doped cellulose surfaces, some low quantum yields occur compared to clean cellulose and bulk solution. Photobleaching behaviours are also observed. Both dyes physisorb rigidly to cellulose and grease models.

The second part of this thesis identifies the pigment palette of the earliest Northumbrian manuscripts pre- and post-1066, by Raman and diffuse reflectance spectroscopy. It develops a suite of multispectral imaging programs in MATLAB® for facile classification of pigments across a page *ab initio*, using data reduction and colour spaces.

Raman and reflectance data are meta-analysed using symmetric permutation to split manuscripts and pigments into groups *ab initio*. It was also generalised, that the palette of the pre-Hastings selected manuscripts contained vergaut, indigo, orpiment, impure red lead, and copper green pigments, as well as orcein purples. Immediately post-1066 white lead, red ochre, vermilion and lapis lazuli appear in the palette in England, though vergaut and indigo disappear and the red lead used is essentially pure.

Contents

List of Figures

List of Tables

Abbreviations

Abbreviation	Meaning
APTMS	(3-aminopropyl)trimethoxysilane (see SAM for APTMS-SAM)
ATR	attenuated total reflectance
C18-OH	*n*-octadecanol
CCCC	Corpus Christi College Cambridge
DAS	diaminostilbene brightener
DCL	Durham Cathedral Library
DCM	dichloromethane
DFT	density functional theory (see also TD-DFT)
DMAc	N,N-dimethylacetamide
DMF	N,N-dimethylformamide
DMSO	dimethylsulfoxide
DRS	diffuse reflectance spectroscopy
DSBP	distyrylbiphenyl brightener
DUL	Durham University Library
EtOH	ethanol
EWIF	evanescent wave-induced fluorescence
EWIFS	evanescent wave-induced fluorescence spectroscopy
FITC	fluorescein-5-isothiocyanate
FORS	fibre-optic reflectance spectroscopy
FTIR	Fourier transform infra-red spectroscopy
FPTMS	(3,3,3-trifluoropropyl)trimethoxysilane (see SAM for FPTMS-SAM)
FWA	fluorescent whitening agent
HFIP	1,1,1,3,3,3-hexafluoroisopropanol
HMDS	hexamethyldisilazane
HOMO	highest energy occupied molecular orbital
IPA	propan-2-ol
IPTMS	(3-iodopropyl)trimethoxysilane (see SAM for IPTMS-SAM)
KT	Kamlet-Taft
LUMO	lowest energy unoccupied molecular orbital
MeCN	methyl cyanide/acetonitrile/ethanenitrile
MeOH	methanol
MSI	multispectral imaging
NNMF	non-negative matrix factorisation
OB	optical brightener
OH	hydroxyl
PCA	principal component analysis
PE	poly(ethylene)
PET	poly(ethylene terephthalate)
PGL	Palace Green Library
PTFE	poly(tetrafluoroethene)
RTP	room temperature and pressure (298 ° K, 1 bar)

continued on next page

continued

Abbreviation	Meaning
SAM	self-assembled monolayer
TCDS	trichlorododecylsilane (see SAM for TCDS-SAM)
TCSPC	time-correlated single photon counting
TD-DFT	time-dependent density functional theory
THF	tetrahydrofuran
TIR	total internal reflection
TMSC	trimethylsilylcellulose
TREWIFA	time resolved evanescent wave-induced fluorescence anisotropy
TREWIFS	time resolved evanescent wave-induced fluorescence spectroscopy
WAXS	wide-angle x-ray scattering

Frequent Symbols

Symbol	Meaning
a^*	CIE Hunter L*a*b* colour space green-red value
α	polarizability, absorptivity, Kamlet-Taft hydrogen bond acidity
b^*	CIE Hunter L*a*b* colour space blue-yellow value
β	Kamlet-Taft hydrogen bond basicity
B	NNMF basis function
c	speed of light, concentration
d_p	penetration depth
$\delta_{d/p/h}$	Hansen dispersive/polar/hydrogen bond parameter
ϵ	dielectric constant
ε	extinction coefficient
Φ	quantum yield
Φ_f	quantum yield of fluorescence
G_{opt}	G-factor due to optics
γ	surface tension
$\gamma_{s/l/v}$	surface tension - solid/liquid/vapour pair as appropriate
γ^{LW}	surface tension - Lifshitz van der Waals'
γ^{AB}	surface tension - acid-base interaction
γ^{TOT}	total surface tension
γ_{zis}	surface tension - Zisman's critical value
$H_{R/S}$	entropy of repeat classification/silhouette (image, information)
h	Planck's constant
I	intensity of light
$\mathcal{K}$	Tadmor line energy
κ	absorptivity
k	number of classes, rate constant
$\hat{k}$	optimal number of classes
k_f	rate constant of fluorescent emission
λ	wavelength
Λ	loading number for model grease molecules
N_A	Avogadro's constant
n	refractive index
Q	quencher, quotient of positive silhouette values
R	reflectance, radius
r	anisotropy
r_0	fundamental anisotropy at time zero
r_γ	in-plane anisotropy
r_ζ	out-of-plane anisotropy
S	silhouette value
S_n	nth singlet state
τ	lifetime
τ_{tot}	natural lifetime
$\tilde{\nu}$	frequency in wavenumbers

Publications

The author declares that they have also contributed to the following six works during the construction of this thesis, stated highest author listing first:

A. Beeby, A. R. Duckworth, R. G. Gameson and C E Nicholson. "Pigments of the Earliest Northumbrian Manuscripts" *Scriptorium* (2015) **69**:33–59

S. Menning, M. Kraemer, A. R. Duckworth *et al.* "Bridged Tolanes: A Twisted Tale" *J. Org. Chem.* (2014) **79:**6571–6578

R. J. Davidson, L. E. Wilson, A R Duckworth *et al.* "Alkyne substituted mononuclear photocatalysts based on [RuCl(bpy)(tpy)](+)" *Dalton Trans.* (2015) **44**:11368–11379

G. Stasiuk, F. Minuzzi, M. Sae-Heng *et al.* "Dual-Modal Magnetic Resonance/Fluorescent Zinc Probes for Pancreatic beta-Cell Mass Imaging" *Chem A Eur. J.* (2015) **21**:2053–5033

R. Kataky, J. H. L. Hadden, K. S. Coleman *et al.* "Graphene oxide nanocapsules within silanized hydrogels suitable for electrochemical pseudocapacitors" *Chem. Comm.* (2015) **51**:10345–10348

D. R. Viete, B. R. Hacker, M. B. Allen *et al.* "Multiple seismic cycles recorded by metamorphism during subduction" *Nature* (2017) *Submitted for peer-review.*

Acknowledgements

I acknowledge first my primary supervisor Prof. Andy Beeby at Durham, who was willing and able to provide me with so many opportunities to excel. I acknowledge also my industrial supervisor Euan Magennis from P&G Newcastle, who was the buffer between academia and industry. I acknowledge and thank P&G at this time as the ultimate source of funding for Part I, and Robert and Felicity Shepherd for making Part II possible.

To my lab mama Dr Kate Nicholson, and my materials chemistry family, I am grateful for the endless emotional support (as well as many foods, talks, and outings) and the instrument time and tutelage you lent me. I know that's not much of a paragraph, but I couldn't afford to print another chapter.

To Richard and Fiona Gameson, I extend especially heartfelt thanks for your time, manners, enthusiasm, infectious love of manuscripts, cat, and delicious consumables. That phrasing, minus the cat, also extends to the inhabitants of Palace Green Library. All of you seemed to me (amidst the flurry that is an exhibition) infinitely patient and tolerant, and that is something I've only come to appreciate more and more as time wears on.

I recognise the Department of Chemistry at Durham for being so supportive and open, and Miriam for talking down the bad days. To Ross and Helen, the other students and unofficial members of Beeby group… I don't know how you put up with me, but you did, and for that among many other things I am specifically grateful. Also, Robek always makes coffee just how I like it, and I already miss that.

Ustinov College and the Graduate Common Room have been a stronghold for me, that has enriched my life with people, culture, responsibility, and fun. I wish them the best of luck with the upcoming move. It's the people that will make it, not the place.

I thank Winona and George Sharpe for giving me somewhere to stay and all four of their shoulders during a difficult and delicate time. Without you, I confess this would never have gotten to print.

Lastly, I name my parents Ian and Ingrid, my sister Emma, her husband Matthew, my nephew Hardy, and of course Boyce the Labrador, whose collective contribution to this work is through my development as a person at all stages and levels. Anne, Liz, Percy, Becci, Neal and Betty, thanks for believing in me and being around while you still could be. I miss you all.

For Drummond & Lister.

Part I

Interactions of Fluorophores with Complex Surfaces

Chapter 1

Introduction

Fluorescent molecules (fluors, fluorophores) absorb light and achieve an *excited state*. This excited state then loses an amount of energy to its surroundings as heat, then returns to the ground state by re-emission of light [1, 2, 3]. The loss of heat causes the emitted light to have a lower frequency than it absorbed. This is *luminescence*. Fluorescence is a short-lived luminescence wherein the total spin-state of the system specifically does not change. The *quantum yield* of fluorescence, also known as the *quantum efficiency*, is the mean number of photons of fluorescence produced from a single excitation. It is therefore a measure of probability on a scale of 0–1, of producing a photon of light by fluorescence.

A white cotton garment which has been washed repeatedly takes on a yellow cast due to absorption of light in the short wavelength region of the spectrum of visible light [4, 5]. This garment is then perceived as dirty or old, and causes the garment to be discarded even though it is still functional. The appearance of garments is restored by optical brighteners; dyes are added to the detergent that absorb invisible ultraviolet light and emit blue light [4, 5, 6]. This re-balances the spectrum of light reaching the eye, and the brightened garment can see extended use.

Optical brightening technology has been in the literature at least as early as the 1960s, and optical brighteners have been based on a multitude of core fluorophore structures [5, 7]. Contemporary brighteners are based on 4,4'-diaminostilbene (DAS) and 4,4'-distyrylbiphenyl (DSBP), as sulfonyl salts for water solubility in washing solutions [5]. The desirable properties of brighteners are even deposition on garments, high quantum yield, low break-down, and the ability to be removed by the action of detergent so that future washes do not accrue excessive dye. The reader is generally directed to [5, Chapter 7] for the history and technical specifications of optical brighteners, which have been treated with rigour there.

Reflectance quantifies the proportion of incident light that is scattered back by a material as a function of frequency [8]. Achromatic (colourless) materials have a "flat" reflectance profile, whilst coloured materials deviate [9]. Fluorescent materials produce complicated reflectance profiles, which include a depletion of reflectance from absorption and an apparent boost to reflectance from the emitted light [4, 10]. This profile helps us to understand what it is that the eye "sees", and so in industrial applications it is often this profile that is interpreted, as it has more practical use for evaluating consumer satisfaction than pure fluorescence. The appearance of these profiles depends on the amount of UV light in the incident light, and so *daylight bulbs* are used which approximate bright sunlight. The appearance of brightened clothing is very different under a UV lamp, as the only profile is the emitted one (*cf.* white cotton laboratory coats show blue in a UV light box used for visualising spots

on chromatography plates).

Bluish casts to white garments, so long as the overall luminance of the fabric is high, give clothes a fresh and clean feel, which is a helping factor in the end goal of positive perception of garments [4]. Greenish casts do not have quite the same effect, therefore the phenomenon of greening in white garments is a problem that has been identified by industry. White garments that are washed many times in brightener can take on a greenish cast that can be perceived as unpleasant; this is especially noticeable in shaded conditions, where the UV component of incident light is low. The cause of this phenomenon is not entirely clear.

Uneven brightening due to *uneven deposition* is an historical problem of brightener structure rather than a contemporary one, though greasy soils on garments such as sebum and colourless oil often fail to brighten adequately, giving the appearance of a dark spot [11]. This problem is a hazard of lifestyle that it would be beneficial to mitigate. It is therefore a possible industrial goal, and it would be useful to understand why it happens on a photophysical level.

Reflectance is a method that has to be used judiciously in order to solve complex or nuanced problems, so its scope is necessarily limited. The relationship of the reflectance, fluorescence, and incident intensity profiles is a complicated one that requires detailed understanding of the substrate [10]. Generally, the assumption is that the system can be approximated by tiny spheres with isotropic absorption and emission. Deviations from this, as with fabrics, invalidate all these assumptions; the system under study is a complicated network of fibres, and as such is anisotropic and potentially fibre-optic. To analyse the fluorescence in complex fibre networks requires an accurate model of the substrate-dye interaction, which is the information that is sought in the first instance. Therefore, the simplest solution is to remove the *complexity* of the substrate material, and retain the substance itself as the one essential factor.

A planar substrate lends itself to spectroscopy because the geometry is extremely well-defined. This simplifies any and all attempts to model the surface, which should also be transparent. The use of evanescent waves, as with total internal reflection fluorescence microscopy, allows one to probe a small, well-defined region of a substrate material, and can excite fluors that lie within the evanescent wave [12, 13, 14, 15]. A flat substrate of fabric substance then represents an idealised model substrate, and in some sense simplifies analysis once the method is sufficiently developed.

Fluorescence anisotropy and time resolved fluorescence spectroscopy in general are a powerful tool for probing the molecular dynamics of fluors [16, 17, 18, 19]. They can show changes to quantum yield, provide evidence of energy transfer, or demonstrate much more complex dynamics of dye. Fluorescence anisotropy also indicates whether a dye is bound rigidly to an interface. Therefore this project seeks to make model surfaces for spectroscopy, and subject them to dye solutions for total internal reflection spectroscopy to provide insight on these industrial problems.

Chapter 2

Photophysical & Spectroscopic Theory

Abstract

General photophysical theory is explained in a stepwise manner from simple principles. Solvent-solute, solute-solute and solute-surface interactions are considered, and the theory of evanescent wave spectroscopy is introduced. It is found, that although the effects of the interface are plural, many are small in the magnitude of their effect and cannot easily be distinguished from one another. It is concluded that time-resolved and wavelength-resolved evanescent wave-induced fluorescence spectroscopy are the most useful interfacial probes, and the use of time-resolved anisotropy measurement should also be insightful regarding the strength of the interactions of the solute with the interface.

—

A mechanistic understanding of photophysics is fundamental to the construction of this thesis. The aim of this chapter is mainly to provide a theoretical basis and justification which will be considered throughout. Readers sufficiently familiar with fundamental photophysics may wish to skip to §2.4 on page 42.

A photophysical process is distinct from a photochemical process insofar that physics and chemistry are distinct at the level of molecular wavefunctions, i.e. the distinction is largely to do with perspective rather than a meaningful dichotomy. For the purposes of this thesis *photochemistry* is concerned with the transformation of molecules from one ground-state species to another *via* absorption of a photon, and any resemblance of photo-initiated processes to ground-state redox chemistry; *photophysics* will mean the underpinning intramolecular processes following absorption of light by a bound electron, i.e. it is concerned with the transitions between states (*cf.* [2, 3, p. 1]).

We will first address the fundaments of light, and its involvement with molecular transitions, using the example of the fate of an arbitrary excited state molecule in an idealised non-interacting system. It follows, that perturbations from this ideality into interaction with external fields of various origins and behaviours, will yield a more representative basis upon which to form hypotheses of molecular behaviour, and interpret spectra. Sources of external fields include solvent dipoles, standing optical waves, other solute molecules, and interfaces.

2.1 Light & Molecular Excitation

Before excited state dynamics can be met with meaningful discussion, the process of excitation to achieve the excited state must be adequately understood. The first law of photochemistry is that *only the light absorbed by a molecule can produce photochemical change in the molecule* [2, p. 10]. We will ignore the details of thermal routes to electronic excitation, and concern ourselves only with the process of photon absorption.

2.1.1 Light Absorption

Light consists of photons, oscillating dipoles that are carriers of the electromagnetic force. For the purposes of photophysics, the representation of a photon may be reduced to a pair of in-phase sinusoidal waves in orthogonal planes, propagating along the same axis. These waves are traces of field vectors $\overrightarrow{E}$ (electric) and $\overrightarrow{B}$ (magnetic) in space and time, of which only $\overrightarrow{E}$ is significant in the interaction with electrons, further reducing the representation to a single wave. The orientation of the $\overrightarrow{E}$ plane, is the plane-polarisation of the photon.

In a medium of refractive index n, the temporal oscillation frequency ν of $\overrightarrow{E}$ is related to the energy E and wavelength λ, *via* the Planck constant h and the speed of light c:

$$E = h\nu = \frac{hc_n}{\lambda_n} \tag{2.1}$$

The subscript n denotes refractive-index dependence (§2.1.2).

A photon close to a molecule may shift an electron in an initially occupied orbital into a final, previously un- or partially-occupied orbital of higher energy, subject to the following equation. Energy states are not easily described for polyatomic molecules, though here they are denoted as i (initial) and f (final) states in a transition:

$$\Delta E_{if} = E_f - E_i = E_{photon} = h\nu_{photon} = \frac{hc_n}{\lambda_n} \tag{2.2}$$

At the end of which process, the photon has been absorbed. The rearrangement $\Delta E_{if}/h = \nu_{photon}$ is the *Bohr frequency condition*. Considering the total wavefunction of the two systems i and f, the *transition dipole moment* μ_{if} is a tensor proportional to the probability of a transition due to interaction with an oscillating electric dipole, constituting a wavefunction overlap integral (where $\hat{\mu}$ is the electric dipole operator):

$$\mu_{if} = \langle \Psi_i | \hat{\mu} | \Psi_f \rangle \tag{2.3}$$

which although too complex for any trivial use, may in turn be intuitively factorised [1, p. 72]:

$$\mu_{if} = \langle \Theta_i | \Theta_f \rangle \langle \psi_i | \hat{\mu} | \psi_f \rangle \tag{2.4a}$$

$$\mu_{if} = \langle \Theta_i | \Theta_f \rangle \langle S_i | S_f \rangle \langle \phi_i | \hat{\mu} | \phi_f \rangle \tag{2.4b}$$

where Θ is the nuclear wavefunction, ψ is the total electronic wavefunction, S is the electron spin component, and ϕ is the spatial distribution of the electrons. The unit vector $\hat{\mu}_{if}$ defines the polarisation of the transition and thus the comparative strength of interaction with individual oscillating dipoles. This leaves the transition probability, $P_{if} \propto |\mu_{if}|^2$. It can be inferred from equation (2.4b), that there exist a set of selection rules for radiative excitation in molecules (*cf.* [2, p. 8]):

1. Initial and final states must share nuclear coordinates

2. The spin state of the system cannot change during absorption

3. The dipole vectors of the initial and final states cannot be identical

Although not an easily applied selection rule, it is also implied that significant orbital hyper-surface overlap must exist between the initial and destination orbitals of the electron, and this will become useful for later computational analyses. Transition between spin-manifolds is not possible during an absorption event (§2.2 for an explanation of spin manifolds). Although so far the events described have been absorptions, the core treatment is identical for radiative transitions; radiative emission of a photon is mechanistically the reverse of absorption (though not a literal reversal), and so the above rules also apply to luminescence (§2.2.5).

Oscillator Strength: In Practical Terms

The Beer-Lambert law is (*cf.* [2, p. 4]):

$$\begin{aligned} A(\lambda) &= \varepsilon(\lambda).c.l \\ &= -\log\left(\frac{I_l(\lambda)}{I_0(\lambda)}\right) \end{aligned} \tag{2.5}$$

where A is absorbance, ε is the extinction coefficient in $M^{-1}cm^{-1}$, c is the molar concentration, l is the interaction length in cm and I_x is the light intensity at interaction length x. This law defines the physical quantity ε at wavelength λ as a constant of proportionality between concentration and absorbance, normalised to l. This quantity may be redimensionalised to give an *absorption cross-section*, an increasingly disused quantity in solution-state studies which it is nevertheless useful to define [20][1, p. 84]:

$$\sigma = 1000\frac{\alpha}{N_A} = 1000\ln(10)\frac{\varepsilon}{N_A} \approx 3.824 \times 10^{-5}\varepsilon \tag{2.6}$$

where σ is the absorption cross section in ^{2} (not shown: conversion factor $1{\times}10^{16}\ ^2/cm^2$). By convention the natural absorption coefficient α is used, whereby the coefficient on the right hand side evaluates $\approx 1.661 \times 10^{-5}$. The utility of this quantity is that its interpretation directly links to the molecular scale rather than the macroscopic, making it less immediately practical though giving an idea of the effective limiting absorbing footprint of a molecule in a 2D system, such as at a bi-phasic interface. For any transition $f \leftarrow i$ giving rise to an arbitrary absorption band spanning $\Delta\tilde{\nu}$, the following integral approximates the *oscillator strength* (*cf.* [1, p. 85]):

$$f_{if} = \frac{2303mc}{\pi N_A e^2 n}\int \varepsilon(\tilde{\nu}).d\tilde{\nu} \approx 4.32 \times 10^{-9}\int \varepsilon(\tilde{\nu}).d\tilde{\nu} \tag{2.7}$$

where m is the electron mass, c is the speed of light, N_A Avogadro's number, e electron charge, n solvent refractive index, and $\tilde{\nu}$ frequency in cm^{-1}. For a Gaussian band, $f_{if} \approx \epsilon_{max} \times \Delta\tilde{\nu}_{FWHM}$. Oscillator strengths are unit-less, directly comparable quantisations of transition probability, where $\mu_{if} \propto f_{if}$. Magnitude of f_{if} is an indicator of transition allowedness:

Range	Allowedness
$f_{if} \geq 1$	fully allowed
$1 > f_{if} \geq 10^{-2}$	allowed
$10^{-2} > f_{if} \geq 10^{-4}$	partially allowed
$10^{-4} > f_{if} \geq 10^{-6}$	forbidden

2.1.2 Refractive Indices & Dielectric Constant

The refractive index n_a of medium a is a bulk property defined:

$$n_a = c_0/c_a \tag{2.8}$$

where c_a is the phase velocity of light in a, and subscript 0 indicates quantity in a vacuum. As outlined in §2.2.2, local non-eigenstates of electron distributions are non-stationary. The oscillating electric dipole of $h\nu$ results in an oscillating induced dipole in a, which although still possessing frequency ν, propagates with a phase velocity dependent upon the polarisability. The dielectric constant is the bulk polarisability in terms of response to an applied field:

$$\epsilon_a(\nu) = |\vec{D}/\vec{E}| \tag{2.9}$$

where $\vec{D}$ is the displaced field, $\vec{E}$ the applied field, and $\epsilon_a(\nu)$ the dielectric constant. These two bulk properties are interrelated at optical frequencies by:

$$n_a^2(\nu) \approx \epsilon_a(\nu) = 1 + 4\pi\chi_a(\nu) \tag{2.10}$$

where n is refractive index, and χ the linear susceptibility. Although the response $\vec{D}$ is linear with respect to $\vec{E}$, a delay due to electron correlation time, resolves as frequency-dependent phase lag between the inductive and propagating wavefronts. Phase offset ϕ is n_a dependent, the range in which n_a falls yields discrete effects:

n real & >0: $0 < \phi < \frac{\pi}{2}$, medium is transparent and usually dispersive

n complex: $\frac{\pi}{2} < \phi < \pi$ medium is absorbing

For complex representations (˜) of refractive index and dielectric constant [21, p. 19]:

$$\tilde{\epsilon}_a(\nu) = \tilde{n}_a^2(\nu) = \epsilon_1(\nu) + i\epsilon_2(\nu) = (n_a(\nu) + i\kappa_a(\nu))^2 \tag{2.11a}$$

$$\kappa_a(\nu) = \ln(10)\frac{\epsilon_a(\nu)c}{4\pi\nu} \tag{2.11b}$$

where $\kappa_a(\nu)$ is an extinction coefficient (not the molar extinction coefficient), and $\alpha_a(\nu)$ a natural absorption coefficient. This is to the effect that $\varepsilon_2(\nu)$ and $\kappa_a(\nu)$ modify the expression for $\varepsilon_a(\nu)$ and $n_a(\nu)$ to model absorption by a.

In summary, the quantities n_a and ϵ_a describe the polarisability of a medium so as to relate the optical properties (refractive, dispersive, absorptive) to molecular structure. The importance of the two quantities is realised first in §2.3.

2.2 The Fate of Excited States

An *adequate summary* of the fate of excited states will now be attempted, including some more detailed explanations of the theoretical framework.

2.2.1 The Jabłoński Diagram

Its precise history aside, the Jabłoński energy level diagram to describe absorption and emission of light, is named for its creator[(i)], and illustrates the common (mostly intramolecular) processes that a system can undergo in terms of excitation and the subsequent possible routes to the ground state [2, 3]. Like the Feynman Diagram of particle physics, the diagram is not of fixed content but of fixed format, construction and conventions. *Horizontal lines* are representative of eigenstates; the y-axis is continuous in energy. The x-axis does not have a fixed scalar representation, though as the overlapping energy levels of multiple electronic states are usually represented together on the same diagram, they are for convenience horizontally segregated into *manifolds*. Arrows denote transitions and are of two forms, *straight arrows* for radiative transitions and *wavy arrows* for non-radiative transitions. Arrows may *only* be either horizontal for isoenergetic transitions, or vertical for non-isoenergetic. Any component of the diagram may be labelled.

The Jabłoński diagram provides no formal representation of time-scale for any process, though as the rate constant of a decay process is dependent on residence time and transition probability between energy states, it makes less sense to give any graphical representation of true transition time. Vertical transitions usually have a high efficiency and are fast. Horizontal transitions between manifolds (including phosphorescence) generally have lower efficiency and are slow, though these can be made to compete effectively against vertical transitions. Isoenergetic transitions are between manifolds, and so the selection rules from page 33 that apply to radiative transitions, forbid diagonal straight arrows (radiative transition accompanied by direct population of a new spin state) with the exception of phosphorescence.

2.2.2 Scattering & The Raman Effect

When a photon $h\nu$ incident upon a dielectric a doesn't result in transition to a new eigenstate, the medium is locally excited to a *virtual state*, wherein the distortion of the electron distribution constitutes a short-lived non-stationary state. In a continuous dielectric (such as a solid) the virtual state propagates as an oscillating electric field (a wave-front) indistinguishable from propagation of a photon, as the *local* return to the ground state induces a counter-oscillation in the surrounding dielectric. In an isolated molecule, the return to the ground state regenerates $h\nu$ and (in the absence of the Raman effect) $h\nu_{in} = h\nu_{out}$.

A fraction, approximately 10^{-8} to 10^{-6}, of incident photons are scattered with $h\nu_{in} \neq h\nu_{out}$. The frequency shift $\nu_{in} - \nu_{out}$ in cm^{-1} is the Raman shift, and peaks correspond to vibrational frequencies of the material. This can be explored using both the classical treatment (using force-fields) and quantum theory. The Jabłoński diagram for Raman scatter is shown in figure 2.1

[(i)] Aleksander Jabłoński: 26 February 1898 - 9 September 1980

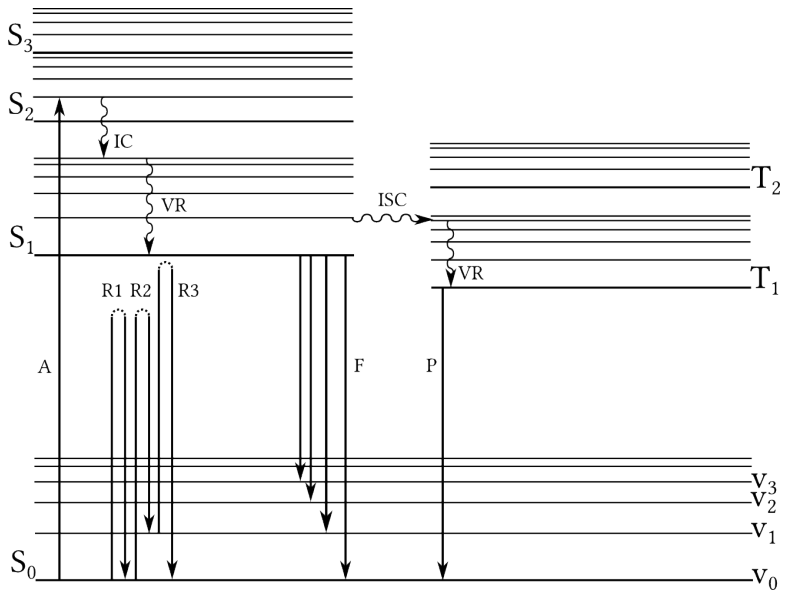

Figure 2.1: Jabłoński Diagram: A Jabłoński energy level diagram showing A) absorption of a photon to an arbitrary upper energy level, IC) internal conversion to a lower electronically excited manifold of the same spin, VR) vibrational relaxation to v_0, ISC) inter-system crossing to a different spin manifold, F) structured fluorescence, P) phosphorescence. Also shown are R1,R2,R3) Rayleigh scattering, Stokes, and Anti-Stokes Raman scattering.

The Raman Effect in Classical Theory

In the classical theory of Raman scatter, we begin by describing the effect of an oscillating dipole $\vec{E}(t) = \vec{E}_0 \cos(2\pi\nu_0 t)$ on a molecule a of polarizability α:

$$|\vec{P}| = \alpha|\vec{E}| \tag{2.12a}$$

$$\vec{P}(t) = \alpha\vec{E}_0 \cos(2\pi\nu_0 t) \tag{2.12b}$$

so-establishing Rayleigh scattering; the induced oscillating dipole vector $\vec{P}$ is proportional to scalar α and of the same frequency as $\vec{E}$. The photon re-emitted/scattered by this molecule will have no change to its frequency. If we fix the orientation of a so that it is no longer isotropic, we must treat α as a tensor matrix $\{\alpha\}$ instead, having three directions of $\vec{P}$:

$$\{\alpha\} = \begin{bmatrix} \alpha_{xx} & \alpha_{xy} & \alpha_{xz} \\ \alpha_{yx} & \alpha_{yy} & \alpha_{yz} \\ \alpha_{zx} & \alpha_{zy} & \alpha_{zz} \end{bmatrix} \tag{2.13}$$

from this we describe then the *polarizability ellipsoid* of a molecule. The nine coefficients of the tensor matrix give six discrete values of α by matrix symmetry:

$$\alpha_{xx}x^2 + \alpha_{yy}y^2 + \alpha_{zz}z^2 + 2\alpha_{xy}xy + 2\alpha_{xz}xz + 2\alpha_{yz}yz = 1 \tag{2.14}$$

If any of the six values of $\{\alpha\}$ change during a vibrational motion, that motion is Raman active because the oscillating dipole can then directly couple to the vibrational motion of the molecule, which

allows it to oscillate with the Rayleigh frequency or the Rayleigh frequency ± a vibrational frequency. For each value of $\{\alpha\}$:

$$\alpha(q_v) = \alpha_0 + \left(\frac{\partial \alpha}{\partial q_v}\right)_0 q_v \tag{2.15}$$

$$q_v = q_0 \cos(2\pi \nu_v t) \tag{2.16}$$

where ν_v is the vibrational frequency of the motion, subscript 0 indicates the value at the equilibrium point of the vibration, and q_v is the vibrational co-ordinate. The vibrational co-ordinate is a measure of displacement from the equilibrium point, for which $q_v = q_0$.

The dipole $\vec{P}$ oscillates with the Rayleigh, Stokes and Anti-Stokes frequencies of the associated vibrational modes, only when any term $(\partial\alpha/\partial q_v)_0 \neq 0$ [22, pp. 230–233]. The magnitude of the tensor $(\partial\alpha/\partial q_v)_0 \propto$ the intensity of Raman lines, and we call this quantity Q_R, the *Raman tensor*.

The Raman tensor is larger when:

- atoms of heavier elements are involved in the motion
- higher-order bonds are involved in the motion

larger elements provide more diffusely distributed valence electrons due to higher principal quantum number, with lower-frequency and smaller displacements due to intertia. Higher order bonding involves orbitals of higher azimuthal quantum numbers, which are *per se* more polarizable.

Quantum Explanation of the Raman Effect

The quantum treatment of Raman scatter serves to explain the difference in intensity between the Stokes and Anti-Stokes lines. The Boltzmann distribution causes the Anti-Stokes lines to be less intense than the Stokes lines by a factor defined:

$$\frac{n_i}{n_j} = e^{-hc\tilde{\nu}_i/kT} \tag{2.17}$$

where n_i/n_j is the population ratio of the ith to jth vibrational level respectively (where $i > j$), $\tilde{\nu}_i$ is the observed vibrational frequency in cm^{-1}, k is the Boltzmann constant, T is temperature in Kelvin. In this way, the Anti-Stokes lines (net transition from higher to lower vibrational level) at ambient temperatures will always be of lower intensity than Stokes.

2.2.3 Spin Multiplicity

The spin quantum number s of an electron may take values $\pm\frac{1}{2}$, which is known also as the spin-orientation, prompting the names "spin up" $(+\frac{1}{2})$ and "spin down" $(-\frac{1}{2})$ electrons. The total spin state of a molecule $S_{tot} = \sum s$, though the more common quantisation of the system is the spin multiplicity $S = 2S_{tot} + 1$, which is the total number of degenerate projections of spin angular momentum presented by the combination of electron spin vectors. The selection rule $\Delta S = 0$ (§2.1.1) prohibits radiative transitions which change the total spin state of the system and thus prohibits spin inversion of the excited electron during radiative transition.

The nomenclature of S is as follows:

S	**Name (Notation)**	**Comment**
1	singlet (S)	typical of ground state configurations
2	doublet (D)	radical species
3	triplet (T)	doubly radical
4	quartet (Q)	triply radical

A subscript numeral after the spin notation is a useful indicator of the excited electronic state of the system, with zero reserved for the ground state.

In the absence of redox chemistry, ionisation potentials, or coordination chemistry, an S_0 organic molecule in a nondescript ambient phase will most typically transition *only* upon the S_n manifold unless either spin-orbit coupling or an energy transfer (§2.4.2) allows a radiationless transition to the T_n manifold. Spin-orbit coupling (conservation of total molecular angular momentum during a multiplicity change *via* transfer between the spin and orbital momenta) becomes significant as the spin-orbit coupling constant $\sigma(n, l, Z^4)$ (where n is the principal quantum number, l azimuthal quantum number and Z atomic number) increases, so principally this becomes accessible to organic molecules most significantly with the intramolecular bonding or intermolecular proximity of heavier atoms e.g. sulfur and xenon, respectively.

2.2.4 Non-radiative Processes

There exist three major routes of intramolecular non-radiative decay: vibrational relaxation, internal conversion, and intersystem crossing.

On the condition that the vibrational energy is capable of dissipating quantum by quantum, a molecule may undergo *vibrational relaxation* (VR) by conferring translational motion to its surrounding environment, usually a solvent shell.

Non-radiative transition between electronic states on the same spin manifold occurs if there exist isoenergetic vibrational states in the initial and destination electronic states. The transition is a rearrangement of electron density accompanied by a vibrational excitation, and so there must be significant overlap of vibrational wavefunctions. This is *internal conversion* (IC).

Should an excited state make a transition of the same sort as IC, but between spin manifolds, this is *intersystem crossing* (ISC).

2.2.5 Luminescence

Luminescence is simply emission of light, and as a result of molecular de-excitation it takes two forms:

Fluorescence $\Delta S = 0$. The transition is spin-allowed (usually singlet-singlet) and the lifetime is characteristically short (ns). It is typical to have slight overlap of $S_1 \leftarrow S_0$ absorption and $S_1 \rightarrow S_0$ emission bands (see below).

Phosphorescence $\Delta S \neq 0$. The transition is spin-forbidden and has much longer lifetimes, but in organic molecules occurs due to T_1 population by ISC and VR. Given that the T manifold has been significantly populated, a return to S by IC must be a poor competitor to phosphorescence, meaning that either there are no "nearby" energy states on the S manifold, or the vibrational wavefunction overlap is poor. Triplet states also possess more densely-packed vibrational manifolds, and this makes

ISC competitive by sheer "brute-force-probability" of an isoenergetic state being available. For T_1 populations, unless higher vibrational levels can be populated that allow ISC to a singlet state, then "the only way out is down". As the energies of excited triplet states are lower than their singlet counterparts, phosphorescence emissions are more red-shifted than fluorescence, exhibiting no $S_1 \leftarrow S_0$ $T_1 \rightarrow S_0$ band overlap.

Unless explicitly otherwise, the remainder of this chapter will focus on fluorescence and the phenomena which affect it.

Two Rules

The spacing ΔE between consecutively higher electronic energy levels, decreases, and similarly so for vibrational spacings. However, in a complex organic molecule in a given spin state with very many vibrational modes, the upper vibrational levels of the nth electronic level may easily overlap with the lower vibrational levels of the $n+1$ level. Given that such a molecule in an excited state in solution will be surrounded by other molecules, vibrational relaxation (§2.2.4) in such a situation is fast. As a direct consequence, we observe two rules:

Kasha's Rule radiative relaxation occurs from the lowest electronic state for that spin state (S_1 or T_1).

Vavilov's Law fluorescence quantum yield is independent of the excitation wavelength

Given the Bohr frequency condition, we thus observe for single photon excitation $\lambda_{lum} > \lambda_{exc}$.

2.2.6 Quantum Yields, Rates & Lifetimes

If one mole of molecule M is excited by absorption of one mole of photons of wavelength λ, to give one mole of excited state molecules M* at $t = 0$, each M* may have multiple available relaxation pathways. The relative efficiency of each pathway, observed as a bulk property, serves then as a relative stochastic measure for probability of individual relaxations (*cf.* [2, §4.3 & §4.4]). Assuming ultimately a return to precisely one mole of M as $t \rightarrow \infty$, the sum of all relaxations will equal the number of excitations, such that for a process m, the efficiency or yield is calculated:

$$\Phi_m = P_m = \frac{N_m}{N_{exc}} = \frac{N_m}{\sum N_{rel}} \tag{2.18}$$

where P_m is probability of m, N_m is the number of incidences of m, N_{exc} the number of excitations and N_{rel} the number of relaxations.

For luminescence, as the relationship between flux and number of quanta is simply per unit time and unit volume:

$$\Phi_l = \frac{I_l}{I_A} \tag{2.19}$$

where I_l is luminescent intensity and I_A is absorbed intensity.

We assert that the rate constant k_m relates to the quantum yield and lifetime of process m, and over all decays we relate to the lifetime of the excited state. We elucidate this starting with the principle that a spontaneous fluorescence decay is first order:

$$-\frac{d}{dt}[M^*] = k_f[M^*] \tag{2.20}$$

$$\text{in integrated form:} \qquad [M^*]_t = [M^*]_0 e^{-k_f t}$$

where the reciprocal of k_f is a characteristic lifetime τ_f. In a real system, f is in competition with multiple processes, chiefly IC and ISC. In which case, we rewrite equation (2.20) as:

$$-\frac{d}{dt}[M^*] = k_f[M^*] + k_{IC}[M^*] + k_{ISC}[M^*] \tag{2.21}$$

$$\text{in integrated form:} \qquad [M^*]_t = [M^*]_0 e^{-k_{tot}t} \quad \text{where:} \quad k_{tot} = \sum k_m$$

and so the fluorescence lifetime measured by intensity decay is $\tau_{tot} = \frac{1}{k_{tot}}$. Equation (2.19) can be rewritten under a steady state approximation as:

$$\Phi_f = \frac{k_f[M^*]}{k_{abs}[M][h\nu]} \tag{2.22}$$

Given then:

$$[M^*] = \frac{k_{abs}[M][h\nu]}{k_{tot}} \tag{2.23}$$

we can substitute $[M^*]$ to arrive at:

$$\Phi_f = \frac{k_f}{k_{tot}} \tag{2.24}$$

The quantum yield of fluorescence is the most important in this work, so the key expression linking all of the above in this section is given in an intuitively understandable form:

$$\Phi_f = \frac{k_f}{k_{tot}} = \frac{\tau_{tot}}{\tau_f} \tag{2.25}$$

For completeness, the case of phosphorescence can be treated similarly on the understanding that a non-zero phosphorescence quantum yield is contingent on $P_{ISC} \neq 0$, and that all other concepts are analogous:

$$\Phi_p = P_T P_{Tr} = \Phi_{ISC}\frac{\tau_T}{\tau_p} \tag{2.26}$$

$$\text{where:} \qquad \frac{\tau_T}{\tau_p} = \frac{k_p}{k_T}$$

where P_T is probability of triplet population (generally = P_{ISC}), P_{Tr} is probability of radiative decay of the triplet state and τ_T/k_T is the triplet analogue of τ_{tot}/k_{tot}.

2.2.7 Quenching

Intermolecular non-radiative processes have in common the transfer of energy from, and thus depopulation of, M* (*cf.* [2, pp. 8–13]).. The energy of an excited state can be lost with a non-radiative return to the ground state, in the presence of a *quencher*, Q *via* the scheme $M^* + Q \rightarrow M + Q$. Equation (2.23) can be expanded to accommodate a first-order quenching process $k_q[Q]$, which carries through equation (2.22) to yield the following realisation about the ratio of unquenched:quenched Φ_f in the presence of $[Q]$:

$$\frac{\Phi_f}{\Phi_{fq}} = \frac{k_f}{k_{fq}} \cdot \frac{k_{fq} + k_q[Q]}{k_f} = 1 + \frac{k_q[Q]}{k_f} = \frac{I_f}{I_{fq}} \tag{2.27}$$

A Stern-Volmer plot of I_f/I_{fq} vs $[Q]$ should be linear, with ordinate intercept of unity and a gradient of k_q/k_f, which is the Stern-Volmer coefficient K_{SV}.

2.3 Solvents

Solvent molecules arrange themselves into a *solvent shell* around solvated species to minimise potential energy, and the effect of these solvent shells is to stabilise the solute. The region of space concerning these shells, is more generally called the *cybotactic* region. Changes to the solute charge distribution cause the cybotactic population to rearrange to compensate to the extent that is possible. The solvated solute including the solvent shell, can be treated as a distinct species of two compartments. With respect to excited states, solvent shells are energy sinks, the rearrangement of which results in solvent-dependent red-shifted emission (*vide infra*). Stabilisation of the excited state by solvent shells increases the lifetime of an excited state and also the Φ_f. The reader is referred to [2, §2.5]) for more fundamental reading about photochemistry in the solution state.

2.3.1 Solvatochromism

Immediately after excitation, the solvent shell and solute exist in the Franck-Condon state, where $\langle\Theta_i| = |\Theta_f\rangle$. The permanent dipoles of the solvent molecules then rearrange in $< 10^{-9}$ s as a response to the change in dipole of the solute, with $\Delta H_{reorg} < 0$, where ΔH is the enthalpy change, usually in kJ/mol. $|\Delta H_{reorg}|$ is more pronounced in solvent systems with greater polarity and greater still for systems that form hydrogen bonds. As mentioned in §2.1.2, the polarisability of the medium has two accessible metrics, n and ϵ. With respect to time dependent polarisability in solvents, n is dependent upon the electronic polarisability of the molecules (and somewhat more incidentally also their radial probability distribution about the point and anisotropy of polarisability), and therefore is a high-frequency function of permittivity due to electron correlation time. ϵ is a lower-frequency function, as the solvent dipole rearrangements largely responsible for ϵ are mostly dependent upon wholesale molecular motion. The condition $n^2 \neq \epsilon$ is imposed by permanent dipoles (and to a degree also anisotropic polarisability), and as the magnitude of non-equivalence is an indicator of the contribution of dipoles to the polarisability, this imposes a condition of non-degeneracy between the Franck-Condon and emissive (rearranged) states.

The difference between n^2 and ϵ is linearly related to $\Delta\tilde{\nu}_{fe}$ (where $\Delta\tilde{\nu}_{fe}$ is $\Delta\tilde{\nu}$ for Franck-Condon vs. emissive states) for an homologous series of solvents, by the Lippert equation:

$$\Delta\tilde{\nu} = \frac{2\Delta f}{hca^3}(\mu_E - \mu_G)^2 + \text{constant} \tag{2.28}$$

$$\text{where:} \qquad \Delta f = \frac{\epsilon - 1}{2\epsilon + 1} - \frac{n^2 - 1}{2n^2 + 1}$$

where a is solvent shell cavity radius, μ_x dipole moment of x, $_E$ denotes excited state, and $_G$ denotes ground state. A derivation of the above is detailed elsewhere [20], though it is more important to note the assumptions:

1. μ changes in magnitude, but not direction
2. the polarisability of the fluorophore is insignificant
3. the solvent shell cavity in which the fluorophore resides, is spherical at all times
4. the solvent is a continuum
5. the polarisability of the solvent is both:

(a) constant over all occupied space and time

(b) isotropic

A Lippert plot of $\Delta\tilde{\nu}$ between absorption and emission peaks against solvent Δf (the *orientation polarisability*, after the *orientation field* caused by orientation of the solvent dipoles) yields a linear relationship [20]. Specific affinities and interaction types (or lack thereof) between solvents and solute, result in a set of discrete linear relationships being observed. E.g. alcohols and ketones regress separately, and water, in having such a large capacity for hydrogen bonding per mole, has an anomalously high $\Delta\tilde{\nu}$ for its Δf and tends to exist separately from the rest of the plot.

2.3.2 Structured Absorption & Emission

Molecules containing many tens of atoms have many more vibrational degrees of freedom, accordingly as their symmetry will allow. Vibronic transitions within these molecules are densely packed across a continuum of energies a few thousand wavenumbers wide, leading to the tens-of-nanometres FWHM seen in absorbance spectra. Accordingly, $S_1 \rightarrow S_0$ emission mirrors features of the $S_1 \leftarrow S_0$ absorption band, unless strong solvent-solute interactions such as hydrogen bonding exist.

The degree of vibronic structure in either spectrum at RTP reflects the strength of interaction with the solvent shell. A featureless spectrum indicates strong stabilisation of the initial state of the associated transition: as absorbance and fluorescence spectra are time and volume averaged, the number of degrees of freedom added by strong solvent shell interactions leads to less-narrowly defined energy levels and thus the superimposed vibronic features are broader.

2.3.3 Quantum Yields

A better-stabilised emissive state has a correspondingly longer lifetime, which by interpretation of equation (2.25) indicates a higher Φ_f.

2.4 Solutes

Unless explicitly otherwise, the discussion of solutes is not general - it refers to the dynamics typical of substituted aromatic molecules used as dyes.

Solute-solute and solute-substrate dynamics affect observed photophysics, showing features that are atypical of the previous case, i.e. that of solvated molecules significantly isolated from other solutes by bulk solvent.

2.4.1 Dye Stacking

On the condition that the interaction strength between dye molecules may sufficiently disfavour dissociation/resolvation, dye molecules can stack with two general outcomes; arising a bathochromically-shifted absorption band (J-type; after discoverer Jelley), or a hypsochromically-shifted one (H-type; hypsochromic shift). In either case, the theory indicates two major considerations (*cf.* []).:

1. excitation constitutes formation of an exciton with an associated mobility
2. stacking causes degeneracy splitting (eventually giving a HOMO-LUMO band structure *vis-a* organic semiconductors)

It is enough to generalise from theory of surfactants that in high concentrations, dyes which form dimers exist in equilibrium with the monomer. In a study of increasing concentration, deviation from the Beer-Lambert law in the monomer absorption band with growth of an associated shifted absorption band leads (by assumption of dimer formation rather than higher polymeric stacks or liquid crystalline phases) to deduction of ε_D from ε_M and the dimer dissociation constant k_d.

2.4.2 Excited State Interactions

For concentrations of dyes or adulterants for which the probability of excited-state collision of any sort is consequently high, it is prudent to understand some ground rules for modelling interactions [1, p. 168–176]. During a collision:

1. $\Delta S = 0$, though the considerations for ISC are essentially unchanged
2. excited states may form complexes with other molecules
3. if the transition dipoles align and ΔE is right, energy transfer between molecules occurs when they are in proximity
4. if close enough, outright electron transfer may occur

Excited state intermolecular energy transfer occurs *via* one of two schemes: Förster or Dexter. Both follow the scheme M* + A → M + A*.

Förster Resonance Energy Transfer (FRET) occurs between a donor fluorophore M* and an absorbing acceptor A exclusively by interaction of their transition dipoles [1][23, p. 430]. If μ_{if} for M* and A align, i.e. relaxation causes the transition dipole of M* to act as exciting oscillating dipole on A, the permittivity of free space *doesn't* result in generation of a photon, and direct excitation of A occurs. ΔE of M* → M must be greater than or equal to that of A* ← A [24].

$$\Phi_F = \frac{1}{1 + (r/R_0)^6} \tag{2.29a}$$

$$R_0^6 = \frac{9000\Phi_{fM^*}(\ln(10))\aleph^2 J}{128\pi^5 n^4 N_A} \tag{2.29b}$$

$$J = \int f_{M^*}(\lambda)\epsilon_A(\lambda)\lambda^4.d\lambda \tag{2.29c}$$

$$\text{isotropic solution:} \quad \aleph^2 \approx 2/3$$

$$\text{otherwise:} \quad \aleph = \hat{\mu}_A \cdot \hat{\mu}_D - 3(\hat{\mu}_D \cdot r)(\hat{\mu}_A \cdot r) \tag{2.29d}$$

where Φ_F is the quantum yield of FRET, r is M*A pair distance, R_0 the value of r at which $\Phi_F = 0.5$, Φ_{fM^*} is the fluorescence quantum yield of M*, $\aleph$ is the transition dipole orientation factor, and $f_{M^*}(\lambda)$ is the normalised emission spectrum of M*.

Dexter Electron Transfer (DET) is donation of the excited electron directly from donor M* to the LUMO of an acceptor A by orbital overlap, and the simultaneous back-transfer of a HOMO electron from A to M*. In this way it is also a fluorescence quenching mechanism. Electron transfer schemes of this nature can also be thought of as electron tunnelling [23, p. 285–286], because the electrons remain in a bound state below the ionisation energy, and must overcome their reaction barriers by tunnelling. The probability of DET is low as it has a strict spatial requirement that contrasts the dipole interactions

of FRET, but the rate k_{Dex} still depends linearly on the spectral overlap of the donor emission and acceptor absorption. Where V_x is the Van der Waals' radius of species x [25, 26]:

$$k_{Dex} \propto Je^{-2r/(V_A+V_{M^*})} \tag{2.30}$$

where J is a spectral overlap integral from equation (2.29c).

Association of an excited state molecule M^* with a ground state molecule M results in an excimer (excited state dimer, molecules are identical in the ground state) or an exciplex (excited state complex, molecules are non-identical in the ground state). Both cases involve the scheme $M + M^* \rightleftharpoons MM^*$ but the stabilisation of the complex to maintain the association involves variable proportions of exciton resonance or charge transfer resonance, depending on the redox chemistry of the pair.

Exciton resonance is transfer of the excitation from one monomer to the other $MM^* \rightleftharpoons M^*M$ and dominates the excimer stabilisation, whilst charge transfer resonance $MM^* \rightleftharpoons (M^+M^-)^* \rightleftharpoons (M^-M^+)^*$ plays a larger part for exciplexes, where the redox properties of the pair are also necessarily non-identical and may favour charge transfer. Excimer and exciplex emissions are both red-shifted with respect to the free fluorophore, and excimer and exciplex formation are [M] and [M^*] dependent. The kinetics of association necessarily transform the time-resolved profile of the excimer or exciplex formation, so that the rise of [MM^*] and therefore the rise of MM^* emission, is dependent on the kinetics of the free fluorophore decay but is not necessarily straightforward to model. This distinguishes these emissive states in time-resolved data from emitters that arise due to dye stacking [1, p. 153].

2.5 Evanescent Waves

At a plane interface between two transparent dielectric media of refractive indices n_1 and n_2, the angle of incidence of a light ray relative to the surface normal in n_1 is $\theta_1 = \theta_i$. The opposed angle for the transmitted portion of the ray into n_2 is called θ_2. We define a critical condition where the transmitted ray is no longer transmitted, based on Snell's law [27][21, p. 13]:

$$n_1 \sin(\theta_1) = n_2 \sin(\theta_2) \tag{2.31a}$$

$$\text{let:} \qquad \theta_2 = 90^\circ$$

$$\therefore \qquad \sin(\theta_c) \equiv \frac{n_2}{n_1} = n_{21} \tag{2.31b}$$

where θ_c is the *critical angle*. This implies that the transmission angle becomes a complex quantity when $\theta_i > \theta_c$, that this condition cannot occur when $n_{21} > 1$, and that $\theta_c \to 90^\circ$ as $n_{21} \to 1$. When $\theta_i \geqslant \theta_c$, *total internal reflection* (TIR) occurs. The phenomenon is illustrated in diagram 2.2.

During TIR, the reflected ray interferes with the incident ray to produce a standing wave normal to the interface [21, p. 25]. This is not nodal at the interface, but decays exponentially into the rarer medium. For a ray which propagates in the (x,z)-plane and totally internally reflects in the plane of the dielectric interface (which lies in the (x,y)-plane) the intensity of the evanescent wave decays into the rarer medium as a function of distance:

$$I_z = I_0 e^{-z/d_p} \tag{2.32}$$

where I_z is the intensity at distance z, I_0 is the intensity of the wave at $z = 0$, and d_p is a characteristic depth at which $I_z = I_0/e$. If the λ can be absorbed by a dye molecule in the rarer medium within d_p of the interface, there is a more significant chance that radiant energy will be lost to the molecule and it

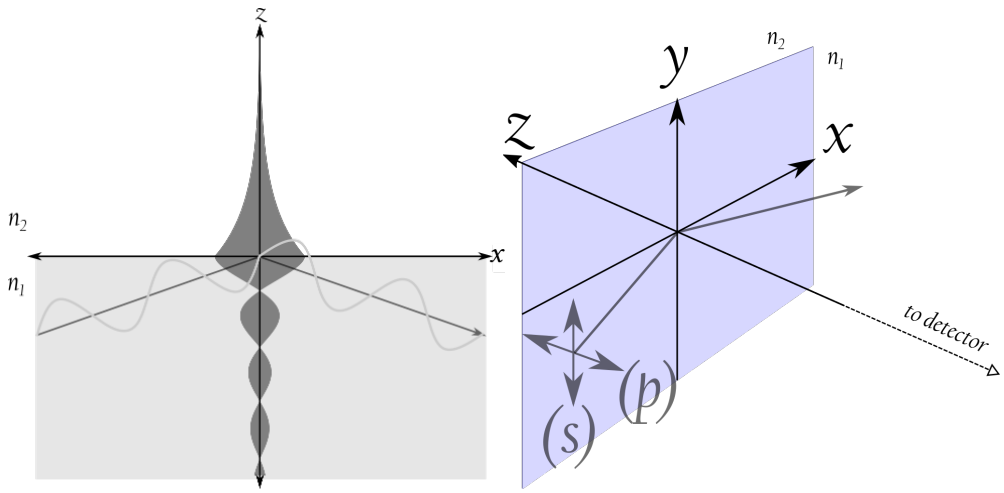

Figure 2.2: Evanescent Waves and the Laboratory Frame: Left: Illustration of the standing wave giving rise to the evanescent wave in n_2 for a 1D geometric light ray. Right: The laboratory axes, showing also the meaning of *s*- and *p*-polarisation.

may fluoresce if $\Phi_f \neq 0$. This is the principle of evanescent wave-induced fluorescence spectroscopy (EWIFS).

For a system with two media and negligible absorption of light, the distance d_p is given by [21, p. 30]:

$$d_p = \frac{\lambda}{2\pi\sqrt{n_1^2 \sin^2\theta_i - n_2^2}} \tag{2.33}$$

where λ is the wavelength of the light ray, and other terms are as per previous convention of this document. For a system of fixed n_{21} and λ, d_p is solely θ_i-dependent. As a result, variable-angle EWIFS data must necessarily contain information about the depth-profile of the concentration and Φ_f of any absorbing species at the interface.

During total internal reflection, the field intensity $E_{(x,y,z)}$ in the rarer medium n_2 at the refractive index discontinuity n_{21} may be broken into three components within the $\mathbb{R}3$ laboratory frame [16, p. 25] [21, p. 27]

$$E_{2x} = E_1 \cdot \frac{2\sqrt{\sin^2\theta_i - n_{21}^2}\cos\theta_i}{\sqrt{(1-n_{21}^2)[(1+n_{21}^2)\sin^2\theta_i - n_{21}^2]}} \tag{2.34a}$$

$$E_{2y} = E_1 \cdot \frac{2\cos\theta_i}{\sqrt{1-n_{21}^2}} \tag{2.34b}$$

$$E_{2z} = E_1 \cdot \frac{2\sin\theta_i\cos\theta_i}{\sqrt{(1-n_{21}^2)[(1+n_{21}^2)\sin^2\theta_i - n_{21}^2]}} \tag{2.34c}$$

wherein E_1 is the inbound field strength in n_1, incident at n_{21}, and E_2 is the field strength at n_{21} experienced in n_2. The evanescent wave from *p*-polarised light generates x and z projections, and *s*-polarisation only y, so that $E_{2p} = \sqrt{E_{2x}^2 + E_{2z}^2}$. Given also that the penetration depth d_p is a polarisation-independent characteristic of the exponential decay of field intensity with increasing distance along z

into n_2:

$$I_z = \left[|E_2|^2 \cdot \frac{c \cdot \varepsilon_0 \cdot n_{21}}{2}\right] \exp\left[-\frac{z}{d_p}\right] \tag{2.35a}$$

$$d_p = \frac{\lambda}{2\pi\sqrt{n_1^2 \sin^2\theta_i - n_2^2}} \tag{2.35b}$$

where the pre-exponential factor is now also the magnitude of the Poynting vector.

Absorbing n_2 We modify n_2 to be complex and define κ as in equation (2.11b) on page 34. Solution of Maxwell's boundary condition equations [12, p. 8] yields magnitudes for I_0 that are θ_i, n_{21} and polarisation-dependent. The expression for d_p is also modified for the *s*-polarisation case:

$$d_p^* = \frac{\lambda}{2\pi\Im} \tag{2.36}$$

where $\Im$ is the imaginary part of $\tilde{n}_2 \cos(\theta_2)$, where $\theta_2 = \arcsin(\tilde{n}_2/n_1)$. It remains that d_p^* is independent of polarisation, however it now becomes important to understand that the effect of $\kappa < 0.05$ is quite small with regard to the process of using angular resolution to deduce $c(z)$ and $\Phi_f(z)$ [28], which are the concentration and quantum yield distributions as a function of z. From the definition of κ we realise that this represents high interfacial concentrations; for $\varepsilon \approx 5 \times 10^4$ $M^{-1}cm^{-1}$ this is approximately 0.2 M, prompting the use of micromolar concentrations (and below). We might assume that the ratio of interfacial to bulk concentration does not exceed $\approx 10^5$ unless proven otherwise, in order to validate the assumption of an essentially non-absorbing n_2.

Both Byrne and Scholes [12, 16] have reviewed, collated and developed the early theory of evanescent wave fluorescence spectroscopy, In particular, Byrne has found based largely on [14, 15], that angular resolution is useful in theory, but in practice experimental data with noise is modelled equally well by a variety of $c(z)$ and $\Phi_f(z)$, even with angular resolution far better than that of the experimental setup at Durham. Therefore angular resolution will be treated in no further detail in this thesis, and the reader is encouraged to see those references for detailed derivations and discussions, as well as the collective work of Masuhara [18]. We will focus instead on time-resolution and anisotropy with regard to interfaces.

There is nevertheless the final depth-dependent caveat, that the wavefront emitted by an excited molecule at an interface, will be subject to partial reflection at that interface. The effect of this is that the interface theoretically stimulates or retards emission in a manner that is z-dependent. All other things being equal, for a population of emissive dipoles distance $z < \lambda$ from an interface, $\Phi_{f,int} \approx \Phi_{f,bulk} \pm 3\%$ [16, p. 38]. As depth-profiling is itself already of very limited use and further perturbed by this, it stands to reason that any deviation of Φ_f, k_f or τ_f from the bulk value at the interface, if within 3% of the bulk value, may simply be due to this phenomenon. However, as the integral of the *variation* is in all cases (even weighted by I_z) near zero when $z \to \lambda$, and $d_p \approx \lambda$ when $\theta_i \approx \theta_c + \partial\theta$, the effect of this phenomenon unless adsorbed layers are thin ($< 0.3\lambda$), can only be merely to broaden the distribution of Φ_f and produce only small shifts to the mean. This phenomenon will prove largely irrelevant to discrete lifetime analysis in this thesis, but is included for completeness.

Multi-Layer Systems In a multi-layer e.g. 3-layer system, the last of which is solvent, the penetration depth achieved at the final interface n_{32} will be equivalent to that achieved at n_{31} (as if n_2 did not

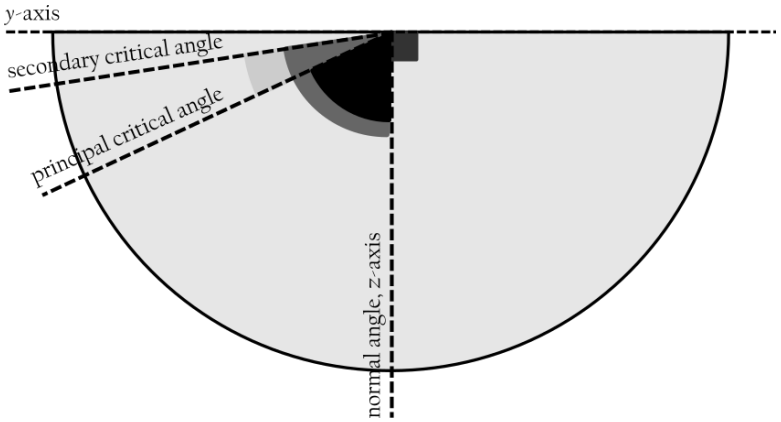

Figure 2.3: The Case of Limiting TIR Angles: The limiting angle in a multi-layer system is always larger than the critical angle for the surface of interest, when the medium to be probed with the evanescent wave has the smallest refractive index in the system. The limiting secondary critical angle here, provides us with a limited range of probe angles, limiting the utility of angular resolution.

exist) because:

$$\begin{aligned} \text{if:} \qquad & {}^{31}d_p = {}^{32}d_p \\ \sqrt{n_1^2 \sin^2(\theta_1) - n_3^2} &= \sqrt{n_2^2 \sin^2(\theta_2) - n_3^2} \\ \therefore \qquad & n_1 \sin(\theta_1) = n_2 \sin(\theta_2) \qquad \text{QED} \end{aligned}$$

where ${}^{ij}d_p$ is the penetration depth of an evanescent wave at interface n_{ij}.

For systems with $x = 3$ plane-parallel dielectric layers of indeterminate depth, $x - 1$ values of θ_c may exist in the system:

$$n_1 \sin(\theta_1) = n_2 \sin(\theta_2) = n_3 \sin(\theta_3) \tag{2.37a}$$

$$\therefore \qquad {}^{21}\theta_c = \arcsin(n_{21}) \tag{2.37b}$$

$$\text{and:} \qquad {}^{31}\theta_c = \arcsin(n_{31}) \tag{2.37c}$$

the term n_{31} arising because of the dependence of θ_2 on θ_1 and the subsequent cancellation of terms that include n_2. However, as long as $n_1 > n_2 > n_3$, we will find ${}^{31}\theta_c < {}^{21}\theta_c$, and the TIR condition at plane interface n_{32} will be met before that of n_{21}. This treatment can be expanded directly to as many layers as actually exist in the system. We consider, that the limiting angle in multi-layer systems will be the second-highest θ_c after the θ_c of interest, and will be called θ_{lim}. Further if $n_2 > n_1 > n_3$, TIR will still occur at n_{32} and there will be no θ_{lim}. This is illustrated in figure 2.3.

The multiplicity of θ_c will in many cases inherently limit the angles that can be explored at a specific interface using evanescent waves. However, as only n_{x1} is of concern for the first interface involving layer x in a multilayer system, and terms for layers 2 to $x - 1$ cancel, so an increase to n_1 will always improve the system.

2.6 Fluorescence Spectroscopy

Time-integrated fluorescence spectroscopy measures the emitted intensity of light from a sample, in response to an excitation wavelength λ_{ex}. This method typically measures either intensity as a function of emitted wavelength $I(\lambda_{em})$ with a fixed λ_{ex}, or intensity as a function of excitation wavelength $I(\lambda_{ex})$ at a fixed λ_{em}. The system is calibrated to accommodate the absolute emission intensity of the excitation light source as a function of wavelength, and also the sensitivity of the detector within its linear range[(ii)], such that the signal from the detector is directly proportional to the response of the sample, relative to the excitation intensity. The results are called *emission spectra* and *excitation spectra*, respectively.

2.6.1 Bulk Solution

In a solution that is sufficiently dilute, the absorption of light by an analyte allows even excitation of fluorophores in the excitation beam, and an even emission intensity throughout the beam path results. The excitation beam, if provided by passing broad-band light through a monochromator, can be spectrally narrow and specific. The emitted light is collected at 90° to the excitation beam and discriminated by wavelength, often with another monochromator. The polarisation of both delivery and collection, can be specified using e.g. Glan-Taylor prisms, and one should be set to the magic angle $\theta_m = \arctan(\sqrt{2}) = \arccos(\sqrt{1/3})$ relative to the other.

Quantum Yields

Barring the effects of very high absorption and assuming isotropic non-interacting fluorescers, the integrated intensity of fluorescence emission of a solution of fluorophores, is related directly to its quantum yield and absorbance *via* (*cf.* [1, p. 101]):

$$I_f = \Phi_f(1 - 10^{-A}) \tag{2.38}$$

Therefore for a fixed collection geometry that collects over a set solid angle of the emissions, across a series of solutions where the above holds true the differential of wavelength-integrated emission intensity with respect to $(1-10^{-A})$ will be linearly proportional to Φ_f, and all such differentials become comparable for identical experimental parameters such as slit width and temperature. Therefore, if they can be calculated, the gradients of $\int I_f.d\lambda_{em} = m(1-10^{-A}) + Const.$ relative to a known (reliable) reference standard, can be compared.

For a fully calibrated fluorimeter at constant λ_{ex}, the *relative method* for calculation of Φ_f proceeds by measuring absorbance and integrated emissions at constant path lengths, then regressing emission against $1 - 10^{-A}$ and using the following equation (*cf.* [29]):

$${}^{S}\Phi_f = {}^{R}\Phi_f \cdot \frac{m_S}{m_R} \cdot \frac{n_S}{n_R} \tag{2.39}$$

where a super- or sub-script R/S indicates a reference and a sample of unknown Φ_f, respectively. The method relies on the accuracy of ${}^{R}\Phi_f$, the calibration of the spectrometers and the quality of the spectra and appropriate preparation of the standard; taking particular care over the purity of the solvents.

[(ii)] the range of incident intensities where the voltage or count response of the detector is linearly related to the intensity

Ideally, the spectra of the emissions of the sample and the reference, should also match approximately in peak position and peak width.

It should simply be apparent at this point, that no such relative method can exist for determination of interfacial quantum yield.

2.6.2 Interfaces

Fluorescence spectroscopyat interfaces differs from the fluorescence spectroscopy of bulk solutions, mostly in the light delivery optics. The many considerations of this will be discussed in detail later. The method uses an evanescent wave generated by a totally internally reflected laser beam as the excitation source, and collects light in the optical plane, the optical axis of the collection lying near or at the normal of the reflection (the z-azis). The TIR element can be quite varied, and there is no single standard element that is used. Hemispheres, hemicylinders, dove prisms, microscope objectives and microscope slides have all been used as TIR elements in the literature. Element design generally considers that collection should be straightforward and the element itself relatively (or entirely) static, whilst beam delivery becomes complex yet adaptable.

The probed region of an interface is many times smaller than the volume excited in bulk solution studies. As a result, to generate a detectable fluorescence intensity either the detector must be sensitive, the light source intense, or both. This necessitates the use of photon-counting photomultiplier detectors, and lasers for excitation. As even low ambient light levels can destroy a powered photomultiplier, care must be taken.

The use of a non-tuneable laser as an excitation source, prohibits the collection of excitation spectra at an interface, which limits the information content provided by interfacial fluorescence measurements. The box diagram of EWIFS is shown in figure 2.4.

2.7 Time Resolved Fluorescence Spectroscopy

The use of a pulsed laser source for fluorescence measurements, provides a train of short pulses that each excite a population of fluorophores. The fluorophores each decay as per the kinetics described in §2.2.6. Therefore, the absorption being an instantaneous coupling to a transition moment, and the emission being an exponential following solvent/environment relaxation, the ideal decay profile of a single fluorophore is [30]:

$$I_f(t) = I_p(t) \otimes Ae^{-t/\tau_f} \tag{2.40}$$

where $I_f(t)$ and $I_p(t)$ are the intensities of the fluorescence and the laser pulse as a function of time, A is a pre-exponential factor, and τ_f is the lifetime of the fluorescent decay. The convolution of a response is illustrated in figure 2.5.

The box diagram of TCSPC for both the bulk and interface case is shown in figure 2.4. In reverse start-stop mode, the first photon from the fluorescence emission acts as a start signal for the time-amplitude converter (TAC), which ramps charge on a capacitor as a function of time until it receives a signal from the laser pulse clock [30]. The charge from the capacitor passes to the multi-channel analyser (MCA), which interprets the voltage and current as a time gap, which is then assigned a data bin according to the time interval it represents. The MCA produces a stream of prompts to the PC software to increment the respective bins, in this way generating a histogram of fluorescence intensity as a function of time.

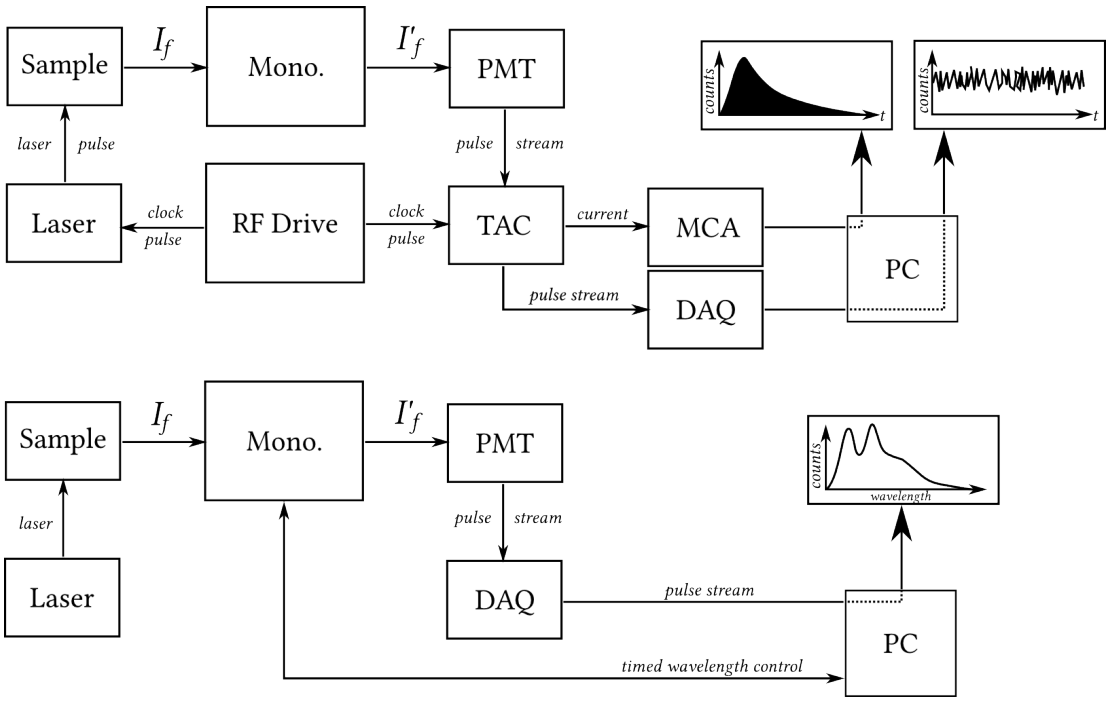

Figure 2.4: EWIFS Box Diagram: Box diagram representation of the EWIFS instrument. Arrows represent energy, data and processes, and are labelled accordingly. Top: Setup *tau*. RF Drive: radiofrequency driver. Mono: Monochromator. PMT: photomultiplier. TAC: time-amplitude converter. MCA: multi-channel analyser. DAQ: National Instruments data acquisition unit. The outputs are a time-resolved intensity and a time-integrated intensity. Bottom: Setup *lambda*. Labels as above, but the output is a wavelength-resolved, time-integrated signal.

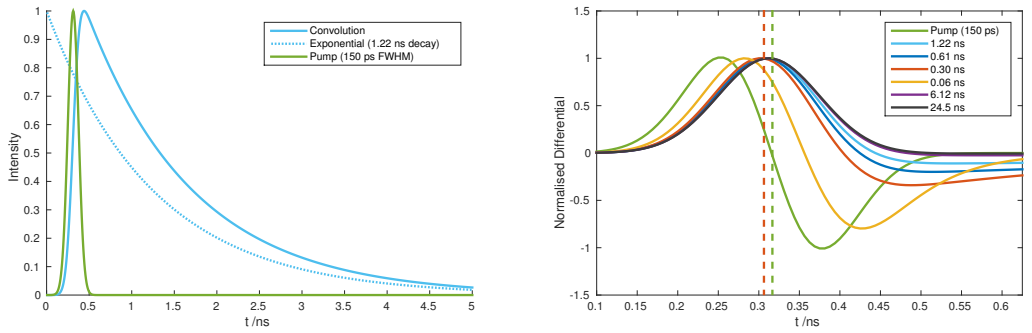

Figure 2.5: Modelled Covolved Responses: Left: The convolution of a Gaussian laser pulse profile with an exponential decay. Right: Even at high time resolution (channel width = 6.25 ps), the turning point of a convolved response, never strays more than 1.5 channels from the maximum of the pump unless the lifetime is shorter than the FWHM of the pump (shown: 150 ps).

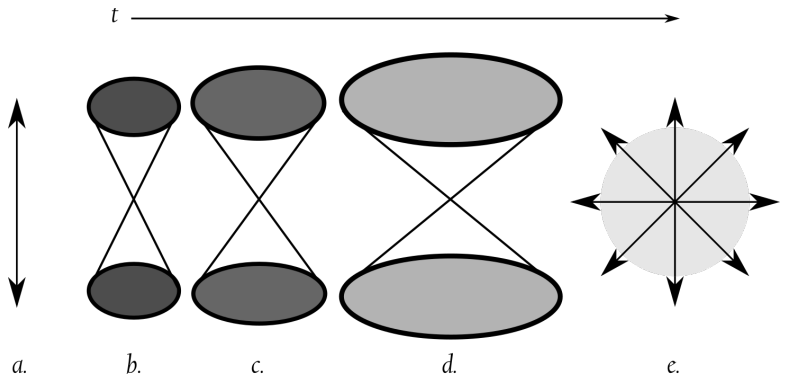

Figure 2.6: Rotational Diffusion: Left to Right: Rotational diffusion over time is the loss of the polarisation that was introduced by excitation. *a*) photoselection, only one transition dipole is shown, though these may be wholesale offset from the polarisation by an angle β to form a hollow cone of initial angles. *b,c,d*) progressive angular diffusion of a single set of initially parallel dipoles, the emissions becoming spread over a wider set of angles over time *e*) isotropic emission, the transition dipoles are randomly oriented relative to the detector.

The bins fall across a span of time equal to 50 ns, and the number of bins is defined by the *gain* on the MCA. The bin widths are shown in table 5.3 on page 109. As the time window is narrow compared to the repetition period of the laser clock (period = 1 μs), it is often necessary to introduce a delay (not shown) to ensure the signal falls within the window.

2.7.1 Quantum Yields

The quantum yield and lifetime of fluorescence for a bulk solution, help determine τ_{tot}, the *natural lifetime* of fluorescence, which is τ_f when $\Phi_f = 1$. From this, the quantum yield at an interface or in a solution or solvent is calculated as in equation (2.25). This can only be done for solutions or interfaces that produce single exponentials in discrete lifetime analysis.

2.8 Fluorescence Anisotropy

Fluorescence anisotropy r is a measure of polarisation retention of fluorescence emissions, given a polarised excitation. An anisotropy of zero typically represents fully depolarised (i.e. isotropic) emission. The orientation of the emission dipole relative to the excitation dipole, results on average in variable observable transfer of fluorescence intensity to the two remaining orthogonal polarisations [20]. Using time-resolved fluorescence measurements of emission polarisations parallel and orthogonal to the excitation polarisation, the depolarisation process is observed with or without time resolution. The progression of anisotropy is illustrated in figure 2.6.

2.8.1 Bulk Solution

For a single, non-interacting, freely decaying spherical emitter in isotropic solution, the time-resolved anisotropy is defined and modelled [20]:

$$r(t) = \frac{I(t)_{\parallel} - I(t)_{\perp}}{I(t)_{\parallel} + 2I(t)_{\perp}} \tag{2.41}$$

$$= r_0 \exp(-t/\tau_r) + r_\infty \tag{2.42}$$

where τ_r is the characteristic rotational correlation time, r_0 is the fundamental anisotropy, r_∞ is the limiting anisotropy at infinite time (t_∞)[iii], and $I(t)$ is a time-resolved decay of fluorescence intensity, where $\parallel$ / $\perp$ indicates parallel and perpendicular emission polarisation relative to the excitation polarisation.

The factors affecting overall depolarisation are several and act multiplicatively as per Soleillet's rule, which states that $r = r_0 \prod_i d_i$, where d_i are depolarisation factors [31]. This is also expressible thus:

$$r = d_1 \cdot d_2 \cdot d_3 = \frac{2}{5} \cdot \frac{3\langle\cos^2\beta\rangle - 1}{2} \cdot \frac{3\langle\cos^2\omega\rangle - 1}{2} \tag{2.43}$$

$$d_3 = \frac{3\langle\cos^2\omega\rangle - 1}{2} = [1 + (\tau_f/\theta_r)]^{-1} \tag{2.44}$$

where d_1 accounts for the excitation photoselection that is *per se* a fundamental maximum anisotropy, $\langle\cos^2\beta\rangle$ is the angular offset between excitation and emission dipoles, and $\langle\cos^2\omega\rangle$ is the angular displacement due to rotational diffusion. The expression for d_3 in equation (2.44) relates to the fluorescence lifetime τ_f and angle of rotation θ_r. The extreme of rotational diffusion (magic angle $\omega_m = \arctan(\sqrt{2})$) yields $r = 0$, but in the $\beta \geq \theta_m$ case, negative anisotropies are achievable. We achieve intuitively the diagnostic relation of $r_0 = d_1 \cdot d_2 = {}^1/_5 \cdot (3\langle\cos^2\beta\rangle - 1)$, and the form of the decay is dependent on $\langle\cos^2\omega(t)\rangle$; we may now explicitly liberate the time-dependence:

$$\theta_r(t) = \tau_f[r_0/r(t) - 1]^{-1} \tag{2.45}$$

For full derivations of the fundamentals, see [20], though it is straightforward now to calculate that for the solutions case $-0.2 \leqslant r \leqslant 0.4$. For completeness, it is worth noting that for alternative molecular shape approximations and chemical environments, the form of d_i changes to reflect implicit restrictions on rotational diffusion and molecular orientation. It is usually satisfactory to make the spherical approximation with the interpretative caveat that, for slightly aspherical small molecules some rotational degrees of freedom will be more favourable than others due to inertia, and that the orientation of the excitation transition dipole relative to the nuclear arrangement, is useful data obtainable from *density functional theory* (DFT).

2.8.2 Interfaces

The symmetry constraint of a planar interface allows two types of anisotropy measurement: *in-plane* (r_γ) and *out-of-plane* (r_ζ). In-plane r_γ measures depolarisation within the interfacial (xy) plane, given

[iii] $r_\infty \neq 0$ only for the case of hindered rotation.

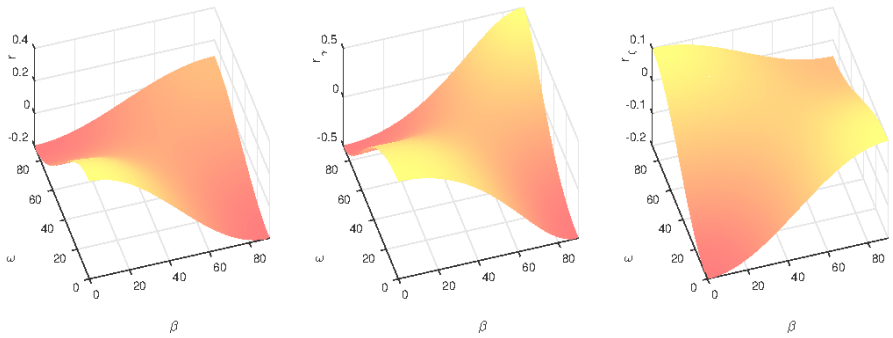

Figure 2.7: Soleillet Surfaces: Left to Right: A Soleillet surface for the solutions case r, interfacial in-plane case r_γ, and interfacial out-of-plane case r_ζ. All show the calculated anisotropy as a function of the angular offset β, and the rotational diffusion ω. A Soleillet surface shows all possible solutions to the Soleillet theorem $r = d_1 \cdot d_2 \cdot d_3$.

also excitement within that plane by s-polarised (y-axis) light:

$$r_\gamma(t) = \frac{I_{sy}(t) - I_{sx}(t)}{I_{sy}(t) + I_{sx}(t)} \tag{2.46}$$

where I_{ab} has polarisation a for excitation and b for emission measurement.

Out-of-plane r_ζ measures depolarisation back into the aforementioned xy-plane, given excitement orthogonally to that plane using p-polarised (xz-plane) light. Nominally the axis-wise polarisation of the p-polarised evanescent wave is in the z-axis, though it is straightforward to realise that there is a minor projection into the x-axis above the critical angle.

Equation (2.43) can be modified for the r_γ case as detailed in [16], to explicitly yield using our previous notation:

$$r_\gamma = d_1 \cdot d_2 \cdot d_3 = \frac{1}{2} \cdot \frac{3\langle\cos^2\beta\rangle - 1}{\langle\cos^2\beta\rangle + 1} \cdot \frac{3\langle\cos^2\omega\rangle - 1}{\langle\cos^2\omega\rangle + 1} \tag{2.47}$$

such that $-0.5 \leqslant r_\gamma \leqslant 0.5$. Similarly detailed in [16], is the transformation for the r_ζ condition:

$$r_\zeta = d_1 \cdot d_2 \cdot d_3 = -\frac{1}{5} \cdot \frac{3\langle\cos^2\beta\rangle - 1}{2} \cdot \frac{3\langle\cos^2\omega\rangle - 1}{2} \tag{2.48}$$

noting the reversal of sign, such that $-0.2 \leqslant r_\zeta \leqslant 0.1$, and we may also define (noting that for r_ζ, the first differential of $r_0(\beta)$ is reversed in sign):

$$r_\zeta(t) = \frac{I_{py}(t) - \frac{1}{2}[I_{sy}(t) + I_{sx}(t)]}{I_{py}(t) + I_{sy}(t) + I_{sx}(t)} \tag{2.49}$$

The possible values of $r(\beta, \omega)$ are shown in figure 2.7 as Soleillet surfaces.

2.9 Conclusion

This chapter demonstrates the straightforward nature of the photophysical *theory* itself, and yet highlights the difficulty of making interfacial measurements in a meaningful way. The most general assumption made by this thesis, is that the relationship between photophysical behaviour in the bulk and interfacial environments is, although not simple, able to be simplified *via* some key statistics.

Namely τ_{tot}, Φ_f, intensity projections I_{xyz} in the rarer medium and absorptivity κ, the latter of which affects only measurements and calculations involving p-polarisation and d_p^* resolution.

This concludes the theoretical basis of general photophysical phenomena and fluorescence spectroscopy.

Chapter 3

Instrumental Design

Abstract

A spectrometer is described from design and programming, to testing and validation. The theoretical concerns of the instrument as applies to measurements are described. A piece-wise description of the instrument follows, with justification for each part. The programs are described in a general way. The procedures for alignment, calibration and spectral correction are described in detail with justification, and the effects of the individual parts are related to the theoretical concerns. The system is tested against a calibrated fluorimeter and an attempt is made to replicate a EWIF spectrum from the literature. The enclosure for the instrument is tested for light leaks and found satisfactory. The operating bandwidth of the instrument is nominally 4.6 nm. The wavelength accuracy is ±0.19 nm.

—

A spectrometer is to be designed, which meets these criteria: It must have the capability to deliver a continuous wave laser beam of variable, controlled polarisation to an internal reflection element, the purpose of which is to excite a sample by an evanescent wave at a determinable varied incidence angle at sub-degree precision. For safety reasons this instrument entire must be enclosed, and beams terminated by beam stops of some design. Light generated by fluorescence must be collected from the excitation volume, be accurately discriminated by polarisation ± 5^o and wavelength ± 0.5 nm, and the intensity of this light accurately recorded with a photon counting detector. The instrument must also have the ability to deliver a pulsed laser of similar controllability to the continuous wave system, for the purposes of achieving time-correlated single photon counting (TCSPC).

3.1 Instrumental Concerns

This preamble section is about the intersection of instrumental design with the established theory. It includes mostly the practical reasoning behind the use of multiple types of G-factor that will be determined by the end of this chapter.

3.1.1 Bulk Solution Anisotropy Measurements

The measurement of $I(t)$ by Time-Correlated Single Photon Counting (TCSPC) must necessarily accommodate loss of counts, as the limiting count-rate to avoid signal distortion from pile-up error, is nominally 1% of the pulse repetition rate [30]. Instrumental live-time (LT) is distinguished from

elapsed real-time, by excluding “dead time" wherein the laser pulse-clock has no associated photon signal within a narrow window of time, or experiences signal outside that window. In the measurement of $r(t)$, $I(t)$ for each polarisation has equivalent LT, such that at t_∞, $r(t) \rightarrow 0$ as in the perfect instrument the traces become equivalent[(i)].

The G-factor at a given emission wavelength is an instrumental correction coefficient that scales $I(t)_\perp$, modifying equation (2.41) in order to accommodate differences in monochromator throughput, giving equation (3.2):

$$G(\lambda) = \frac{I(\lambda)_\parallel}{I(\lambda)_\perp} \tag{3.1}$$

$$r(t)_\lambda = \frac{I(t)_\parallel - GI(t)_\perp}{I(t)_\parallel + 2GI(t)_\perp} \tag{3.2}$$

Alternatively, if the assumptions hold true regarding $r(t) \rightarrow 0$, then it is rather more straightforward and reproducible to *tail-match* decays by calculating G from $\int I(t).\mathrm{d}t$ over a range of t for which $log(I(t)_\parallel) - log(I(t)_\perp) = c(t)$ where the constant $c(t) = \log(G) \pm \sigma(t)$, where $\sigma(t)$ is a heteroscedastic uncertainty. Thus over this range we redefine G semantically:

$$G_{int} = \frac{\int I(t)_\parallel.\mathrm{d}t}{\int I(t)_\perp.\mathrm{d}t} \tag{3.3}$$

Given then, that G has become an internally-determinable factor, the need for equivalent LT and constant G is negated, and traces of $I(t)$ can instead be acquired with arbitrarily high signal-to-noise ratios. A representative value of G *via* equivalent LTs and equation (3.3), does however still act as a fiducial metric.

In the described solution, τ_r should be on the scale of tens to hundreds of ps for small molecules [20, p. 304–305], extending to the ns range only for molecules with very large radius.

3.1.2 Interfacial Anisotropy Measurements

The EWIFS setup makes interfacial anisotropy singularly distinguishable from bulk anisotropy measures in a standard right-angle collection geometry, insofar that the optical element itself causes systematic overestimation of r in both the time and frequency domains, due to concomitant angular differences in both collection efficiency and fluorescence intensity distribution. As the possibility of high local viscosity and restricted rotation becomes more real at interfaces, even in contact with solutions of small fluorophores for which the spherical approximation holds, the assumption of $r(t) \rightarrow 0$ is invalidated. The technique becomes reliant on accurate LTs and appropriately-derived correction factors.

[(i)] in practice t_∞ is simply a time significantly longer than the apparent τ_r

Interfacial measurement correction of $r_\gamma(\lambda)$ should theoretically be:

$$G_{op} = \text{mean}\left[\frac{G_+(\lambda)}{G_-(\lambda)}\right] = 1.10 \pm 0.01 \tag{3.4}$$

$$G_{LT} = \frac{LT_{sv}}{LT_{sh}} \tag{3.5}$$

$$G_{ang}(\Delta\theta) \approx \cos(\Delta\theta) \qquad 0.96 \leqslant \cos(\Delta\theta) \leqslant 1 \tag{3.6}$$

$$G_{com} = G_{op} \cdot G_{LT} \cdot G_{ang}(\Delta\theta) \tag{3.7}$$

$$r_\gamma(\lambda) = \frac{c_v(\lambda)(I'_{sv}(\lambda)) - G_{com} \cdot c_h(\lambda)(I'_{sh}(\lambda))}{c_v(\lambda)(I'_{sv}(\lambda)) + G_{com} \cdot c_h(\lambda)(I'_{sh}(\lambda))} \tag{3.8}$$

where G_{op} is a ($\approx \lambda$-invariant) G-factor correction coefficient for the optical element, $G_\pm$ is the G-factor with or without the optical element, $G_{ang}(\Delta\theta)$ is a correction factor for anisotropic emission intensity within the optical plane, $\Delta\theta$ represents the angle within the optical plane between the optical axis of the collection apparatus and the z-axis of the interfacial plane, G_{LT} is a correction factor for LT discrepancy, $c(\lambda)$ is an instrument response correction factor specific to the designated polarisation in the absence of an optical element (accounting for the G-factor of the monochromator, λ-dependent quantum yield of the detector, and attenuation by the collection apparatus), and $I'(\lambda)$ is a background-subtracted intensity profile. It is assumed, that time-decorrelated signal will be negligible. By a similar logic, interfacial corrections of $r_\gamma(t)$ should proceed:

$$r_\gamma(t) = \frac{I_{sv}(t) - G(\lambda) \cdot G_{com} \cdot I_{sh}(t)}{I_{sv}(t) + G(\lambda) \cdot G_{com} \cdot I_{sh}(t)} \tag{3.9}$$

Before applying the same compensation to the definition of r_ζ, we must include a new term to correct for the differences in s- and p- excitation. From equations (2.34a) through (2.34c) we now define (invariant of the incident field E_1 and $(c\varepsilon_0 n_{21}/2)$ by factorisation):

$$G_E(n_{21}, \theta_i) = \frac{E_{2y}^2}{E_{2x}^2 + E_{2z}^2} \propto \frac{\int_0^\infty I_s.\mathrm{d}z}{\int_0^\infty I_p.\mathrm{d}z} \tag{3.10}$$

The purpose of G_E is, assuming an isotropic distribution of fluorophores at an isotropic interface, to correct for the p-polarisation field-strength bias, which is in essence the ratio of the integrals of the two exponential fields with respect to dz, making spectra comparable in terms of total intensity.

$$r_\zeta(\lambda) = \frac{c_v(\lambda) \cdot I'_{pv}(\lambda) - \frac{1}{2}[c_v(\lambda) \cdot I'_{sv}(\lambda) + G_{com} \cdot c_h(\lambda) \cdot I'_{sh}(\lambda)]}{c_v(\lambda) \cdot I'_{pv}(\lambda) + c_v(\lambda) \cdot I'_{sv}(\lambda) + G_{com} \cdot c_h(\lambda) \cdot I'_{sh}(\lambda)} \tag{3.11a}$$

$$r_\zeta(t) = \frac{G_E(n_{21}, \theta_i) \cdot I'_{pv}(t) - \frac{1}{2}[I'_{sv}(t) + G_{com} \cdot G(\lambda) \cdot I'_{sh}(\lambda)]}{G_E(n_{21}, \theta_i) \cdot I'_{pv}(\lambda) + I'_{sv}(\lambda) + G_{com} \cdot G(\lambda) \cdot I'_{sh}(\lambda)} \tag{3.11b}$$

The case of an anisotropic distribution of excitation dipoles becomes deducible after full correction, and so then we might demonstrate or accept some or all of the following as part of the analysis:

1. that the excitable populations for a given projection are different in number by some calculable amount, after proving Φ_f invariance
2. that the emissive states have calculably different Φ_f, and thus different brightness factors
3. that the excitation and emission dynamics are convolved in a manner that is not straightfor-

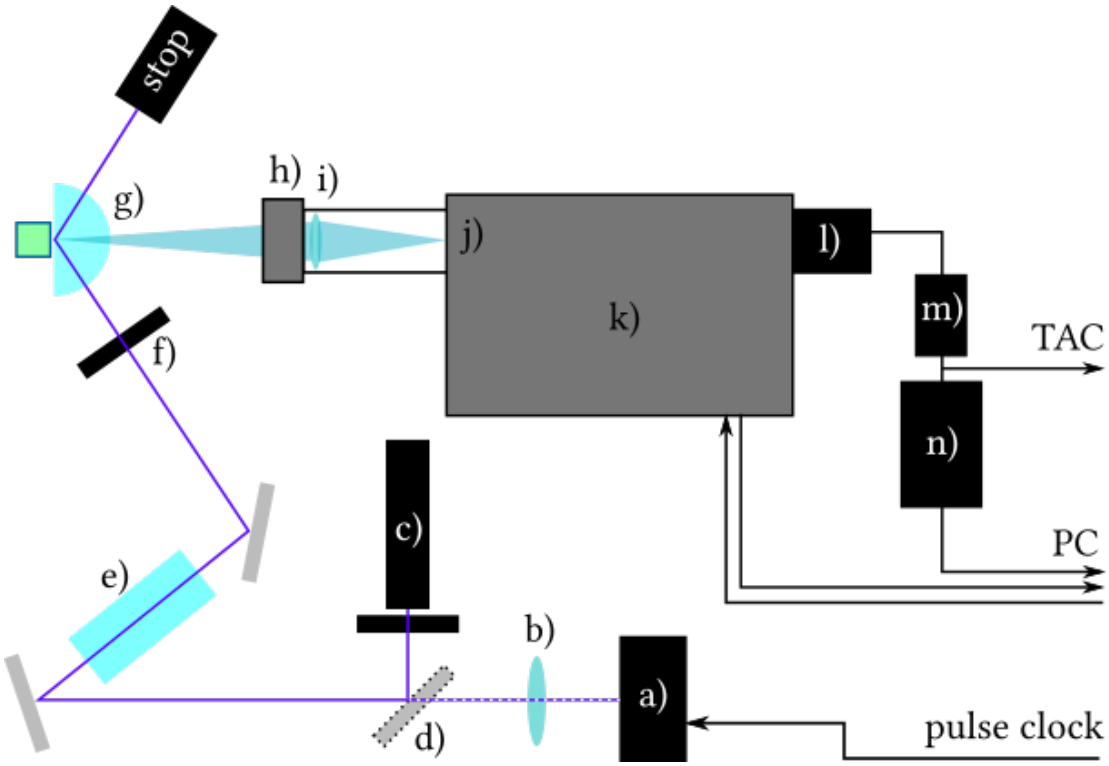

Figure 3.1: EWIFS Spectrometer Layout: Schematic representation of the EWIFS instrument, viewed from above. Note the collinearity of the CW and pulsed beams after the flip-mirror. *a) pulsed laser; b) collimation lens; c) CW laser; d) flip-mirror; e) double fresnel rhomb; f) scatter cleanup aperture; g) TIR element and beam stop; h) Glan-Thompson prism; i) f-matching lens; j) position of filter wheel; k) monochromator; l) photomultiplier; m) PMT power control; n) DAQ unit.* Beam path shown in purple, data and signal travel along black arrows.

wardly resolvable

3.2 Components

The components of the designed spectrometer, as lain out in the schematic representation in figure 3.1, are discussed piece-wise in this section.

3.2.1 Lasers & Delivery Switch

The system has two lasers, a 371 nm pulsed laser (IBH/Horiba NanoLED: N-375L) 4 pJ/pulse running at 1 MHz repetition rate, and a 377 nm continuous wave laser (Power Technology: IQ1C16(375-20)G2), total output 13 mW. For brevity, these will be specified as simply pulsed or continuous wave (CW) respectively. Both lasers are set *(s)*-polarised by default. The CW laser passes through an interference filter (Comar Optics: 380 IL 12) to remove extraneous output and an iris aperture to set the beam diameter to <1 mm.

The pulsed source has a beam divergence, which over the path length of beam delivery yields a beam diameter much greater than 1 mm. It passes through a collimating lens to correct this, and at the flip mirror location (figure 3.1.d) the CW and pulsed laser paths become collinear. The state of the

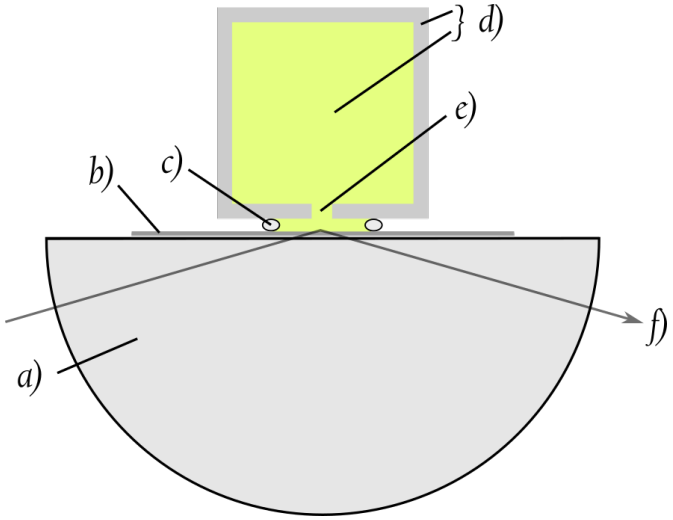

Figure 3.2: TIR Element: Schematic representation of the TIR element, viewed from above. *a) prism; b) substrate, optically-coupled to prism; c) PTFE o-ring; d) solution held in cuvette/cell; e) pore through which solution contacts substrate; f) an example TIR light ray.*

flip-mirror determines which laser is delivered to the TIR element.

An optional double Fresnel rhomb (Comar Optics: 02 JR 16, BK7 glass refractive index 365 nm = 1.5363, lateral offset 21.6 mm, angle 55 ± 5°) in the beam path rotates the polarisation of the lasers to *(p)*-polarisation, though the transmission for both wavelengths is 0.74. The two fixed mirrors in the system in a z-configuration set the level and angle of the beam, whilst the second iris aperture on a vertically and horizontally adjustable mount eliminates any forward-scattered light prior to ultimate beam delivery.

3.2.2 TIR Element & Stage

The current design of the TIR element is based upon earlier versions designed and built by Dr Valentina Manici of Beeby Group, with which it has in common the exact models of translation-rotation parts, and prism. Historically to Beeby Group, a Multiple-TIR element was designed first by Dr Kate Nicholson for use with microscopes.

The optical system used to create TIR is centred on a hemicylindrical prism (ThorLabs: LJ4107 - formally a cylindrical lens, referred to here as a prism in order to distinguish its usage), which turns upon its cylindrical axis. Immersion oil (Aldrich 10976, $n = 1.518$) couples a soda glass substrate (VWR 631-0154) to the plane face of the prism. Attached within a housing, a cell is held pressed in place by screws, and the vertical alignment of the prism in the (x,y)-plane is adjustable by bracing the plane-face against machined-flat aluminium supports using plastic-tipped grub-screws. In this way, both the prism and cell are fully adjustable as required within the housing.

The housing of the element is of machined aluminium, and is attached *via* screws to two stacked lateral-adjustment stages set orthogonal to one another, allowing translation of the housing in the z- and y-directions within the laboratory frame described in figure 3.3. This is in turn mounted upon a rotation stage with fiducials at each degree mark. The TIR element is shown in figure 3.2.

3.2.3 Collection Optics

Optimal throughput through a monochromator system is reliant upon precise positioning as with all imaging systems, but also it relies upon f-matching the in-plane light rays to the f-number of the monochromator ($f_{mono} = 4.1$). A silica lens (diameter 25 mm, focal length 100 mm: $f_{lens} = 4.0$) achieves matching. A Glan-Thompson polarising prism (Melles Griot, calcite, 30 mm path length, $n_\varepsilon = 1.486$, 5^o increment fiducials) discriminates polarisation of collected light. When ray-tracing, the refractive index experienced by the extraordinary ray causes a slight extension of the effective focal length of the matching lens on the side of the TIR element, which must be duly accommodated - similarly the effect of the interference filter requires an offset on the side of the monochromator. All optics in this setup are mounted securely into or on a single length of 25 mm diameter TubeMount (Comar Optics), which in turn fits securely to the monochromator *via* a machined aluminium adapter.

The aperture of the polariser is square, and the focal length of the prism is not equivalent in the *(x,z)* and *(y,z)* planes, therefore the collection efficiency of light by the prism will be non-equivalent between collection polarisations despite the peri-normal condition of the system. This is to be measured in section 3.3.

3.2.4 Monochromator & Detector

Light from the excitation volume is delivered by the collection optics to a USB-controlled monochromator (Bentham: TMc300 model, 252 order-sorting filter wheel, grating T312H0U25 1200 gr/mm, working range 250-1100 nm, reciprocal dispersion 2.70 nm/mm, manual micrometer slits). The manufacturer specification states a spectral accuracy ±0.2 nm and reproducibility ±0.05 nm across the working range of any installed grating. The fixed entrance/exit slit width of 3 mm for all experiments (excepting wavelength calibration), results in a spectral bandwidth of 4.6 nm.

The monochromator is controlled via USB by two programs written in LabVIEW: `EWIFScan.vi` and `EWIFSCAN-timebase.vi` as detailed in §3.2.5.

At the exit slit of the monochromator, a photomultiplier (Hamamatsu H10682-01) fitted with a proprietary voltage-controlled circuit-breaker to avoid overload, is powered by and relays TTL pulses to a data acquisition (DAQ) card (National Instruments: USB-6210). It is fitted with a voltage-detecting circuit breaker that cuts power to the PMT in the event that the PMT voltage output goes beyond the limit of its linear working range (+4 V).

There are two main configurations for data collection from the PMT and monochromator, nominally *tau* and *lambda*. Both are represented in figure 3.1. In the tau configuration, the monochromator is controlled by PC to fix the observation wavelength and the TTL signal from the PMT passes directly to a multi-channel analyzer (MCA). The MCA is connected to the pulsed laser control, which generates a RF clock signal for both the MCA and the laser unit. The flip-mirror is down, using the pulsed laser. In the lambda configuration, the MCA is disconnected and the TTL signal passes to the DAQ unit, which routes the pulses to the PC for time-integration as part of a scan of intensity as a function of wavelength. The flip mirror is up, using the CW laser.

3.2.5 Programs Used & Written

The monochromator was controlled in LabVIEW using `ewifscan.vi`, which is included in the supplementary data. This program calls the manufacturer's DLL files to simultaneously handle the USB control of the monochromator and report accurate wavelength values, whilst itself handling the

timing and loop iterations necessary to produce a wavelength scan. The output is a plain text file of uncorrected photon counts.

The data from the lambda configuration was visualised and corrected both in `specview .vi` and in MATLAB®, and presented using MATLAB®. The data from the tau configuration was collected using the software provided with the MCA, exported to plain text with LabVIEW, processed using MS Excel and MATLAB®, and presented using MATLAB®.

3.3 Calibration & Validation

3.3.1 System Alignment

The laboratory frame is shown in figure 3.3. The optical plane lies within *(y,z)*. A ray propagating within the optical plane, possessing plane polarisation *(s)*- or *(p)*-, totally internally reflects against the reflecting plane. The precise angle of the detector relative to the z-axis varies by as much as 15 degrees during a VA-EWIFS experiment, though this theoretically has no significant effect [16].

The TIR element and lasers are aligned by analysis of specular reflections, requiring six major steps total.

Firstly, the prism is approximately centred with a slip in place. The (x,z)-stage is adjusted until its central axis is within 1 mm of the axis of rotation. The prism is aligned and accurately centred using specular reflections; the grub screws are adjusted to tune the "uprightness" of the prism and (x,z)-position until the specular reflection from the curved face of the prism does not deviate during the rotation of the prism.

The laser is normalised to the prism's curved face: the beam must lie in the *(x,z)*-plane, the centre of the specular reflection from the curved face is collinear with the incoming beam, and the centre of the specular reflection from the flat face is collinear with the incoming beam when $\theta_i = 0°$.

A *fine adjustment* of the angle of the laser beam is made in (x,z) until a laser scatter peak at ≈ 565 nm is minimised during TIR. This occurs due to the variation in the exact thickness of the slip, and may not always be necessary. The adjustment is very slight.

The tau configuration is aligned by passing the tau laser through the collimating lens and three apertures that lie along the path of the CW laser. Before setting up apertures, the tau laser must therefore have its central axis collinear with the aligned CW laser *both with and without the collimating lens*.

Finally, the position of the double Fresnel rhomb is adjusted by ensuring that the back-reflected rays from the laser are collinear. This must be repeated every time this is inserted in the system.

3.3.2 λ-calibration

The wavelength calibration used two light sources; an OceanOptics Hg-Ar standard lamp to calibrate and a Ne lamp to validate. The monochromator relates the step-motor position of the diffraction grating

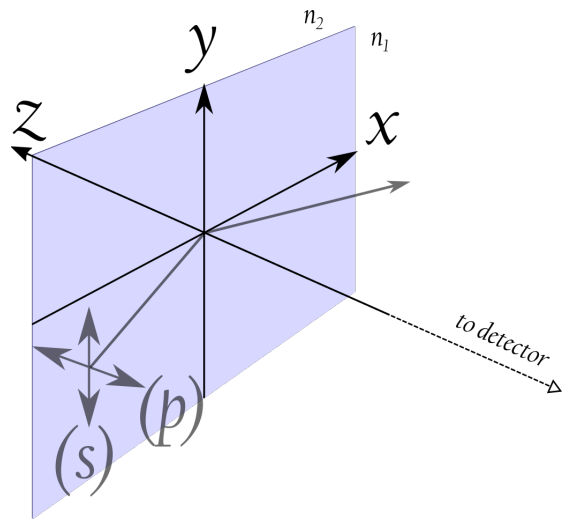

Figure 3.3: Laboratory Frame: The laboratory frame axes are defined relative to the plane of reflection *(x,y)*, which lies *in* the plane of the interface, parallel to the plane face of the prism and thus the frame rotates with the TIR element.

to the wavelength of maximum throughput efficiency *via*:

$$\lambda = 2d \sin\theta \cos\beta \tag{3.12a}$$

$$\cos\beta = 0.9727 \tag{3.12b}$$

$$\theta = \arcsin\left[\frac{\lambda \cdot R_D \cdot 10^{-6}}{1.9454}\right] = \arcsin\left[\frac{\lambda}{2d\cos\beta}\right] \tag{3.12c}$$

$$x_\lambda = \theta\alpha\left(\frac{500,000}{360}\right) + x_0 \tag{3.12d}$$

where d is the inter-groove spacing of the grating, θ is the angle of the incoming ray relative to the normal angle, β is a fixed function of the system geometry, R_D is the groove density of the grating in grooves/mm, the zero ordinate x_0 is the integer step position of zero order diffraction, x_λ is the step position required to produce throughput of wavelength λ, and α is a coefficient. When the value of x_λ would be a non-integer, the monochromator chooses the nearest integer step and reports the nm value of λ to the nearest pm. This is not the value used to create a spectrum, however, as these values would make it less straightforward to compare spectra between calibrations. From the above equations, it is straightforward to calculate, that the 385-600 nm range with $\alpha = 1$ represents exactly 11,088.84915 steps for a whole spectrum, yielding 51.57 steps/nm to 2 d.p. with a range of 2.31 steps. Meaning that at an average of 0.019 nm/step, the given values of λ have a systematic resolution of $\pm 9.69 \times 10^{-3}$ nm (one average half-step of the motor), and any spectral step size below this has no meaning to the monochromator. The limiting wavelength accuracy of the spectrometer is therefore nominally ±10 pm and increments smaller than this have no meaning.

The practical implication of equation (3.12d) is that calibration is completed by setting two parameters in a setup file: α and x_0. We set x_0 iteratively; first get an approximate value for x_0 by observing the resultant position of the zero-order line directly inside the monochromator at $\lambda = 0$, and then fine-tune the position by maximising intensity measurements with the monochromator reassembled.

Hg-Ar Peak	Literature	|Residual|	Ne Peak	Literature	|Residual|
312.50	312.57	0.07	597.40	597.46	0.06
313.00	313.15	0.15	602.80	602.99	0.19
364.90	365.01	0.11	607.20	607.43	0.23
366.30	366.32	0.02	609.60	609.61	0.01
404.50	404.65	0.25	614.20	614.30	0.10
407.60	407.23*	0.47	616.20	616.35	0.15
435.60	435.83	0.23	621.60	621.72	0.12
546.00	546.07	0.07	626.60	626.64	0.04
576.80	576.95	0.15	638.40	638.29	0.11
578.80	579.06	0.26	640.20	640.22	0.02
624.70	624.31*	0.39	650.60	650.65	0.05
696.40	696.54*	0.14	653.20	653.28	0.08
763.30	763.51*	0.21	659.80	659.89	0.09
	Mean	0.19		**Mean**	0.16

Table 3.1: Calibration Table for Hg-Ar and Ne lamps: The modulus of the residual between the peak positions in nm given by the EWIFS instrument, and the corresponding literature values of Hg and Ar emission lines as given by [32]. The mean value characterises the wavelength accuracy of the instrument: ±0.19 nm. Argon peaks denoted with an asterisk (*). The neon equivalent is given to the right. The spectra from which these positions were found are presented in figure 3.4.

We determine α, which is close to 1, in a similar manner by making small changes to the value until, for a 0.1 nm increment scan, the centroids of the calibration peaks are on average within 0.2 nm of their literature positions. We state therefore the wavelength resolution of the instrument as 0.2 nm, meaning that the spectral bandwidth of the monochromator is a more significant limitation in the determination of spectral features in fluorescence. The spectral bandwidth of the monochromator is the FWHM of a delta function (such as an atomic emission line) passing through it: the shape of the signal produced is a convolution of the entrance and exit step functions, such that a delta function passing through two identical thin slits at a spectral increment smaller than the bandwidth, will produce a triangular peak with its apex at the centroid. The spectrum of the calibration-validation sources is given in figure 3.4 and the table of values for the calibrated instrument is given in table 3.1.

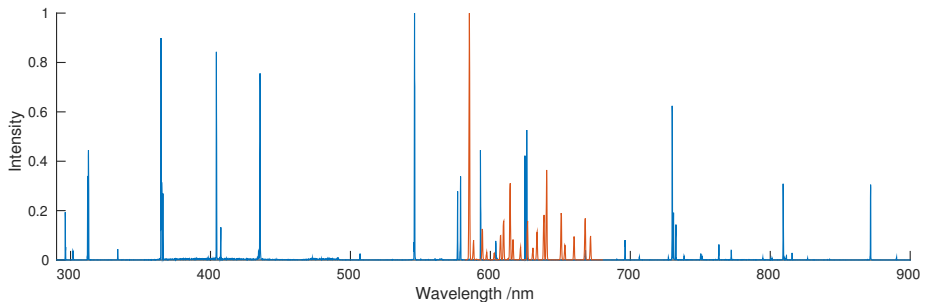

Figure 3.4: EWIFS Calibration-Validation Spectra: Shown for demonstration. Blue: HgAr lamp. Red: Ne lamp. The most intense peaks were picked automatically in MATLAB®.

3.3.3 Correction Files

A wavelength-calibrated system can have its output calibrated to conform to a standard. An OceanOptics standard lamp with known quantum intensity $I_Q(\lambda)$ was passed through a spectrolon integration sphere (equal transmission for all wavelengths), and its output was collected by the collection optics. A spectrum of this output was collected by an in-specification Horiba JY Fluorolog with a collection polariser set to θ_m, and compared to $I_Q(\lambda)$ to confirm that the output from the integration sphere was appropriate.

The following equation describes the correction procedure. This was applied to the monochromator throughput at $\theta = 0°$, $\theta = 90°$ and $\theta = \theta_m$.

$$I_Q(\lambda) = c(\lambda) \cdot I_M(\lambda) \tag{3.13}$$

where I_M is the uncorrected monochromator output and c is a correction factor. In this way, the standard lamp output measured by the instrument matches its true quantum intensity. The correction factors and an optics G-factor (*vide infra*) are shown in figure 3.5.

3.3.4 G-factors

The G-factors at each wavelength are calculated in either of the following ways, based on the definition in equation (3.1):

$$G(\lambda) = \frac{c_h(\lambda)}{c_v(\lambda)} = \frac{I_v(\lambda)}{I_h(\lambda)}$$

where subscript *h/v* indicate horizontal (x-axis) and vertical polarization (y-axis) collection polarisation, respectively. The calculation of an optics G-factor is from a linear regression of $G_{-}(\lambda)$ against $G_{+}(\lambda)$, the result of which has been given previously. Experimentally, the necessary spectra are acquired by placing the output of the integration sphere directly at the polariser, and also passing the light through a 400 μm optic fibre to the point where the fluorescent spot would exist at the prism. The intrinsic polarisation excess introduced by the prism might have been partly explained by Fresnel's reflectance equations [27, Chapter 4]. These would result in equal transmission of all polarisations of fluorescent emission in the *(x,z)*-plane but an incremental excess of y-polarised light transmission as the angle between the emitted ray and the (x,z)-plane increases - however, the effect of this is minimised along the optical axis. The value $G_{op} = 1.10$ also does not change when the output port of the integration sphere is directly behind the prism, without using an optic fibre to mimic a fluorescent spot, therefore it is probably due to the curved face of the prism.

It is suggested then, that the factor can be explained by the path of the rays through the polariser; when diffuse light enters the polariser with even intensity, the ensemble of rays doesn't yield any bias in its direction through the system. Light passing through the prism is uneven in its intensity, and the path taken through the polariser becomes significant with regard to how well it is directed toward the slit. The extraordinary ray that is (p)-polarised with respect to the air-gap of the Glan-Taylor polariser is transmitted by it, whilst the (s)-ray is reflected. Light not incident at exactly the normal angle to the front face of the polariser is deviated according to Snell's law. When the polariser is rotated, if it does not rotate perfectly about the optical axis, the deviation of the rays passing into the collection apparatus will shift, and this only becomes apparent once the intensity of light entering the polariser

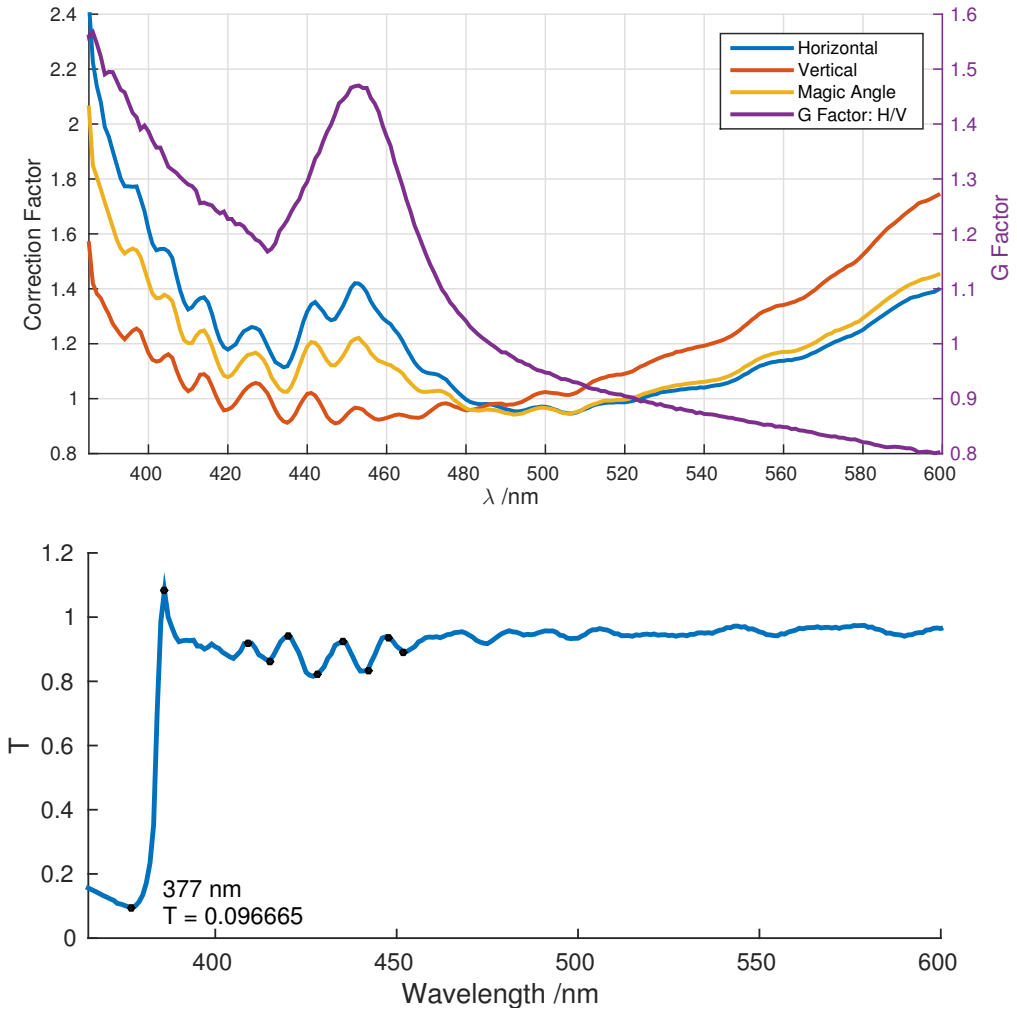

Figure 3.5: Correction Factors: Top: The correction factors for the three Glan-Taylor polariser positions, calculated in equation (3.13). The interference from the cutoff filter in the monochromator filter wheel is plainly visible, but cancels in the calculation of G from c. Bottom: The transmission of the filter according to the EWIFS monochromator. The feature at 386 nm is due to an un-corrected time delay, caused by the filter wheel changing position in later revisions of the software. The most prominent features of the transmission spectrum are marked, and occur at 409, 415, 420, 427, 435, 441, 447, and 452 nm. Note that the scales of the top and bottom figures are not comparable - the top figure shows the useful portions of the correction spectra and excludes anything below 386 nm, the bottom figure shows also the transmission of the laser.

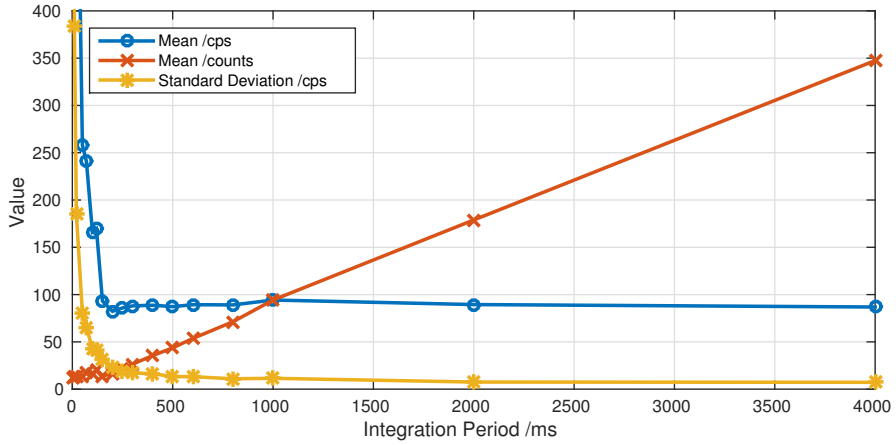

Figure 3.6: Quantitative Effect of Integration Time: Average values of flat 200-point "dark spectra", as a function of integration time. Below 150 ms, both the mean normalised values and the relative standard deviation (RSD) increase sharply. A 200 ms integration time produces means comparable to multi-second integration times, at the cost of slightly increased RSD.

is not diffuse and even.

3.3.5 Dark Current

The Hamamatsu photon-counter produces a constant count-rate in the dark, called *dark current* or *dark counts*. This dark count is easily subtracted from a fluorescence spectrum using a spectrum of a blank, but it is also well-placed for characterising the quantitative effect of integration time of the monochromator, as it is monochromator independent. The integration time is the residence time of the monochromator grating at a step motor position x_λ before moving to the next value in the scan. As the counter continues to count pulses from the PMT in order to expedite a scan without having to continually start and stop the counter, and there is a finite gap of time between loops, there exists a between-integration count during movement of the grating and after reporting the photon count, that adds to the total loop count.

To account for these time deviations that occur during loops, LabVIEW normalises the photon count for each whole loop (move → integrate → report) by the recorded loop time with millisecond accuracy. As integration time increases, the relative magnitude of deviation between loops must decrease, and vice versa; as the integration time decreases, the loop time decreases and the normalised value must become larger, as the limiting count occurring between loops ceases to get proportionally smaller. This is shown in figure 3.6. It is demonstrated by that figure, that any integration period at or below 150 ms produces a mean that is *not* comparable to that of longer integration periods, and so the minimum integration time for this instrument is set to 200 ms.

3.3.6 System Testing

The performance of the EWIFS instrument in lambda-mode was tested against a Horiba JY Fluorolog. A sample of 0.2 μM OB49 in dimethylsulfoxide (DMSO) was prepared and spectra of solvent and solution were acquired by both instruments. In both cases, the collection polarisation was at the magic angle,

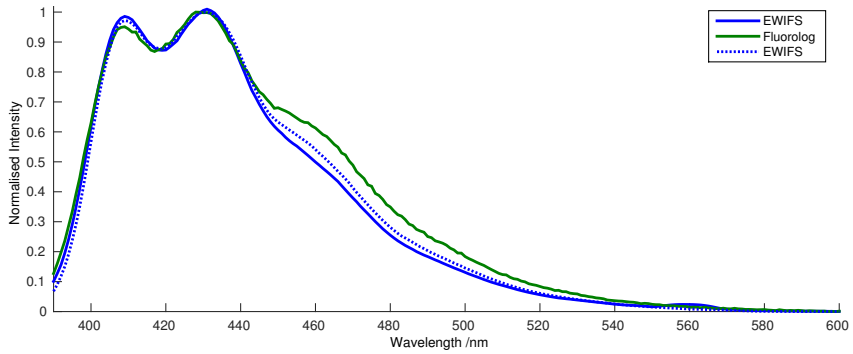

Figure 3.7: Comparison of EWIFS Instrument with Horiba Fluorolog: The two instruments produce comparable spectral forms for an OB49/DMSO standard.

excited at 377 nm. The EWIFS beam delivery was (*s*)-polarised and delivered below the critical angle. The EWIFS instrument collected a second spectrum with a fluorescence cuvette in place of the prism. The beam was diverted with prisms to mimic a right-angled fluorescence experiment. The result is shown in figure 3.7.

A stack of 20 glass slips of the brand used for EWIFS were crushed carefully in a pestle and mortar and transferred to a quartz tube in an integrating sphere. The emission spectrum of the empty quartz tube was subtracted from the profile of the filled tube. The excitation was at 375 nm. The fully corrected fluorescence of glass slips is presented in figure 3.8.

The fluorescence of the glass substrates in the visible region is appreciably low across the wavelengths of interest (385–600 nm), but must be subtracted from fluorescence profiles on a case-by-case basis as part of a background spectrum.

The effectiveness of the EWIFS enclosure was tested by acquiring a spectrum of an empty TIR element with the lasers off and the room light on. The spectrum was taken with the enclosure open and closed. The spectra are presented in figure 3.9.

The bandwidth of the instrument at a working slit-width of 3 mm is calculated from figure 3.9. It is given as the FWHM of the 436 nm line of mercury, which is 4.6 nm. The atomic line is assumed to be a Dirac delta function.

The TIR aspect of the EWIFS instrument was assessed using the literature spectrum for auramine

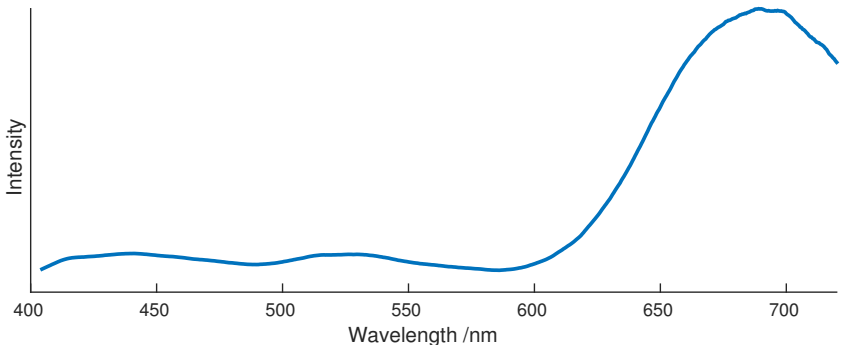

Figure 3.8: Glass Autofluorescence: Fluorescence emission of glass substrates, crushed. This fluorescence is exaggerated here by sheer excitation volume.

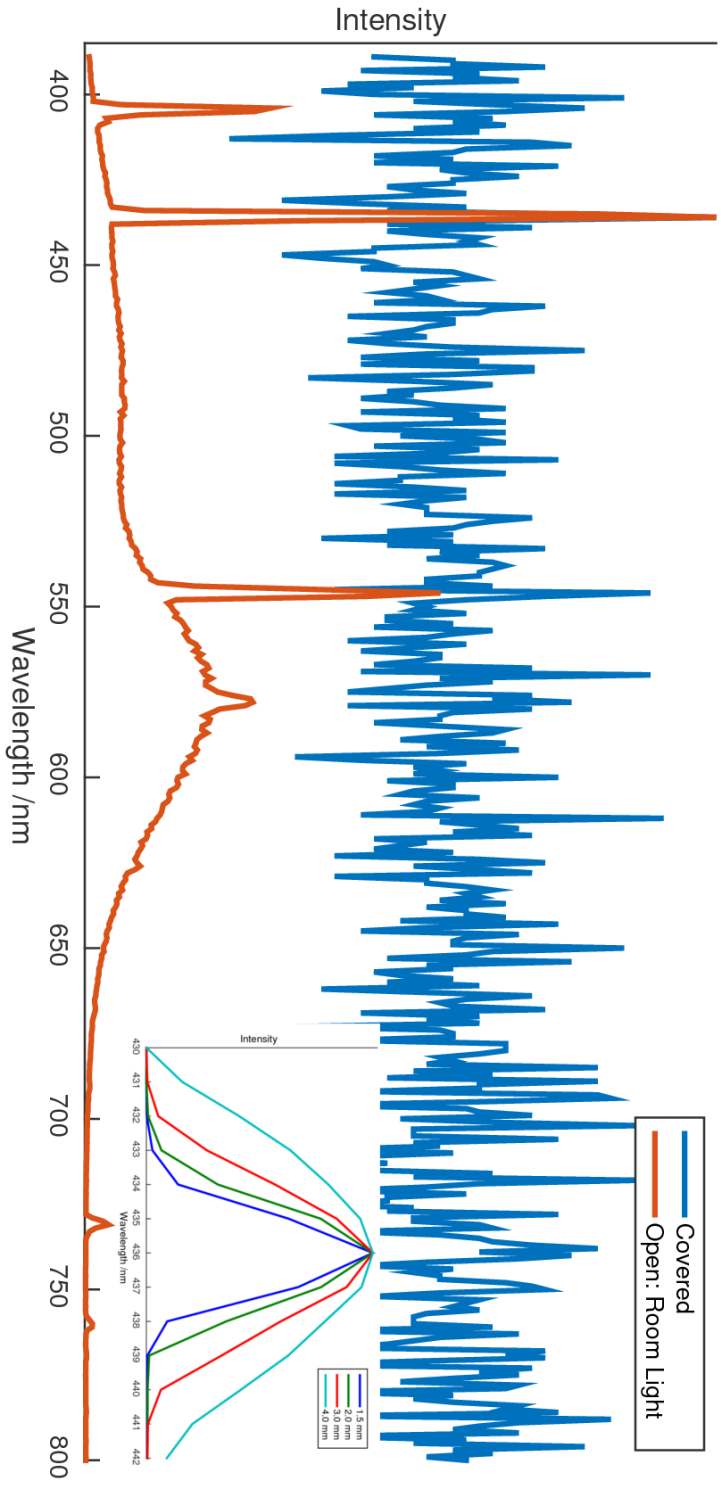

Figure 3.9: Lightproofing Test: Main: The effect of opening and closing the enclosure. The effect is satisfactory, producing a flat noise profile with a mean of $\approx 85 \pm 15$ cps (see figure 3.6). The profiles have been normalised to have a maximum value of 1, though the peak of the room light spectrum is in excess of 10^6 cps. Inset: Normalised spectra of the 436 nm spectral line of mercury from a HgAr lamp, with variable slit-width.

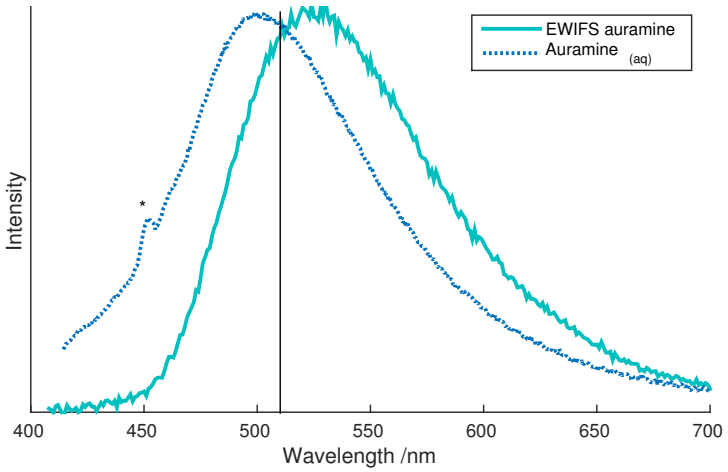

Figure 3.10: Auramine Fluorescence: Background-subtracted, fully corrected fluorescence emission spectrum of auramine on a hydrated silica substrate. The spectrum is red-shifted further than that in [33], whose $\lambda_{max} \approx 510$ nm is shown as a vertical line. The asterisk (*) labels what is likely a Raman peak of water in the literature spectrum.

on silica, which is known to adsorb to silica and both shift its emission maximum and increase its Φ_f in the process [33]. Auramine-O chloride (Aldrich, approx 80 % dye content) was purified by passing aqueous solution through activated charcoal and recrystallising from methanol 3 times. A solution of 1.00 μM auramine was prepared in water and loaded into the TIR element with a hydrated silica substrate. The fully corrected EWIF spectrum of auramine ($\lambda_{max} = 522$ nm) is presented in figure 3.10 atop the literature spectrum of auramine in water ($\lambda_{max} = 500$ nm).

As $G_+ = 1.10G_-$, the effect of the correction being incorrectly applied could be significant. As an order-of-magnitude assessment, the effect on the bulk anisotropy (for which the relative deviation should be largest) is shown in figure 3.11. The bulk anisotropy is calculated in that figure by varying the quantity $I_\perp$ in equation (3.2) and assuming $I_\parallel \equiv 1$. The bulk case is used to demonstrate this, as it produces the largest relative error. The relative error associated with erroneously leaving out this factor is small, yet still larger than if it were included. It will be used, even though including it introduces a systematic error.

3.4 Conclusion

An instrument has been built, that is capable of making evanescent wave-induced fluorescence measurements in both the frequency and time domains, as well as fluorescence measurements of bulk solutions. The wavelength accuracy has been determined as ±0.19 nm, and the spectral bandwidth is 4.6 nm (resolution ±2.3 nm) at a working slit-width of 3 mm. The minimum value of integration time in the frequency domain is set to 200 ms as the instrument is fundamentally incapable of resolving shorter periods of time accurately.

The deviation of the G-factor from the "pure instrumental" value due to the presence of optics has been demonstrated. The deviation has only a small effect on the calculated anisotropy, though the effect of erroneously *not* including $G_{opt} = 1.10$ in calculation of anisotropy is larger than the effect of erroneously including it, and so it will be used.

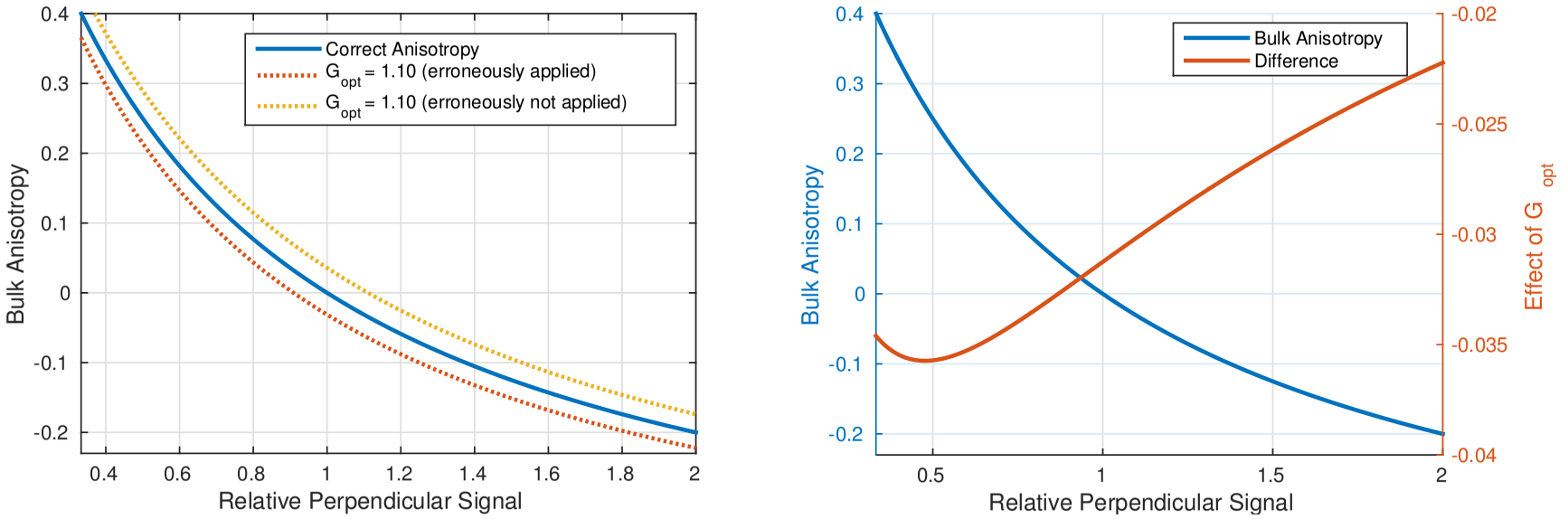

Figure 3.11: Effect of G_{opt}: Vertical scales are comparable. The bulk anisotropy is calculated by varying the quantity $I_\perp$ in equation (3.2) and assuming $I_\parallel \equiv 1$. Left: The maximum direct effect of erroneously introducing an optics G-factor of 1.1 exactly, assuming all other corrections to be perfect. Right: The difference between the blue and red traces on the left. Not shown on right: effect of erroneously *not* applying the optics G-factor, which resembles the shown difference function reversed in sign but of larger magnitude.

Chapter 4

Surfaces & Dyes

Abstract

Optical brighteners are introduced, and their basic chemistry is discussed. The context of the project is expanded on, as mimicking fabric surfaces for the purpose of brightener spectroscopy, and breadth of the greasy soils problem is narrowed. The three main fabric polymers are discussed; cotton cellulose, polyester and nylon, and the general methods for getting them into solution for preparation of thin films is outlined.

The characterisation of thin films by surface tension is discussed, as well as the connection between energy terms and spectroscopy, before outlining surface modification of silica directly.

The DFT investigation of optical brighteners indicates that their lowest lying excited state is being populated directly by the EWIFS instrument. It is a $\pi^{\leftarrow}\pi*$ transition and produces free rotatability about the styrenyl double bonds, allowing *(E)–(Z)* isomerisation. The dianion of optical brightener 49 (OB49) has a lowest energy conformation in the ground state with a high dipole moment and eclipsed sulfonyl groups, creating a hydrophobic "spine" and two polar head groups on the opposite side.

The other main findings of this chapter are that films of nylon and polyester produced from hexafluoroisopropanol and chloroform are unsuitable for spectroscopy, whilst appropriate cellulose and grease-doped cellulose films from trimethylsilylcellulose and *n*-octadecanol are both facile and straightforward. A suitable model grease has also been produced from trichlorododecylsilane, and another from benzoyl chloride modification of a previously modified silica surface may be useful in the future also.

This chapter is concluded by presenting four surfaces for use in the succeeding chapter.

—

The aim of this chapter is to make fabric polymer- and grease-mimicking surfaces, which are suitable for interfacial spectroscopic methods such as EWIFS, and discuss some methods of their characterisation. The main concern is transparency and physicochemical homogeneity, as such characterisation by surface tension components describes the capacity to interact with a dye. The dyes require context and introduction, whilst their general properties and structures need to be outlined and some properties calculated. Rather than create a separate chapter, this chapter concludes by presenting the results of these characterisations, as they are brief and relatively straightforward.

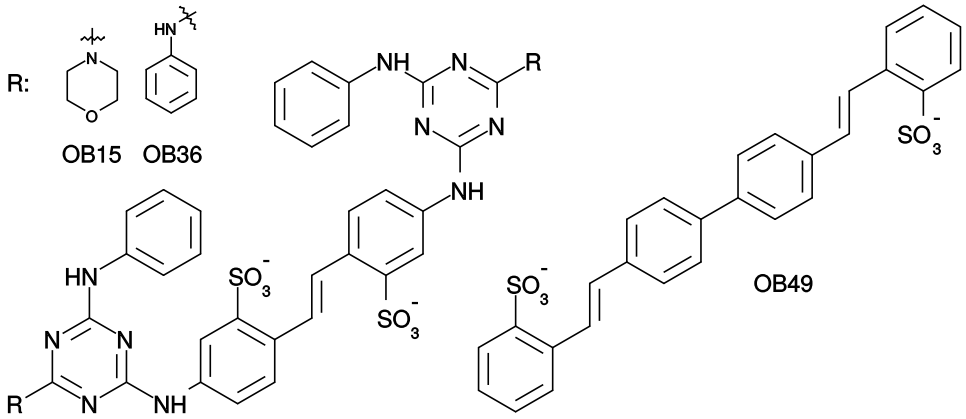

Figure 4.1: Structure of Optical Brightener Anions: Shown anions of disodium salts OB15 ($Na_2C_{40}H_{38}N_{12}O_8S_2$; 924.91 g mol^{-1}), OB36 ($Na_2C_{44}H_{34}N_{12}O_6S_2$; 936.93 g mol^{-1}) and OB49 ($Na_2C_{28}H_{20}O_6S_2$; 562.56 g mol^{-1}).

4.1 Introduction

Optical brighteners (OBs, aka *fluorescent whitening agents* FWAs) are applied to garments in a wash cycle to combat the appearance of *yellowing*. Yellowed or discoloured clothing is perceived as dirty and is discarded, therefore optical brighteners lengthen the working life of garments and are industrially important. They absorb ultraviolet light and emit blue light, which directly compensates for the lack of blue reflectance that causes yellowing. For further reading on the history and applications of optical brighteners, the reader is directed to both [4] and [5, Chapter 7], where the subject is treated authoritatively in detail.

Reflectance is the quantity of diffuse reflection. When light is incident on a finely divided medium, the interfaces result in reflections whilst the transmitted portion of the light which passes into the bulk, undergoes absorption. The complex pathways of a light ray entering such a medium result in its scattering, and any net reflection is diffuse (mostly undirected). For a white light incident on a coloured surface, the colour arises from the deviation of the reflectance profile from flatness - the proportions of the intensities of different frequencies reflected by the material are not the same as the light that entered it. For a more complete treatment and explanation of reflectance and perception of colour, see equation (7.7) and its surrounding text on page 152.

Three OBs will be used in this work; OB15, OB36 and OB49. These are shown in figure 4.1. The fluorescence spectra of OB15 and OB49 in aqueous solution are already known in the literature, as is their wavelength of maximum absorbance ($\approx$ 350 nm) [4].

The conditions of a typical wash are pH 9.5–10.5 in a wash volume of around 13 litres in Europe [6][4, p. 60]. A washing powder typically has a loading of 0.1 w/w % brightener [6, pp. 71–74][4, p. 60]. Given a dose of 4–6 g powder to a litre of wash water, this is 4–6 mg/L brightener in aqueous solution. The wash concentrations of brightener are presented in the table below. The concentration of dye in a wash is therefore to the order of micro-molar.

Component	wt% [37]	wt% [38]	wt% [39]
cholesterol	2	6	1.5–2.5
cholesterol esters			3–6
free fatty acids	5–20	28	15–30
triglycerides	25–45	35	30–50
wax esters	30–40		26–30
–sapienic acid	*25–35*		
squalene	12–17		12–20
unsaponifiable		30	

Table 4.1: Components of Sebum: the major components of human skin grease. Sapienic acid ((*Z*)-6-hexadecenoic acid) is reported on its own but is integrated across its contribution to the free fatty acids, triglycerides and wax esters, as it is the major fatty acid in human skin secretions. Glycerides, wax esters and fatty acids make up the greatest portion of all skin grease.

FWA	Mol. Wt. /g mol^{-1}	[OB] /M
OB15	924.91	$4.32–6.48 \times 10^{-6}$
OB36	936.93	$4.26–6.40 \times 10^{-6}$
OB49	562.56	$0.71–1.06 \times 10^{-5}$

There are two isomers (*(E)-* and *(Z)-*) for OB15 and OB36, whilst OB49 has 3 isomers (*(E,E)-*, *(E,Z)-*, and *(Z,Z)-*). The *(Z)*-isomers have blue-shifted absorbance relative to the *(E)*-isomers; the *(E)*-isomers are more stable than the *(Z)*-isomers, but the *(Z)*-isomers are formed by exposure of the *(E)*-isomers to the shortest wavelength that they absorb [34]. The *(Z)*-isomers are also non-fluorescent [4, pp. 94–97], and absorb at shorter wavelengths [34].

Ultimately, the course of relaxation of the excited state of a FWA falls into two categories: photophysical regeneration of the original active brightener (even if it passes through a ground state that is not fluorescent), or photochemical change into a photoproduct that is distinct from the original molecule and may be entirely non-fluorescent. In the latter case, either the photoproduct is formed by photo-oxidative cleavage (forming aldehydes and carboxylic acids), or it is formed by aromatic substitution (forming an alcohol) [4, 35]. The formation of reactive oxygen species such as superoxide may be involved [36]. Importantly, the half life of FWAs with the core structure of OB15/OB36 is minutes in upper waters of lakes and rivers, and the same for OB49 is to the order of several days [4, pp. 180–185].

Soiling

Soiling is the introduction of an undesirable material or substance (a *soil*) to a garment or surface. It is claimed, that brighteners work best only on clean, well-prepared substrates [7]. For simplicity, the meaning of *clean* is assumed here to mean freedom from soiling; soils take many forms, but we will choose here to focus on *greasy soils*, of which *sebum* is both the most prevalent and also lifestyle-independent. Sebum is the protective grease exuded by skin, which has several functions including prevention of moisture loss from skin. The major components of sebum are given in table 4.1. The fatty acids, alcohols and ethers are all long-chain (C-10 chains and above) water-insoluble compounds.

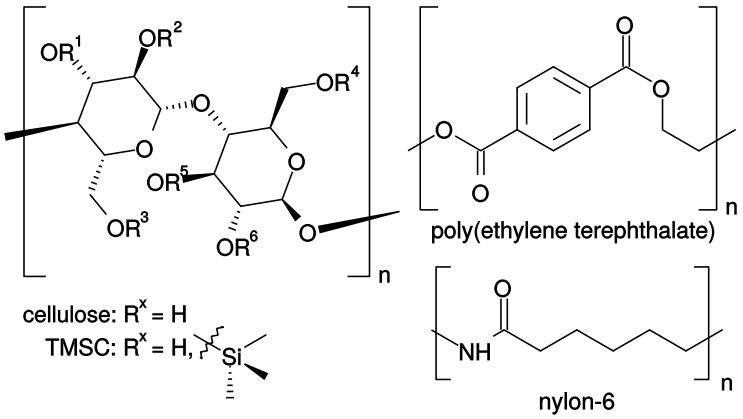

Figure 4.2: Structure of Polymers: Structure of cellulose, trimethylsilyl cellulose (TMSC), poly(ethylene terephthalate) and nylon-6. In the case of TMSC, the degree of substitution $0 \leqslant D_s \leqslant 3$ is calculated based on a single glucose unit.

4.1.1 Fabric Polymers

The three main fabric polymers of interest are cellulose, nylon and poly(ethylene terephthalate) (figure 4.2).

Cellulose is the $(1 \rightarrow 4)$ linked polysaccharide of β-D-glucose, and is the major constituent of cotton. The structural repeat unit is frequently drawn as the dimer cellobiose, and cellulose is a solid thanks to an extensive network of hydrogen bonds. It has several crystalline phases termed I/II/III, and of type I there are two morphs termed I-α and I-β. These two have only recently had their structures solved crystallographically [40, 41], though wide-angle x-ray data for cotton fibre as evidence for crystallinity goes back at least as far as 1954 [42]. Crystalline ordering in cellulose involves domains of parallel chains, and reactivity and availability of cellulose functional groups is primarily through disordered regions in the first instance [42]. Dye molecules are expected to adsorb most strongly to the amorphous phase due to the availability of hydroxyl groups. Cotton cellulose is approximately 70-90 w/w % crystalline and has a degree of polymerisation over 9,000 [43, 44].

Raw cotton fibre has a structure made up of concentric tubes of cotton fibrils, an outer layer of protein and a hollow inner. The protein cuticle is removed during processing. The porous arrangement of cotton fibril layers constitutes the majority of the cotton cellulose [43, 45].

As the EWIFS system uses a flat TIR surface, cellulose films on this surface are of interest for probing optical brighteners. Cellulose films have been prepared from cellulose acetate and cellulose ethers as early as the 1960s, and it is common knowledge that modified cellulose pre-dates that in the form of nitrocellulose from the early days of photography. More recently a deprotection scheme using the trimethylsilyl (TMS) moiety has been used for spin-coating films. Though the molecule trimethylsilylcellulose (TMSC) was first reported as early as 1951 according to [46], and N-methylmorpholine N-oxide is used as a solvent for cellulose in the Lyocell process to this day [47], the synthesis of TMSC has been made easier over time by the development of new solvent systems and more facile trimethylsilylation schemes [48].

Cellulose can be solvated in a number of ways. The classic demonstration is Schweizer's reagent tetraamminediaquocopper(II) hydroxide $[(NH_3)_4(H_2O)_2Cu](OH)_2$. This dissolves cellulose in aqueous solution, and regenerates cellulose when passed into aqueous acid. This works by substitution of the

aquo groups on the coordination complex with deprotonated C2 and C3 cellulose hydroxyl groups, and this scheme has been used to develop complexes based on Ni and Cd [49]. This general scheme simultaneously breaks hydrogen bonds, and stabilises the chains, precluding re-formation of those hydrogen bonds. Acidic solutions favour the breakdown of the complex to form water soluble products such as aqueous copper(II) and ammonium chloride, precipitating cellulose. Cellulose precipitated from solution is amorphous [50].

The second main method is the use of ionic liquids. Ionic liquids are salts which have low melting points because their ions co-ordinate relatively weakly to one another. Hydrated N-methylmorpholine N-oxide dissolves cellulose, as does the lithium-dimethylacetamide complex among others [51, 52, 53]. In the lithium-dimethylacetamide system, a solution of 9% w/w LiCl in anhydrous dimethylacetamide (DMAc) stabilises the lithium ion by coordination to DMAc, leaving the chloride anion to accept a strong hydrogen bond from the hydroxyl groups in cellulose. The stabilised lithium complex closely associates with the bonded chloride ion, stabilising the polymer chain and hindering re-association of chains [54]. Introduction of water to this system dissolves both the DMAc and LiCl, allowing dissolved cellulose to precipitate.

It was found by simple experiment at Durham, that regeneration of cellulose directly from DMAc/LiCl solution is problematic for spectroscopy, insofar that the cellulose gels formed by exposure of a solution to water are easily detached from a glass substrate and, in the event of successfully forming a film, are at risk of flaking away as they dry. Not only this, they require washing to remove any extraneous solvent molecules or metal ions that could induce quenching or alter the surface tension of the cellulose.

Derivatisation of cellulose with a subsequent deprotection, has been demonstrated in the literature and successfully used to form films of cellulose [55]. The ionic liquids in a biphasic system have been used to synthesise TMSC which, in a thin film, deprotects within minutes on exposure to HCl vapour [56, 57]. The literature indicates that the solubility of TMSC in a range of solvents is indicative of its degree of substitution [58]. The DMAc/LiCl solvent system with hexamethyldisilazane (HMDS) as a trimethylsilylating agent in excess, has been shown to produce high degrees of substitution (D_s = 2.7 – 2.9) of hydroxyl groups. This is comparable to the use of high-pressure ammonia as solvent with HMDS [48, 59].

Nylon-6,6 is a polyamide that can be formed from adipoyl chloride or adipic acid, and hexan-1,6-diamine. Nylon-6 is formed from 6-aminohexan-1-oic acid with itself. The result of either reaction is a poly(ethylene)-like chain punctuated with amide linkages. In nylon-6,6 the amides are in alternating directions, in nylon-6 they are all in the same direction. The nomenclature is intuitive. The carbon chains separating the amides, dominate the interfacial properties of the polymer, though the amide groups impart a small amount of polarity. Nylons are therefore inherently hydrophobic, nearly (though not wholly) comparable to poly(ethylene) in terms of surface tension contributors (see table 4.2). Nylons are used in fabrics to impart a silky feel, and were originally developed in the search for a cheap substitute for silk. Nylon-6 is soluble in 1,1,1,3,3,3-hexafluoroisopropanol (HFIP).

Poly(ethylene terephthalate) is a polyester formed by condensation of ethylene glycol with terephthalic acid. It is often referred to simply as *polyester*, as it is the chief polyester used in polyester fabrics. Polyester is exceptionally resistant to dyeing - it can only be coloured at specific points during its manufacture, else it must be dyed under high pressure and temperature using nonionic *disperse dyes*. A disperse dye dissolves in a solvent and is adsorbed onto or absorbed into the substrate material. They contrast to reactive dyes, acid dyes and vat dyes; although the exact distinctions are more precise than

Polymer	γ_{zis}	γ_s^{LW}	γ_s^+	γ_s^-	γ_s^{AB}	γ_s^{TOT}	ΔG_{sl}^{IF}	W_s	Ref.
Sigmacell 101		54.49	0.11	47.83	4.49	58.98	20.56	-3.54	[60]
Sigmacell 20		52.94	0.11	41.70	4.24	57.18	12.99	-9.11	[60]
Sigmacell 20*		53.72	0.00	54.83	0.00	53.72	33.41	-3.75	[60]
Avicel		51.82	0.00	50.14	0.00	51.82	28.23	-8.15	[60]
Avicel*		52.10	0.01	58.43	1.09	53.19	38.66	-0.27	[60]
Cellulose	35.5–49.0								[61]
Cellulose						60.5–66.1			[62]
Nylon(6,6)						43.0			[63]
Nylon(6,6)	40.2	36.9	1.5	12.1	3.3	44.3			[64, 65]
Nylon(6,6)		32.5			14.0	46.5			[66]
Nylon(6)	43.9	42.5	0.2	9.6	2.8	45.4			[64, 65]
Nylon(7,7)	43.0								[64]
Nylon(12)	37.1	37.0	0.6	7.6	4.3	39.3			[64, 65]
Nylon(12)		35.9			4.9	40.7			[66]
PE		35.7			0.0	35.7			[66]
PE		35.3			0.0	35.3			[66]
PE	31.7	31.5	0.1	0.9	0.2	33.5			[64, 65]
PET	39.0	42.6	0.3	3.7	1.8	45.3			[64, 65]
PET		35.6			9.0	44.6			[66]
PTFE	19.4	19.9	0.1	1.6	0.9	21.8			[64, 65]
PTFE		18.4			1.6	20.0			[66]

Table 4.2: Literature Surface Tensions of Polymers: γ_{zis} is the critical surface tension by the Zisman method, γ_s^{LW} is the Lifshitz van Der Waals energy, γ_s^+ is the electron acceptor contribution, γ_s^- is the electron donator contribution, γ_s^{AB} is the total acid-base contribution, γ_s^{TOT} is the total surface energy of the solid, ΔG_{sl}^{IF} is the interfacial free energy of water spreading, and W_s is the work of water spreading. Values are presented in mJ/m^2. Values from references [64, 65] are averaged values collected from extensive literature for comparison, and therefore do not relate to one another precisely. The

this, these respectively work by covalently bonding to, adsorbing to and precipitating within fibres.

Polyester is dissolved effectively by HFIP [67], phenol/*o*-dichlorobenzene cosolvent [68], nitrobenzene/trichloroethane cosolvent [68], and *o*-chlorophenol/chloroform cosolvent [69, 70]. It has been cast into films, and its structure has been studied in the literature [71].

Spin-Coating

A rotating solid substrate with a volatile solution atop it, generates a force that pushes the solution away from the axis of rotation. For a solution that completely wets the surface, a film is left behind and, as the remaining solvent in the film evaporates, the solute is left behind as an even film. This is the process known as *spin-coating*. It has been proven that the film left behind is made progressively even as evaporation runs to completion [72, 73]. The exact thickness and surface evenness of the film is dependent on the rate of evaporation of the solvent, the starting viscosity, the spin-speed and the resultant viscosity change of the solution over time [73, 74, 75, 76].

For polymers with extremely limited solubility, the remaining controllable variables are therefore spin-speed and polymer concentration. Although all volatile solutions of polymer that wet the surface will leave a film, the optical properties of those films may not be ideal for spectroscopic applications. Opaque or translucent films will scatter a laser beam; the assumption of the EWIFS experiment is that a film is non-absorbing, non-scattering and texturally smooth. On glass, this presents itself to the eye as a transparent film indistinguishable from the substrate, with no defects. Therefore the first concern is to create a non-scattering film by spin-coating, and from there to characterise smoothness and surface energy of viable films.

4.1.2 Surface Tension

We begin discussion with the well-known *Young equation*: $\gamma_{sv} = \gamma_{sl} + \gamma_{lv} \cos\theta_{eq}$. Where γ is a surface tension, θ_{eq} is the equilibrium contact angle and subscript *v/s/l* indicate vapour, solid and liquid pairings respectively. This balances the forces arising from surface tension acting on the three-phase line of a sessile liquid drop resting on a surface. Contact angle measurement with liquids of known surface tension is a standard method of surface characterisation. The basis of the method is shown in figure 4.3.

In reality, the quantity θ_{eq} cannot be directly determined, as the surface inhomogeneity causes *pinning* of the three-phase line; peaks and troughs in the surface result in a much more complex physical reality than the ideal situation of the Young equation. The equilibrium contact angle exists somewhere in the range between the angle which causes the liquid to advance (the advancing angle) and the angle which causes it to recede (the receding angle). This range of angles is the contact angle hysteresis $\Delta\theta$. We therefore use [77] to calculate equilibrium angle from the advancing and receding angles as per Tadmor's relations:

$$\theta_{eq} = \arccos\left[\frac{\Gamma_A \cos\theta_A + \Gamma_R \cos\theta_R}{\Gamma_A + \Gamma_R}\right] \tag{4.1a}$$

$$\Gamma_A \equiv \sqrt[3]{\frac{\sin^3\theta_A}{2 - 3\cos\theta_A + \cos^3\theta_A}} \tag{4.1b}$$

$$\Gamma_R \equiv \sqrt[3]{\frac{\sin^3\theta_R}{2 - 3\cos\theta_R + \cos^3\theta_R}} \tag{4.1c}$$

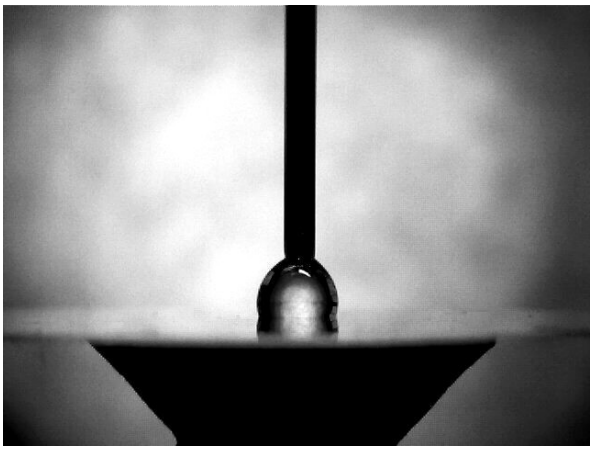

Figure 4.3: Goniometry: Water on TCDS-SAM: A small bridging drop of water on a trichlorododecylsilane self-assembled monolayer (TCDS-SAM). The drop is fed water through the cannula to expand it and obtain θ_a, and water is removed to obtain θ_r. The angle θ_{sess} is obtained by allowing the drop to rest on the surface without the cannula, and θ_{eq} is calculated as described in equation (4.1a). The TCDS-SAM is described in table 4.5 on page 86.

where θ is a contact angle, and subscript *eq/A/R* indicate the equilibrium, advancing and receding conditions respectively. We also define from the same source a value $\mathcal{K}$, which quantifies the surface irregularity as a function of the hysteresis. In contrast to $\Delta\theta = \theta_A - \theta_R$ which is a non-normalised value that is not linear in energy, $\mathcal{K}$ is the *line energy*, which is the basis for calculating Tadmor's relations in equation (4.1a). The line energy is the normalised interfacial energy investment required to deviate to the current contact angle from θ_{eq}. The line energies for the advancing and receding angles are natural limits for the system and θ_{eq} is assumed to lie exactly between these two extremes of energy, as the contact angle hysteresis arises from the same surface imperfections. As the significance of hysteresis changes nonlinearly with θ_{eq}, we use instead $\mathcal{K}$ to quantify surface irregularity [77]:

$$\mathcal{K} = \left(\frac{\cos\theta}{\cos\theta_{eq}} - 1\right) \cdot \sqrt[3]{\frac{3}{\pi} \cdot \frac{\sin^3\theta}{2 - 3\cos\theta + \cos^3\theta}} \tag{4.2}$$

Importantly, $\mathcal{K}(\theta_A) \equiv -\mathcal{K}(\theta_R)$, $\therefore \mathcal{K}_{max} \equiv \pm\mathcal{K}(\theta_{A,R})$.

Once we have θ_{eq} from equation (4.1a) for a set of solvents on a surface, we can solve for the VanOss parameters, the theoretical basis of which is described and discussed in references [60, 78, 79, 80, 81] and will be summarised here.

The surface tension has several contributors that ultimately split into two additive types: dispersive and polar. The dispersive interactions (London, Keesom, Van der Waals forces) aren't distinguished from one another and are grouped into the Lifshitz-Van der Waals term γ^{LW}. The polar interactions are split into lewis acid and base monopolar terms γ^+ and γ^- respectively, from which we produce the total acid-base term $\gamma^{AB} = 2\sqrt{\gamma^+ \cdot \gamma^-}$, and the total surface energy is $\gamma^{TOT} = \gamma^{LW} + \gamma^{AB}$. We relate these quantities to the equilibrium contact angle by the work of solvent spreading for a given solid-liquid pair:

$$W_s = \gamma_{lv}(1 + \cos\theta_{eq}) = 2\left[\sqrt{\gamma_s^{LW} \cdot \gamma_l^{LW}} + \sqrt{\gamma_s^+ \cdot \gamma_l^-} + \sqrt{\gamma_s^- \cdot \gamma_l^+}\right] \tag{4.3}$$

Liquid	γ_l^{TOT}	γ_l^{LW}	γ_l^{AB}	γ_l^+	γ_l^-
Diiodomethane	50.8	50.8	0.0	0.01	0.0
Formamide	58.0	39	19	2.28	39.6
Glycerol	63.4	40.6	22.8	3.92	57.4
Water	72.8	21.8	51.0	25.5	25.5

Table 4.3: VanOss Surface Tension Parameters for Test Liquids: VanOss Surface Tension Parameters used for test liquids at 20° C [82, pp. 151–153]. Values given in mJ/m^2.

Using four liquids of known γ_l parameters, we can create solutions to these functions as a difference minimisation problem to yield the three values γ_s^{LW}, γ_s^+ and γ_s^-. The four test liquids are shown in table 4.3.

The Zisman method for determination of *critical surface tension* [83], is performed for an homologous series of liquids by regressing $\cos\theta_{eq}$ against γ_{lv}, and extrapolating to $\cos\theta_{eq} = 1$. Any liquid with a surface tension below this value γ_{zis} will spread to wet the surface, and as such it is a characteristic value of that surface.

4.1.3 Other Parameters

Although it will become apparent that these parameters are largely irrelevant to this thesis experimentally, they should nevertheless be explored in brief as a discussion of the cybotactic region at interfaces.

Kamlet-Taft Parameters

The Kamlet and Taft (KT) parameters were originally developed, justified, and published in a series of papers by authors of the same name [84, 85, 86, 87, 88]. They are neatly summarised in a simple equation:

$$\Delta\tilde{\nu} = (a \cdot \alpha) + (b \cdot \beta) + (s \cdot \pi^*) + \Delta\tilde{\nu}_0 \tag{4.4}$$

where $\Delta\tilde{\nu}$ is the solvatochromic shift of a dye in cm^{-1}, $a/b/s$ are susceptibilities in units of cm^{-1} for a probe dye, $\alpha/\beta/\pi^*$ are unit-less parameters for a solvent and $\Delta\tilde{\nu}_0$ is a baseline solvatochromic shift when $a = b = s = 0$.

The terms α and β quantify the donor and acceptor character of hydrogen bonds formed between solvent and dye. The π^* term encompasses mainly dipole interactions and the effects of solvent polarizability, therefore we expect the KT parameters to:

1. predict and explain deviations from a Lippert plot caused by hydrogen bonding

2. characterise the sensitivity of a dye to its cybotactic environment

Hansen Solubility Parameters

The square of the Hildebrand solubility parameter δ is the cohesive energy density of a substance. Splitting the energy contributions into three contributors according to interaction type gives:

$$\delta^2 = \frac{E_{coh}}{V_{mol}} \tag{4.5a}$$

$$= \frac{E_d + E_p + E_h}{V_{mol}} \tag{4.5b}$$

$$= \delta_d^2 + \delta_p^2 + \delta_h^2 \tag{4.5c}$$

where δ^2 is in MPa, E is an energy, subscript d/p/h indicate interaction types dispersive, polar and hydrogen bonding respectively, E_{coh} is the energy of vapourisation and V_{mol} is the molar volume. The distance R between two solvents in a normalised *solubility space* is given by:

$$R^2 = (2\Delta\delta_d)^2 + (\Delta\delta_p)^2 + (\Delta\delta_h)^2 \tag{4.6}$$

where $\Delta\delta$ is the difference in value between a probe solvent and a reference compound, and the scalar 2 is a normalisation factor justified in [89, Chapter 2]. The practical upshot of this, is that all the solvents that dissolve or permeate a reference compound will be bounded within the solubility space in a sphere of radius $R' \geqslant R$ about the coordinates of the reference. Further, it is only necessary to assess qualitatively whether a solvent interacts strongly with a reference.

Solvatochromic $E_T(30)$

The shift of an absorption peak of a dye in different environments (solvatochromism) reflects the relative change in stabilisation of the initial and final states of the transition. Positive solvatochromism is a bathochromic shift in more polar environments, whilst negative solvatochromism is a hypsochromic shift. 2,6-diphenyl-4-(2,4,6- triphenylpyridinium-1-yl)phenolate (a.k.a. betaine 30) demonstrates appreciable negative solvatochromism, and the molar electronic transition energy of this dye in kcal mol^{-1} is [90]:

$$E_T(30) = hcN_A\tilde{\nu}_{max} = 28,591/\lambda_{max} \tag{4.7}$$

where hc is Planck's constant multiplied by the speed of light, N_A is Avogadro's constant and $\tilde{\nu}_{max}$ and λ_{max} are the wavenumber and wavelength of maximum absorbance, respectively. This number quantifies the ability of a given solvent to stabilise a polar excited state relative to the ground state.

Inter-relationships Between Parameters

The relationship between surface tension and Hansen parameters is known empirically [89, Chapter 6]:

$$\gamma^{TOT} = 0.0715 \cdot V_{mol}^{1/3} \cdot [\delta_d^2 + 0.632(\delta_p^2 + \delta_h^2)] = \gamma^{LW} + 2\sqrt{\gamma^+\gamma^-} \tag{4.8}$$

though it makes little mechanistic sense to interpret interfacial spectra in terms of Hansen's parameters directly; the Hansen parameters are proportional to the energy available for solvation in bulk. Surface tension is the energetic excess at the interface, which is also the energy available for interaction with a dye. However, neither of these quantities are spectroscopic, and conversely the KT parameters are empirical quantities that don't directly relate to cohesive energy, only to the availability of energy

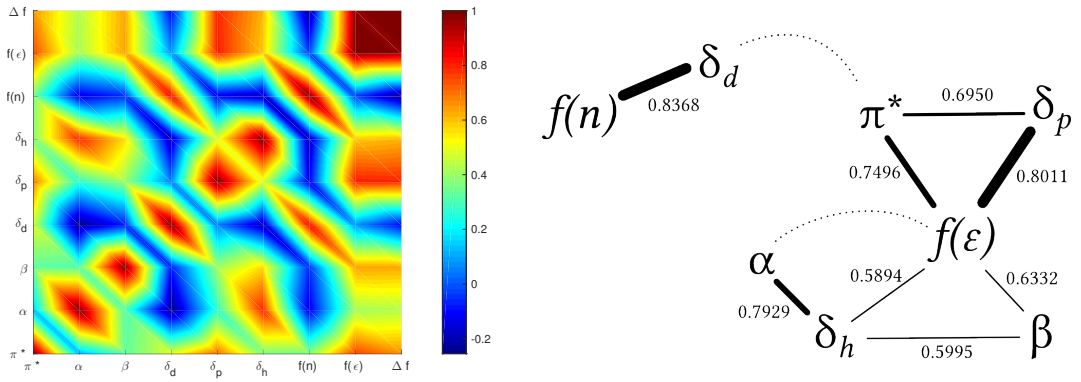

Figure 4.4: Correlations Between Kamlet-Taft and Hansen Parameters. Left: Showing the correlation coefficients between discrete pairs of values across 68 solvents. Right: Graph showing pairing of parameters with coefficients over 0.55. Line weight approximately represents the scale of coefficients. Dashed lines indicate a coefficient between 0.4 and 0.5. For clarity, we consider $f(\epsilon) \approx \Delta f = f(\epsilon) - f(n)$. See equation (2.29a) on page 43 for a discussion of Δf.

and its impact on solvatochromism. Although there is a thematic link between the VanOss monopolar terms γ^+/γ^-, the α/β KT parameters and the δ_h parameter, the correlation between KT and VanOss has already been discussed in [91] and found to be inconclusive, and presumably for similar reasons the relationship between $(\delta_p^2 + \delta_h^2)$ and $2\sqrt{\gamma^+\gamma^-}$ has not been addressed at all.

Kamlet-Taft parameters are linear with respect to the effect of dye and solvent on net solvent rearrangement energy, which is the total heat lost to solvent during relaxation. This is dependent on the relative change in stability of the two pairs of Franck-Condon states; the excitation/absorption pair and the relaxation/fluorescence pair. In this way they encompass a complicated relationship that is not addressed at all by other parameters, but they are not linearly proportional to the Hansen parameters.

Interfacial studies at liquid-liquid interfaces have found that dyes at that interface experience the mean of the dielectric constants of the two solvents. Whether this is the case at solid-liquid interfaces remains to be seen; the distinguishability of the interfacial response through absorption and fluorescence spectra and fluorescence kinetics is of more concern in TIR applications.

Figure 4.4 shows Pearson's correlation between KT and individual Hansen parameters across a sample of 68 solvents' data. Although no exact relationship between these parameters is known or offered here, the linear correlation coefficients provide an indicator of how closely these parameters do associate.

In conclusion of this subsection, the Hansen parameters are not directly useful for interfacial spectroscopy. In the absence of UV-vis attenuated total internal reflectance, the KT and $E_T(30)$ solvatochromic parameters for an interfacial environment cannot be calculated accurately, or cannot be calculated at all, respectively. The surface tension parameters of VanOss will be useful for interpreting the effects of, and dye affinity for, an interface.

4.1.4 Surface Modification of Silica Glass

Hydrated silicon dioxide glass exhibits a critical surface tension (§4.1.2) approximately that of the liquid-vapour surface tension of water [92]. As a result its surface tension parameters cannot be

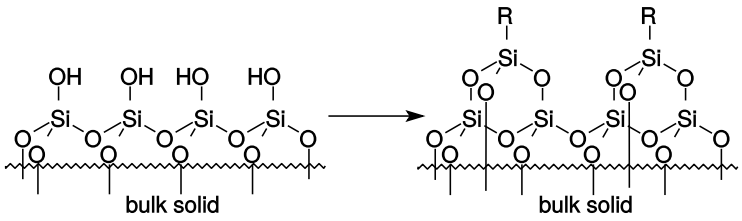

Figure 4.5: Surface Modification Scheme: Surface modification scheme for adjusting the surface tension of hydrated silica glass. The silanol groups on the left react with $RSiCl_3$ and $RSi(OR^2)_3$ to produce the modified surface product on the right.

probed using the probe liquids in table 4.3, nor in fact most common laboratory liquids. However, the free silanol groups are available for surface-specific reactions to modify the surface tension. By assuming similar surface tension properties to water, the effects of an interface are modelled well on bare silica-water interface.

The surface tension can be adjusted by using the scheme in figure 4.5. Both $RSiCl_3$ and $RSi(OR^2)_3$ react with silanol groups to covalently bond the group R to the surface by a concerted condensation reaction that occurs at room temperature. In both cases this produces self-assembled sub-monolayer coverage, and protocols exist for reproducibly yielding this at room temperature and pressure, without requiring annealing. Annealing steps were introduced in earlier papers for trialkoxysilane reactions when it was believed that the self-assembled monolayer (SAM) required heat to undergo condensation with the substrate. However, recent papers have revealed that even if the SAM were not covalently bonded without annealing, it certainly associates so strongly with the substrate that it cannot be removed except by cleaning protocols that also remove a covalently bonded layer [93].

The arrangement of R-groups results in (in the case of alkyl chains) an ordered structure of parallel chains. There is a risk during these reactions of forming an inverted, second SAM on top of the product SAM (effectively a self-assembled bilayer) due to hydrophobic interactions. These layers, if present, are removed easily by sonication.

Due to the concerted nature of the reaction with the surface, SAMs from trialkoxysilanes produce a degree of surface coverage that is dependent on the length of the alkoxy chain, with trimethoxysilane species producing the most dense coverage and liberating methanol. Amine-terminated chains such as (3-aminopropyl)trimethoxysilane (APTMS) produce a reactive surface that can be further treated to achieve subsequent reactions. However the surface tension and hydrophobicity of these SAMs increase as a function of time and do not recover, due to adsorption of atmospheric pollutants. The reactivity of the terminal is also much lower than for the free solvated amine, therefore subsequent amine-directed reactions require more reactive reagents such as acyl chlorides and active esters. APTMS SAMs also therefore require that they be used immediately once dry, or enter into another reaction.

The main caveat of surface modifications, is contamination and "work-up" of reactions. As defects in a SAM cannot be rectified nor the surface groups purified, the build-up of defects in second- and third- generation reactions can prove significant. The inefficiency of surface reactions and the need to cover defects, is demonstrated well in treated-silica HPLC columns. It is well known that packed, hydrophobised silica is finished through use of a capping agent; a small, silanol-reactive reagent such as dichlorodimethylsilane or trichloromethylsilane reacts readily with any remaining silanol groups that became inaccessible to the primary reagent, making them unavailable for mobile-phase interaction and

further hydrophobising the stationary phase.

4.2 Experimental

4.2.1 DFT

The symbolic z-matrices and connectivities of optical brighteners 15, 36 and 49, were generated in GaussView 4.0, and submitted to Gaussian 09 for DFT optimisation with the `b3lyp/GEN` keyword using the split basis set in Table 4.4 to save computational demand.

Atom Type	Basis
H	3-21G
C N O	6-31G
S	6-31+G(d)

Table 4.4: *Basis Set:* Basis set used for computational work in Gaussian 09

The optimised geometries were submitted for a frequency calculation, including the Raman activity using `freq=raman`. Time-dependent DFT calculations were submitted for the optimised geometries using `td=(50-50,nstates=10,root=1)`. Solutions-phase UV-Vis spectra were calculated by the inclusion of the `scrf` keyword in a separate TD-DFT calculation with option `(solvent=water)`.

Vibrational Spectroscopy

Infra-red and Raman spectra of the solid materials were collected for comparison to the calculated spectra.

A Nicolet™ ATR-FTIR spectrophotometer with a Thunderdome™ accessory was used in %T mode. Solid brightener was placed in intimate contact with the Ge total internal reflection element, and 128 scans acquired at a resolution of 4 cm^{-1}.

A Horiba JY LABRAM HR equipped with a Leica 50x long-working distance (NA=0.55) objective lens, a 600 g/mm grating and a HeNe 632.8 nm laser was used for the collection of Raman spectra. The instrument was calibrated using a reference spectrum of (111)-Si ($\tilde{\nu}$ = 520.07 cm^{-1}) and validated against spectra of cyclohexane and toluene (spectrophotometric grade, Aldrich). Resolution 1 cm^{-1}.

Absorbance Spectroscopy

Solutions of optical brightener were made using grade A volumetric glassware and analytical balances, with supplied solid brighteners (P&G Newcastle, used as provided) and mΩ ion-exchanged high purity water. The same Suprasil quartz cuvette (nominal useful range 200-2000 nm) was used to collect first solvent, then solution spectra.

4.2.2 Synthesis of TMSC

Solvent-exchanged cellulose was prepared by dispersing microcrystalline cellulose (5 g, Fluka) in milli-Q water (200 ml) for 24 hours. Cellulose was filtered under vacuum to dryness and re-dispersed in methanol (150 ml, anhydrous) for 2 hours. Cellulose was filtered and re-dispersed in methanol (150

ml, anhydrous) 3 more times, then with DMAc (150 ml, anhydrous) 3 more times. The filtration of DMAc was not completed to dryness due to the hygroscopic nature of DMAc and the textural quality it achieves. The final weight was 6.7 g.

LiCl/DMAc 9 w/w % ionic liquid was prepared by dissolving 42.3 g LiCl (anhydrous, Lancaster) in 500 ml DMAc (anhydrous, Aldrich). Solvent-exchanged cellulose (6.7 g) and a clean teflon coated stir-bar were added, and the mixture was stirred to dissolve cellulose overnight. The solution was passed through a fine sintered glass filter under reduced pressure and stored in an airtight glass bottle until use. The concentration of cellulose in this stock solution is 10 w/v %.

A suba-seal and a reflux condenser with calcium chloride guard tube, were fitted to a 50 ml two-neck round-bottom flask. A clean teflon coated magnetic stir-bar, 5 ml cellulose stock (0.5 g cellulose equivalent) and 5 ml LiCl/DMAc ionic liquid were introduced. The flask was heated to 50° C in a water bath with stirring under reflux. Hexamethyldisilazane (HMDS, 5.0 ml, 3.8 g, 5.1 times stoichiometric excess) was added slowly via the suba-seal and left to react. After 30 minutes, the solution had begun to turn into a fine dispersion of solid. After a further 30 minutes, toluene (anhydrous, 20 ml) and HMDS (10 ml, 7.7 g, total 15.3 times stoichiometric excess) were added, this re-dissolved the dispersion.

After leaving overnight, the mixture had precipitated again, and was allowed to settle. The supernatant liquid was removed with a syringe. The crystalline solid was washed with toluene, dried, and found to be water-soluble. The solution clouded on addition of silver nitrate. The toluene washings were added to the supernatant liquid, and washed gently with deionised water (3× 100 ml) in a separating funnel. The hydrophobic phase was transferred to a 250 ml round-bottom flask and rotary-evaporated. Whilst adhered to the flask, the polymer was soaked in deionised water (250 ml) made basic with 5 drops 0.88 ammonia. The water was discarded and the polymer was rotary-evaporated to a dry solid.

The solid polymer was dissolved in a minimum volume of diethyl ether, and added dropwise to methanol (anhydrous, 150 ml) in a beaker, stirred by a teflon-coated magnetic stir bar. The methanol was replaced 3 times. The white, fibrous product "TMSC wool" was dried in a vacuum chamber and weighed (1.01 g, yield 91% at $D_s = 2.7$, minimum D_s based on complete recovery: 2.25).

4.2.3 Surface Modification

Piranha solution (a mixture of sulfuric acid (98%, Fisher, 60 ml) and hydrogen peroxide (30%, Aldrich, 20 ml)) was prepared in a 200 ml beaker in a salt-ice bath. This was immediately transferred to a custom-blown glass container, made at Durham by Mr Aaron Brown and shown in figure 4.6. The substrates (silicon wafer or glass slip) were loaded into the apparatus before the solution and wetted with sulfuric acid. The substrates were left for 1 hour, the solution emptied, the substrates washed in-situ in deionised water (6 × 40 ml) before being allowed to soak in deionised water for 30 minutes. Universal indicator paper, indicated that the pH of the final wash water was that of the deionised water. The substrates were dried by washing with acetone (3 × 30 ml) and sending a stream of dry nitrogen (BOC) through the apparatus. The spent piranha solution was deactivated with saturated iron(II) sulfate, and neutralised with saturated sodium hydroxide.

Surface treatment reagents were each prepared as separate solutions in toluene or methanol (anhydrous, 100 ml) at-need to a concentration of 10 mM, specified in table 4.5. The solutions were applied to substrates in the custom apparatus immediately after substrate preparation. The treatment time was 4 hours. The substrates were washed *in situ* with toluene or methanol (2 × 30 ml) respectively

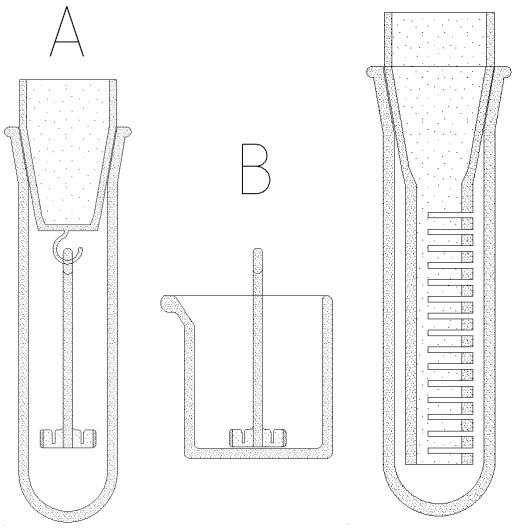

Figure 4.6: Custom Glassware: Left (A–B): Original design, for small batch testing, made by Mr Malcolm Richardson, Department of Chemistry, Durham University. The apparatus could suspend in a solution or stand freely in a beaker. The slips would sit in the vertical slits in the glass. Right: Larger scale treatment. The slips would fit in the horizontal slits. Made by Mr Aaron Brown, Department of Chemistry, Durham University.

and sonicated for 5 minutes each in ethanol and dichloromethane (DCM). The substrates were stored under toluene and dried in a stream of dry nitrogen when required. Only transparent SAMs which gave consistent contact angles with water were accepted as useful. Notably, the perfluoro surface is prepared using the undissolved reagent, using a drop on the surface.

Second-generation SAMs (i.e. sequentially modified SAMs) were prepared by following the steps presented in table 4.5, using the standard protocol (*vide supra*) to prepare and use each reagent solution. SAMs were stored under toluene in the reaction vessel (figure 4.6); toluene was removed from the vessel, and secondary modification solutions were immediately introduced to produce a sequential modification by reaction with the terminal R-group.

Silver nanoparticles were prepared using a borohydride reduction of silver nitrate [94]. Aqueous sodium borohydride (10 cm^3, 2×10^{-3} M) was chilled in a salt-ice bath. A teflon-coated magnetic stir-bar was added, and aqueous silver nitrate (3 cm^3, 10^{-3} M) was added dropwise with gentle stirring. The resultant yellow dispersion was left stirring at room temperature for at least 2 hours to hydrolyse excess borohydride. The clear yellow dispersion was allowed to partly evaporate on a surface, depositing a fine layer of silver on top of the surface prior to making a Raman measurement. The surface-enhanced Raman spectra of surfaces were collected using a Horiba JY LabRAM HR, with a 100× objective fitted with a 632.81 nm HeNe laser and a 532 nm frequency-doubled Nd:YAG laser. The detector was a peltier-cooled CCD array.

4.2.4 Spin-Coating

TMSC (0.1 g) was dissolved in a minimum quantity of THF (Aldrich, spectroscopic grade, <0.5 ml) and made to 10 ml with toluene (Aldrich, spectroscopic grade). This was left to equilibrate for 24 hours, and centrifuged at 2,000 rpm for 5 minutes to minimise the presence of aggregates. The top half of the supernatant was removed with a pipette, and the bottom half of the supernatant was discarded.

Substrate	Reagent	R	Name
Silica	toluene or MeOH	-	Blank
Silica	$(SiCl_3)(CH_2)_{11}CH_{3(PhMe)}$	$-(CH_2)_{11}CH_3$	TCDS-SAM
Silica	$(Si(OMe)_3)(CH_2)_3NH_{2(PhMe)}$	$-(CH_2)_3NH_2$	APTMS-SAM
Silica	$(Si(OMe)_3)(CH_2)_3I_{(PhMe)}$	$-(CH_2)_3I$	IPTMS-SAM
Silica	$(Si(OMe)_3)(CH_2)_2CF_{3(PhMe)}$	$-(CH_2)_2CF_3$	FPTMS-SAM
APTMS-SAM	toluene or MeOH	-	APTMS Blank
APTMS-SAM	$ClCOPh_{(PhMe)}$	$-(CH_2)_3NHCOPh$	phenyl
APTMS-SAM	$(SO_2F)(CF_2)_7CF_3$	$-(CH_2)_3NH(SO_2)(CF_2)_7CF_3$	perfluoro
APTMS-SAM	$ClCO(CH_2)_{16}CH_{3(PhMe)}$	$-(CH_2)_3NHCO(CH_2)_{16}CH_3$	stearyl
APTMS-SAM	$ClCO(CH_2)_{14}CH_{3(PhMe)}$	$-(CH_2)_3NHCO(CH_2)_{14}CH_3$	palmityl
APTMS-SAM	$ClCO(CH_2)_8CH_{3(PhMe)}$	$-(CH_2)_3NHCO(CH_2)_8CH_3$	capryl
IPTMS-SAM	toluene or MeOH	-	IPTMS Blank
IPTMS-SAM	$NaN_{3(MeOH)}$	$-(CH_2)_3N_3$	azido
APTMS-SAM	fluorescein-5-isothiocyanate	fluorescenyl	fluorescein
APTMS-SAM	dansyl chloride	dansyl	dansyl

Table 4.5: Surface Modification Reaction Steps: To produce the terminal R-group in the **R** column, the substrate in the *substrate* column is reacted with the corresponding *reagent* according to the protocol in §4.2.3, page 84. The resultant product substrate is named in the final column.

Nylon-6 (Aldrich) was dissolved in HFIP at concentrations of 0.3–0.9 g/L. Poly(ethylene *m*-terephthalate) poly(ethylene *p*-terephthalate) copolymer (Dr Richard Thompson, Durham University) was dissolved in HFIP or chloroform at concentrations of 0.1–0.5 g/L.

A piranha-cleaned (§4.2.3) substrate was first washed with a flow of ethanol whilst spinning at 2,000 rpm to remove any settled dust. This was immediately covered with the maximum volume of a given polymer solution possible without flowing over the edge, and spun for 30 seconds. The spin-speed was varied between 1,000 and 10,000 rpm.

TMSC-coated substrates were suspended in a glass chamber containing an open 3 ml vial of HCl (36%) for 2 minutes. The Raman spectra of surfaces were collected using a Horiba JY LabRAM HR, with a 100× objective fitted with a 632.81 nm HeNe laser and a 532 nm frequency-doubled Nd:YAG laser. The detector was a peltier-cooled CCD array.

To produce grease-doped cellulose films, a microlitre-scale volume v_d of *n*-octadecanol (C18-OH, Aldrich) in THF at concentration c_d was added to a class-A 10 ml volumetric flask, and filled to-volume with stock 10 g/L TMSC solution. The *loading number* Λ of C18-OH was calculated as the molar ratio of C18-OH to cellobiose units in TMSC solution, assuming $D_s = 2.7$:

$$\Lambda = \frac{c_d v_d (324.28 + 72.15 D_s)}{m_{TMSC}} \tag{4.9}$$

where m_{TMSC} is the mass of TMSC of degree of substitution D_s in the final volume of spin-coating solution. The number 324.28 is the molar mass of a cellobiose monomer unit in g mol^{-1}, whilst 72.15 is the net gain in molar weight per TMS substitution in g mol^{-1}. The cellulose was regenerated in the same manner as an un-doped film.

4.2.5 Goniometry

A Veho VMS-004 USB microscope was controlled using MATLAB® or Cheese[(i)] to grab a close-up photograph of a sessile drop on a test surface in profile, lit from behind by an LED through a paper diffuser (figure 4.3). Geogebra 4.0 [95, 96], a piece of free geometry software, was used to fit a conical function to the profile of the drop surface and determine the internal angle of the three-phase line. The surface of the substrate was assumed to fit to a straight line - the internal angle was calculated at the intersection of the conical with the straight line, using the tangent of the conical function. The test liquid was deposited using a glass syringe clamped at a normal to the test surface, fitted with a modified cannula (blunted, square-profile tip). Advancing and receding contact angles were obtained by slowly increasing and decreasing the drop mass using the syringe, and taking the photograph at the appropriate moment or acquiring a video and picking the appropriate frame. The system was tested by taking photographs of prisms on the stage with known angles (90/45°), and measuring those angles in Geogebra - these were confirmed within ±0.1°. The test liquids were the VanOss liquids (table 4.3).

4.3 Results & Discussion

4.3.1 DFT

The main absorption transitions of the brighteners are shown in table 4.6 with accompanying illustrations of the major transitions.

The configuration-interaction (CI) singles coefficients are mixing coefficients for the orbital transitions, indicating how much of each individual pair of calculated orbitals contributes to the change of state, which is illustrated by:

$$\left\langle \psi_i | \psi_f \right\rangle = a \left\langle \psi_i | \psi_{fa} \right\rangle + b \left\langle \psi_i | \psi_{fb} \right\rangle \ldots$$

where a and b are CI singles coefficients and ψ is the electronic wavefunction where subscript *i/f* indicates initial and final occupancy in the Franck-Condon state. The dyes have no triplet excitations.

Transition dipole moments indicated for the HOMO→LUMO transitions in the three dyes are all along the length of the molecule, shown as a dashed line. Interestingly, the lowest energy DFT configuration of (*E*,*E*)-OB49 is with the sulfonyl groups in eclipsed configuration with respect to the long axis of the molecule, and a considerable dipole moment which is shown as an arrow. This is consistent with Ramsey [97], who finds by crystallography and Monte-Carlo simulation of larger systems, that OB49 prefers this configuration, which should allow it to act like a surfactant with an atypical geometry. The transition dipoles will allow meaningful interpretation of anisotropy later.

We can understand from the orbital hypersurfaces, that the $S_1 \leftarrow S_0$ transitions are allowed $\pi^* \leftarrow \pi$ transitions. In all three dyes, the rotatability of the styrenyl double bond(s) is increased in the first excited state by lowering of the bond order; there is a node within the LUMO on each double bond. This is understood in terms of the known photo-induced *(E)–(Z)* isomerisation of these dyes [4]; the lowering of the bond order in the excited state decreases the activation energy E_a of geometric isomerisation, increasing the rate of isomerisation k_I as per the Arrhenius equation [98, p. 807]:

$$\ln k_I = \ln A_I - \frac{E_a}{RT} \tag{4.10}$$

[(i)] Default Linux camera controller.

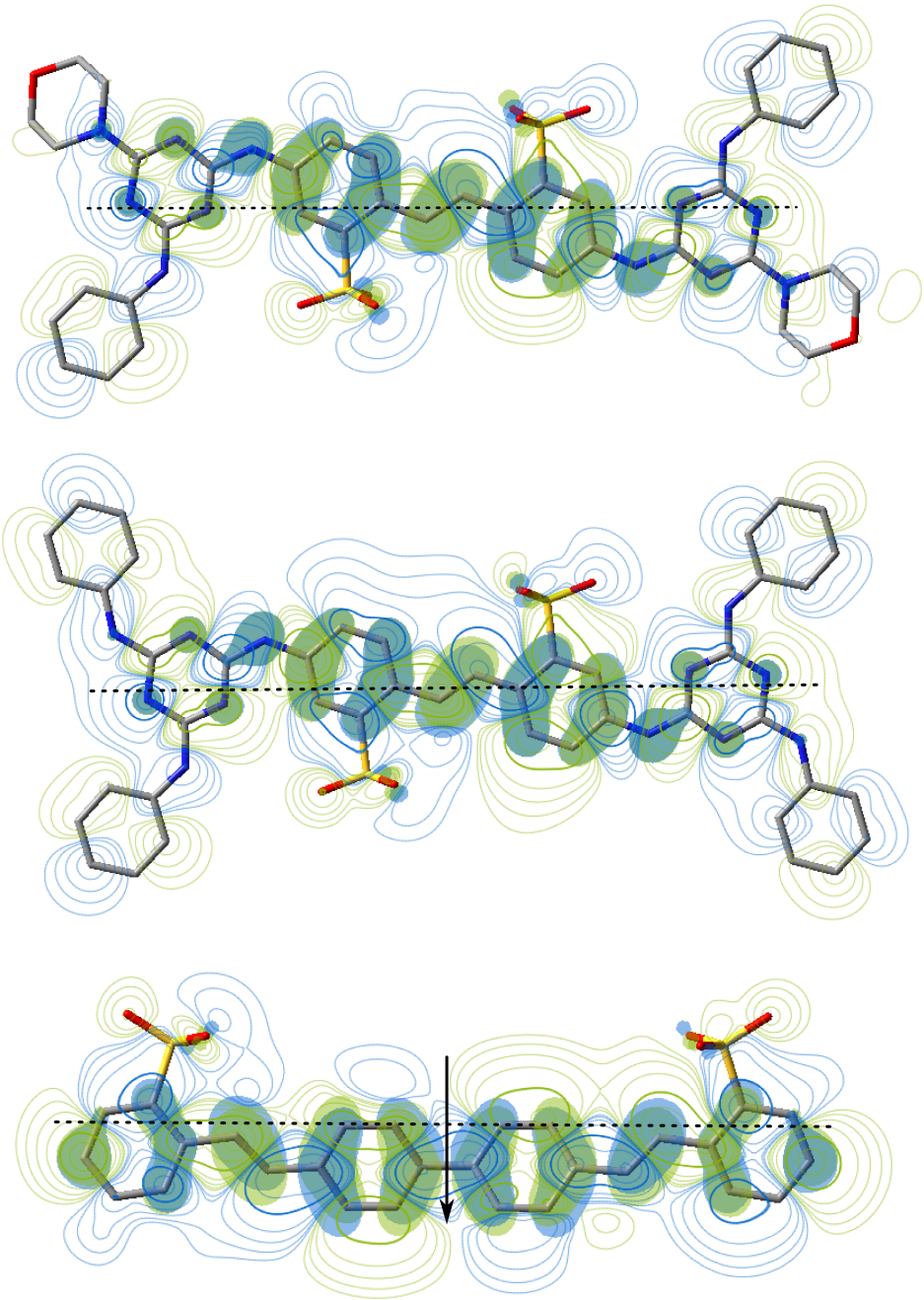

Dye/Transition	x	y	z	f (λ_{ex} /nm)	CI Coefficients
OB15/$S_{1,0}$	5.4561	0.0406	-0.1600	2.38 (379.76)	$(H \rightarrow L)$ 0.698
OB36/$S_{1,0}$	5.5324	0.0901	-0.0599	2.39 (388.83)	$(H \rightarrow L)$ 0.697
OB49/$S_{0,0}$	0.0000	0.0000	-29.3412	-	-
OB49/$S_{1,0}$	-0.0889	5.3425	0.0000	2.22 (390.53)	$(H \rightarrow L)$ 0.704

Table 4.6: TD-DFT Calculated Transitions of Dye Anions: 3D surfaces indicate the initial lower energy orbital ψ_i, and a contour the destination orbital ψ_f. The contour plane is 0.5 Å above the plane of the molecule. Bold contours indicate the same probability density as the 3D surface. Hydrogen atoms are not displayed. See §4.3.1 for discussion.

where A_I is a frequency factor of isomerisation in s^{-1} and T is the absolute temperature. The implications of this are in turn readily understood from undergraduate physical chemistry: the rates of the spontaneous forward and reverse isomerisations in the excited state are temperature-dependent and generally favour the (*E*)-isomer due to steric effects.

In contrast to the styrenyl moiety, the rotatability within the *biphenyl* moiety of OB49 is decreased and the molecule kept more planar, by increasing bond order in the region between the biphenyl rings.

In all dyes the involvement of the lone pair electrons on the sulfonyl groups in the transition is minimal.

4.3.2 Synthesis of TMSC

The identity of the product as TMSC is confirmed by ATR-FTIR and comparison to literature which indicates that $D_s \approx 2.7$ [56, 57, 58]. The Raman and IR spectra of TMSC in bulk and as films are given in figures 4.7, 4.8 and 4.9 on pages 90, 91 and 92 respectively. Strong bands at 1251 and 2957 cm^{-1} in the IR spectrum of TMSC are characteristic methyl bending and stretching modes respectively, whilst bands at 840 and 750 cm^{-1} are Si-O modes. The 2957 cm^{-1} band is also present in the Raman spectrum of TMSC and is considered reasonably diagnostic in this spectral region in the absence of the hydroxyl (OH) band. This broad OH band at 3340 cm^{-1} in cellulose, diminishes and shifts to 3487 cm^{-1} in TMSC as per [57, 58]. Kondo [99] indicates that the OH stretching modes in amorphous cellulose are made up of a several discrete bands, but substitution of OH groups does not simply subtract a portion of the band.

4.3.3 Spin-Coating

No combination of spin speed and polymer concentration in the solvents used, gave a satisfactory film for PET or nylon. Nylon was prone to buckling of the surface, whilst PET produced translucent films. These films were not subjected to further characterisation, though [100] indicates that low-boiling solvents produce uneven films due to rapid evporation, and the hygroscopic nature of solvents can produce clouded films, presumably due to the presence of water domains.

The 10 g/L solution of TMSC yields a transparent film by spinning at 2,000 rpm. Low scatter was demonstrated by passing a 532 nm laser beam with an output of 20 mW through the regenerated cellulose film on glass, and observing no visible laser spot. The structure of substituted cellulose rearranges its conformation to yield new patterns of hydrogen bonding, but the FTIR peak is blue-shifted and narrowed by partial substitution in any positions (and obliterated by complete substitution) [99]. Wide-angle x-ray scattering (WAXS) experiments in the literature find mostly a very broad feature with some superimposed broad peaks for cast cellulose films, in contrast to the crystalline structure in fibres. The WAXS profile of a thicker film (20 g/L TMSC, 1000 rpm spin speed) of regenerated cellulose on silicon is given in figure 4.10.

The form of the WAXS profile is a featureless “halo”, indicating that there is either no single crystalline structure present (mixed crystalline domains) or there is no measurable crystalline structure at all. The signal is consistent between four films produced by the same method. This is consistent with the change to the -OH stretching region of the regenerated material, as the blue-shifted stretches indicate less hydrogen bonding. The precursor micro-crystalline cellulose and a sample of cotton fibre both exhibit more red-shifted -OH modes in their Raman spectra, and also in the literature [101]. The TMSC is a “hairy rod” molecule, with uncontrolled (random) bulky substitutions along the polymer

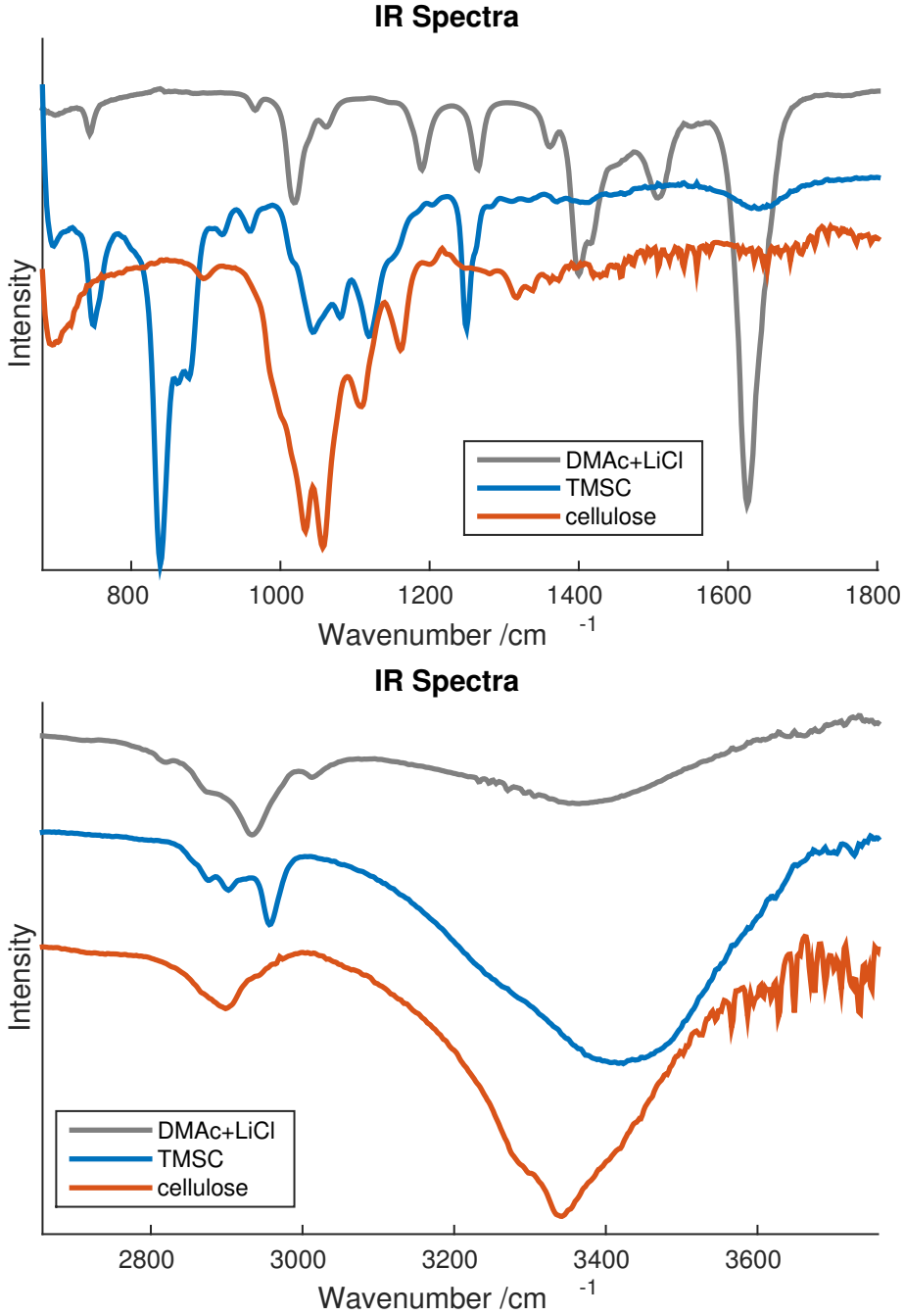

Figure 4.7: FTIR of cellulose and TMSC: The IR spectra are presented in two portions, independently normalised for clarity. The IR spectrum of the ionic liquid is presented also.

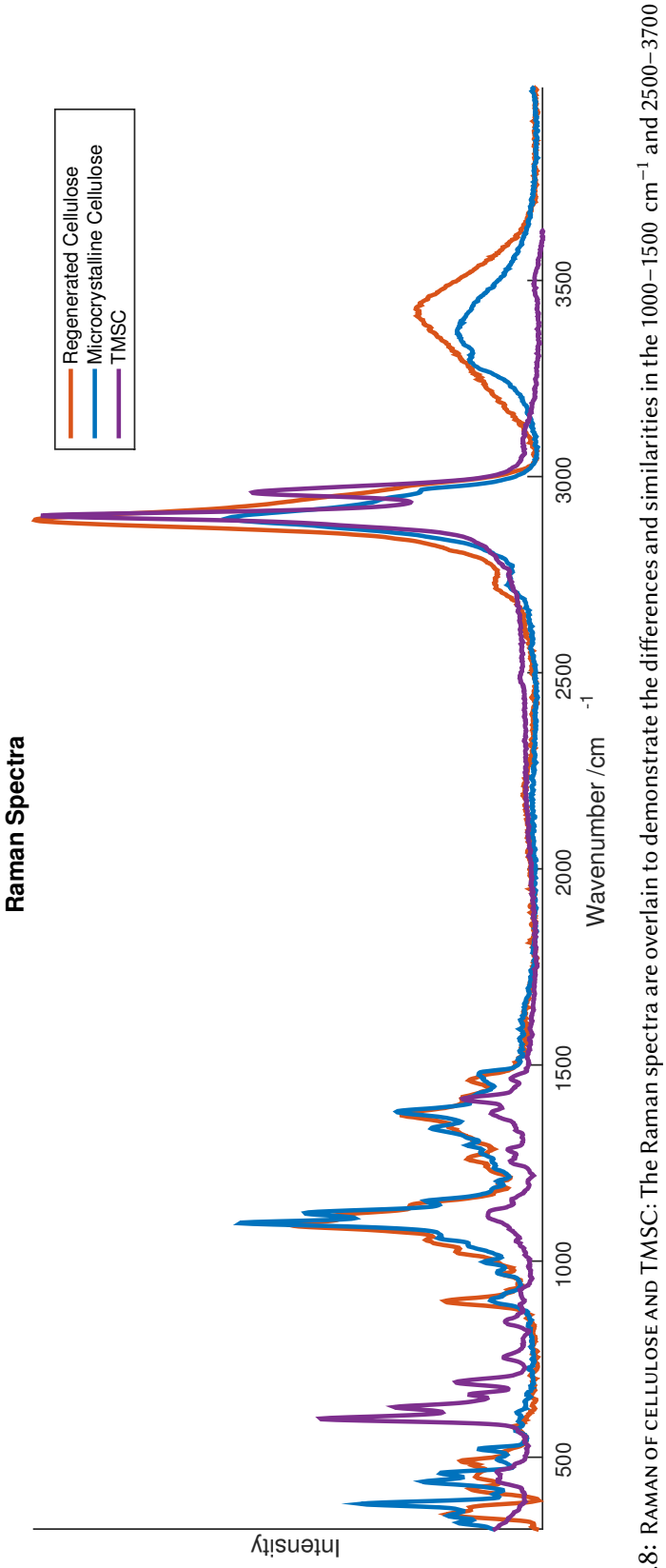

Figure 4.8: Raman of cellulose and TMSC: The Raman spectra are overlain to demonstrate the differences and similarities in the 1000–1500 cm^{-1} and 2500–3700 cm^{-1} regions.

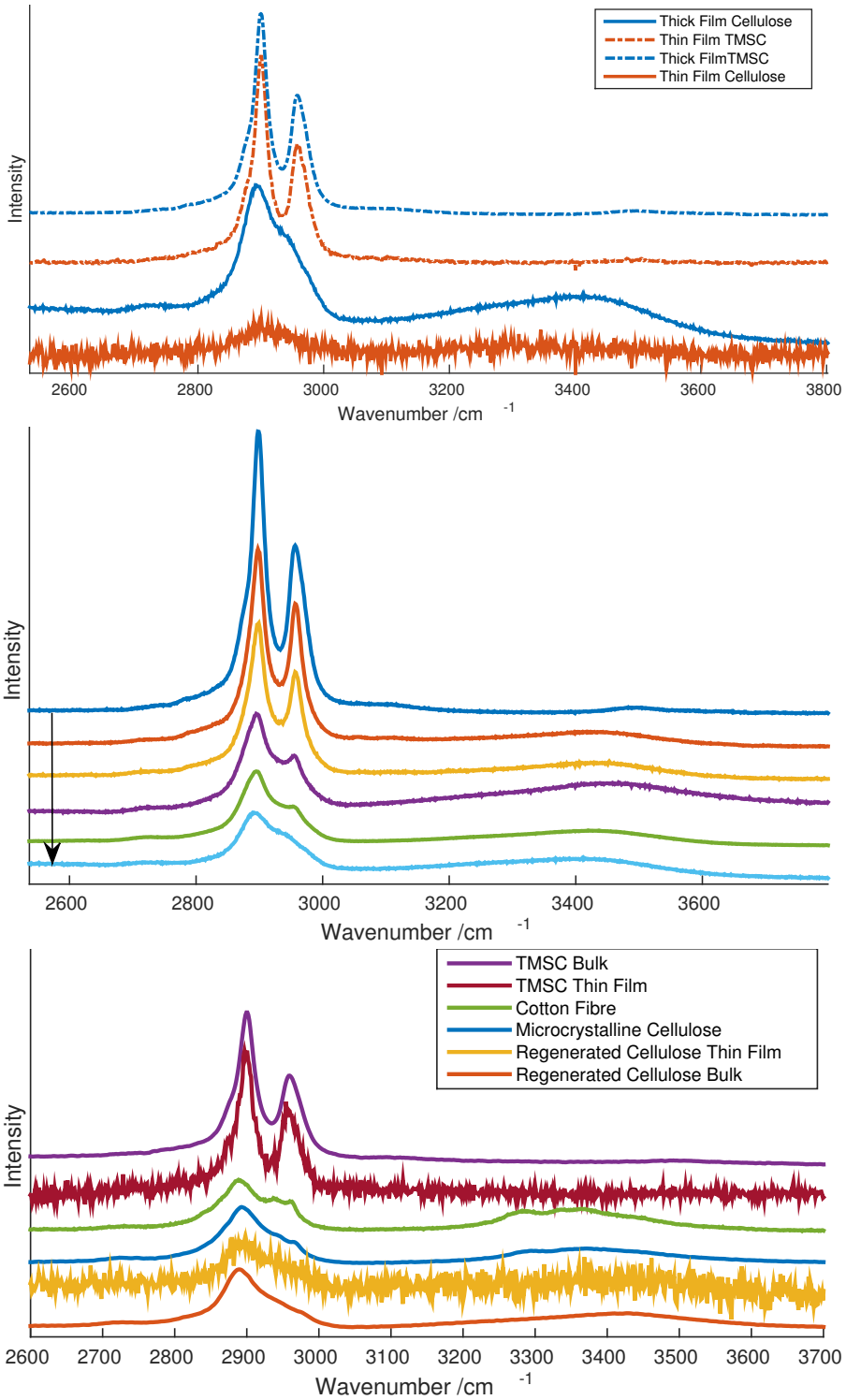

Figure 4.9: Raman Spectrum of Films of Regenerated Cellulose: Top: Comparison of thick and thin film spectra for clarity. Middle: Progressive regeneration of a thick film of cellulose. Hydrolysis times 0, 5, 10, 30, 45, 120 s. The arrow indicates the progression of the hydrolysis. Spectra have been scaled and offset for clarity. Bottom: Comparison to standard spectra of bulk materials. The spectra have been normalised and offset for demonstration. The thin films of TMSC and regenerated cellulose produce easily differentiated spectra. TMSC yields a spectrum in a far shorter time as it is more Raman active.

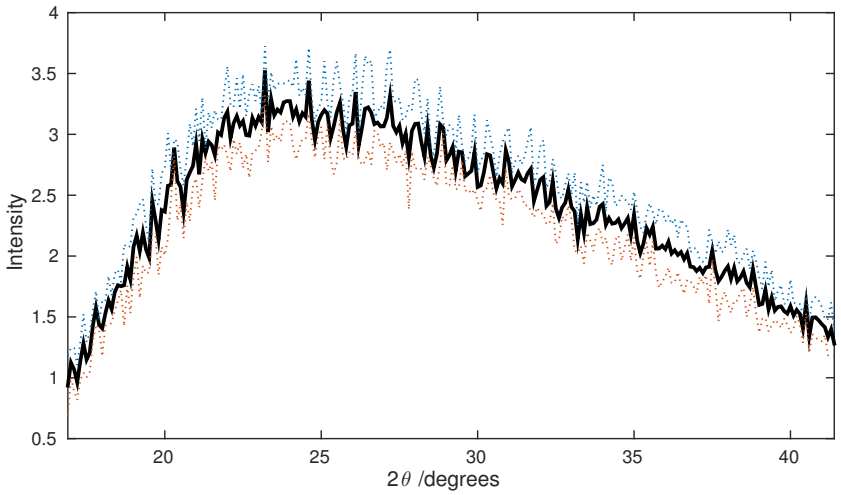

Figure 4.10: WAXS of regenerated cellulose film: The WAXS profile of a thick regenerated cellulose film on silicon, left to hydrolyse for 10 minutes to increase crystallinity [56, 57]. The film was confirmed to be cellulose by Raman spectroscopy. The measurement was repeated four times, collecting each spectrum over 45 minutes, and the mean is presented here. The red and blue dotted lines represent one standard deviation.

backbone, and the spin-coating method provides little time to form ordered structures. The backbone being set in place, the deprotection step "unveils" the cellulose chain and hydrogen bonds form based on immediate proximity of the proper groups. Taken together, we expect that the films produced this way (when used immediately) are entirely amorphous for our purposes, and we need not concern ourselves further with crystalline cellulose.

The implication of a totally amorphous film is that it is prone to swelling in contact with water. The finding of [102] is that Langmuir-Blodgett films of cellulose from TMSC swell appreciably even in humid air, which is not a characteristic of crystalline domains of cellulose. However, the finding of [103] in the same journal in the same *year* implies by functionalisation kinetics, that these films are nevertheless appreciably ordered to some degree. These apparently conflicting findings are reconciled by understanding that polymer crystallinity and order is different to that of small molecules. Order arises from partial alignment of lengths of chain, potentially in very small domains of only a few monomer units. The smaller the degree of polymerisation, the higher the degree of crystallinity that can be achieved in the film. Therefore, the finding of [103] might be explained by their degree of polymerisation, which is known to be relatively small ($\approx$ 150) compared to cellulose ($>$ 9,000). The degree of polymerisation of the TMSC and cellulose used (and that of others cited) is not known.

Figure 4.9 demonstrates by Raman that the regeneration time of 120 s in the acid vapour chamber is enough to hydrolyse a film designed to be thicker than the thin film. The thick film was produced from a 20 g/L TMSC solution spun at 1,000 rpm. Spectra were acquired on silicon substrates.

Doped TMSC and cellulose films with $\Lambda > 0.4$ were translucent or opaque. A grease-doped film with $\Lambda = 0.1$ was used for photophysical comparison to cellulose films without VanOss or γ_{zis} characterisation; the dopant is partly soluble in at least one of the hydrophobic VanOss probe liquids, and all of the γ_{zis} liquids. The results of the VanOss characterisation is given in table 4.7.

The mean values of θ_a and θ_r were used to calculate θ_{eq}, and the reproducibility of these angles was typically $\pm 2^\circ$. The values of γ_s^{TOT} and γ_s^- for cellulose are comparable to the literature for natural

Part-Reproduction of Table 4.2 for Comparison

Polymer	γ_{zis}	γ_s^{LW}	γ_s^+	γ_s^-	γ_s^{AB}	γ_s^{TOT}	ΔG_{sl}^{IF}	W_s	Ref.
Sigmacell 101		54.49	0.11	47.83	4.49	58.98	20.56	-3.54	[60]
Sigmacell 20		52.94	0.11	41.70	4.24	57.18	12.99	-9.11	[60]
Sigmacell 20*		53.72	0.00	54.83	0.00	53.72	33.41	-3.75	[60]
Avicel		51.82	0.00	50.14	0.00	51.82	28.23	-8.15	[60]
Avicel*		52.10	0.01	58.43	1.09	53.19	38.66	-0.27	[60]
Cellulose	35.5–49.0								[61]
Cellulose						60.5–66.1			[62]

VanOss and Zisman Characterisations

Surface	γ_{zis}	γ_s^{TOT}	γ_s^{LW}	γ_s^{AB}	γ_s^+	γ_s^-	$\mathcal{K}$
cellulose	23.3	56.88	37.89	18.99	1.73	52.13	0.22
TCDS-SAM		27.81	26.14	1.67	0.34	2.05	5.19

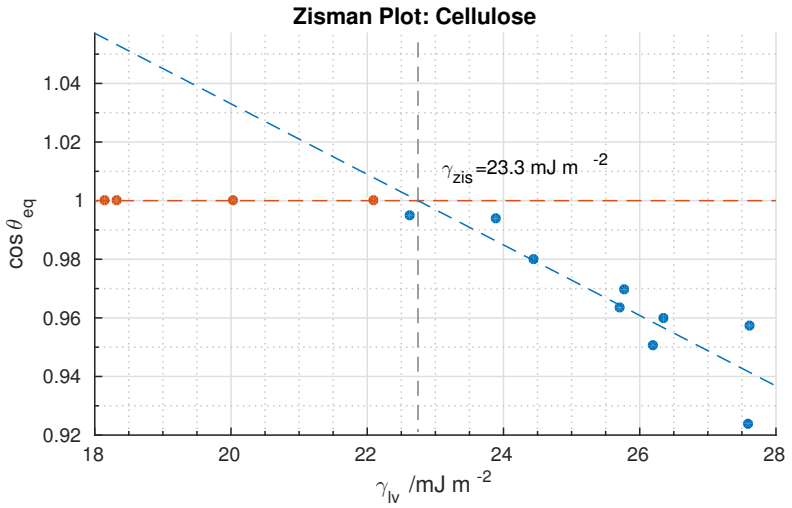

Table 4.7: VanOss and Zisman Characterisation of Surfaces for Spectroscopy: Top: Literature values from a previous table. Middle: The value of $\mathcal{K}$ was calculated from the advancing and receding angles of water. Their values indicate that the cellulose surface is the less heterogenous of the two surfaces. The value of γ_{zis} was calculated from the results in the graph. Bottom: The Zisman plot for a batch of regenerated cellulose films. From left to right the solvents used are hexane, trimethylpentane, heptane, ethanol, nonane, decane, undecane, pentanol, tridecane, heptanol, tetradecane, nonanol, and hexadecane.

cellulose (table 4.2, reproduced in part in table 4.7), though γ_s^{AB} increases as a consequence of increasing γ_s^+. Unexpectedly, γ_s^{LW} decreases. This can be explained either by the fact that amorphous cellulose is the minor component of the literature substrate, or that amorphous cellulose is prone to swelling, which introduces water. Cellulose film also has a low critical surface energy compared to the literature. It is hard to rationalise why the dispersive component of amorphous cellulose surface tension would be lower than for the crystalline form. However, cellulose hydroxyl groups not involved in hydrogen bonding with cellulose, will be available for hydrogen bonding with probe liquids and adsorbed water, and increase the γ_s^+ term.

Pre-hydrolysis grease-doped TMSC film was depth-probed by Raman spectroscopy by shifting the sampling voxel progressively deeper into the film in 10 nm increments. Relative to the TMS modes, the CH stretching modes of C18-OH were in visibly greater proportion at the top of the film than in the bulk, without any sign of deprotection in the OH region - this at least partly explains the translucence of the high Λ films. When solvent is evaporating during spin coating, a skin can form in the early stages depending on the nature of the solute and the rate of evaporation. It would make sense for a concentration gradient to form, though the Raman spectra indicate only a slight excess compared to the bulk of the film. With a higher Λ comes the chance for a layer of dopant to form at the top surface, or for the proportion that has not associated with the polymer to form its own domains as solvent evaporates.

4.3.4 Surface Modification

The table 4.8 summarises the findings of the surface modification, and the results of the VanOss characterisation of the trichlorododecylsilane self-assembled monolayer (TCDS-SAM) are presented in table 4.7.

First Generation SAMs

These were produced directly from silica, and include SAMs formed by reaction with trichlorododecylsilane (TCDS-SAM), (3-aminopropyl)trimethoxysilane (APTMS-SAM), (3-iodopropyl)trimethoxysilane (IPTMS-SAM) and (3,3,3-trifluoropropyl)trimethoxysilane (FPTMS-SAM). These are represented in the upper top section of table 4.8. In all cases, the surfaces are significantly different to a silica blank treated with toluene, which remains unchanged. In all cases except FPTMS-SAM, first-generation SAMs are highly reproducible surfaces by sessile-drop goniometry. At this time it is simply unclear as to why FPTMS-SAM reacted to generate such an irreproducible surface tension, although there are grounds to speculate.

Far from being apolar, a substituted halide terminal possesses a permanent dipole moment, which is dependent on the electrophilicity of the substituent atoms and the number of substitutions. It might be speculated, that this dipole moment plays a role in a physisorption mechanism that creates defects; given that the dipoles present within the R-groups interact, an occasional inverted molecule of (3,3,3-trifluoropropyl)trimethoxysilane is one possibility. For comparison, the dipole moment of trifluoromethane is 1.65 D [32, **9**-7], though as the dipole moment of iodomethane is 1.62 D [32, **9**-7] and the IPTMS-SAM is satisfactory, this alone doesn't satisfy as an explanation. However, the orientation of that dipole moment and the size and geometry of the substituent may well be important; in a monosubstituted terminal, there is scope for dipoles within the R-group to form favourable dipole-dipole interactions, whereas for a trisubstituted terminal a consistent parallel alignment of the dipoles

Name	Different to Blank?	θ_{sess}
TCDS-SAM	✓	107.2 ± 1.3°
APTMS-SAM	✓	38.1 ± 3.4°
IPTMS-SAM	✓	79.3 ± 1.9°
FPTMS-SAM	✓	40 − 50°
phenyl	✓	85.4 ± 2.2°
perfluoro	-	-
stearyl	✓	40 − 70°
palmityl	✓	40 − 70°
capryl	✓	70 − 80°
azido	✓	75.1 ± 0.5°
Name	**Different to Blank?**	**EWIFS?**
fluorescein	-	-
dansyl	-	-

Table 4.8: Surface Modification Reaction Schemes - Results: Top: θ_{sess} is the sessile (resting) contact angle of a drop of distilled water on the surface. Broad ranges are used to indicate where the sessile angles were inconsistent from slip to slip. *Different to Blank?* indicates whether the contact angle is different to the blank. First- and second- generation SAMs (see text) are separated by a horizontal rule. Bottom: The results of reacting fluorescent dyes with an APTMS SAM. Neither dye produced a signal in the EWIFS instrument. *Different to Blank?* indicates whether the fluorescence spectrum is different to that of the blank.

is unfavourable and repulsive, which in turn may not result in monolayer coverage - see figure 4.11 for clarification. This interaction type may also in part explain the ease with which an APTMS-SAM is produced, and also the reduced reactivity of that surface compared to a bulk primary amine.

Being a prospective model grease, it is beneficial that the TCDS-SAM is among the first generation treatments as it is fast and facile to produce in quantity in a single reaction, using also smaller volumes of solvent than second-generation treatments. It demonstrates a reproducible sessile contact angle of $107.2 \pm 1.3°$ in contact with water, and in table 4.7 it can be seen that the main contribution to its surface energy (94%) is from apolar interactions; its monopolar contributions are much smaller than the total surface energy, compared to the strong monopolar and total acid-base contributions of cellulose. Its total surface energy is low, comparable to the γ_{lv} of hydrocarbons such as dodecane (25.35 mJ m^{-2} [104]) and below the γ_{zis} value of cellulose in the literature. Finally, like all the other SAMs, it is optically transparent, making it useful for spectroscopic studies of fluorescence.

Second Generation SAMs

Second-generation reactions were carried out by reaction of APTMS-SAM with benzoyl chloride (BzOCl), perfluorooctylsulfonyl fluoride (PFOSF), and 18-, 16- and 10-carbon linear alkanoyl chlorides. Also, by reaction of IPTMS-SAM with sodium azide.

As well as the blanks detailed in table 4.8, second-generation SAMs were also tested against a secondary blank which sought to react the second-generation reagent with the silica surface. In all tests, the silica surface was unaffected by the second generation reagent, as a water drop spontaneously spread across the surface before and after treatment.This indicates that the silanol groups did not react significantly with the reagents or adsorb any side-products, which in either case should have reduced

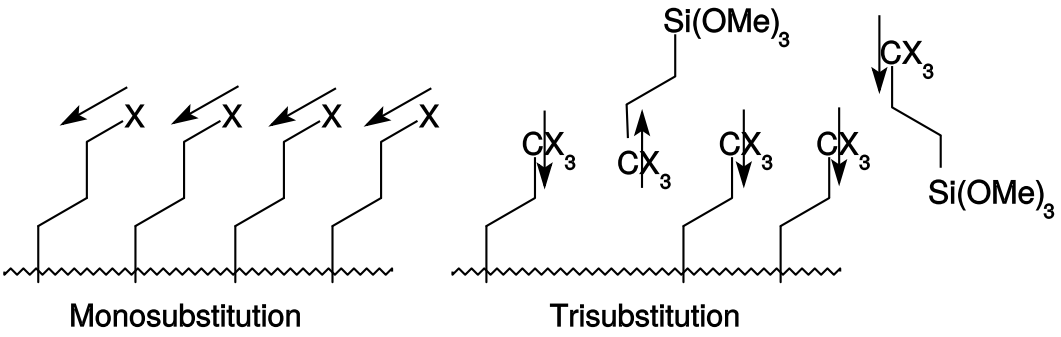

Figure 4.11: Potential Role of Dipoles in Monolayer Formation: Arrows indicate the direction of dipole moments, offset for clarity. Left: Permanent dipoles within halo-monosubstituted terminal groups may interact favourably to aid monolayer formation and packing through formation of attractive forces. Right: the same within halo-trisubstituted terminal groups appears far less favourable, potentially generating repulsive forces between groups or less-welcome attractive forces.

the surface energy, preventing spreading.

The general finding of goniometry is that the second generation SAMs based on APTMS produce a surface with less reliable surface tension properties than first generation. As previously discussed, the reactivity of the APTMS amine group is diminished once part of a SAM and requires very reactive reagents in order to covalently modify it [93]. The sulfonyl fluoride, isothiocyanate, acyl chloride and sulfonyl chloride groups were chosen specifically for their reactivity toward amine groups, however there is still a question of how to rationalise the observed results; the more reactive aliphatic acyl chlorides produce smaller, less reliable contact angles in contact with water, than the one aromatic that was tested.

In the bulk phase, an acyl chloride reacts with two equivalents of amine to produce the amide product and an amine hydrochloride side-product [105]. The side-product is in equilibrium with HCl and the free amine, but in favour of the side-product. The reaction rate of an aromatic acid chloride with an amine should be greatly hindered by the lessened reactivity of the acid chloride (caused by resonance stabilisation), yet its sessile contact angle is both high and reproducible. By contrast, the more reactive 10-, 16- and 18-carbon aliphatic analogues produce poorer surfaces overall. The lower rate of reaction of benzoyl chloride may be responsible for its reproducibility, in that it should produce a more ordered layer and be less prone to formation of side products with contaminant nucleophiles such as water.

Although the observed results do not contradict the established theory (that the leaving group in the reaction of a reagent with an APTMS-SAM has to be a good leaving group [106]), it is counter-intuitive that the more reactive reagents produce poorer second generation surfaces but better first generation surfaces. The reactant solution in the described protocol will always contain a large molar excess of reagent compared to the available silanol groups [93], and it is also speculated that the surface treatment might *not* be controlled by lowering the concentration and using longer reaction times; this is based on the theory of physisorption and chemisorption.

A Freundlich isotherm [98] is an example of an empirical relationship between bulk concentration of an arbitrary molecule and some measure of mass of that molecule, physisorbed on a surface placed in

contact with that bulk medium. In this case, that molecule is a solute and the medium is a solution. The theory behind the empirical relation, states that the solute achieves a dynamic equilibrium between the physisorbed and solvated bulk state. At high concentrations, the adsorption sites are nearly fully occupied due to the favourable kinetics, and the difference of increasing the concentration is minimal, though at sufficiently low concentrations, the isotherm is essentially linear with a non-zero gradient of adsorption vs concentration. A chemisorbed molecule however, forms a much stronger bond to the surface in a deep potential well - this may constitute a reaction to form a covalent bond.

Assuming that surface treatment agents follow a chemisorption model (which they already demonstrably do), the solute partitions between bulk and physisorbed states, and steadily loses both molecules *and* adsorption sites to the chemisorbed state. If the rate of chemisorption is *high* for properly oriented physisorbed molecules (i.e. there is a small or nonexistent potential energy barrier between the physisorbed and chemisorbed states), then in principle the physisorbed molecules have less opportunity to form a self-assembled ordered structure, and instead chemisorb at random. In contrast, an array of physisorbed molecules may be free to reorient themselves into a very ordered structure that does not easily desorb, and then slowly chemisorb.

Therefore it might be speculated, that the high reactivity of the linear alkanoyl chlorides is problematic. However, it remains that the trichlorododecylsilane surface (TCDS-SAM) is highly reproducible despite its reactivity. Therefore, there is yet no satisfactory explanation for this, and more data (such as from atomic force microscopy) is required. However, in closing on this matter, it is worth noting that the benzoyl chloride reagent is extremely rigid and planar, and is in principle more liable to form ordered structures for that reason alone.

The apparent failure of the reaction of APTMS-SAM with PFOSF, could have been caused by a film of toluene on the APTMS-SAM, as PFOSF is insoluble in toluene. Equally, the reaction could simply yield an identical contact angle to APTMS-SAM, which itself ages over time to give a range of angles [107]. As contact angles were measured immediately after removing from toluene and drying in a stream of nitrogen, and the ageing of APTMS-SAM occurs reasonably rapidly, the contact angle for the APTMS-SAM and perfluoro surface might be distinguished by measuring sessile contact angle as a function of time, to see if their profiles differ. This surface, like the others, would of course benefit from further characterisation per the method of Van Oss. Nevertheless, a low surface tension (high contact angle) surface was reasonably expected from this method, and this was not obtained.

Iodide Substitution Reaction The reaction of sodium azide with the IPTMS-SAM, gives a distinguishably more polar surface by sessile-drop goniometry. This would be caused by the charge distribution of the azide moiety, in which the terminal nitrogen atom has a partial charge. Click reactions have not been attempted, and so the availability of discussion is extremely limited. It is not known to what extent the iodine atoms were substituted, though the presence of iodine atoms might act to quench interfacial fluorescence or allow phosphorescence, and so future uses of the IPTMS-SAM might focus on those phenomena.

Regarding Surface Complexity In the literature, surfaces and surface treatment silanes have been produced that have complex functionality, properties, or structure [106, 108, 109, 110, 111, 112, 113, 114]. In those studies, the bulk of the R-group is often significant, purely due to the fact that the surface reaction is generally the last step. A bulky molecule is designed which, when reacted with the surface, gives sufficient coverage to achieve the designed function. Against the general leaning of the liter-

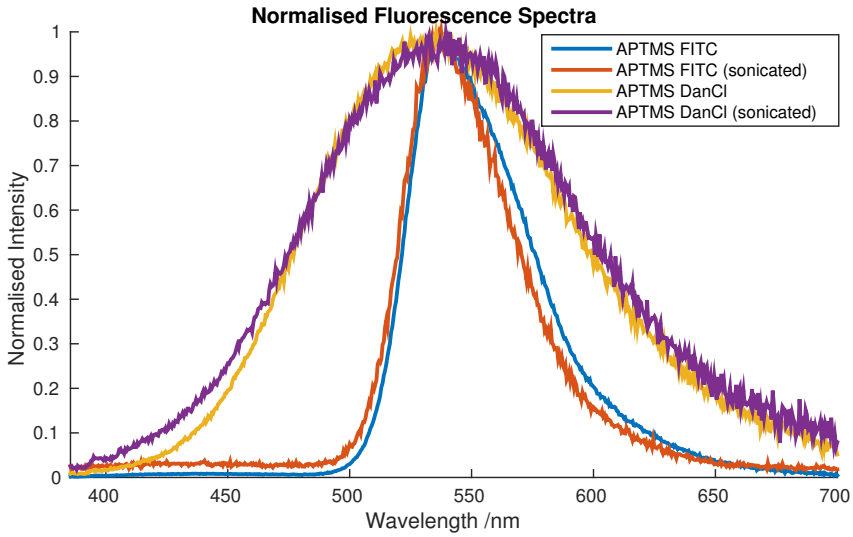

Figure 4.12: Silica Gel Fluorescence: Silica gel treated with dye or APTMS produces the same weak spectrum as plain silica. However, silica gel treated with APTMS then reactive dye solution, yields fluorescence spectra that are almost completely unchanged by sonication in solvents. Note that the sonication washing process was repeated until the effluent ethanol did not visibly fluoresce when placed in the 5 mW beam of a 405 nm handheld laser.

ature, this thesis has (in passing) tested the idea that sequential surface reactions are viable. Given that typical bulk reactions give the opportunity to purify the reactant, those studies effectively have more controlled surface reactions, producing only linkages to the surface that are desirable, with little or no redundant surface groups produced. It may be desirable in the future to test the parameters of sequential surface reactions to avoid complex, inefficient bulk chemistry in favour of specific surface reactions, though as the results of characterisation can be counter-intuitive using macroscopic methods, such studies may necessarily be carried out through microscopy and elemental analyses such as x-ray fluorescence.

For the purposes of future experiments with controlled surface tension parameters, first generation reactions are preferable, and so e.g. click chemistry between azides and alkynes are possibly a better avenue for creating surface treatment agents when the surface chemistry must necessarily be "pure".

Reactions with Dyes

Reactions with dyes were successful in the literature [115] but were not reproducible with the APTMS-SAM on the time-scale of the reactions used. However, they did react with silica gel treated with APTMS, and produced fluorescence that could not be removed by sonication in ethanol or DCM. The fluorescence spectra of these powders as measured in an integrating sphere, are presented in figure 4.12. This is *per se* inconclusive as the APTMS could be aggregating on, or in pores of the gel, creating hydrophobic pockets or regions where the dye can adsorb especially strongly and become trapped.

Regardless, this presents a dichotomy: either the dyes do not react with the SAM but adsorb to/react with its aggregates, or the dyes *do* react slowly with the SAM (and possibly also its aggregates), but the greatly increased surface area of the silica gel compared to flat silica slips makes it possible to acquire a spectrum.

4.4 Conclusion & Further Work

The TD-DFT results on the three dyes demonstrate that the lowest energy transition of the dye is to the S_1 state, and that it is a HOMO-LUMO $\pi^* \leftarrow \pi$ transition. The lowest-energy ground state conformation of the dye OB49 takes an unpredicted geometry irrespective of the starting geometry, which is supported by computational and experimental evidence from elsewhere [97].

Cellulose film would benefit from characterisation by atomic force microscopy (AFM) to confirm the surface roughness, but otherwise its characterisation is satisfactory for the required purpose.

It is necessary and sufficient to say, that the surface energy of the transparent TCDS-SAM is both reproducible and like that of an oily substance.

Second generation SAMs based on APTMS-SAM are unreliable in comparison to the first-generation TCDS-SAM, and will not be pursued further for model greases. There is conflicting evidence as to whether the APTMS-SAM is what one would expect; on one hand there is a change to the surface tension, producing a contact angle in agreement with the literature (and benzoyl chloride treatment produces the expected change to APTMS-SAM without causing any changes to bare silica). Yet, the treatments with FITC and dansyl chloride in ethanol (prepared as per histological stains) elicit no change to the fluorescence spectrum of an APTMS-SAM, though they create a fairly weak fluorescent response in silica chromatography gel that has undergone the same treatment. Further, although the SERS spectra of intentionally aggregated APTMS-SAMs are different to those produced by the regular protocol with peaks that are expected, this doesn't specifically prove the absence of e.g. a multilayer system. The phenyl surface is nevertheless promising but as a VanOss characterisation has not been performed, it will be reserved for future work.

Similarly to the APTMS-SAM, the IPTMS-SAM is a reasonably hydrophobic surface that was proposed as a means to an end. The substitution of iodine by azide would produce a surface appropriate to click chemistry in the future. However, as the application is with fluorophores at interfaces it would make more sense to see first if IPTMS-SAM is an effective quenching interface, and if this quenching can be used for analytical purposes. From there, the extent of substitution by azide could be measured using energy-dispersive x-ray spectroscopy (EDX) to give an elemental analysis of the interface.

Whether the amine groups on APTMS-SAM form into hydrochlorides at all as part of the acyl chloride surface reaction is yet to be seen, though EDX would give an indication about this too.

Atomic force microscopy would be useful for the investigation of the grase-doped interfaces, as the apparent surface excess of the dopant could be more fully described. However, at this stage the mostly even distribution of dopant is of more interest, as this is an intermediate step between the two extremes of cellulose and TCDS-SAM. One is a disordered polymer and the other is an ordered model grease, and the grease-doped polymer is a greasy cellulose with unknown properties.

A simple yet unexplored surface is silica hydrophobised by hexamethyldisilazane (HMDS), the silanating agent used to create TMSC. This should produce a very "pure" surface modification as in the following schemes where Z represents an immobile bulk:

$$(Me_3Si)_2NH + Z(OH)_n \longrightarrow (Me_3Si)NH_2 + Z(OH)_{n-1}(Me_3SiO)$$
$$(Me_3Si)NH_2 + Z(OH)_{n-1}(Me_3SiO) \longrightarrow NH_3 + Z(OH)_{n-2}(Me_3SiO)_2$$

$$(Me_3Si)_2NH + H_2O \longrightarrow Me_3SiOH + (Me_3Si)NH_2$$
$$(Me_3Si)NH_2 + H_2O \longrightarrow Me_3SiOH + NH_3$$

almost all silane products in toluene solution are known to be surface-reactive with respect to remaining surface silanol; though the reactivity of trimethylsilanol toward surface silanol groups is unknown, it is volatile and should be easily lost. There is no scope for cross-linkage and the net result of reaction with surface water would be dehydration rather than producing defects.

In the following chapter, the silica, cellulose, TCDS-SAM and grease-doped cellulose surfaces will be pursued as models for spectroscopy.

Chapter 5

Photophysics of Dyes

Abstract

The brightness of dyes is first calculated from the relative quantum yield and the extinction coefficient. The brightness values of the dyes OB15, OB36 and OB49 are 0.092, 0.034 and 0.902, respectively. The natural lifetimes of the brighteners are $6,700 \pm 109$, $5,971 \pm 712$ and $1,685 \pm 22$ ps respectively.

A bulk solution solvatochromism experiment in the wavelength- and time-domains has been undertaken, and both data have been fitted to a linear Kamlet-Taft model. Lippert plots establish the relationship between polarity and solvatochromic shifts. The dye coefficients in each model are commented on. OB15 exhibits a lifetime vs solvatochromic shift gradient of -0.15 ps/cm^{-1}, whilst OB49 is +0.25 ps/cm^{-1}.

EWIFS spectra differ to bulk spectra in all cases explored.

The origin of greening is explored. It is determined to be due to reabsorption effects, and the same phenomenon might invalidate some other results in the literature using diffuse reflectance to determine emission.

—

5.1 Brightness

The quantum yields and extinction coefficients of optical brighteners in water are given in figure 5.1. The Beer-Lambert stock solutions were prepared with deionised water, grade A volumetric glassware and an analytical balance, to concentrations of 1.621×10^{-3} M (OB15), 3.201×10^{-3} M (OB36) and 8.887×10^{-4} M (OB49). Test solutions were made to 10 ml in volumetric flasks, from 0, 5, 7, 9, 9, 10, 12, 14, 15, 17, and 20 μL aliquots of stock solution using a 20 μL adjustable micropipette. The absorbance measurements were taken at a wavelength of 350 nm in a quartz cuvette and had the absorbance value for a solvent blank subtracted from the measurement. Absorbance measurements were noted to 3 decimal places. Extinction coefficients of the brighteners were calculated from the mean value of A/c and the standard deviation of that is presented as the precision, where A is the absorbance and c the molar concentration. The extinction coefficients of the brighteners are presented in table 5.1. The solutions for the relative method for quantum yields were prepared arbitrarily from the stock solutions to give an appropriate value of absorbance. The stated precision of quantum yields is the regression error carried through.

Brightener	ε_{350}	f_{osc}	Φ_f	B
OB15	35, 590 ± 170	0.84	0.11 ± 0.001	0.092
OB36	15, 010 ± 80	0.43	0.08 ± 0.004	0.034
OB49	60, 060 ± 350	1.27	0.71 ± 0.007	0.902
QS	5, 500 ± 45	-	-	-
QS (lit.)	5, 577	-	0.58	-

Table 5.1: The Brightness of Brighteners: Quantities have been described previously in the text. ε_{350} is the extinction coefficient at 350 nm in $M^{-1}cm^{-1}$.

The extinction coefficient being known, we scale the absorbance spectrum and approximate the oscillator strength f_{osc} from equation 2.7. The brightness is given by $B = f_{osc} \cdot \Phi_f$.

We can see from table 5.1 that the performance of these brighteners in aqueous solution is variable. The industrial concern of OB36 is that it brightens poorly on nylon, even when deposition is assured. In the absence of a suitable nylon film this cannot be tested, and although the performance of the brightener in solution is poor, this doesn't indicate anything specific about the photophysics on surfaces *vis a* auramine.

In both OB15 and OB36 the ground state is planar due to conjugation between the core stilbene group and terminal anilino rings across the triazine rings *via* nitrogen lone pairs. Population of the LUMO creates a loss of conjugation due to the spread of antibonding character. There is an antibonding interaction in the stilbene double bond, and across all three nitrogen atoms bonded to the triazine ring. This lowers the rotational energy barrier that exists due to delocalisation.

The difference in Φ_f between OB15 and OB36 can be related to their single structural difference: the extra rotational degrees of freedom in the anilino group compared to the morpholino group. Population of the LUMO in OB15 only very slightly alters the electron density in the peripheral groups on the triazine ring, and the electron probability density is concentrated in the core of the molecule and on the aromatic substituents. The same in OB36 produces a more delocalised electron density across all four anilino groups. In any case, with more rotational degrees of freedom, the scope for internal conversion directly to the ground state increases, which competes effectively with fluorescence.

Being the smallest molecule, OB49 is (predictably) the molecule with the highest quantum yield and brightness. We rationalise that although there is twice the scope for (*E*)-(*Z*)-isomerisation in OB49, the major rotational degrees of freedom in the ground state *gain* π-bond character in the S_1 state. This

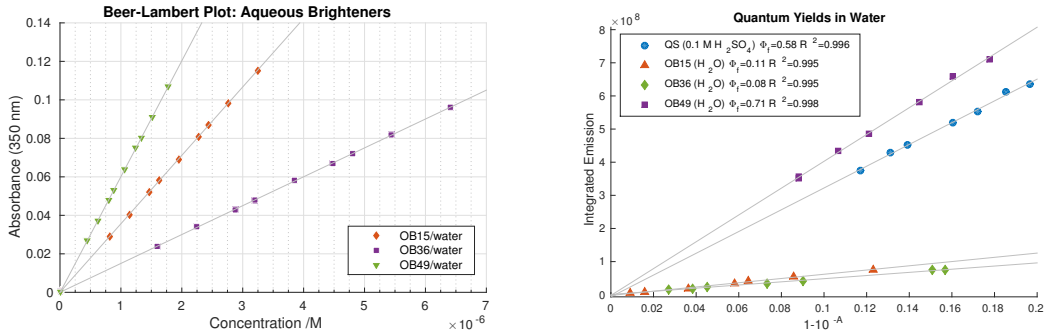

Figure 5.1: Brightness of Brighteners: Left: The Beer-Lambert plot. All R^2 values for the least-squares regression lines are >0.9999. Right: Photoluminescent quantum yields of three brighteners, relative to quinine sulfate. λ_{exc} = 350 nm.

Liquid	α	β	π^*	n	ϵ	δ_d	δ_p	δ_h
acetic acid	1.12	45	0.64	1.372	6.2	14.5	8	13.5
acetone	0.08	0.43	0.71	1.358	21.01	15.5	10.4	7
dioxane	0	0.37	0.55	1.422	2.25	19	1.8	7.4
DMF	0	0.69	0.88	1.430	38.25	17.4	13.7	11.3
DMSO	0	0.76	1	1.479	47	18.4	16.4	10.2
ethanol	0.86	0.75	0.54	1.361	24.6	15.8	8.8	19.4
formamide	0.71	0.48	0.97	1.447	111	17.2	26.2	19
propan-2-ol	0.76	0.84	0.48	1.377	17.9	15.8	6.1	16.4
acetonitrile	0.19	0.4	0.75	1.344	36.64	15.3	18	6.1
methanol	0.98	0.66	0.6	1.328	32.6	15.1	12.3	22.3
NMP	0	0.77	0.92	1.47	32	17	2.8	6.9
pyridine	0	0.64	0.87	1.510	12.3	19	8.8	5.9
THF	0	0.55	0.58	1.407	7.52	16.8	5.7	8
water	1.17	0.47	1.09	1.333	78.54	15.5	16	42.3

Table 5.2: Properties of Solvents for Solvatochromism: from left to right: literature KT parameters [116], refractive index and dielectric constant [32, p. **8**-44], Hansen parameters [89].

reduces the probability of internal conversion to S_0, such that there are fewer competing deactivation rates.

5.2 Bulk Solution Solvatochromism

The absorbance, excitation and emission spectra in bulk solution are presented in the supplementary information. The numerical values of the parameters of the liquids are tabulated in table 5.2.

5.2.1 Models

The solvatochromic shifts of all three dyes are presented in figure 5.2. The linear KT model is the result of fitting the linear function in equation (4.4) using regression analysis in MATLAB®. The excitation and emission spectra were initially deconvolved into a sum of 4–5 Gaussian terms in the wavenumber domain, dependent on how much vibronic structure was present. Generally, four were preferred, and five were used only when the R^2 of the four Gaussian fit was <0.999. The solvatochromic S_1v_0-S_0v_0 shift was determined from the approximate positions of the v_0 bands as given by deconvolution ($\Delta\tilde{\nu}'$). Although this method seems to work well, the Lippert plots indicate that almost everything except water is skewed toward lower $\Delta\tilde{\nu}$. The deconvolution is both presumptive and derivative and the repeats variable, and on that basis it has been disregarded.

Due to the presence of variable vibronic structure, which causes the wavenumber of maximum emission to skew by several hundred wavenumbers, the centroid of the emission spectrum (the mean wavenumber, weighted by emission intensity) is used to give a reliable figure that accounts for the whole emission, and is analogous to an expectation value. This also averages out the noise of the spectrum, and allows a much higher number of digits of precision to be used for calculations.

The Lippert plot is presented in figure 5.3. The use of the emission centroid has de-exaggerated the spread of data in the y-direction, but not changed the overall order of the data compared to plots that were produced from the wavenumber of maximum emission (not shown).

Overall, the KT model gives a numerical indication of what can be readily seen in the Lippert plots.

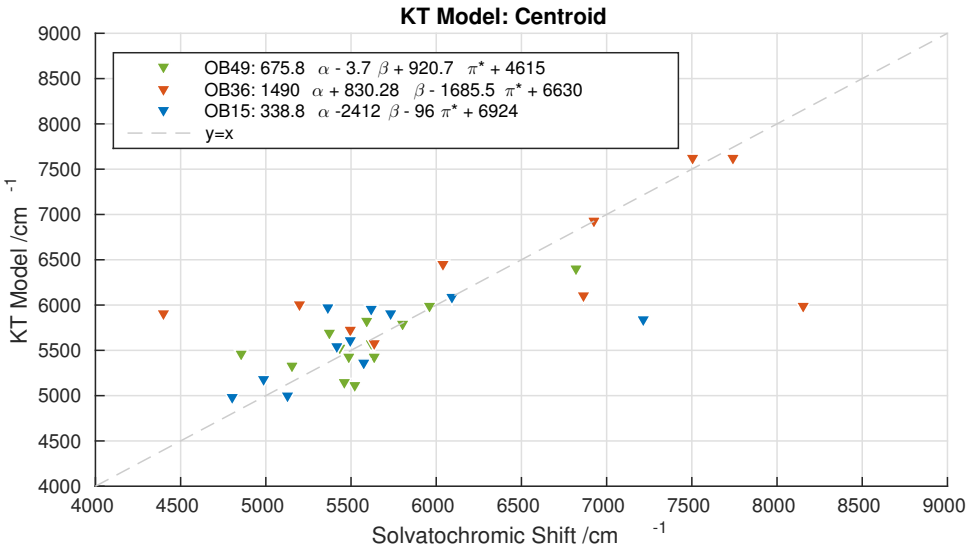

Figure 5.2: Kamlet-Taft Model of Brighteners: Kamlet-Taft linear model as a function of $\Delta\tilde{\nu}$. For a perfect model, all points lie along the equivalence line. The process of deriving the solvent parameters produces values which average out across a large number of solvent-solute interactions. This maximises their general utility but also makes plots like this one quite diffuse.

OB15 has little to no overall gradient across a range of polarities of the cybotactic region ($\pi*$), and it has a large Stokes' shift in apolar media. It responds only slightly positively to hydrogen bond donors, and emission undergoes a blue shift in the presence of hydrogen bond acceptors. OB36 also has a large Stokes' shift. It responds much more strongly to hydrogen bond donors and acceptors both, but has a compensating negative solvatochromism on a purely dipolar basis. OB49 is stabilised by hydrogen bond donors, responds neutrally to hydrogen bond acceptors and is stabilised well by the polarity of the supporting media.

Whilst care must be taken in making conclusions from this model, we might extrapolate an hypothesis from these loose and descriptive observations. OB49 should respond well to polar substrates with hydrogen bonding capability such as amorphous cellulose, though it is reasonably unperturbed by the presence of lone pairs. This corresponds well to its strong permanent dipole in the ground state. OB15 in being negatively solvatochromic with regard to hydrogen bond acceptors, might experience an increase to its quantum yield in the presence of an appropriate interface, as the higher energy spacing disfavours internal conversion to the ground state. Finally, although OB36 will not be used for EWIFS experiments, it is *speculated* based on the KT model that the general lack of polarity of nylon and the availability of hydrogen bond donors *and* acceptors (amide groups) could further lower the quantum yield of OB36 on nylon.

As a final note on bulk excitation and emission, it should be noted that the excitation spectrum of OB36 in some solvents is strange. It would appear that emission results almost exclusively after excitation to the v_0 band in the first and second excited singlet states, so that the quantum yield varies with excitation wavelength. No specific explanation for this is offered at this time.

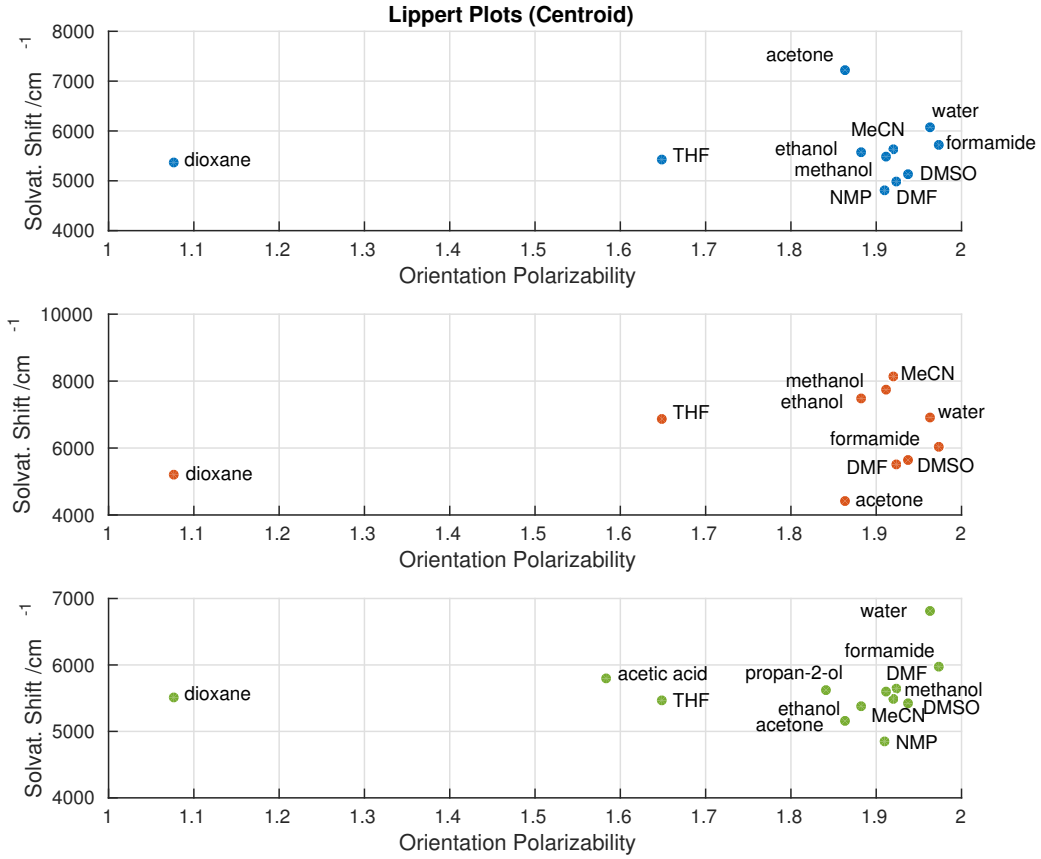

Figure 5.3: Lippert Plots of Brighteners: Top, Blue: OB15. Middle, Red: OB36. Bottom, Green: OB49. In all cases we can see that the general insolubility of these dyes hampers analysis by excluding many solvents.

5.3 TCSPC Data Analysis

Time-correlated single photon counting (TCSPC) decay data, $I(t)$, of a sample containing n emissive states at emission wavelength λ_{em}, is assumed to be of the form:

$$\mathbf{D}(t) = \left[i.r.f.(t) * \sum_{j=1}^{n} A_j e^{\frac{t}{\tau_j}} \right] + B \cdot i.r.f.(t) \tag{5.1}$$

where the final term on the right is a scattering function to compensate for very short emissive processes. We assume a residual noise present in the data, and so the objective function of the fit is to minimise:

$$\chi^2 = \int_{t=0}^{\infty} \left[\frac{I(t) - \mathbf{D}(t)}{\sigma(t)} \right]^2 .dt \tag{5.2}$$

under the assumption that the heteroscedastic uncertainty $\sigma(t) = \sqrt{I(t)}$, is a characteristic of the expected photon-counting noise, which we make no further attempt here to model. We therefore aim to iteratively find the set $\{A_j, \tau_j\}$, and characterise the goodness-of-fit of this set with the final χ^2 parameter. We then derive the quantity:

$$S_j = \frac{\int_{t=0}^{\infty} A_j e^{\frac{t}{\tau_j}} .dt}{\int_{t=0}^{\infty} \sum_{j=1}^{n} A_j e^{\frac{t}{\tau_j}} .dt} = \frac{A_j \times \tau_j}{\sum_{j=1}^{n} A_j \times \tau_j} \tag{5.3}$$

which is the proportion of the emission accounted for by the j^{th} emissive state, as a useful metric whilst A_j is an as-good-as-arbitrary fitting parameter.

The residual from the iterative fitting, should itself contain no residual information (i.e. maximum entropy, only noise), which would indicate that the form of $\mathbf{D}(t)$ represents the form of $I(t)$. The unbiased, normalised cross-correlation of the residual with itself, is the autocorrelation function $\mathfrak{a}$ of the residual, and any hidden functions and correlations become apparent on examination across a range of lags j:

$$\mathfrak{a}(j) = \left[\frac{1}{m} \cdot \sum_{i=l_1}^{l_1+m-1} r(t_i) r(t_{i+j}) \right] \left[\frac{1}{l_3} \cdot \sum_{i=l_1}^{l_2} [r(t_i)]^2 \right]^{-1} \tag{5.4}$$

where r is a residual of a fit to decay series $I(t)$, $m = l_3 - j$, $l_3 = l_2 - l_1 + 1$, and the maximum value of j is $l_3/2$. Among acceptable χ^2 values, the criterion for the *best fit* is flatness of $\mathfrak{a}(j)$.

The Durbin-Watson (DW) parameter is the sum of the squared differential of the residual, normalised to the sum of squared residuals. The value of the DW parameter should lie within the range $1.7 < DW < 2.0$, but it presents the same difficulty in interpretation that other single-statistics of complex problems suffer from. Therefore its utility is limited and it is presented here only as a literature standard. High values in the given range indicate that the residual contains mostly high-frequency noise, but values higher than 2.0 can in principle arise from the presence of sharp curves with a zero mean. In contrast, values below this range indicate the presence of a consistent signal present in the noise that causes the mean residual to deviate from zero, or curves with a zero mean. Further, data with very large or very small amounts of noise can give anomalously high or low values of DW, despite e.g. a flat $\mathfrak{a}(j)$.

t_b /ps	gain	t_d/t_b
3.125	16,000	5.76
6.250	8,000	2.88
12.500	4,000	1.44
25.000	2,000	0.72
50.000	1,000	0.36

Table 5.3: Significance of Time Offset: The significance of the time offset $t_d = 18$ ps relative to the bin width of the various gain settings for the MCA is signified in the last column, which signifies the maximum number of bins needed to correct for the maximum monochromator offset in the iterative reconvolution.

5.3.1 Time-Shift Correction for Anisotropy

In practice, the difference in monochromator geometry between λ_{ex} at which $i.r.f.(t)$ is measured, and λ_{em} at which the decay data is collected, gives rise to a shift between $I(t)$ and $\mathbf{D}(t)$. We introduce $\mathbf{D}(t-\partial t)$ by substituting $i.r.f.(t)$ with $i.r.f.(t-\partial t)$ in equation 5.1. The justification for the magnitude of ∂t is that the maximum wavelength-dependent offset $t_d(\lambda) = (N \cdot m \cdot \Delta\lambda/c)$, such that for the 60 mm 1200-grating, the first-order offset between $\lambda_{ex} = 371$ nm and $\lambda_{em} \approx 430$ nm, $t_d = 18$ ps. The effect of ∂t becomes significant to analysis when the bin width $t_b < t_d$, as shown in table 5.3, but cannot exceed this stated value.

Analysis of the differential of the pump and the decay-rise with respect to t, places the maximum of the decay differential at the zero of the pump differential. The time difference between these two points is ∂t.

There is a time-shift between (p)- and (s)-polarised signals, and another (very slight) between vertical (V) and horizontal (H) collection. The (p)-(s) shift occurs because of the placement of the double Fresnel rhomb, which creates a constant offset of ≈280 ps. The effect is shown in figure 5.4. The difference in time is calculated as the difference between the centroids of the instrument response functions, as this doesn't rely on subjective judgement, and averages out the effect of noise. Time-resolved data used to produce anisotropy curves, is shifted to match the IRF positions before calculation.

5.3.2 Bulk Lifetime Analysis

The results of iterative reconvolution of OB15 and OB49 data are reported in tables 5.4 and 5.5 respectively.

Brightener 36 produced multicomponent decays that could not be fit satisfactorily with iterative reconvolution. This was particularly pronounced in acetone, dioxane, HFIP, MEK and THF. As all fluorescence decays of OB36 include a significant contribution from more than one lifetime, it is not clear which of each is most useful. As the solutions are dilute, show no sign of aggregation or scattering in their absorption spectra at these concentrations and the form of the decays is not distorted, it simply is not clear why this should be the case. However, as the relative yield of each state is resolved by the reconvolution process, the quantum yields of aqueous OB36 can be resolved also. We calculate the natural lifetime of fluorescence regardless, by assuming that the two component decays are from

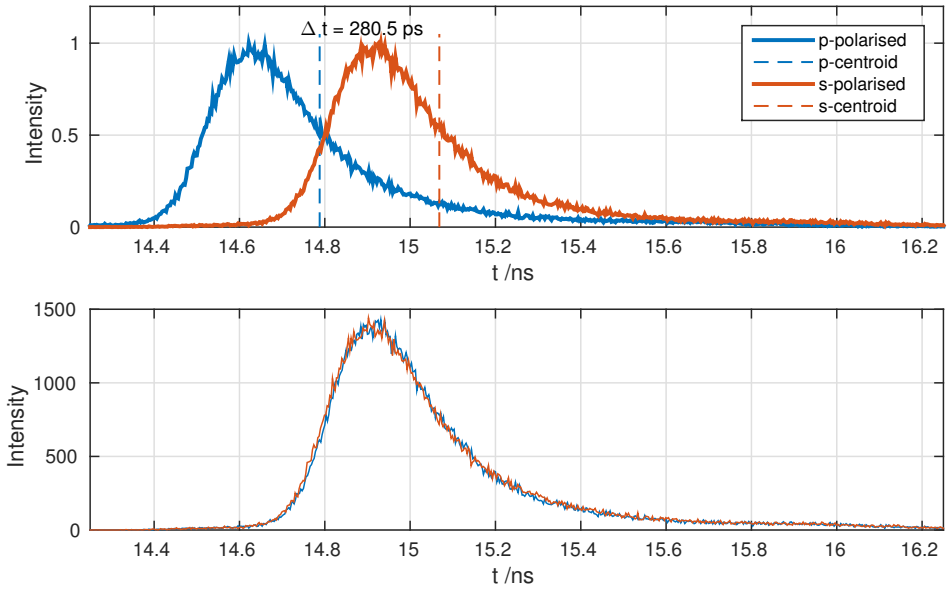

Figure 5.4: (*p*)-(*s*) Time Shifts: The effect of correction for time shifts, which is achieved by analysis of IRF centroids. Top: Normalised instrument responses. The signal for the (*p*)-polarised instrument response is shifted in time due to the double Fresnel rhomb. As the TCSPC runs in reverse start-stop mode, the effect also appears to be in reverse. Bottom: The corrected signals, which are identical in form.

OB15: Lifetimes in Bulk Solution

Solvent	α	β	π^*	τ_1 /ps	f_1	τ_2 /ps	f_2	DW	χ^2
acetone	0.08	0.43	0.71	715	1.07	320	-0.07	2.09	1.03
DMF	0	0.69	0.88	902	0.92	344	0.08	1.96	0.95
DMSO	0	0.76	1	919	0.97	380	0.03	1.76	1.15
ethanol	0.86	0.75	0.54	836	0.82	442	0.18	1.95	1.02
formamide	0.71	0.48	0.97	782	0.94	427	0.06	2.08	0.99
MeCN	0.19	0.4	0.75	836	0.92	247	0.08	1.92	1.08
methanol	0.98	0.66	0.6	716	0.9	278	0.1	2.09	1.05
NMP	0	0.77	0.92	931	0.96	395	0.04	2	0.99
water	1.96	0	0.65	**737**	1.02	131	-0.02	1.82	1.14

Table 5.4: Fluorescent Lifetimes of OB15 in Dilute Solution: excitation 371 nm, emission 430 nm. The bold entry for water is carried forward into table 5.6.

OB49: Lifetimes in Bulk Solution

Solvent	α	β	π^*	τ_1 /ps	f_1	τ_2 /ps	f_2	DW	χ^2
acetic acid	1.12	45	0.64	951	0.9	372	0.1	1.9	1.14
acetone	0.08	0.43	0.71	943	0.98	120	0.02	1.97	1.03
dioxane	0	0.37	0.55	930	1.03	245	-0.03	1.94	0.92
DMF	0	0.69	0.88	920	0.95	136	0.05	1.32	1.23
DMSO	0	0.76	1	899	0.96	310	0.04	2	1.01
ethanol	0.86	0.75	0.54	938	1.11	341	-0.11	1.63	1.15
formamide	0.71	0.48	0.97	1092	0.88	591	0.12	1.96	1
propan-2-ol	0.76	0.84	0.48	946	1.16	509	-0.16	1.91	0.98
MeCN	0.19	0.4	0.75	994	0.97	198	0.03	1.37	1.3
methanol	0.98	0.66	0.6	992	0.94	274	0.06	1.82	1.14
NMP	0	0.77	0.92	928	0.88	438	0.12	1.93	1.04
water	1.17	0.47	1.09	**1197**	1.07	266	-0.07	2.05	1.05
DMAc	0	0.76	0.88	903	1.09	270	-0.09	1.93	0.97
HFIP	1.96	0	0.65	1169	0.96	108	0.04	1.72	1.12

Table 5.5: Fluorescent Lifetimes of OB49 in Dilute Solution: excitation 371 nm, emission 430 nm. The bold entry for water is carried forward into table 5.6.

competing processes within the same molecule:

$$\begin{aligned} \Phi_f &= \frac{\tau}{\tau_{TOT}} \\ f_1\tau_1 + f_2\tau_2 &= \tau_\Phi \\ \tau_{TOT} &= \frac{\tau_\Phi}{\Phi_{obs}} \end{aligned} \tag{5.5}$$

whereby as quantum yield scales linearly with τ and the observed relative quantum yield is the average over all emissions, then the single component lifetime we *would* observe for the time-unresolved quantum yield, is the weighted average of the two component lifetimes: τ_Φ.

The photophysical parameters of the dyes from lifetime analysis are presented in table 5.6.

Lifetimes are plotted against the solvatochromic shifts for both the experimental and KT model data in figure 5.5. Both KT models have been calculated from the respective data. Although broadly applicable, the KT parameters are derived by averaging across any solvent-solute interactions, and as such lack specificity with regard to distinct classes of molecule. The plot in figure 5.5 (right) shows comprehensively that the two dyes behave very differently. OB49 is stabilised in the excited state by polar environments such as water, which can be seen in its companion plot whose y-axis is directly comparable.

Photophysical Parameters from Bulk Solution

Brightener	Φ_f (water)	τ_f (water) /ps	τ_{TOT} /ps
OB15	0.11	737 ± 12	6,700 ± 109
OB36	0.08	923 ± 19 (0.27) / 313 ± 71 (0.73)	5,971 ± 712
OB49	0.71	1,197 ± 16	1,685 ± 22

Table 5.6: Photophysical Parameters of Optical Brighteners

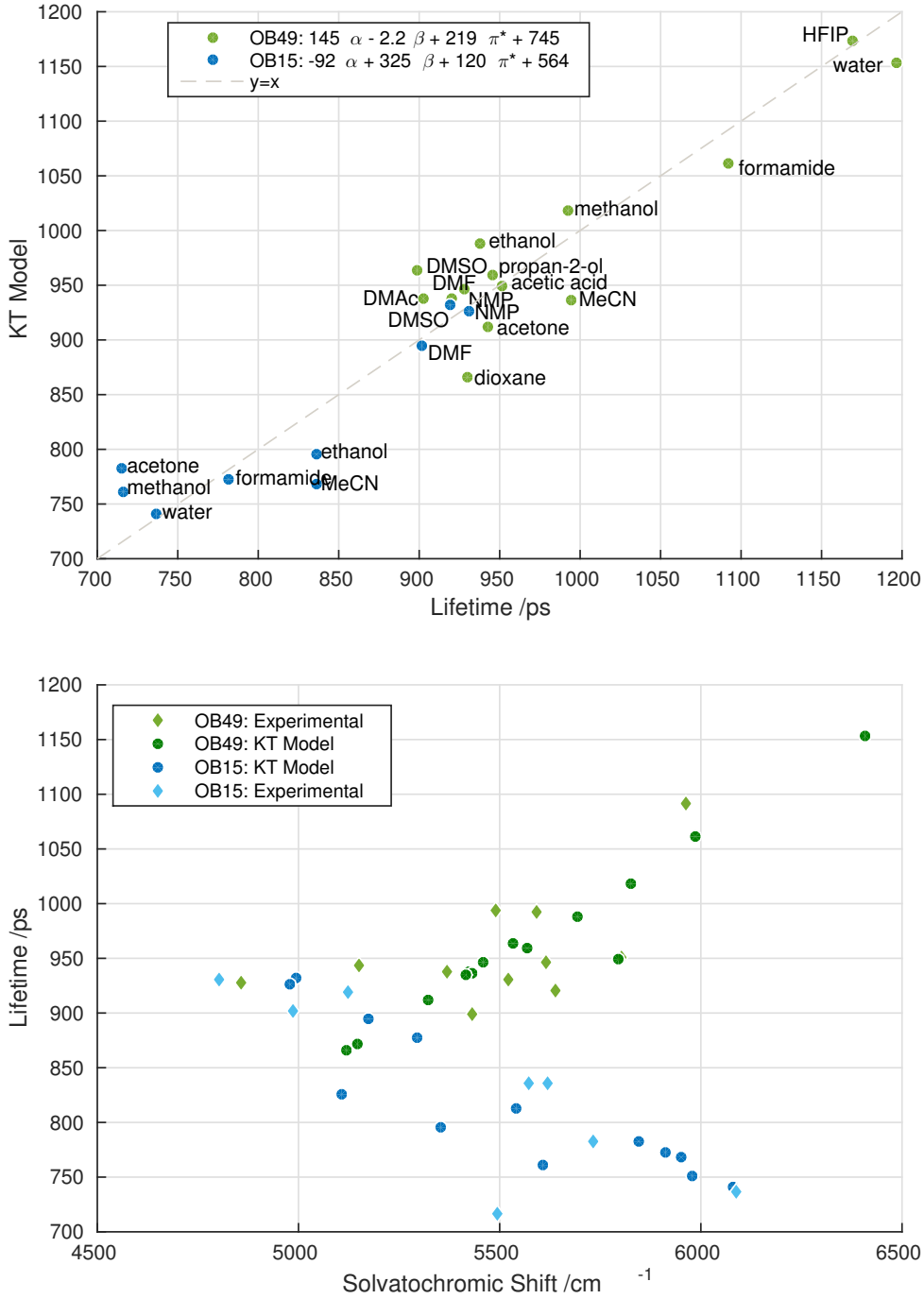

Figure 5.5: Kamlet-Taft Models for Solvatochromic Shifts and Lifetime: Top: KT model of lifetime data. The basis of the KT relationship can be applied to many metrics. Bottom: KT models for OB15 and OB49 are plotted with the data. In both cases the modelled data from the KT parameters includes more solvent data than was used to derive it.

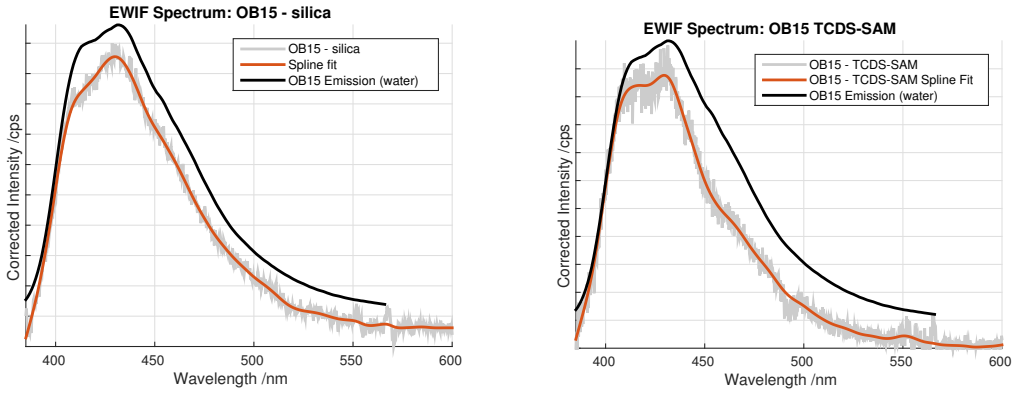

Figure 5.6: EWIFS - OB15 on Silica and TCDS-SAM: Left: EWIFS emission spectrum of OB15 on hydrated silica. The bulk solution is in carbonate buffer. Right: EWIFS emission spectrum of OB15 on TCDS-SAM. The bulk solution is in carbonate buffer.

5.4 Surfaces

5.4.1 Wavelength Resolved Spectra

On all surfaces except pure cellulose, OB15 and OB49 underwent significant photobleaching using the CW laser (and later the tau-laser, which at an output of 0.4 mW should be low-risk for such). Most of the analysable spectra collected, are presented here. The incidence angles are set to be either 67° or 62°, dependent on whether TIR or beam transmission into the solution is required.

Silica Both brighteners gave EWIF emission spectra on silica, though these were always very weak such that background noise artefacts were difficult to fully accommodate. The signal level typically remained low in contact with solution, and photobleached quickly after drying. For clarity, a spline curve is overlain on the EWIF spectra with an $R^2 > 0.999$. Noise artefacts are classed as outliers for the spline fit. The spectra are in figure 5.6 and 5.7.

TCDS-SAM Only OB15 produced a useful spectrum on the TCDS-SAM. OB15 is presented with comparison to the bulk fluorescence in figure 5.6.

Cellulose Both brighteners consistently gave useful spectra on cellulose film, facilitating a more in-depth analysis.

We begin with figure 5.9, which shows the difference between fabric fluorescence and single-fibre fluorescence. As the sampling size of fabric decreases (by unraveling and discarding fibres) the resultant spectra tend toward the form of the EWIF spectra. Single-fibre spectra were obtained by suspending fibres of decreasing number and diameter in a fluorescence cuvette in a conventional fluorimeter. Cotton fabric samples washed with specific dyes were provided by Mr Andrew Moon, P&G Newcastle. The remittance function of silica chromatography gel rinsed with the respective dye and washed with methanol, is shown to demonstrate that this is a reabsorption effect. When even so much as single woven thread (diameter approx. 0.5 mm) is analysed by this method, the spectrum is distorted considerably, and the spectra of fabrics in the literature typically appear to lack vibronic structure - the obliteration of this structure is problematic for modelling fluorescent responses, as the models rely on

the information that is present rather than that which is absent. The effect is particularly pronounced in fabrics observed from a steep angle from the normal.

The emission spectra of OB15 and OB49 are presented with polarisation resolution of the excitation and emission in figure 5.10. The *p*-polarised spectra for cellulose in contact with solutions of each dye, lack vibronic structure in their emissions. Broadly, this means that the character of the emissive state is clearly different, and very possibly well-hydrated/fully solvated. In contrast, the *s*-excited species have vibronic structure which is likely caused by association with cellulose. By looking at the spectrum of OB49 on a film after it has been allowed to dry on (figure 5.11), we can see that the emissions from *p*-polarised excitation have gained vibronic structure but also kept the overall out-of-plane anisotropy. Putting the film back into contact with a large reservoir of deionised water, depletes this signal significantly but the overall in-plane anisotropy is nearly unchanged. Taken together we now understand that the *z*-oriented dipoles are less strongly associated with the chains than the in-plane dipoles. This is interpreted to mean that the long and winding axes of the amorphous cellulose chains are majority in-plane, and that the transition dipoles of OB49 lie parallel to them rather than across them.

Although the in-plane anisotropy of OB49 on cellulose is within the normal range, its out-of-plane anisotropy of approximately -0.5 at 430 nm is below the limit of photoselection - a key assumption of the out-of-plane model is that the excitable transition dipoles are isotropically oriented, even if the emissions aren't. Therefore the deviation is explained easily as anisotropic absorptivity. A difference arises either due to two subtly different species being present (differently-solvated OB49; different solvatochromic shifts and absorption peaks) or two different concentrations. Given the differences in their spectra, it may well be both, and we must turn to time-resolved spectroscopy to provide further insight. If there are two populations (one of which has more rotational freedom), the out-of-plane anisotropy will have a short lifetime. Tightly bound dye molecules will have a limiting value of anisotropy at long times due to hindered rotation, and will take a long time to reach that value.

Doped Cellulose Neither brightener consistently yielded useful spectra on doped cellulose.

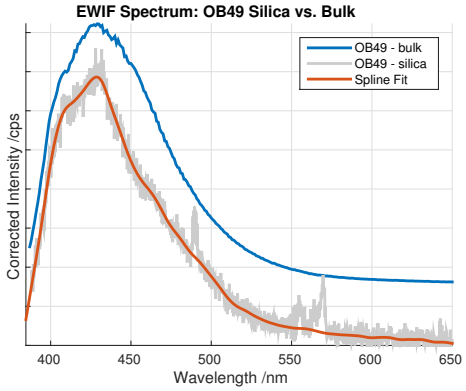

Figure 5.7: EWIFS - OB49 on Silica: EWIFS emission spectrum of OB49 on hydrated silica. The bulk solution is in carbonate buffer, shown here as a spectrum taken below the critical angle.

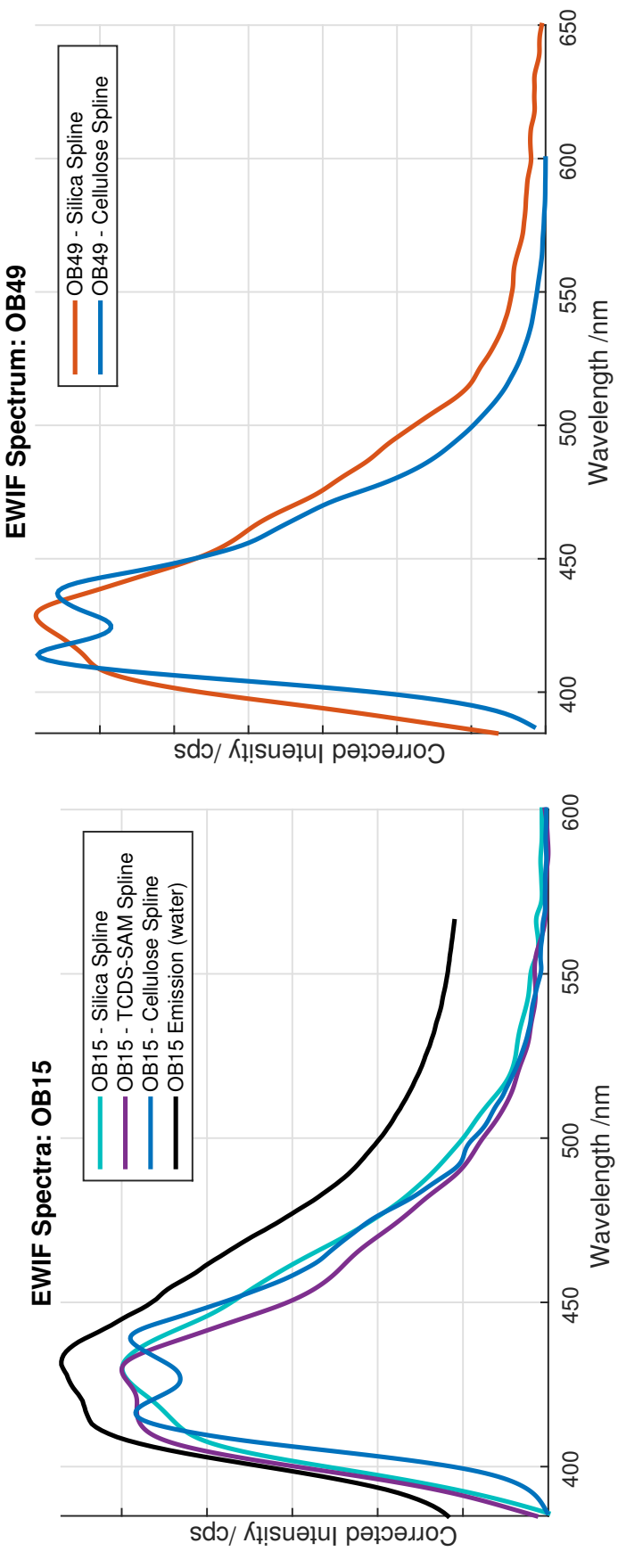

Figure 5.8: EWIFS - Summary: Left: The fits of the EWIF profiles of OB15, overlain for comparison. Right: The fits of the EWIF profiles of OB49, overlain for comparison.

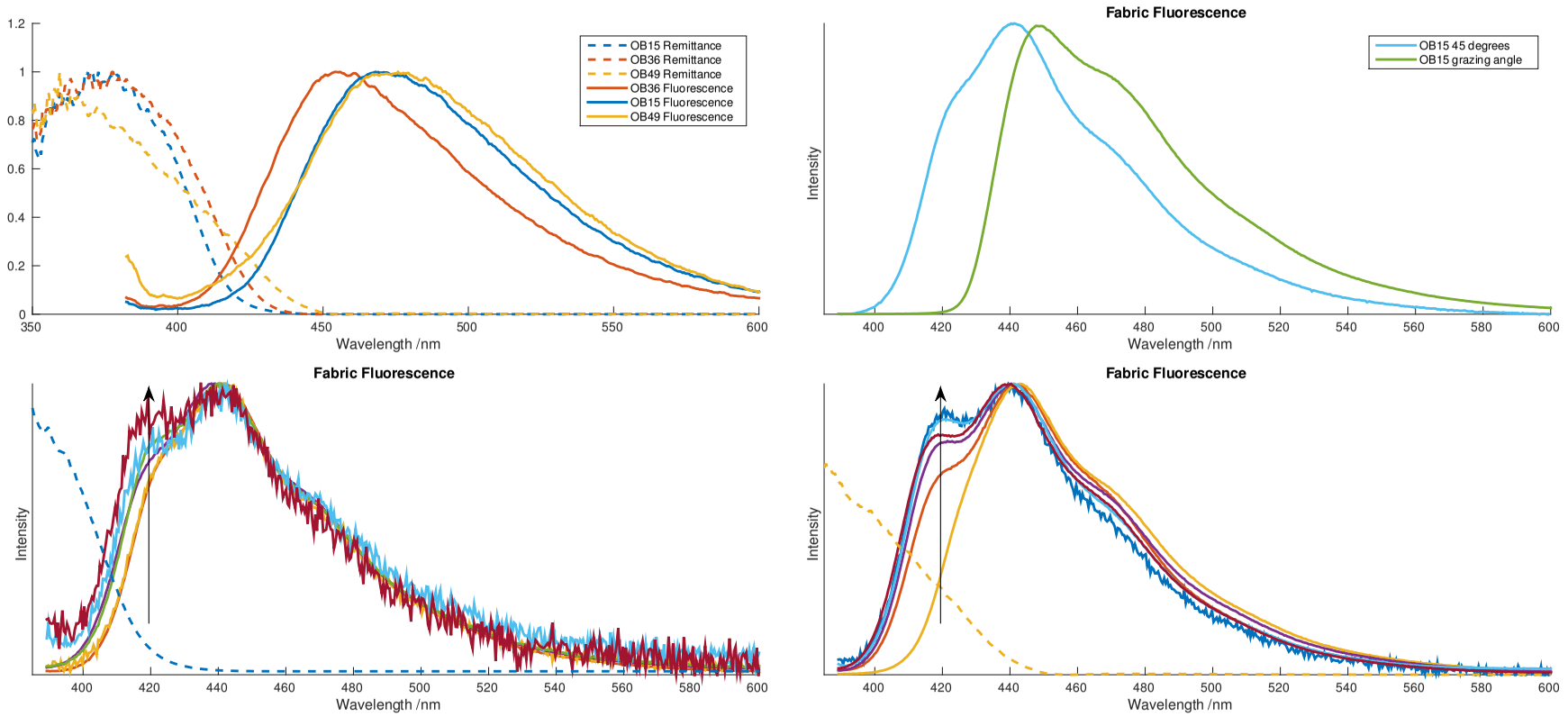

Figure 5.9: Fluorescence of Dyed Solids: Top Left: Remission-Emission spectra of silica chromatography gel washed with aqueous dye solutions at wash concentrations. The excitation wavelength for the fluorescence trace was 365 nm. Top Right: Fabric fluorescence with collection at an angle to the normal of the fabric surface of 45° and >80°. Bottom Left: Fibre fluorescence of OB15 on cotton fabric. The arrow indicates decreasing fibre diameter and number of fibres. Bottom Right: Fibre fluorescence of OB49 on cotton fabric. The arrow indicates decreasing fibre diameter and number of fibres.

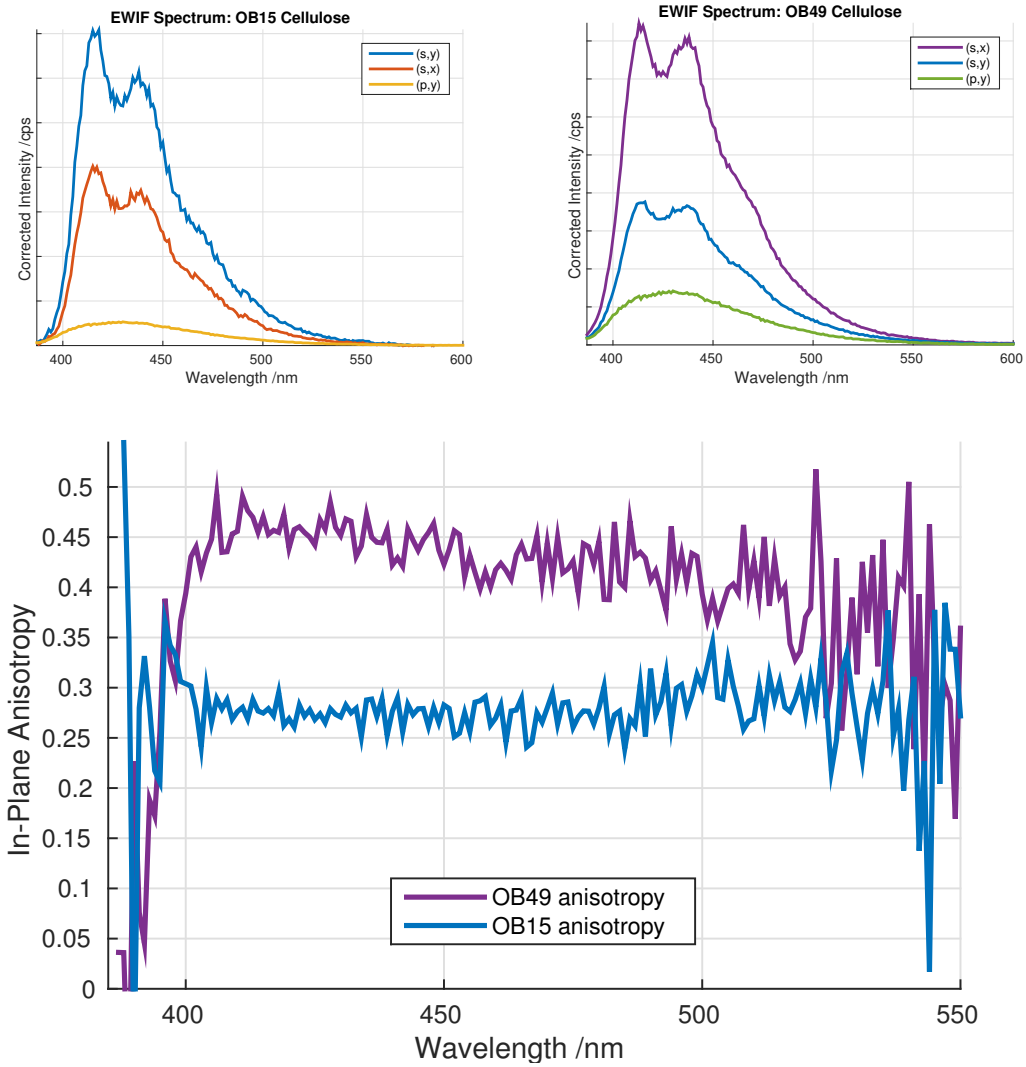

Figure 5.10: (*s*)- and (*p*)-polarised excitation of brighteners on cellulose: *Top*: Fully corrected spectra with polarisations designated (excitation, emission). *Bottom*: In-plane anisotropy of brighteners on cellulose.

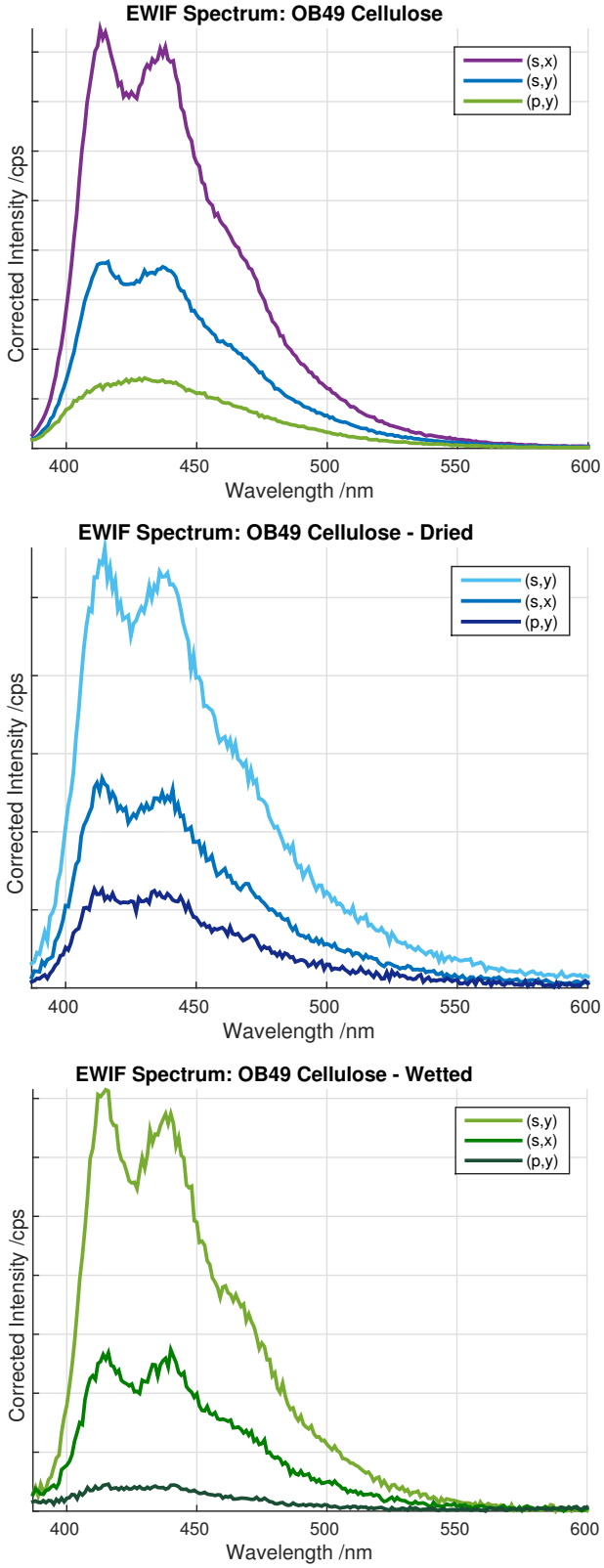

Figure 5.11: Effect of drying cellulose on the spectrum of OB49 on cellulose: Fully corrected spectra with polarisations designated (excitation,emission). *Left:* Spectra in contact with solution. *Middle:* Spectra after drying. *Right:* Spectra after re-wetting.

OB15: TREWIFS

Surface/Condition	τ_1 /ps	Φ_1	f_1	τ_2 /ps	f_2	DW	χ^2
Buffer	*1,269* ± 21	0.1894 ± 0.0001	*1.08*	*237*	*-0.08*	*1.66*	*1.17*
Silica	852 ± 23	0.127 ± 0.001	0.51	300	0.49	1.29	1.58
dry	-	-	-	-	-	-	-
TCDS-SAM	-	-	-	-	-	-	-
Cellulose	974 ± 26	0.145 ± 0.001	1.01	100	-0.01	1.93	0.97
dry	1,027 ± 16	0.1533 ± 0.0001	0.81	379	0.19	2.03	1.06
Doped Cellulose	-	-	-	-	-	-	-

OB49: TREWIFS

Surface/Condition	τ_1 /ps	Φ_1	f_1	τ_2 /ps	f_2	DW	χ^2
Buffer	*1,212* ± 3	0.7192 ± 0.0076	*0.91*	*336*	*0.09*	*1.53*	*1.24*
Silica	1,206 ± 12	0.7157 ± 0.0022	1	-	-	1.79	1.11
TCDS-SAM	1,262 ± 20	0.7489 ± 0.0021	1.06	123	-0.06	1.72	1.18
dry	1,220	0.7240 ± 0.0095	0.90	236	0.10	1.80	1.12
Cellulose	1,156 ± 25	0.6860 ± 0.0059	1.08	100	-0.08	1.73	1.21
Doped Cellulose	1,020 ± 38	0.6053 ± 0.0146	0.91	460	0.09	1.89	1.11

Table 5.7: Interfacial Lifetimes of OB15 & OB49: Obtained exclusively from *s*-polarised excitation and *m*-polarised collection. Dashed lines across a row indicates photobleaching, which was understood to be the case where the count-rate dropped by more than 10–20% over the course of the measurement and did not recover by being left in the dark for one hour. Where an entry indicates *dry*, the experiment was repeated after washing the surface with deionised water and allowing the surface to dry. Values of f, τ_2, DW and χ^2 are for the best fit.

5.4.2 Lifetime Analysis

The lifetime analysis is summarised wholesale in table 5.7. The lifetimes are collected using *s*-polarised excitation exclusively, as the instrument response function for *p*-polarised excitation takes an exceptionally long time to reach the required number of counts for the reconvolution. Long run-times are good neither for the dye (photobleaching) nor the laser (limited working lifetimes, heating, necessary lack of supervision).

The in-plane lifetimes of OB15 are lower than the solution state lifetime in a pH 10 carbonate buffer solution. Both silica and cellulose have labile protons to lose to the buffer solution, though the difference in zeta potential between glass and regenerated cellulose is quite large. Crystalline cellulose has a zeta potential close to -10 mV whilst values for swollen and regenerated celluloses are less negative [117]. It is known that glass has a very negative zeta potential at high pH (<-10 mV) and so we can reconcile this with what we already know of the lifetime response to polarity. Byrne and Scholes [12, 16] each recognise that the interaction of an oscillating dipole emitter is affected by the interface within the range of a few percent (previously discussed - the threshold to distinguish is 3%, which for OB15 is ±38 ps, and for OB49 is ±36 ps) and the rest is explained by specific interactions in and around the surface layer of solvent. For both dyes, lifetimes which are distinguishable from the bulk lifetime, are also outside of this range.

We have established already that the polarity of the TCDS-SAM surface is low. Therefore it appears that despite what we might expect from the KT model in bulk, the recovery of OB15 on both model greases is essentially nil. In both cases it is photobleaching that is to blame for the lack of signal, rather than a straightforward failure to deposit. As these measurements are taken in contact with

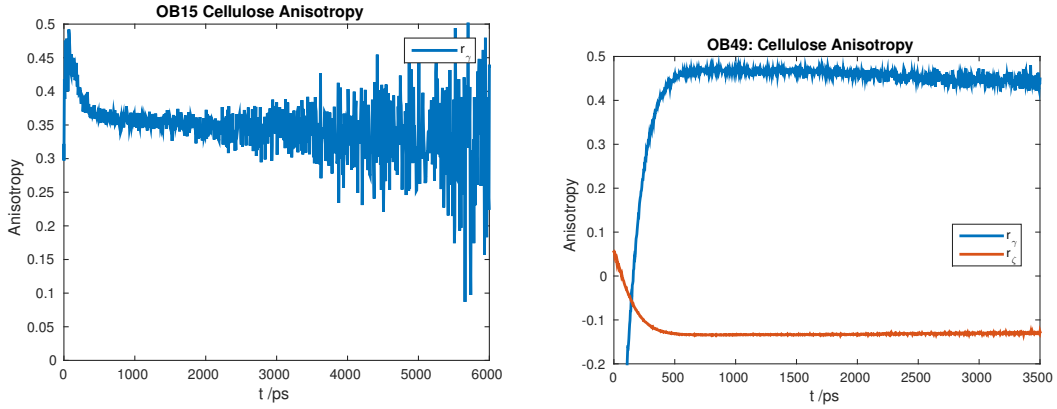

Figure 5.12: Time-Resolved Anisotropy of Brighteners on Cellulose: Left: In-plane anisotropy of OB15 on cellulose in contact with buffer solution. The out-of-plane trace could not be collected due to low count rate. Right: In- and out-of-plane anisotropy of OB49 on cellulose in contact with buffer solution.

solution (which in the case of an equilibrium is able to replenish brightener as it is converted to non-fluorescent species) it can be cautiously asserted that the affinity for the substrate is sufficiently high and dissociation sufficiently disfavoured, that available sites for adsorption by more brightener become completely occupied by non-fluorescers. It is notable also that in adjusting the site of either laser spot with a prism, visible fluorescence is seen which quickly bleaches.

From what has just been stated with regards to surface polarity at high pH, a mostly straightforward pattern with OB49 is seen. The transition from cellulose to doped cellulose reduces the Φ_f of OB49, and the main lifetime component of OB49 on the silica surface is almost indistinguishable from the buffer. However, the TCDS-SAM produces a higher Φ_f and is otherwise more comparable to cellulose, so we must now turn to fluorescence anisotropy to resolve the dynamics. If the major component is from solvated or part-solvated molecules perturbed by interaction with the surface, this should become evident.

5.4.3 Time-Resolved Anisotropy

The time-resolved anisotropy curves are presented in figures 5.12 and 5.13.

In figure 5.12 it can be seen that OB15 has a short decay and a limiting anisotropy at long times. In contrast, OB49 has either a long decay, a limiting anisotropy, or both. OB15 has no out-of-plane anisotropy curve on cellulose due to photobleaching. The out-of-plane anisotropy for OB49 on cellulose in contact with solution shows that not only is the signal for the *p*-polarised light very weak, but the rotational diffusion is constrained in that direction also - contrary to the hypothesis that it should be freely-rotating.

In figure 5.13, it can be seen that OB49 on TCDS-SAM has a slow rotational diffusion, but does not appear to be limited. The doped cellulose has some of the qualities of both: the early portion of the curve forms like TCDS-SAM on both counts, showing a slight, short diffusion, but otherwise exhibits strong binding as well. Although the cellulose surface slightly lacks excitable dipoles oriented in the *z*-direction, the values for cellulose are close to normal bounds. The greasy model surfaces both lack this to a much greater degree. As a fiducial, we note that in the absence of any *z*-oriented transition dipoles, the most negative value for out of plane anisotropy becomes -0.5.

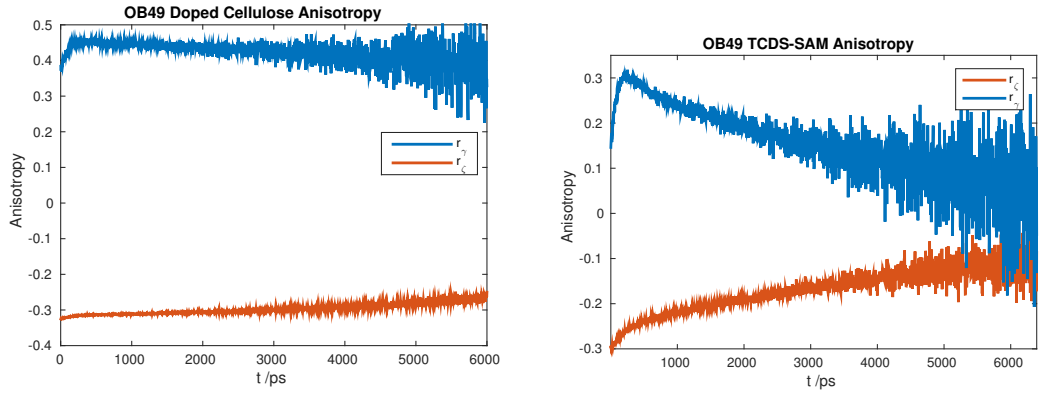

Figure 5.13: Time-Resolved Anisotropy of OB49 on Model Greases: Left: In- and out-of-plane anisotropy of OB49 on doped cellulose in contact with buffer solution. Right: In- and out-of-plane anisotropy of OB49 on TCDS-SAM in contact with buffer solution.

5.5 Discussion

It became apparent during the course of these experiments, that the dyes were prone to photobleaching - a finding consistent with the half-lives of minutes to days by the action of sunlight on aqueous solutions. Dyes on surfaces are known to recover activity due to (*E*)-(*Z*)-isomerisation, which recovers the (*E*)-isomer [4]. However, this process takes place in the dark over the course of 12–24 hours, and in the cases of photobleaching, no such recovery was found with either the lambda or tau laser. It is not explicitly clear from the data collected, whether those surfaces are promoting photochemical depletion of dye, maintaining a photo-induced excess of the (*Z*)-isomer by reducing the rate of recovery, or the dyes are stacking into H-aggregates at the interface (which do not fluoresce).

It is clear from the data collected on fabrics in figure 5.9, that the phenomenon of greening is due to reabsorption effects as brightener fluorescence exits the substrate. This also demonstrates that the EWIF spectra of brightener on cellulose are true to the emissions on cellulosic fabric.

As the emission spectra at the interface have reproducible forms distinct from that in the bulk phase, we identify that the interfacial species has its own distinct cybotactic region and orientation field. The interfacial emissions exhibit either a degree of vibronic structure that is not present in the bulk, or they have an adjusted proportion of vibronic structure. This arises due to changes in the Franck-Condon factors between vibrational levels of the excited and ground states.

An angle-resolved experiment would produce spectra where the emission originating from bulk and interface are in different proportions as a function of θ_i, and non-negative matrix factorisation (NNMF; see Part II) would help re-express that data usefully. However, angle-resolved experimentation was stopped in the early stages, with the reasoning that a) the angle resolution with manual operation across a 15° arc would provide insufficient data to fit the functions in [12] to $I(\theta_i)$, and b) the instrument was still in the building stage, and development of the tau system was considered more important and powerful. With a limiting angle near 81° that occurs due to the edges of the prism rather than the refractive indices of the different layers, we can say that the penetration depth range is 305.8–105.9 for time-resolved EWIFS (TREWIFS) or 310.8–107.7 nm for EWIFS; unless the differences between spectra are significant across that range, the ability to resolve basis-spectra with NNMF will be extremely limited. Further, as the acquisition of EWIF spectra takes a minimum span of time due to the use of a scanning monochromator and requires a blank spectrum to be taken at each wavelength

to correct for background fluorescence, the complication of acquiring such spectra accurately and free of instrumental or photobleaching artefacts should be apparent: it is almost definitively impossible to monitor photobleaching whilst acquiring a EWIF spectrum.

The form of the fluorescence kinetic decays at the interface are either a single exponential, a bi-exponential or very closely described by a bi-exponential. Where the short component is small and positive, this indicates in the literature that there is energy transfer, whilst short components with a negative amplitude indicate that the shape of the rise of the decay is skewed in a way that resembles excimer kinetics.

Solvation of the interface leads to the zeta potential, which describes the spontaneous potential difference across the interfacial boundary, including charge double layers - it describes the region accessible to adsorbing molecules. This is neglected in discussions of fluorophore adsorption because the early studies on which fluorescence models are based are neutral organic molecules [1], and it is generally justified to create a simpler model if it is predictive. The adsorption onto the surfaces can no longer be described in simple terms on a scale, as the interfacial environment is necessarily incompletely described by surface energy terms.

The Kamlet-Taft model might be used to characterise surface polarity using the linear lifetime model, save for the effect of interfacial anisotropy. It is known that for molecules with the ability to reach the ground state non-radiatively, the effect of lying parallel to the interface can enhance Φ_f, and this is modelled irrespective of the surface polarity - it is regarded merely as a planar dielectric in the literature.

The solvatochromic shift increases with polarity for all dyes; excluding dioxane, there is a clear positive solvatochromism for OB15 and OB49, and OB36 has a less clear relationship. However, OB15 is destabilised more in the excited state as its solvatochromic shift increases, which is interpreted that as the two states come closer together in energy, the upper vibrational levels of the ground state offer internal conversion pathways. This makes sense insofar that OB15 has many more vibrational modes than OB49, which displays the opposite relationship. Therefore by extrapolation to interfaces, it can be expected that polar interfaces should decrease the quantum yield of OB15 and increase the quantum yield of OB49. This is shown to be the case except for the TCDS-SAM, which has the opposite effect.

The excess or exclusion of fluors at an interface is dependent on the behaviour of the solvent layer. Inaccessibility of the surface itself prevents the dye from interacting with it directly and forces the dye to interact exclusively with the solvent layer. This can be seen in the re-wetting study of OB49, which yields no vibronic structure from *p*-excitation until the solvent has evaporated, after which point the vibronic structure remains.

While OB49 has a long in-plane anisotropy decay, OB15 has a two-part decay - a short decay on the same order as solution-state, and a long limiting anisotropy. This is a dual-behaviour; free rotators and rigid-fixed molecules.

Comparison of OB49 on TCDS-SAM, cellulose and doped cellulose shows that cellulose and TCDS-SAM are two opposite ends of a scale of cellulose and grease behaviour. While the anisotropy on doped cellulose is essentially indistinguishable from that of cellulose, it also shares features of its early rise with the TCDS-SAM anisotropy. The TCDS-SAM anisotropy appears to have a two-component decay much like that of OB15 on cellulose, but its decay doesn't appear to be limited - merely long.

5.6 Conclusion & Future Work

Taken all together, we can summarise both brighteners as being less active on most substrates than in the buffer solution they were deposited from, exhibiting the same solvatochromic pattern as in solution but with TCDS-SAM as a notable exception. The dyes exhibit opposed patterns of behaviour.

OB15 photobleaches on all tested greasy surfaces and does not recover. Although there is no mechanistic insight with regard to what the fate of the OB15 molecules is, it is suspected that the effect is permanent. The industrial concern has thus been addressed in a preliminary way.

In the future, the reversal of the scheme would be insightful and require less surface characterisation. Surface bound fluors as probes in the presence of solvents would be useful but would require a higher refractive index of the prism for some solvents. Trimethoxysilanated brighteners could become surface bound in the same reaction scheme as R-trimethoxysilanes. Though this doesn't tell us anything about deposition mechanisms, it allows the content of the cybotactic region to be both controlled and forced upon the dyes. Experimentation with more photostable dyes is preferable to establish the method.

Time resolved anisotropy and time-resolved fluorescence are probably the way forward with brighteners, as the problem of photobleaching will distort wavelength resolved spectra but not time-resolved data.

Photobleaching of dyes is problematic; if the tau laser photobleaches, then that is the least powerful laser that can reasonably be used in this system. Flash photolysis experiments in solution would establish the rate of brightener recovery as a function of polarity.

Chapter 6

Conclusion

The first part of the thesis has successfully begun to address the phenomena of greening and the failure of brighteners to brighten greasy soils effectively. It presents at least two model greases for spectroscopy, and confirms the suitability of a pre-existent model cellulose.

6.1 Instrumentation

The instrument that has been built has been shown to work, though deviations from idealised anisotropy have been observed on cellulosic surfaces. These deviations are explained by revisiting the theory of interfacial anisotropy: the theory of Scholes [16] assumes that the distribution of ground state transition dipoles is isotropic. Removing this assumption under the justification of an anisotropic distribution of adsorption site orientations, we obtain new limits for the values of out-of-plane anisotropy ($-0.5 \geqslant r_\zeta \geqslant 0.5$) that the results fall within, and so the results are satisfactory. An anisotropic distribution of surface-adsorbed dipoles is illustrated in figure 6.1. The illustrated case of anisotropic excess, enriches the (s)-polarised photoselection, therefore skewing the value of r_ζ to higher values.

Anisotropic transition dipoles during photoselection are justifiable in three ways. Firstly, the *implicit* isotropic distribution assumption has never been properly justified in the first place, merely regognised after the fact. Secondly, an interface is inherently anisotropic as both it and its interactions are necessarily oriented. Finally, even if it is justified to assume that the EWIFS probe region for a spin-coated cellulose surface is filled entirely with a disarray of polymer chains, and swollen by isotropic dye solution, there is reasonable basis to assert that the polymer chains themselves are largely parallel to the interface, and that therefore the adsorption sites are not isotropically distributed.

During spin-coating, an appreciable amount of strain is placed on the polymer solution, in a direc-

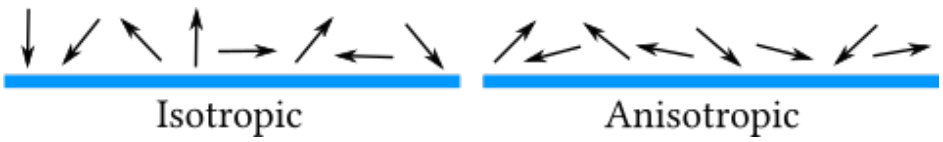

Figure 6.1: Inherent Photoselection Anisotropy: The arrangement of transition dipole moments (arrows) on a surface (blue). Left: The isotropic assumption of adsorbed transition dipole distributions. Right: The anisotropic case, showing an excess in favour of surface-parallel photoselection.

tion that always points outward from the axis of rotation, within the plane of the rotating disc. Polymer stretching occurs when the product β of the *strain time* τ and *strain rate* $\dot{\gamma}$ experienced by a polymer in solution is greater than unity [118]. The strain rate is necessarily 0 when adjacent particles are moving at the same rate, though as the spinning disc also necessarily generates strain as a function of distance from the axis of rotation, the strain rate is always >0. Given that the strain rate must be high for a high rate of spin, even for short strain times there is likely a degree of chain stretching, which would force sections of polymer chains to lie preferentially in the plane of the film, with the degree of inherent anisotropy then existing as a function of β.

There is also the problem that the metric in this thesis is fluorescence intensity. The fluorescence quantum yield, Φ_f, and oscillator strength at the excitation wavelength, f_λ, are assumed to be constant over all possible photoselections. If there are distinctly different environments within the probe region, the brightness of the dye within those environments will also be represented in the data, acting to weight the relative contributions of each subpopulation of excited dipoles to the observed spectral form.

The distribution of transition dipole moments is usually probed in the literature by using the *dichroic ratio* (DR, R_D) from interfacial measurements of absorbance. In a DR experiment, the absorbance A (not the fluorescence) of the (s)- and (p)- polarised rays are measured, and their ratio $R_D = A_s/A_p$ determines the relative in-plane excess of transition dipoles and therefore characterises the inherent photoselection anisotropy. This makes DR a desirable quantity to measure in future.

6.2 Photophysics of Dyes in Solution

The DAS brighteners OB15 and OB36 have low oscillator strengths, low quantum yields and a correspondingly low brightness in water. Their excited states have the potential to be long lived in comparison to the DSBP brightener OB49 if their quantum yields can be improved, though the quantum yield of OB15 remains low in later experiments and generally decreases as a function of excited state stabilisation. Due to its low brightness, OB36 was excluded from further experimentation, as it is included in formulations primarily for the brightening of nylon.

Solvatochromic data, taken together with lifetime and quantum yield data, shows a trend for the smaller dye OB49 to increase its lifetime in solution as a function of the solvatochromic shift, which is the relative excited state stabilisation energy due to the cybotactic region/orientation field. The opposite can be observed for OB15. This can be rationalised in terms of the efficiency of non-radiative deactivation rates of the excited state. The excited state is lowered in energy by the reorganisation of the orientation field but the ground state is of a higher energy, so the solvatochromic shift is the net closing of the energy gap between the excited and ground states when the dye is in an emissive state relative to immediately after absorption. Therefore, the upper vibrational energy levels of the ground state offer internal conversion pathways that become increasingly competitive with fluorescence, as the excited state of OB15 becomes more stabilised. Being a smaller molecule, OB49 has fewer vibrational energy levels but a similar absorption maximum, therefore the energy separation is sufficient for the stabilisation of the excited state to offer a longer emissive lifetime, without promoting internal conversion.

Alternatively, increased photochemical degradation of OB15 is a possibility that should not be ignored, but the data provides no insight on this matter. The dye merely exhibits approximately linearly decreasing quantum yields in increasingly polar solvents; although water is an extreme of solvent

polarity and a good hydrogen bond donor, brightener dissolved in water still fits to an approximately linear relationship between stabilisation and quantum yield. Internal conversion has superior explanatory power, as for a Morse potential the Franck-Condon factor between $S_1 v_0$ and $S_0 v_n$ increases (up to a point) with decreasing n, assuming that the π^* character of S_1 yields a more relaxed nuclear arrangement due to the loss of bond order. As $S_1 \rightarrow S_0$ gap decreases, the value of n isoenergetic with $S_1 v_0$ also decreases.

6.3 Photophysics of Dyes on Surfaces

6.3.1 Wavelength-Resolved Spectra

Brighteners exhibit structured emission (vibronic bands) in the plane of the surface on cellulose, and to a lesser extent, on the TCDS-SAM grease model. Spectra of dyes on silica have similar emission maxima to those in the bulk solution. Although the form of the spectrum does alter when deposited on surfaces, spectra of the same dye on different surfaces, superimpose well.

It appears that the surface energy components of the surfaces used have a discernable impact on the spectral form of the adsorbed fluor. Silica has similar properties to water and produces similar spectra. Cellulose possesses extremely polar groups and a considerable contribution to its high surface energy from dispersive interactions, and produces an emission comparable to that of the dyes in water, but highly structured. TCDS-SAM is entirely apolar but is a low energy surface overall - it offers few interactions with dye molecules compared to bulk solvent, but the spectra that could be gained demonstrate that the emissions are slightly structured but are otherwise still similar to spectra in bulk.

However, consider that the dyes on greases almost universally photobleach to some extent, and while time-resolved data does not suffer distortions due to this, the process of the time-integrated spectrum acquisition itself means that the spectrum of OB15 on TCDS-SAM must be interpreted with extreme caution. Consider the spectra of OB15 on silica and on TCDS-SAM; one might well imagine that the degradation of the dye on TCDS-SAM could lead to a spectrum much closer to that in the bulk, being reduced in intensity with increasing wavelength as the acquisition progresses.

Out-of-plane spectra of dye on cellulose show that the emission is closer to that of the bulk solution, therefore the nature of the two emissive states created is very different. The out-of-plane excitation leads to something close to a freely solvated (yet bound) molecule. Allowing the system to dry makes out-of-plane excitations gain structure in their emission, which supports the idea of partial binding, whilst re-wetting the system with solvent (not solution) reduces the activity and structured emission of the out-of-plane fluors relative to the in-plane, possibly by desorption and partial solvation. In the drying and re-wetting experiment, it is not clear whether the polymer rearranges itself to form interchain hydrogen bonds.

In conclusion, only EWIF spectra on cellulose and silica are considered useful, and the anisotropy of the dyes is high. Photobleaching of OB15 is considerable. Dye molecules of OB49 adsorbed parallel to cellulose chains are tightly bound, whilst those perpendicular are more weakly bound.

Fabric Fluorescence

Measurement of the fluorescence spectra of dyes on fabric samples, gives a fluorescence spectrum which is dependent on the angle of observation. Observing at a grazing angle compared to a 45 degree angle to the plane of the fabric, reveals that the bluest portion of the spectrum becomes cut off. A

similarly extreme spectrum of an optical brightener losing the intensity of the blue edge of its emission (most evident when compared to the spectra in this thesis which contain obvious structure) is shown in [5, p. 588], [4] and [10]. It is likewise shown in this thesis, that the reduction of sample size for collection of fluorescent responses from fabrics, increases the intensity of the blue edge, and so the conclusion there is that greening must be a reabsorptive phenomenon.

The approximate emission centroid of 45 degree fluorescence is around 460 nm, whilst the grazing angle spectrum is closer to 485 nm. Light with a wavelength of 480–500 nm is generally considered to be the blue-to-green transitional region of the visible spectrum [9, p. 23], and of course the intensity of the excitation light of the instrument used in that experiment is quite high, leading to a decreased representation of the effect compared to lower light conditions. This in hand, it is reasonably straightforward to conclude that the greening phenomenon has been observed directly, though as the effect has not been treated in the academic literature before now, it can only be noticed from previously available data by seeing the variations in many, many spectra from different sources using similar dyes at high levels of deposition.

6.3.2 Luminescent Lifetimes

The lifetimes of the dyes on surfaces show that the quantum yield on most surfaces is higher than in aqueous solution, with the exception of OB49 on cellulose. OB15 is progressively more long-lived than in solution on silica, cellulose in contact with solution and dyed cellulose allowed to dry. OB15 in contact with a greasy cellulose or a grease model surface photobleaches very quickly, that is, although no data exist regarding the fluorescent response of the sample, it was noted that a fluorescent response *did* exist long enough to be manually noted, but the instrumentation used was incapable of recording this short-lived response at the time of the experiment. From this we learn, that on silica the presence of solution (or even water) is integral to the continued activity of OB15, though whe the solution is in contact with a greasy cellulose or model grease, the luminescent intensity does not increase again when allowed to re-equilibrate in the dark. This behaviour can be understood in terms of two proposed general models. The data is inconclusive regarding which of these models best represents the behaviour, though the first model is the simplest.

In the first model, the dye is photochemically changed into a non-absorbing, non-fluorescent photoproduct. This photoproduct, which could be a geometric isomer, has high affinity for the adsorption sites which the dye would generally occupy, and so the fluorescent dye is unable to adsorb further. I.e. the dye solution cannot replenish spent dye. In the second model, the dye aggregates on the surface, and the aggregates are either self-quenching, self-reacting (see the first model), absorb a different frequency of light, or any combination of those.

OB49 is more long-lived on silica or a model grease - dry model grease is roughly equivalent to a silica surface in contact with solution in terms of quantum yield. However, OB49 on a cellulose surface has a *lower* quantum yield than in water, and this drops by 15% when the cellulose is intentionally contaminated by grease. In contact with solution, OB49 on a surface retains its activity consistently; any dark spots on greasy soils are due to decreased quantum yield on that surface, and any further darkening due to photobleaching, may well be reversible in the wash if the grease is removed.

It would of course be useful in future to test the effect of drying all the surfaces, or of using a variety of dye concentrations - when the solution replenishes deactivated dye at a variety of rates, the role of photobleaching is better understood.

6.3.3 Anisotropy

Only OB49 is photo-stable enough to study the spectra of the dyes for wavelength-resolved anisotropy. The luminescent lifetime measurement of OB15 dried onto cellulose was reasonably serendipitous; the laser is dim enough to take a single measurement of the lifetime per experimental run, but bright enough to photobleach so that a repeat within the same experiment is not reasonable.

The anisotropy of OB15 is lower than that of OB49. As the wavelength-resolved anisotropy tells us the mean anisotropy weighted by intensity across the whole lifetime of the time-resolved decay, the values at the peak of the decay have the highest contribution to the wavelength-resolved value. Therefore the anisotropy gives an indication of the relative values of the earliest portions of the decay to come, given that the decays are of a similar length.

The anisotropy spectra have already been discussed (*vide supra*). The absence of vibronic structure in the out-of-plane spectra is indicative that these molecules are either a freely-solvated minority subpopulation, or that binding sites for dye molecules that lie across or between polymer chains, offer a greater proportion of hydrogen bonding than those that lie along chains. It is also reasonable to say, in support of the polymer stretching hypothesis, that molecules lying along polymer chains are more rigidly bound in general due to the distribution of polymer-dye interactions along their length, whilst those across or between chains are less-well bound and tend to be better-solvated. Alternatively, there are no adsorbed dipoles within the probe region of the (*p*)-polarised evanescent wave, and only solution is observed.

Time-Resolved Anisotropy

The dye OB15 on cellulose exhibits a two-part anisotropy decay profile. The shorter portion has a lifetime of the order of picoseconds, which is consistent with freely-solvated molecules. The rest of the decay is exceptionally long, and may or may not have a limiting value. Photobleaching has severely hampered the analysis of OB15 before now, and this is no exception. The presence of the freely-solvated molecules is consistent both with an evanescent wave which excties a small volume of the bulk solution, and with cellulose films that are swollen with dye solution.

For OB49, the polymer stretching hypothesis is well-supported by the data. Neither the in-plane nor out-of-plane anisotropy of dye solution in contact with cellulose (or doped cellulose), contains significant indication of a short lifetime component. Given that the out-of-plane spectrum of OB49 solution in contact with cellulose has no vibronic features, this absence becomes telling of the fact that these molecules are not solvated, but are interacting with polymer chains, to which they are rigidly bound. This in-hand, it seems perhaps more likely that inter-chain water molecules allow the drying film to form hydrogen bonds between chains which are then no longer available to dye molecules, though this is purely speculative.

The short decay within the in-plane anisotropy of OB49 solution in contact with the TCDS-SAM grease model, might be an indication of a small amount of freely solvated molecules near that interface. However the shape of this feature, concomitant lack of such a feature in the out-of-plane decay, and the disproportionately negative value of the out-of-plane anisotropy, show several things. Firstly, an inherent anisotropic excess of in-plane transition dipoles indicates that the molecules are adsorbed at the grease model surface parallel to it. Secondly, some of those molecules are freer to rotate than others. Taken with the straightforward lifetime analysis of that surface using in-plane excitation, OB49 certainly stacks plane-parallel to this surface without quenching or excimer formation, as disorganised

layers of dye.

6.4 General Conclusions

Brightener molecules are rigidly bound to cellulose when they adsorb with their principal axis parallel to the polymer chain. Molecules straddling a chain, or between two chains, are partially solvated or are strongly hydrogen bonding to cellulose. On drying, it is unclear as to the reason, but the proportion of out-of-plane transition dipoles remains the same (but loses hydrogen bonding). Re-wetting with water diminishes that proportion significantly and demonstrates multiple adsorption environments.

On greasy surfaces, the photobleaching of OB15 becomes significant, though whether this change is a degradation of the dye or formation of a non-absorbing isomer of the dye, is not clear.

OB49 is very much photostable, but its quantum yield on greasy cellulose is lower than on clean cellulose. The quantum yield of OB49 on a planar model grease surface increases and is strongly adsorbed parallel to the interface, which is in line with the general theory that an increase in molecular rigidity (i.e. a lowered availability of competing relaxations that require molecular motion) increases the quantum yield of fluorescence [33].

6.4.1 Hypotheses for Future Work

For optical brightening studies, future work with OB15 is not particularly advisable for method development, unless a study can be completed with OB49 first. OB49 is a strong candidate for method development involving optical brightener photophysics, as it demonstrates photostability and has appropriate photophysics.

As the EWIF intensity at equilibrium is directly proportional to the interfacial concentration (at constant Φ_f), the kinetics of adsorption of dye on cellulose can be studied with a Freundlich isotherm, which is [98, p. 922]:

$$I_f = A \cdot c^{\Omega} \tag{6.1}$$

where I is the integrated EWIF intensity observed, A is an *ad-hoc* factor related to the number of adsorption sites, c is the bulk concentration of dye and Ω is the dye-substrate affinity factor. By varying the concentration of dye in contact with a film, the affinity factor can be fitted to the isotherm data. At low enough concentrations, the isotherm is essentially linear in form, whilst at high concentrations it approaches a limiting intensity.

For a reversible photochemical transformation of adsorbed species A $\rightleftharpoons$ B, where A represents active "bright state" fluorophores, B represents non-fluorescent "dark state" isomers of A, the forward reaction rate k_1 is dependent entirely upon the rate of production of excited state molecules A^*, which is in turn dependent on the intensity of absorbable light. The net rate of replenishment, k_2 is dependent on the light-independent relaxation rate, and the rate of exchange of adsorbed A and B with a very large volume of free solvated A (and therefore also on the bulk concentration). When the intensity of the excitation light (from an evanescent wave) is altered suddenly, k_1 immediately changes, as does I_f. The proportion of A and B adjust to the change, until the system restores *photostatic equilibrium*. Photostatic equilibrium, equally called a *photostationary state* of the system, is the quality of having a proportion of A and B within the excitation volume that satisfies the condition of zero net change, including diffusion into and out of the excitation volume. It is in some ways analogous to the temperature dependence of an equilibrium position, detailed in [98, p. 805], and behaves similarly. What has

been described so far is an illustratively simple, yet reasonably representative case.

As the intensity of light I_f is proportional to [A], the decay of $I_f(t)$ directly follows [A], and immediately following a sudden, known change of light intensity (such as through use of a neutral density filter), we set I_0 such that:

$$I_f(t) = I_0 e^{-kt} + I_\infty \tag{6.2}$$

where $k = k_1 + k_2$ and I_∞ is the value of I_f at the new photostatic equilibrium. A *photobleaching recovery* study based on transitioning between photostationary states, within the linear range of the isotherm, would require a means to trace the EWIF intensity over time, preferably using a low-power pulsed laser to time-gate the intensity measurement (reducing noise), and a series of neutral density filters of known transmittance to adjust the laser power output. For this purpose the tau-laser is ideal.

In this way, the relative rates of dye recovery on different surfaces can be compared directly (even if their component rates remain somehow unresolved) and the affinity of dyes can in any case be compared *via* Ω.

Although the study of simpler models is beneficial, it has already been realised that the departure from a simple, planar dielectric interface and the approach of "dopant" models for greasy celluloses produces idiosyncratic results that do not match one another due to different degrees of representativity. The production of doped cellulose films with a variety of dopants at different values of Λ, would be interesting to compare to the original model grease, in an effort to fully quantify any effects of different grease components, and the adsorption kinetics could give insight into increased rates of photobleaching and the kinetics of irreversible darkening.

Part II

Analysis of Ancient Documents

Chapter 7

Introduction

Abstract

The literature around pigment analysis and manuscript studies as an interdisciplinary field is reviewed, explaining the motivation behind this part of the thesis. Ancient pigments' history and chemistry is reviewed, as well as that of some binding materials. The manuscripts to be analysed are discussed with respect to their history and pigment content. The theory of μ-Raman spectroscopy is addressed, as well as its pitfalls and how they are overcome, with theoretical justification. The reflectance theory of Kubelka and Munk is addressed, along with its shortcomings and why they are largely irrelevant, then pre-justification is provided for the reflectance setup made at Durham. Spectral imaging is discussed with respect to multi-spectral imaging and standard colour imaging. The conversion of both spectral and RGB data to co-ordinates in a colour space is shown in explicit terms. Principal component analysis is discussed as a treatment for multi-spectral images, and followed by a comparison to non-negative matrix factorisation. Clustering methods are briefly reviewed for assessment of their utility, and their proposed application as regards imaging data is made clear.

Two simple protocols based on this information are outlined, that will form the basis of the experimental method and analysis in the next chapter.

—

7.1 Introduction

An historical manuscript (MS) is any hand-written article in a collection, and may take the form of a scrap, single sheet (folio), or book/volume in whole or in part [119]. The binding of stacked folia into books, up until recent centuries was not necessarily seen as a permanent fate; many manuscripts have been divided and re-bound as additional material to existing volumes for purposes ranging from vanity to practicality and assumed posterity. On occasions such as library fires, this process has preserved MS that would otherwise have been lost.

An opportunity arose during the 2013 Lindisfarne Gospels exhibition at Palace Green Library (PGL) Durham, to examine sets of related MS contemporary with one another for the analysis of pigments. Some of these were potentially from the same scriptorium as the headlining Gospels. MS do not lend themselves to changes in their storage conditions, destructive sampling or anything other than the gentlest handling, meaning that analytical methods applied must be capable of moulding around these

needs. The complication of this undertaking is that as the books themselves are entirely irreplaceable and often rest in diverse locations. A host of separate appointed guardians require a certain level of guarantee, that the artefacts will not be damaged by the measurements. These MS had never been assembled in a single location, and so once both the requisite permissions for insurance purposes and of the proper authority for each MS were assured, the scene was set for a detailed analytical study.

Until the nineties, the non-destructive identification of pigments used in manuscripts has been based on anecdotal evidence alone and intelligent guesswork [119]. The chemical analysis of pigments via spectroscopy can give the unambiguous identification of a broad selection of materials, whether by a positive inference or by a process of elimination. Clark *et al.* [120, 121, 122, 123, 124, 125, 126, 127, 128], have reviewed and collated information on methods in use for the identification of pigments for the purposes of conservation, and carried out a diversity of characterisations in laboratory materials and historic samples. The concerns of conservators and the utility of spectral identification are a common theme to much of the work. Burgio [129, 130, 131, 132, 133, 134] has worked in collaboration with Clark *et al.* to make use of Raman spectroscopy, including addressing the degrading effects of high intensity laser light. X-ray fluorescence (XRF) [135, 136]; diffuse reflectance spectroscopy (DRS) and its fibre-optic counterpart fibre-optic reflectance spectroscopy (FORS) [137]; have been listed by Clark in his reviews, and are in widespread use at present. There has been a drive in recent years to miniaturise and make portable these methods, for more in-field analyses. In many of these studies, Raman or micro-Raman spectroscopy is a gold standard or complementary method, though it has also been used as a solo technique and has been used far more prominently in multi-modal identification [124, 125, 126, 130, 131, 138, 139, 140, 141]. The use of alternative methods can be necessary, as Raman spectroscopy relies on the Raman activity of a material in order to obtain a signal. Other methods such as XRF can make inferences based on the presence of certain types of atom.

Some of these techniques have been applied in a mapping mode, which in a general sense creates an image containing specific spectral information, rather than standard red-green-blue intensities (sRGB, or just RGB). The obvious advantage to this is that a manuscript may be fully characterised by a spectral method, with spatial resolution, in a manner that may in principle be analysed *to completeness* by that method. However, as only either spatial or spectral resolution is available to any one mapping process at any one point during collection, either mapping must be laborious or it must be automated. It is not necessarily straightforward to automate a process where the surface of a large sample deviates significantly from flatness as, for example, focusing is frequently a necessity for spectroscopic methods. Additionally, a characterisation of z data points across $x \times y$ pixels, produces $x \times y \times z$ data points total (potentially upwards of 1 billion), many of which may be redundant or require pretreatment. There is therefore the question of affordable data storage and efficient handling during analysis, and it is not *per se* plausible to assert straightforward quality control of each spectrum. Methods in the literature which have produced maps include XRF [142], IR, and micro-Raman.

Imaging techniques (figure 7.1) largely circumvent the problems of correct focus and the labour of moving a probe in spectrophotometric mapping, whilst sacrificing spectral resolution. Imaging techniques however, have a paradoxical advantage in that the information collected may be judiciously selected by filter-based design. For instance, multispectral imaging (MSI) collects typically across 4 to 12 spectral bands, whilst Raman imaging might collect only a handful of relevant bands using a narrow bandpass filter. Hyperspectral imaging bridges this gap, by collecting across potentially hundreds of individual spectral bands for analysis.

As will be demonstrated later, an increased abundance of information in imaging, does not al-

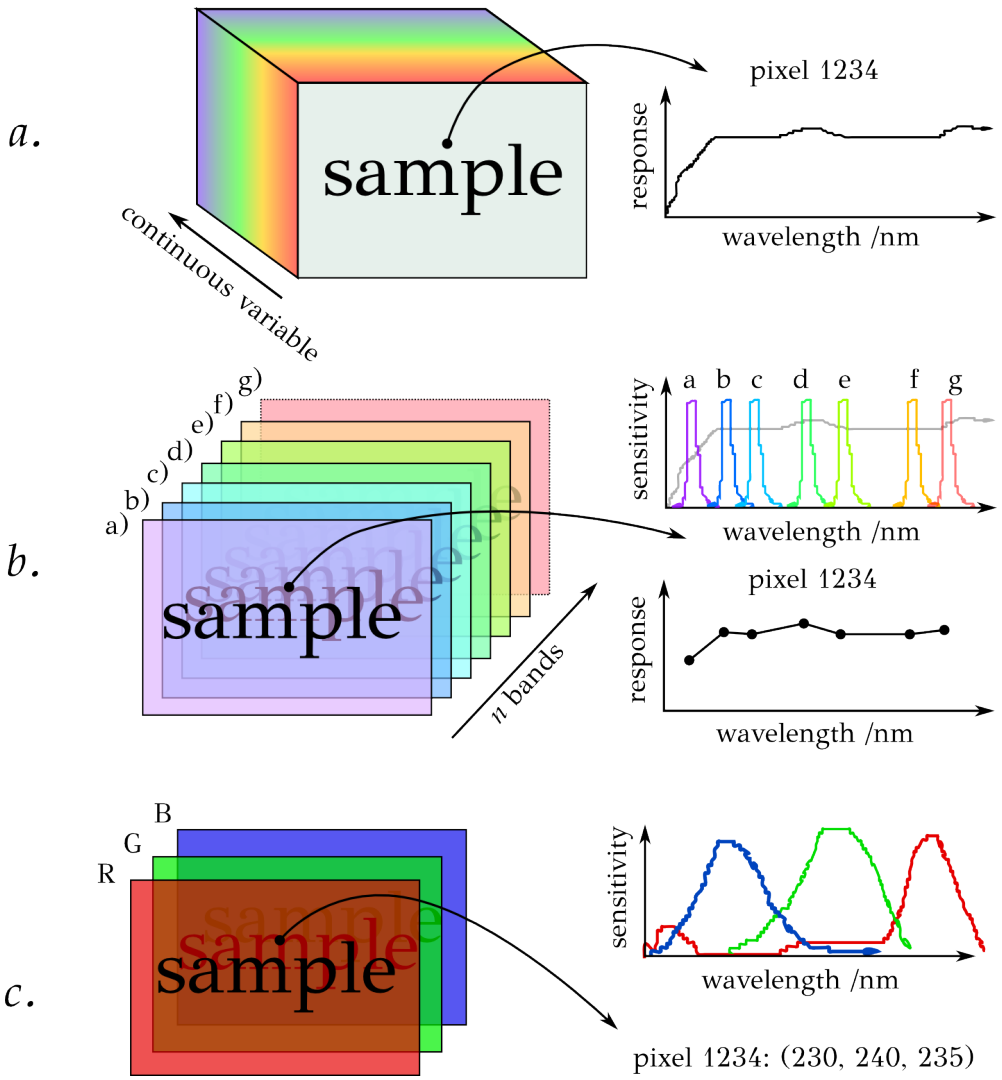

Figure 7.1: Schematic Comparison of Imaging techniques: The general result of three types of imaging under consideration. Panel *a.* shows spectral mapping, the aim of which is to generate a spectrum from each point on the sample, and generate images *post-hoc* based on this information. For simplicity, diffuse reflectance spectroscopy is depicted, though for example Raman spectroscopy or x-ray diffraction are known alternatives (see text). The data for a given pixel takes the form of a spectrum vector $I(\lambda)$. Panel *b.* depicts multi- and hyper-spectral imaging, the aim of which is to generate an image from each of a set of spectral bands using a camera coupled to a system that discriminates by wavelength (generally filters), and spectra may in principle be generated *post-hoc* based on this information (but this is generally not the case). The data for a given pixel in a set of n images takes the form of a vector of form $(I_1, I_2, I_3, \ldots I_n)$. Panel *c.* for completeness depicts sRGB imaging, which is distinct from multi- or hyper-spectral imaging in its use of just three broad bandpass filters, that simultaneously collect data. The data for a given pixel is presented as a vector of form (I_R, I_G, I_B).

ways make for improved distinguishability of image regions if that information is largely degenerate. Imaging in the context of manuscripts, also suffers from the effects of uneven illumination, uneven topography of the manuscript, and specular reflections from shiny interfaces. However, it is clear that for all its analytical shortfalls spectroscopically, imaging is a preferable method to mapping insofar that it might speedily provide preliminary analyses, suggestive that visually indistinct regions are in fact spectroscopically distinguishable.

7.1.1 Expected Palette

In [139] and again in [140], an extensive library of Fourier-transform Raman spectra has been compiled, and the salient history of these pigments and materials is discussed in brief in [139] also. This information is supplemented by chapters in [143, 144, 145], which as well as providing further historical detail, also note the features of reflectance spectra along with microchemical and microscopic identifiers. Here follows a summary of the history, chemistry, and spectroscopic features of some common pigment materials, based largely on these references. The interested reader might also seek [9, 146, 147] and [148] for general reading about pigments and dyes, which are lucid and well-organised texts. The aim of this section is to understand the materials under study as broadly as possible, and point out some potential adulterants or contaminants that could show up in spectra.

White Pigments

White Lead Lead hydroxycarbonate ($2\,PbCO_3 \cdot Pb(OH)_2$) is a dense, white solid that has been used in powdered form as the gold standard white pigment since antiquity. The desirable qualities are conferred by the properties of low absorption of visible light, small particle size (and resultant optical density), and relative chemical stability. At temperatures >100° C, thermal decomposition and dehydration liberate CO_2 and H_2O, leaving solid lead oxides as per $2\,PbCO_3 \cdot Pb(OH)_2 \longrightarrow 3\,PbO + H_2O + 2\,CO_2$ [144, p. 71]. White lead reacts with H_2S to give slate-gray PbS. In the presence of sulfides, white lead also reacts (especially in intimate contact or mixture) to form PbS, and it was known to artists that white lead should not come into contact with e.g. orpiment or realgar. Contact is, incidentally, not necessary, with close proximity being sufficient [149] (*cf.* [150]). Studies in oil media do not show any such problems [144, p. 72].

White lead may be manufactured from lead metal and vinegar, with the main changes to the core process having been only for increased efficiency and industrial up-scaling. The historic "Dutch" or "stack" process imminently yields basic lead acetate by reaction of moist acetic acid vapour with the lead oxide passivation layer, which by the action of CO_2 yields white lead and lead acetate. The lead acetate reacts further with lead oxide to yield more basic lead acetate, and the cycle uses up $\approx$ 70% of the lead metal used [148, p. 78]. In antiquity, the metal would be suspended above the vinegar in pots, the pots left in a warm place, and the patina of white on the lead periodically harvested by scraping until the lead metal was mostly gone and had to be replaced. As fermenting dung was frequently a source of both CO_2 and heat, it is possible that PbO could be a contaminant in white lead due to uncontrolled temperature [146, p. 229]. Although still available for use in paints, the restrictions to sale and distribution of lead compounds have lessened the popularity of lead white in favour of the non-toxic titanium dioxide and others.

Typically white lead exhibits poor Raman response at most visible frequencies due to its reflective nature, which in theory excludes the bulk of the pigment particles from the scattering volume (§7.2.1).

A down-shifted carbonate stretching mode presents a sharp major double-peak at 1051 and 1055 cm^{-1} [140].

Chalk Calcium carbonate ($CaCO_3$) is a soft white solid commonly found in large sedimentary deposits along coastlines, or as forms of limestone rock. A reactive carbonate, $CaCO_3$ liberates CO_2 by thermal decomposition or acid hydrolysis to yield the oxide or hydroxide[(i)], or a salt respectively. Historically, the chemical transformations of lime were well known within their own paradigm, and it is reasonable to infer that calcium carbonate could have been made available synthetically, (*cf.* the *bianco sangiovanni* in Italian fresco painting [144, p. 206]), though this makes less sense than simply mining for an abundant resource. The two major crystal polymorphs of calcium carbonate, calcite (trigonal) and aragonite (orthorhombic) are most likely to be encountered, though magnesium calcium carbonates such as dolomite may reasonably coincide with calcite if the source mineral is limestone [146, p. 80, 148]. Other sources of calcite for pigment include cuttlefish bone, eggshells, seashells and coral [144].

Being in fact fairly transparent in mixtures, chalk is less frequently found as a pigment, instead being utilised as an extender, or as a base for lake pigments [146, p. 98]. Extenders are substances added to give bulk to paints that make the pigment go further or lighten hues by dilution; ideally they have little to no hue, and lend very little albedo to mixtures - in this sense, chalk is almost ideal.

The Raman response of calcite is quite weak, but provides a diagnostic carbonate peak at 1087 cm^{-1}.

Gypsum Calcium sulfate dihydrate ($CaSO_4 \cdot 2\,H_2O$), the base material for plaster of Paris and gesso primer, is a water-insoluble white mineral, rarely explicitly referred to as being a pigment in its own right other than as a whitewash or base [146, p. 184]. It is an especially stable mineral with varying crystallinity, the best (selenite) exhibiting fibre-optic properties along the axis of its fibrous growth which lends a faint pearlescence to its crushed paste. Being so inert, it is stable to mixture with most if not all pigments here-listed, and like the other white pigments has a poor Raman signal provided mostly by the symmetric stretch of the anion, in this case sulfate [151, 152, 153] at 1005 ± 1 cm^{-1} [154].

Red, Orange & Yellow Pigments

The selection of red, orange and yellow inorganic pigments is particularly broad, consisting of chalcogenides of lead, iron, arsenic and mercury.

Red Lead *a.k.a.* minium Lead (II,IV) oxide, lead tetroxide, Pb_3O_4, is a bright orange semiconducting material with tetragonal crystal structure, that reacts with H_2S to give dark grey PbS. Pb_3O_4 has been manufactured and mined since antiquity. Regarding the ancient nomenclature of red lead, there is confusion between pure red lead and varying mixtures of iron oxides, realgar, and even vermilion with or without red lead, and it was often adulterated with iron oxide or used to adulterate vermilion [146, p. 235]. In particular, the term minium could mean vermilion, red lead or explicitly a mixture of both [143, p. 109]. In this document the names *red lead* and *minium* will be used interchangeably to mean Pb_3O_4 alone.

[(i)] As polysaccharide gums are polyprotic weak acids, acid attack by gum arabic binder was found at Durham to be problematic in practice, as the resultant paint can quickly become foamy or diminish in opacity

It was made historically by roasting and agitating powdered white lead or PbO slag from molten lead in the presence of oxygenated airflow at 300–500 °C, until the desired colour was achieved [146, p. 235], which likely places it among the earliest of manufactured pigments. With increasing temperature, the decomposition of lead white yields massicot, which then transforms to litharge before incorporating oxygen to form red lead [144, p. 71]. Vitruvius (1st Century BCE) indicates that the artificial material was considered superior to the natural pigment, and superseded it at that time [143, p. 110]. At temperatures >550 °C, of the oxides of lead only PbO is stable; this leads to PbO being the most likely contaminant even when produced from white lead, if temperature is not appropriately controlled. In later centuries AD, methods are reported in the US that involve sodium nitrate and nitrite, giving sodium nitrite and hydroxide as (post-eighteenth-century) contaminants.

Red lead suffers the same fate as white lead in contact with sulfides and H_2S, leading to gross interfacial darkening to PbS - a discolouration which spreads to cover; it is also less stable overall to environmental exposure, able to form both PbO_2 and lead white dependent on conditions [143, §3.3, §3.4]. This doesn't prevent its use with vermilion, in mixture or in layers [143, p. 113].

As all modes are Pb-O or Pb-Pb modes, the Raman shifts are appreciably low - the most active peaks are present at 121 and 549 cm^{-1}, though less active peaks are present at 150, 223, 313, 390 and 480 ±4 cm^{-1} [139, 140] (see figure 7.2).

Litharge & Massicot Lead (II) oxide PbO, exhibits crystal dimorphism, having a yellow orthorhombic form (massicot) and a less thermodynamically stable red tetragonal form (litharge). Both exist naturally as lead ores. Heat treatment induces transition from massicot to litharge, and the heating profile during manufacture from white lead in an inert atmosphere influences the proportion of each formed, forming massicot, then litharge, then red lead, and finally decomposing back to PbO above 550 °C. Modern synthetic methods with precise temperature and atmosphere control, produce both forms selectively in high purity.

As these two pigments can be found in mixture with one another and red lead (*vide supra*), it would be useful to be able to separate their Raman responses. There exist differences, though they are small; the strongest peaks are at 142 and 144 cm^{-1} for massicot and litharge respectively, which is close to the 150 cm^{-1} peak of red lead, for which they are the chief contaminants (*vide supra*). The 633 nm spectra from [139] are presented in figure 7.2 atop the spectrum of red lead for comparison.

Orpiment Arsenic (III) trisulfide (As_2S_3) is a bright golden yellow, polymeric, arsenical semiconductor, which occurs naturally as an ore of arsenic [155, p. 349], occurring in hydrothermal veins as well as being a product of arsenical mine fires [145, p. 54]. It is thermally very stable, though it hydrolyses slowly in the presence of dilute strong acids to give white As_2O_3, itself found as an arsenic ore. Orpiment may be manufactured either by reaction of H_2S with As_2O_3, or, like realgar (*vide infra*), by direct co-sublimation of stoichiometric amounts of arsenic and sulfur [156]. There is however no convincing evidence that this knowledge was available between the sixth and twelfth centuries, and it is known that medieval artists used orpiment imported from Asia Minor [145, p. 49], which is the larger part of modern-day Turkey on the coastal side and also included Cyprus.

The Raman response of orpiment is very strong, and its main peaks are at 350, 305 and 289 cm^{-1} [140].

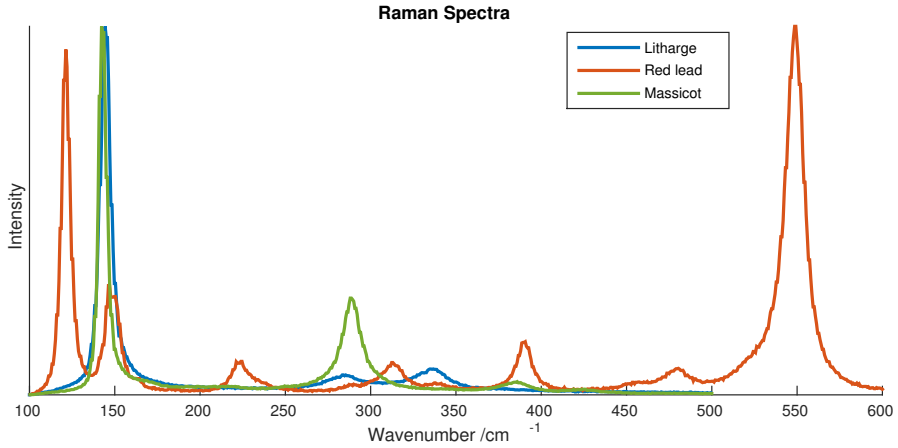

Figure 7.2: Lead Oxide Spectra: The spectra of three lead oxides, red lead, massicot and litharge. From [139].

Realgar & Pararealgar Two isomers of As_4S_4. Both molecular materials, burnt-orange realgar isomerises to canary-yellow pararealgar on exposure to light, and the change is reversible by elevated temperatures [156]. This light may be incident at the point of manufacture of the book, during display, or during Raman measurement if the wavelength of the laser is 500–670 nm [156]. Both are found in connection with other sulfides in mining, orpiment in particular. The major peaks of realgar are 355, 231, 193 and 183 ± 0.5 cm^{-1}, whilst the major peaks of pararealgar are 236 and 230 ± 0.5 cm^{-1} [140].

The natural formation of pararealgar in samples of realgar is concerning, because the colour change is both easily effected by sunlight and essentially permanent from a conservation standpoint - it is not possible to expose artifacts to the high temperatures necessary for the restoration of realgar. It is also not clear, if the transformation is visually complete, whether the original pigment was realgar or pararealgar. Pararealgar is also notably more friable, detaching easily from its parent realgar crystals [156] and, in the context of manuscripts, it is not clear what effect such a change will have on the durability of pigment regions.

Vermilion Mercury (II) sulfide (HgS), as the mineral *cinnabar* has been mined since at least 3000 BC [157], and alchemical recipes exist widely in the west at least as early as Theophilus' seminal collection *Divers Arts*, where its synthesis was described. The earliest recorded recipe is from the early eighth century, credited to the Persian alchemist Jabir ibn Hayyan [158], though Cennini's recipes in the twelfth century include it [159].

A deep red semiconducting material, vermilion exhibits a characteristic band-gap feature in its reflectance spectrum. The main Raman peak is strong, appearing at 250 cm^{-1}.

Mercury (II) sulfide exhibits crystal trimorphism, a dark grey/black cubic morph *meta-cinnabar* which forms at lower temperatures, the familiar red trigonal form, and a black hexagonal morph *hypercinnabar* which forms at high temperatures [144, p. 166]. Recipes from antiquity claim that a black substance they call *Aethiopes mineralis* [158] forms initially on mixture of elemental mercury with elemental sulfur, which upon gentle sublimation or heating yields a solid red deposit of cinnabar; the crystal morphs were thus known within the alchemical paradigm. This black substance is well-recognised in both dry and wet synthetic processes, not all of which require sublimation, but all of which required heat. The post-medieval recipes include the use of potassium hydroxide to remove excess free sulfur

from the final product, or in the reaction mixture to generate polysulfides of potassium which were said to increase efficiency and work at a lower temperature [148, p. 104].

As vermilion was expensive and sought after in its time [160], red lead and brick dust are expected as potential impurities to vermilion due to widespread adulteration by merchants [159], and feasibly red lead could be used as a base layer or extender depending on the desired aesthetic and school of production. All three crystal morphs of vermilion can be found in association with one another in mining, though the red trigonal form used as a pigment is most common and the hexagonal form is unstable [144]. Single large crystals are rare; generally cinnabar is found deposited hydrothermally in a microcrystalline layer across a support mineral such as quartz or calcite, leading to concerns over purity. As with many other sulfides it is frequently associated with pyrite (FeS), though stibnite, realgar/pararealgar, calcite, barite, quartz and dolomite are feasible contaminants in the case of mining.

Iron Oxides The oxides and hydroxides of iron take two major forms that are in use to this day, and have been in use in Europe since at least before the eruption of Vesuvius (*cf.* the ruins of Pompeii). Red iron oxide (iron(III) oxide, α–Fe_2O_3) can be natural (*red ochre*, *haematite*) or synthetic (*mars red*). Yellow iron hydroxide (iron(III) hydroxide, $Fe(OH)_3$) *mars yellow*, is a synthetic pigment similar to the naturally occurring *yellow ochre* ($FeO(OH) \cdot nH_2O$). The roasting of iron hydroxide or yellow ochre yields red iron oxide by dehydration. The ubiquity of iron compounds, the extensive export of red ochre from Asia Minor [146, p. 326–327] and the late references by Cennini to the use of haematite [159] indicate that the use of iron oxide was as a natural pigment until at least the 12th century in Europe, despite the existence of later recipes calling for medieval ingredients such as iron sulfate [146, p. 207]. Most recipes explicitly for making mars colours were of the 19th century [140] (*see also* [148, p. 128]).

Regardless of the natural or synthetic origin, the Raman response of haematite type iron oxide is reasonably strong, and can be easily distinguished from iron hydroxide. The exact positions of the Raman peaks vary some small amount between the natural and synthetic varieties [139], though the major peaks of haematite are at 408, 299/290 and 224 ± 2 cm^{-1} [139, 140].

Green & Blue Pigments

Azurite & Malachite The basic copper carbonate *azurite* ($Cu_3(CO_3)_2(OH)_2$), is a deep blue and highly prized mineral, always found intimately associated with the more common malachite in copper ore deposits. In Europe, azurite was sourced principally in the copper mines of Germany, Hungary and France, leading to historical terminology referencing the mountainous regions and Germanic origins which can be traced back to azurite [146, p. 39] [144].

The other basic copper carbonate *malachite* ($Cu_2CO_3(OH)_2$) is found in association with the less common azurite (*vide supra*), and both are associated with cuprite (copper oxide), and chrysocolla (basic copper aluminium cyclosilicate) [146, p. 39, 254–255]. Malachite is found both in fibrous and pyramidal crystal forms, dependent upon mechanism of growth.

Verdigris There exists a certain contention regarding the term *verdigris*. The name literally interprets as "green-grey", and it is cited as being a basic copper acetate of varying stoichiometry [148, p. 160][144, p. 133]. Although ultimately there is scope for a verdigris to be chemically identical to *malachite* due to reaction of copper with the atmosphere, verdigris differs from malachite in that it is not a crustal mineral, and by accident or design it is usually anthropogenic in origin. Verdigris (presenting as

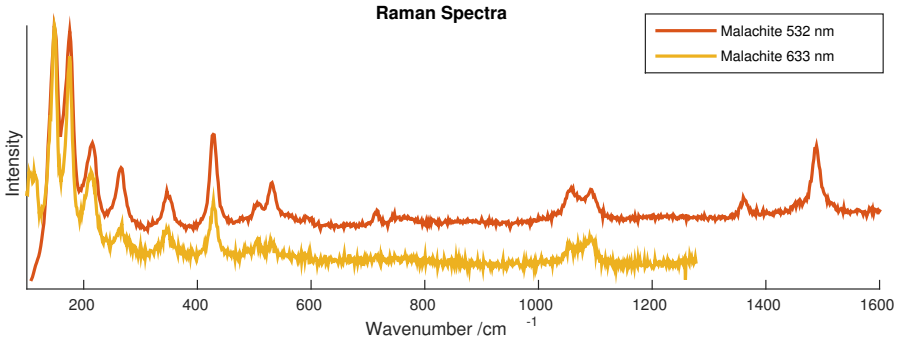

Figure 7.3: Malachite Spectra: The Raman spectra of malachite under two different wavelengths of laser light. The 633 nm laser spectrum gave low signal, and at sufficient power both lasers were able to decompose the sample.

malachite) is almost iconic, observable as the green patina of passivation layer which forms on exposed copper and bronze *via* weathering [146, p. 391].

Copper (II) acetate, as well as the acetate hydroxide and basic carbonate, may be synthesised by the action of warm acetic acid vapours on copper metal, in a process similar to that which yields basic lead carbonate (p. 138). It is reasonable, given some recipes, that copper citrate and synthetic atacamite may be found on some manuscripts [161]. Raman spectra of some copper compounds under several lasers are presented in the next chapter. These were obtained at high incident power that could not be used with manuscripts, as low incident power would not yield a spectrum at all. The spectra of malachite are presented in figure 7.3.

In contrast to the basic copper carbonates, verdigris has strong peaks at around 940 cm^{-1}, as well as relatively strong CH_x modes in the 2950 cm^{-1} region [139].

Lapis Lazuli The bulk of lapis lazuli is lazurite, an inert aluminosilicate matrix mineral of varied composition and stoichiometry, found alongside pyrite and calcite [146, p. 223–224][144, p. 37]. The chromophore of lapis lazuli, is matrix-isolated sulfur species $S_3^{-\cdot}$ & $S_2^{-\cdot}$, which reside in the above matrix. These radicals present themselves as the odour of H_2S and SO_2 upon crushing of the mineral, or dissolution of the matrix with strong acid. Simply crushing lapis stone produces a blue-grey powder, and recipes such as that of Cennini [159] from the twelfth century produced many deep shades of blue; these involved mixing the greyish powder with melted gums and waxes, kneading the hardened aggregation, and washing with lye to extract an intensely blue powder [144, p. 38]. Whether the improved chroma is due to removal of excess matrix, protection of the radicals, or filling in cracks in the matrix with index-matched materials (thus reducing scattering reflections), is not known. It may reasonably be expected, that finely-ground lapis will produce less Raman signal due to loss of sulfur species to the atmosphere, whilst treated lapis might yield spectral artefacts from the treatment agents.

Lapis lazuli has been mined in Afghanistan for millennia, and is also sourced from Chile in modern times. The presence of lapis therefore, indicates a complete trade route from Persia through to the scriptorium of interest.

Indigo Indigotin ($C_{16}H_{10}N_2O_2$) is a vat dye harvested from the woad plant *Isatis tinctoria*. In solid form it is a deep black-blue pigment, but dyed on fabrics it can exhibit much lighter (though not necessarily very bright) shades. Indigo, being a small molecule (figure 7.4), absorbs long wavelengths solely

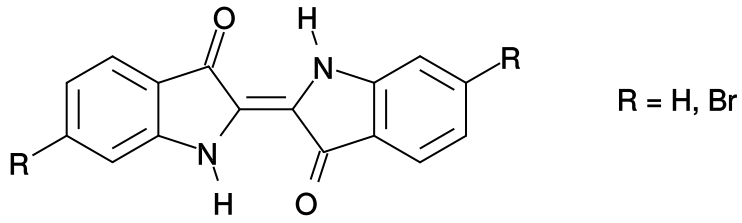

Figure 7.4: Molecular structures of indigo & Tyrian purple: Molecular structure of both *indigos*. R = H for indigo, R = Br for Tyrian purple.

due to the effects of dye aggregation - single molecules in vacuum appear red (λ_{max} = 540 nm [9, p. 107]), but in the solid state the molecules are extensively aggregated through hydrogen bonding, with each indigo molecule bonded to four others. This explains not only its colour, but low solubility and high melting point (390–392 C). Indigo can be extracted from the woad plant in relatively low yields.

Indigofera tinctoria is the plant known as *true indigo* and is, broadly, native to parts of Africa and Asia. It produces indigo in high yields, and has been the chief worldwide source of natural indigo dye from the Victorian era to the present day. By comparison, *Isatis tinctoria* is the woad plant, native to much of Europe including Britain, and was a far earlier source of indigo in the British Isles.

Indigo fares well as a pigment when extended with white, producing only the dullest blue-black colour when pure [145, p. 86]. Extended with or precipitated on orpiment, indigo gives the green pigment *vergaut*, whilst precipitation onto the white clay *attapulgite* gives the bright turquoise *maya blue* [145, p. 84]. The major Raman peaks of indigo are at 1572, 1226, 599 and 253 ± 2 cm^{-1} [140].

Purple Pigments

Tyrian Purple Formally 6,6'-dibromoindigo ($C_{16}H_8Br_2N_2O_2$), may be extracted from the shells (and its precursor from the hypobranchial glands) of the *Murex* genus of aquatic snails, and also dogwhelks, similarly to the vat methods employed to extract indigo [146, p. 379]. Its structure is shown in figure 7.4. The depth and vivid nature of the colour, its rarity, taken with its permanence, stability and insolubility, made it a valuable pigment of antiquity in the absence of other purple-hued dyes [146, p. 379][9, p. 4]. Diffuse reflectance indicates that the position of the bromo substitution makes little difference on the ultimate reflectance maximum [121].

The main Raman peak of Tyrian purple is a doublet at 1584 and 1565 cm^{-1}, and this does not change appreciably for the monobromoindigo components. [121, 140].

Orcein An organic dyestuff extracted from *orchil* lichen, orcein is not a single compound but a mixture of phenoxazone chromophores with similar solubilities and acid-base indicator properties (see figure 7.5) [162]. All forms are soluble in ethanol. Although the extraction of orcein from lichen is laborious, it is nevertheless straightforward and abundant when in season. The use of orcein as a substitute or impostor Tyrian purple for the dyeing of parchment has been demonstrated in the literature alongside *folium* [163], and although other purples including mixtures were known during the high middle ages, the early middle ages saw a sparsity of purple. Orcein dye is fugitive in sunlight [164].

The Raman response of orcein is appeciably weak, and it has a strong luminescence with $\lambda_{max} \approx$

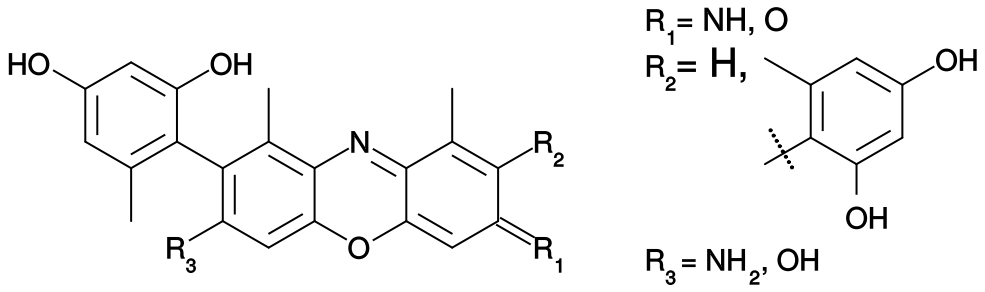

Figure 7.5: Molecular structure of orcein: 14 compounds (including some not shown here) have been isolated from *orchil* extract in the literature [162].

640 nm; the strongest Raman peak is at 1644 cm^{-1}, and to obtain a clear spectrum requires methods such as Subtracted Shifted Raman Spectroscopy [164].

Black Pigments

Carbon Wood char (*charcoal, carbon black*), bone char (*bone black*), or the collected soot from incomplete combustion of gas (*lamp black*) are largely indistinct by Raman in their major component of graphitic carbon with varying proportions of amorphous-like domains [165, 166]. Bone black can be distinguished by infra-red spectroscopy due to incomplete collagen breakdown and leftover inorganic phosphate, though by Raman spectroscopy only the weak phosphate peak could be called diagnostic between these pigments [139].

Char may well have been used as a black pigment since the discovery of fire-making, and has been used ubiquitously as the major black of stone-age cave paintings. The word *black* itself has its etymological beginnings in a Germanic word meaning "burnt", inextricably linking the colour of this permanent pigment with its most obvious synthesis. Carbon black is still used today in pigmented black inks. The two main graphitic peaks of carbon black occur at 1360–1370 and 1580–1600 cm^{-1} [165].

Iron Gall Called oak gall or iron gall, the general chemical identity of this mixture of iron complexes has been guessed at least since late nineteenth century[(ii)]. Both ferrous and ferric ions will form deeply-coloured, water-insoluble co-ordination complexes with tannins in wine or tea, as well as gallic acid from oak. The pure iron (II) gallate is a purple-grey solid when dry, though suspended in a binder and allowed to oxidise aerially, the complex darkens to black. The structure of iron gall has only very recently been described with x-ray crystallography [167].

Although the pigment is called iron gall, transition metals such as copper can form dark complexes, sitting in place of the iron centre. The Raman response of iron gall ink is not known at this time.

Other Materials

In addition to pigments, binding materials and synthetic "gold" are materials that are expected to be encountered in manuscripts.

[(ii)] Ambrose Bierce, in his coup-de-grace social commentary *The Devil's Dictionary*, describes *Ink* as a "cruel gallotannate of iron, with which journalists often *claim* to write".

Yolk A suspension of lipids in water, stabilised by globular albumen proteins. Yolk is the binder medium used in tempera painting; properly employed by tempera methods, yolk-based paint is touch-dry in seconds, and establishes a satisfactorily permanent water-repellency (though it is not impervious to soaking on its own) after 24 hours. The gradual saponification of fats by basic pigments, as per the case of oil paint, may be suggested in cases of degradation where a spontaneous "bloom" and fragility of tempera is of concern - the crystallinity of the organic salts formed, reduces the elastic flexibility for which tempera is generally valued. The high sulfur content of yolk albumens may be responsible for extensive wholesale auto-degradation of lead pigments to PbS in otherwise well-conserved MS, though this is not attested. In particular those bound MS that do not exhibit preferential degradation from the outer edges inward, and do not have contraindicated pigments in contact with one another, could imply this mechanism. Slight yellow colouration in tempera, photobleaches in a matter of weeks given sufficient incident UV flux from sunlight; this would be the case during the preparation phase prior to binding of MS [119], and subsequent exposure during use.

Albumen Purified egg white *glair*, contains much less protein per gram water than its counterpart yolk, and only a trace of lipid. It also takes longer to dry in bulk application due to its high water content, making it much less MS-friendly. Dried albumen protein alone as binder yields a far more fragile, though instantly colourless matrix in which to suspend pigment. Glair was considered by Theophilus to be a binder or glaze of superior quality in painting, and they recommended it for use as a fixative for gold leaf.

Gums Polysaccharide mixtures, exuded after injury to living tree bark vasculature. Gums are water soluble polymers with surfactant properties, capable of both stabilising aqueous suspensions of pigment and forming a binder matrix after drying. Cherry resin is mentioned by Theophilus in a recipe for iron gall ink, and acacia gum *gum arabic* has also been used for many centuries. Gum arabic in solution at working concentrations, has a pH comparable to concentrated citric acid solution. On drying, films of the solid polymers have a flexibility dependent upon the species from which they were obtained. Gum arabic is often fragile on its own; it is prone to cracking and flaking away from the substrate. Addition of honey to gum arabic makes the dried substance both more pliable and more easily re-worked with water. Gums can, like proteins, complex with metal ions or form salts pH-dependently. Over long times with the action of residual water, gum arabic acts as a mild reducing agent, and in solution is capable of reducing silver nitrate to give silver nanoparticles.

Tin sulfide In substitution of shell gold, mosaic gold (synthetic tin sulfide SnS_2) provided an appropriate metallic sheen and colour at a fraction of the cost of gold. Tin metal, sulfur, ammonium chloride and mercury were mixed in an iron flask and heated to high temperatures, and when cool the mixture could be painted; tin metal was also used in place of silver [119, pp. 33-34].

7.1.2 Manuscripts

Maccabees: *DCL B.IV.6 f.169*

A half-page of uncial text (from Latin for *inch*, referring to the large style of the hand), produced in the sixth century [168, p. 22]. This is identified with Benedict Biscop and Ceolfrith, i.e. the first Abbots of

the scriptorium at Wearmouth-Jarrow[iii] at the end of the seventh century, *via* unique correspondences to subsequent manuscripts (in this case, rare spelling variants that have been directly copied from this page). Uncial is a hand typically associated with Mediterranean Europe, and this is believed to be the remnants of a manuscript produced and obtained in Rome. This leaf contains no illumination, and the remaining ink is brown.

Gospel or New Testament: *DCL A.II.10 ff.2-6*

Produced at some point mid-seventh century, by scribes of Irish origins or tutelage writing pre-vulgate Latin in Insular half-uncial [168, p. 24]. The most notable portion in terms of illumination is an *incipit*[iv]. The text also includes in-fills of yellow pigment and emphasis with red-orange dots, at the beginning of the Eusebian sections[v]. This manuscript contains orange, blue, green and yellow pigments, and a black ink.

Gospel Book: *DCL A.II.17 ff.103-111*

Made in Wearmouth-Jarrow, this book passed to the Community of St. Cuthbert shortly after completion around the end of the seventh century [168, p. 28]. This contains only black ink and (in calligraphic rather than palaeographic terms) “artificial" Uncial; the ink in several places appears to both have imprinted brown on opposed pages, shows through the page from the opposite side, and occasionally shows haloes of brown.

Durham Gospels: *DCL A.II.17 ff.2-102*

Containing not least the earliest-dated depiction of the crucifixion of Christ in a manuscript, but several highly-decorated early initials as well, including full-page incipits, this is the holy book used in the appointment ceremony of a new Bishop of Durham. This book originates most likely from Lindisfarne at the end of the seventh century [168, p. 30], and was possibly the exemplar or inspiration for the Lindisfarne Gospels. This is the first manuscript in this set chronologically, that contains purple, though it does not appear to contain any blue pigment whatsoever. The pigments are purple, green, orange, and yellow, and appear throughout; though portions of “white" do exist, they appear dirtied, and are applied where orange would be used elsewhere in the manuscript. The script is Insular half-uncial.

The Durham Cassiodorus: *DCL B.II.30*

Finished in Northumbria in the eighth century [168, p. 34], this abbreviated version of Cassiodorus' *expositio psalmorum* is a large (442×295 mm), bound volume with full-page patterned illustrations and decorated capitals, and written mostly in a formal Insular Minuscule. Aside from the black ink, the work makes extensive use of purple, orange, now-faded yellow, a blue-green and what appears to be an intentionally-applied white. The orange pigment is used for small portions of text.

[iii] a scriptorium based in what is now Monkwearmouth-Jarrow abbey by the river Wear, founded by Benedict Biscop as the Monastery of St. Peter's - the acquisition of books from the continent as exemplars to copy, was necessary for successful establishment

[iv] an introductory line of text beginning with the word “incipit" (Latin, “here-begins"), often including enlarged, decorative title letters and one or more coloured and decorated capitals

[v] pre chapter-verse division of the gospels into portions that have similar sense, morals, and/or theological meaning across the four gospels; a form of equivocation which, used with canon tables, allows the content of the gospels to be straightforwardly cross-referenced for study and/or sermon

Gospel Book: *DCL A.II.16*

Again Northumbrian in origin, the use of pigment in this eighth century gospel [168, p. 38] is sparse, and consists solely of a frequently-discoloured orange (for small, penned Eusebian sectioning references and silhouetting[vi]) and yellow (in-fills in Eusebian sections). Despite being very conservative in pigment, it contains an example of an ornamented initial, some decorated capitals in a style similar to those in the Cassiodorus, coloured text, and the penmanship of more than one scribe.

Cambridge-London Gospels: *CCCC 197b*

From Lindisfarne in the early eighth century, this manuscript is slightly more modest than The Durham Gospels in its overall composition [169]. It nevertheless has a palette of orange, purple, yellow, green, and a brown-black ink. The surviving pages[vii] contain of note mostly decorative illustrations, and enlarged initials for Eusebian sections.

Collectar: *DCL A.IV.19*

Dated to around the late ninth/early tenth century, the collectar is a small book of sermons written in Latin using Insular minuscule[168, p. 42], and rubricated in Old English[viii]. This book was rubricated by the scribe Aldred, who also rubricated the Lindisfarne Gospels. The main script is black, the rubric is a deep and almost-dull red. Decoration takes the form of inventively-drawn capitals in the same colour as the text.

CCCC 183

Wood [170, p. 18] writes that Corpus Christi College Cambridge MS 183 dates to just before 940 AD during the reign of King Æþelstan. It enjoyed royal patronage, is written in Anglo-Saxon square minuscule hand and contains an illustration in the first few pages. The colours within are purple, orange, yellow, white and blue, and the designs of the illuminated initials have insular influence.

Benedictine Gradual: *Cosin V.v.6*

Originating from Christ Church Cathedral Priory in Canterbury, late eleventh century [171, p. 35], the gradual is an example of written choral music with words and notes, but no stave. The title of each piece is in title capitals, with an historiated initial. Coloured capitals of two sizes are used to show the beginnings of verses, and mark the beginning of a new sense/phrase. Coloured lines seem to dictate the tie of a given syllable to a set of subsequent notes, similarly to modern choral notation. Colours include red, yellow, dull orange, blue, green and purple.; the ink is brown. The green pigment appears to be bleeding, staining or otherwise degrading the parchment, and there are instances of layered pigmentation in historiations.

[vi] decoration frequent in Insular scripts, taking the form of an outline of small, regular dots

[vii] this manuscript was part of the Cotton library, which holds the Lindisfarne Gospels (*Cotton Nero D.IV*) and which suffered a fire in the eighteenth century. A tendency for owners to re-bind portions of manuscripts with portions of other manuscripts into a bespoke tome, ultimately saved these remaining portions from destruction

[viii] rubric is annotation (generally in red, hence the name) between the lines. It is also known as an *interlinear gloss*, from which we inherit the modern glossary. A gloss is penned after completion for the purpose of providing a general meaning in another language, by use of comparable words without using a real sentence structure

Augustine: *DCL B.II.13*

Possessed of explicitly Norman script and illumination, this manuscript is dated eleventh century, originating Normandy[168, p. 56]. It contains historiated initials[(ix)] and capitals, as well as coloured text for incipits/explicits. The colours are red, green and blue. In several places, the green pigment appears to be degrading the parchment slightly.

Symeon of Durham: *Cosin MS V.II.6*

Written explicitly in Durham near the beginning of the twelfth century, *tract on the origins and progress of this church of Durham* at least *professes* a true account of the building of Durham Cathedral in every sense of the word [171, p. 36]. The scribe writes in a brown ink of varying hue and darkness. The artist paints highly decorated and historiated initials in layers using a red, off-red/orange, yellow, blue, green and white. Top-line capitals at the introduction of a page are in alternating red-blue or alternating red-green, and contrast the style of the text. Like many others, the green appears to stain, bleed into, or corrode the parchment.

Laurence of Durham: *Cosin V.III.1*

The works of Laurence of Durham are plays, written most likely at Durham Cathedral Priory mid-late twelfth century [171, p. 38]. The ink is a brown of variable intensity, whilst the colour decoration is predominantly red.

Psalter: *Bamburgh Select 6*

The final instalment in the set is simply "Britain *c.* 1200" [171, p. 44], written in black text with red, green, and blue capitals and decorations. The illumination (which features burnished gold) also features red, green, and blue, furnished also with white and orange.

7.2 Spectroscopy

The main spectroscopic methods employed during this project are μ-Raman Spectroscopy and Diffuse Reflectance, which will be treated here with respect to theory. Experimental details are provided in Chapter 2.

7.2.1 μ-Raman Spectroscopy

A photon of frequency $\tilde{\nu}_{in}$ scattered by a substance, may undergo an elastic or inelastic interaction with that substance to produce $\tilde{\nu}_{out}$. Elastic (Rayleigh) interactions result in $\tilde{\nu}_{in} - \tilde{\nu}_{out} = \Delta\tilde{\nu} = 0$, whereas for inelastic collisions $\Delta\tilde{\nu} \neq 0$. The oscillating electric field $\tilde{\nu}_{in}$ perturbs the electrons of the substance into a *virtual state* (and is absorbed). A virtual state is an excited non-eigenstate of the system, which immediately decays back to the ground electronic state, yielding a new photon $\tilde{\nu}_{out}$. If at the end of this interaction, the substance in its ground electronic state occupies a different *vibrational* level to the one it began in, then $\Delta\tilde{\nu}$ will be equal to the difference between those energy levels - this difference, reported in reciprocal centimetres, is the *Raman shift*. The proportion of inelastic scattering is to the order $< 10^{-6}$ of all scattered light, to the effect that Raman spectroscopy requires high-intensity

[(ix)] letters containing illustration, or depiction of an "inhabitant" person, plant or animal

monochromatic light of known frequency, typically from a laser. The spectrum of $I_{out}(\tilde{\nu})$, converted to Raman shift, is a characteristic vibrational spectrum of a substance. The theory of Raman spectroscopy is treated fully in part I of this thesis.

Spectral Contributions & Laser Intensity

All other things being equal, the integrated Raman scatter from a given isotropic sample, is linearly proportional to the amount of $\tilde{\nu}_{in}$ flux it receives. The volume through which $\tilde{\nu}_{in}$ passes in a sample, and from which the collection efficiency is significant, is the *scattering volume*. In the μ-Raman setup, the delivery of $\tilde{\nu}_{in}$ is *via* a confocal microscope objective; by ray-tracing alone, a microscope objective focuses down to an infinitesimal point, at which the collection and delivery efficiency through the lens is optimal, to the effective exclusion of other regions. In reality, an objective produces a beam waist rather than a point, with two characteristics of note:

1. within the focal plane, the beam intensity profile is that of an Airy disk (*vide infra*)
2. along the beam-axis, the beam intensity profile about the focal plane is approximately Gaussian

These two characteristics generalise a *point spread function* (PSF), which is a deviation from the (impossible) infinitesimal point; the sampling region occupies a finite volume due to wave interference. This ultimately determines that the scattering volume is a 3-dimensional pixel (termed a *voxel*). Therefore for samples which are inhomogeneous on the scale of the voxel, the integrated Raman response from each spectral contributor, is determined not only by the degree of inclusion of those inhomogeneities within the scattering volume, but their position within it as well.

An *Airy pattern* or *Airy Disk* is the diffraction pattern in a focal plane, where the interference fringes pass a majority of the light intensity through a well-definable region, bounded inside concentric circles of light intensity. Figure 7.6 shows in cross-section the Airy function:

$$I(q) = I_0 \left(\frac{2J_1(x)}{x}\right)^2 \tag{7.1}$$

$$x = \pi q/\lambda f \tag{7.2}$$

where I_0 is a normalisation factor (1), $J_1(x)$ is a Bessel function of the first kind, $q = x\lambda f/\pi$ is the radial distance from the optical axis, λ is the wavelength of light, and f is the f-number of the lens. The quantity x has been converted to units of q in nm. It can be demonstrated on this numerical evaluation, that the value of q at which the first minimum occurs is equal to $q_{min} = d_A = 1.22\lambda f$, where d_A is the nominal diameter of the Airy disk; when $q = d_A/2$, $I(x) = I_0 e^{-1}$.

Luminescence & Interference

The low efficiency of Raman scattering has already been discussed. As the quantum yield of a luminescent process can approach unity, and is frequently many orders of magnitude greater than that of Raman scatter, luminescence is an efficient competitor when $\tilde{\nu}_{in}$ lies in an absorption band of a luminescent sample. Such broad-band emissions can mask the appearance of Raman bands completely. Although it is well-known that excitation to the lowest vibrational level of an excited state results in a resonance effect that boosts Raman efficiency, there exists a risk insofar that absorbed light can be converted to heat by non-radiative relaxations, and cause localised damage to the sample.

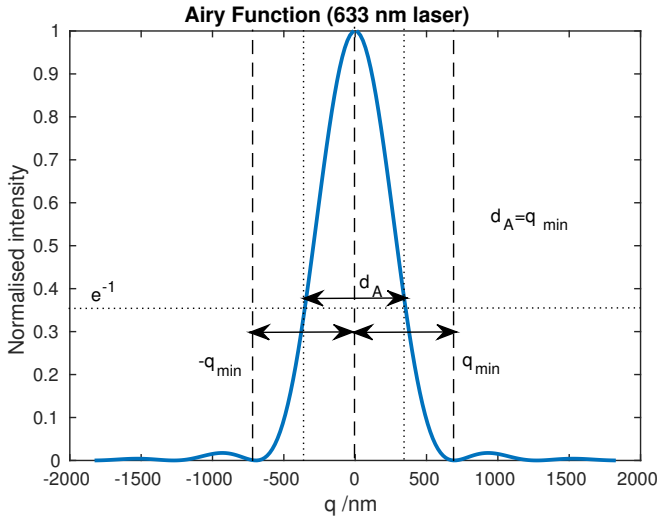

Figure 7.6: Airy function: The Airy function, shown for a 632.1 nm He-Ne laser line. The quantity d_A is shown graphically, and the equivalence $d_A = q_{min}$ is plainly visible.

Use of interferential filters in Raman instruments, leads also to noticeable interference effects when broad-band light of any origin passes through the spectrometer. Thus,

$$B(\tilde{\nu}) = T(\tilde{\nu})I_L(\tilde{\nu}) + N \tag{7.3}$$

$$A(\tilde{\nu}) = T(\tilde{\nu})[I_S(\tilde{\nu}) + I_B(\tilde{\nu})] + N \tag{7.4}$$

where $B(\tilde{\nu})$ is a background spectrum consisting of N noise, lamp intensity $I_L(\tilde{\nu})$ and the transmission of the interference filter $T(\tilde{\nu})$. The analyte spectrum $A(\tilde{\nu})$ differs in that it contains a signal intensity $I_S(\tilde{\nu})$ and a baseline $I_B(\tilde{\nu})$.

Then, by assuming noise N is random and has no distinct spectral features of its own, we may express an approximate corrected spectrum:

$$\frac{A(\tilde{\nu})}{B(\tilde{\nu})} = C(\tilde{\nu}) = \frac{I_S(\tilde{\nu}) + I_B(\tilde{\nu})}{I_L(\tilde{\nu})} + N' \tag{7.5}$$

So long as the features of baseline $I_B(\tilde{\nu})$ and lamp $I_L(\tilde{\nu})$ are approaching flatness on the scale of the features of a Raman spectrum, the distortion to the form of the Raman signal $I_S(\tilde{\nu})$ and features of the new apparent baseline $I_B(\tilde{\nu})/I_L(\tilde{\nu})$ will be negligible by comparison to the effects of $T(\tilde{\nu})$. A new noise term N' is included simply as an acknowledgement that the random noise must propagate into the new spectrum. Care must be taken to evaluate the utility of this correction on a spectrum-by-spectrum basis; introduction of noise from $B(\tilde{\nu})$, applies to the peaks as well as the baseline.

7.2.2 Diffuse Reflectance Spectroscopy

Specular reflection is the mirror-like reflection, which straightforwardly diverts the path of a light ray with equal angles of incidence and reflection; the efficiency of specular reflection is reflectivity, and so a discussion or calculation of reflectance necessarily and implicitly excludes single specular reflections. Reflectance is the quantity of diffuse reflection, the same sort of reflection that is responsible for the

visual effect of e.g. matte-finish paint. A detailed phenomenological discussion of reflectance, reveals that the formalisms surrounding reflectance are heavily dependent upon the source, collimation and geometry of illumination and detection, and complicated greatly by polarisation and any anisotropy or inhomogeneity within the substrate.

Kubelka-Munk Theory

A depolarised light ray which is downwardly incident upon a flat, sharp interface between two transparent dielectric media, is partially reflected and transmitted according to the angle of incidence. The transmitted portion will be subject to any frequency-dependent attenuation within the bulk, whilst the reflected portion will have an angle-of-incidence-dependent excess of some light polarisations, but otherwise by comparison will not experience meaningful attenuation. In the case of incidence upon an isotropic, granular medium n_2 whose grains are suspended in medium n_1, the reflected light from the initial grain will likely be incident upon a new grain and be subject to a new reflection event, whilst the partially-attenuated transmitted light will be subject to an internal reflection event as its trajectory leads it to exit n_2, with the possibility for total internal reflection. From there the exiting ray may be incident upon new grains, and so on and so forth. Light penetrating the granular medium, is progressively less likely to reach the topmost limit of the granular medium again the more deeply it penetrates. Light upwardly exiting the granular medium possesses a continuum of ray trajectories; it has been scattered, and this wholesale process is called *diffuse reflection*.

A ray of light passing through a transparent medium, experiences a wavelength-dependent attenuation of intensity according to Beer's Law, $I = I_0 10^{-\varepsilon \cdot c \cdot l}$, leading to the definition of absorbance A and the most common expression of Beer's Law:

$$A(\lambda) = -\log(T(\lambda)) = -\log\left(\frac{I(\lambda)}{I_0(\lambda)}\right) = \varepsilon(\lambda) \cdot c \cdot l \tag{7.6}$$

where I is an intensity at a point along the ray's path through the material, I_0 is the initial intensity, ε is the extinction coefficient in $\mathrm{M}^{-1}\ \mathrm{cm}^{-1}$, c is the molar concentration of absorbers and l is the path length of the ray (the total distance travelled through the absorbing medium) at the chosen point. Transmittance T is defined here opportunistically for completion. The quantity ε is characteristic of the material under study. Reflectance is the quantity:

$$R(\lambda) = \frac{I(\lambda)}{I_0(\lambda)} \cdot R_0(\lambda) \tag{7.7}$$

where $I(\lambda)$ is an intensity profile of reflected light, $I_0(\lambda)$ is the intensity profile of reflected light from a diffusely-reflecting white standard, and $R_0(\lambda)$ is the absolute reflectance profile of the standard material, which ideally may be assumed to be unity at all wavelengths.

Reflectance is the measured quantity of diffuse reflection, whereas reflectivity is the quantity of specular reflection. For the purposes of spectroscopy and imaging, reflectance is the quantity of concern. The treatment of Kubelka and Munk makes assumptions about the above described process to refine it into a model. They assume, that:

1. the dimensions of the layer of scattering medium are infinite in-plane (x, y), and either
   (a) finite in depth (z), with a substratum
   (b) infinite in depth

2. the substratum is either a perfect attenuator or perfect diffuse reflector
3. all particles in the superstratum are isotropic scatterer-absorbers
4. layer thickness is very large compared to the average particle dimension for isotropic scatterer-absorbers
5. illumination and collection are perfectly diffuse, or the transition from air to the medium instantaneously changes the illuminant from directional to diffuse
6. a white standard exists, for which there is a known spectrum $R_0(\lambda)$

Their treatment in equation 7.8 is the solution to a set of bi-directional coupled differential equations; the working is described elsewhere in detail, though their treatment of the model yields the *remission function*, numerically double the *espat function* that produces scalars proportional to the bulk absorbance of the particles so long as the values of R are at neither extreme [8]:

$$F(R(\lambda)) = \frac{(1 - R(\lambda))^2}{2R(\lambda)} = \frac{K(\lambda)}{S(\lambda)} \tag{7.8}$$

Decrease of grain dimensions increases the surface area to volume ratio of the suspended material, increasing the contribution of reflection events at interfaces (scatter S) and relatively decreasing the effect of bulk attenuation (absorption K) on the spectral form of the diffusely reflected light.

Luminescence

An implicit assumption of the Kubelka-Munk treatment, is that the attenuation of the light field does not result in fluorescence. In this event, broadband excitation of the material results in an intensity profile which includes contributions from both emission of light, and any reabsorption of light on the blue edge of the emission band where spectral crossover with absorption occurs. The addition of a term for luminescence is not straightforward, and must include the quantum yield, concentration terms, and differentials for the emissions which are yet susceptible to attenuation. Furthermore, as emission dipoles have a non-zero emission probability for a continuum of directions orthogonally about their axis, the direction of the emission terms are orientationally decoupled from the attenuation terms that spawned them. Luminescence models for reflectance spectra have been constructed in the literature [10], but their applicability holds only for the case of well-characterised analytes, for which spectra for multiple samples with known concentration can be generated. In the in-field analysis of many "one-off" luminescent substrates, these cannot be obtained for use with these models, and even if the pure emission spectrum can be obtained, the decoupling of the luminescent response from the effect of attenuation is non-trivial and little more than presumptive; the propagation of uncertainty between R and $F(R)$, yields significant uncertainty in $F(R)$ for $R < 0.1$ or $R \to 1$, to the effect that strong or very weak attenuation can completely mask the appearance of structure. The emission at the blue edge in both the pure emission (obtained using monochromatic illumination) and the R spectra can also be misleading in form, or completely lost. It is straightforward to infer, that ignorance of this can lead to spurious conclusions in the reflectance analysis of luminescent samples.

Assuming no luminescence, under broadband illumination the Kubelka-Munk model holds for many systems which are otherwise strictly non-ideal, such as layers of analyte upon substrates that don't conform to the perfect reflector or perfect attenuator assumptions. The basis for this is that for

thick layers, the contribution of the substrate to the spectral form is greatly minimised. In any case, the purpose of this assumption is to provide a limiter to the extent of z. Introducing luminescence invalidates some of the diagnostic capability of $F(R)$, on the basis that the shape of the $F(R)$ spectrum, for $R > 1$, can anomalously indicate absorption. Further to this, the effect of error propagation is to reduce the certainty in the spectral form for parts of the spectrum brought closer to $R = 1$ by the effect of luminescence.

Due to the near-ubiquity of luminescence, there is no reason *ab intio* to assume its total absence in a broadband spectrum of an unknown. Testing with monochromatic excitation can rule out luminescence, though an emission spectrum of the substrate is not sufficient (*vide supra*) to recover the pure absorptive component.

Collection Geometry

There exists an equivocation within this part of this thesis, that requires prior justification. Although a theoretical point, it is included here for clarity.

The Kubelka-Munk formalism specifies, that the illumination of the substrate material is of indeterminate collimation (i.e. diffuse) and that the collection apparatus likewise collects with an indeterminate collimation. However, it will be made clear that the illumination and collection are focused beams within the experimental setup, thus the reflectance quantity used for this thesis is the bi-directional reflectance rather than the diffusive Kubelka-Munk reflectance. This equivocation is justified, because although the assumptions of a bi-directional illumination-collection with a semi-infinite substrate are not equivalent to those of the original Kubelka-Munk, the former approximates the latter for isotropic substrates.

Using the geometry of the bi-directional system, we can use Lambert's law of reflectance to generalise that the observed brightness B of any surface [8]:

$$B \propto \cos i \cdot \cos e \tag{7.9}$$

where i is the angle between illuminating ray and surface-normal, and e is the angle between observation trajectory and surface normal. Therefore if $\cos e = 1$ and $\cos i \neq \cos e$, no speculars are observed, but a maximised diffuse intensity *is*. The collimation of the collection apparatus ensures that the observed light is exiting the substrate at the normal to the surface plane, and an assumption of negligible angular dependence on the observed spectral form of the diffusely reflected light holds for isotropic substrates. Thus, as the absolute quantitation of reflectance is not of concern, and only spectral features are of importance, this approximation is both necessary in practice and satisfactory in theory.

The above equivocation is useful in the discussion of layered substrates; the treatment for a bidirectional semi-infinite diffusive reflectance is much more straightforward than KM, yielding intuitive solutions far more easily. For a given layered system, the significance of the signal from the sub-layer is $\propto \exp[-4\gamma\tau_0]$ (where albedo is $\gamma = (1-r_0)/(1+r_0)$, τ_0 is optical thickness of the top layer, and r_0 is the reflectance of the top layer. It is intuitive to consider that when τ_0 is sufficiently large, the lower layer becomes insignificant in its overall contribution to the observed signal. The expression [8, p. 244]:

$$\tau_0 = N_E \cdot \sigma \cdot Q_E \cdot dz \tag{7.10}$$

where N_E is effective density of the medium in g/cm^3, σ is the cross-sectional area in cm^2, Q_E is the

extinction efficiency in cm/g, and dz is the thickness of the top layer; elucidates the nature of optical thickness.

7.3 Multi/Hyper-Spectral Imaging

Optical imaging devices consist of an array of detectors which, with suitable control of ray-paths via optics, then spatially resolve the intensity of light reaching the detectors in order to re-construct an image. This image is intrinsically based on the responses of those detectors and the known geometric variables of the system. The ability of imaging to sample and spatially resolve small features within large objects, is the principal advantage of its use as a base method. Digital images provide parametrisation of samples (pixels within a frame), and will be the sole basis of imaging discussion here.

The most familiar form of image is the arguably the digital colour photograph. Although the format of the data in a colour photograph can be re-represented for the purposes of printing in CMYK (cyan-magenta-yellow-black), the most common domestic format is sRGB (standard red-green-blue). Non-sRGB images, or sRGB images containing more than 3 spectral bands or bands explicitly outside the visible range, are multispectral images from multispectral imaging (MSI). MSI containing more than 12 bands are instead called hyperspectral images from hyperspectral imaging (HSI), and may extend to hundreds of spectral bands or consist of spectra. The purpose of MSI/HSI (spectral imaging, SI) is to extend the spectral resolving capacity of imaging, in order to classify regions of an image by spectral behaviour. MSI has in recent decades received considerable development for applications in industry, science, and defense [172, 173]. Among non-destructive techniques, the utility of MSI/HSI for conservation is to characterise and reveal features within an artifact that may otherwise require small-footprint methods such as Raman microscopy and XRF to detect. It is the aim of this current work to explore the application of MSI and digital colour imaging to qualitative analysis of ancient manuscripts.

7.3.1 Imaging

The methods for collecting image data employ a single camera with a high dynamic range, with appreciable sensitivity covering UV-B through NIR. The scene receives then variable illumination or collection, either in discrete frames using LEDs or filters, respectively. The general term for this is a staring-array or a focal plane array. Alternatively, other forms of scanning raster a 2D image over time, but provide more spectral information in a different format.

From the perspective of spectroscopic information, the cost of facile spectral resolution is complexity in achieving spatial resolution and meaningful spatial information. That is, imaging and spectroscopy are on either end of a scale, with each providing either spatial or spectral information easily, and very limited amounts of the other. However, qualitative multispectral imaging for the discrimination between pigment materials need not rely on the precise and accurate reporting of relative reflectance *between* bands *per se*, only on the non-random, non-systematic variance within each band that originates from the pigments. That is to say, spectral resolution isn't an issue if major distinguishing behaviours/features of the reflectance profile aren't excluded from the choice of bands. So long as the reflectance profiles of the pigments within MS *don't* have redundancy for the chosen bands (i.e. they don't behave identically), then they can be discriminated by variance alone.

SI methods capture as much spectral information as possible without regard for the precise utility of

that information, which is assumed to be either purely reflective or inconsequentially combined with fluorescence. The exact contribution of fluorescence to the reflectance profile is contentious as discussed in §7.2.2, and relatively speaking in this form its contribution to the apparent spectral variation between similarly absorbing materials may be very small.

7.3.2 Reflectance & Imaging

Images that don't include shiny surfaces and light sources, solely collect diffusely reflected light. A monochrome image of a single reflection band with a properly equalised histogram, sets the brightest pixel to unity (or 255), and the darkest pixel to 0, in effect range-scaling the image to provide the most contrast. This standardises the entropy H of the image, providing the maximum information that that image can convey. According to the equation for image entropy provided by [174, p. 673]:

$$H = -\sum_{k=1}^{G} p_k \log p_k \tag{7.11}$$

where G is the number of bins, and p_k is the frequency of any given grey value. The upshot of this, is that for a set number of bins (typically 256), the flatter the histogram, the more significant the individual pixels are. Quantification of reflectance in multispectral images, is of less concern than maximising the information content, as separation of pixels into classes requires sufficient information to be present.

7.4 Colour Spaces & Perception

RGB data are 3D arrays of integers on a scale of 0-255, representing the nearest value of intensity for each coloured sub-pixel within the camera. Transformation of RGB values is explained in section 7.4.2, though automated procedures in MATLAB® generally produce values re-scaled to match the scale of the input. Unsigned 8-bit integers from 0-255 as per RGB images, produce values on that same scale, and non-integer RGB data on the scale 0-1 produces non-integers on the scale 0-1. Once transformed, the achromatic point (a.k.a. grey-point) in the a*b* plane is commonly either (127.5,127.5) or (0.5, 0.5), though for some purposes we may find it more useful to subtract this vector from all data or transform between systems. The scale of the numbers and the position of the grey-point should now make the system of numbers used in future, self-evident.

The L*a*b* system is intended to represent the visual importance of change to colour and brightness. The changes are meant to be linear or very close to linear, within the L*a*b* colour space. That is to say, a colour with twice the value of a* than a reference in the positive direction, appears 'twice as red' than that reference, to the average observer. This simplifies colourimetry at the expense of spectral information, and allows colour changes to be defined as displacement vectors whose magnitudes and directions can be straightforwardly compared.

The utility of using L*a*b* as opposed to the human eye, is that:

1. quantification rather than qualification of colour is intuitively more useful analytically for comparison, as it is more informative

2. it is definitively not subject to deviations from a standard average observer as humans are, though it is reliant on the detector nonetheless

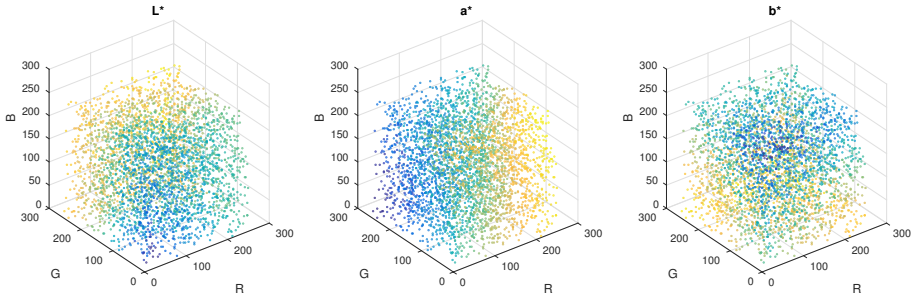

Figure 7.7: Scatter Graphs of sRGB to L*a*b* Conversion: Random RGB co-ordinates converted to L*a*b*, shown here in top-down diagonal view and coloured by the indicated L*, a* or b* value on a scale from blue-yellow.

3. it is not subject to optical illusions such as perception of relative lightness and hue shift for colours in close proximity to one another

7.4.1 Illuminants

An illuminant is a light source that illuminates a surface. In the current discussion, this surface diffusely reflects any light which is not absorbed or irretrievably scattered. The spectral profile of the diffuse scatter is the basis of what is then perceived by the eye. A material with a given reflectance profile, generates a spectrum of diffusely reflected light that is intrinsically recoverable from the definition set forth in equation 7.7. CIE has defined a set of illuminant spectra, which approximate the black-body radiation of the sun, minus the portions absorbed by the atmosphere at a given time of day. Figure 7.9 on page 159 shows the standard D65 illuminant spectrum.

7.4.2 Conversion

It is useful to be able to convert directly between systems such as reflectance, sRGB and L*a*b*, though notably the conversion from reflectance is irreversible due to the summation term (*vide infra*). The L*a*b* co-ordinate system is approached through an intermediate set of co-ordinates called the XYZ tristimulus values. XYZ seeks to characterise the relative levels of stimulation, of the three types of cone cells in the human eye, as caused (typically) by a diffusely reflective surface. The XYZ values are then mapped on to the L*a*b* co-ordinate system.

The ultimate effect of mapping from sRGB is illustrated in figures 7.7 and 7.8.

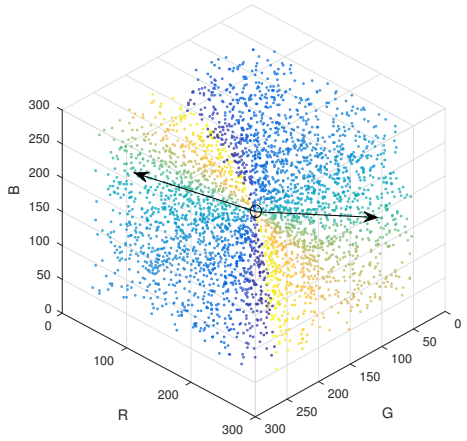

Figure 7.8: Scatter Graphs of sRGB to L*a*b* Conversion: arctan(b*/a*): The a*b* values from figure 7.7 have been converted to $\theta_{a*} = \tan^{-1}(b^*/a^*)$ which gives the angle between the a* axis and each a*b* co-ordinate expressed as a displacement vector from the grey-point ($a^* = b^* = 0$). The points are coloured by θ_{a*}, and the viewing axis is along $R = G = B$. In this way, two general families of hue can be seen either side of the yellow-blue discontinuity ($\theta_{a*} = \{90°, 270°\}$). The two vectors approximate $\theta_{a*} = \{0°, 180°\}$, the rightmost of which is 0°, with hue-angles progressing clockwise numerically through the figure.

Converting $R(\lambda)$ to XYZ

For a reflectance spectrum $R(\lambda)$, the XYZ tristimulus values under a D65 illuminant, are yielded directly by

$$X = \frac{1}{N}\sum_{i=1}^{N} \bar{x}(\lambda)_i \cdot R(\lambda)_i \cdot I_{D65}(\lambda)_i \tag{7.12}$$

$$Y = \frac{1}{N}\sum_{i=1}^{N} \bar{y}(\lambda)_i \cdot R(\lambda)_i \cdot I_{D65}(\lambda)_i \tag{7.13}$$

$$Z = \frac{1}{N}\sum_{i=1}^{N} \bar{z}(\lambda)_i \cdot R(\lambda)_i \cdot I_{D65}(\lambda)_i \tag{7.14}$$

where $\bar{x}, \bar{y}, \bar{z}$ are tristimulus sensitivities provided by CIE as shown in figure 7.9, and $I_{D65}(\lambda)$ is the illuminant D65 spectrum; all of this assuming that the ith element for each spectrum is for an equal wavelength.

Converting sRGB to XYZ

For the sets $\Delta = \{R, G, B\}$ which is a set of sRGB values set to the scale 0–1 from 0–255, and $\delta = \{r, g, b\}$ which is linear with respect to incident power:

$$\begin{cases} \delta = \Delta/12.92 & | \quad \Delta \leqslant 0.04045 \\ \delta = \left(\frac{\Delta+0.055}{1.055}\right)^{2.4} & | \quad \Delta > 0.04045 \end{cases} \tag{7.15}$$

Set δ, for the D65 illuminant undergoes the transform:

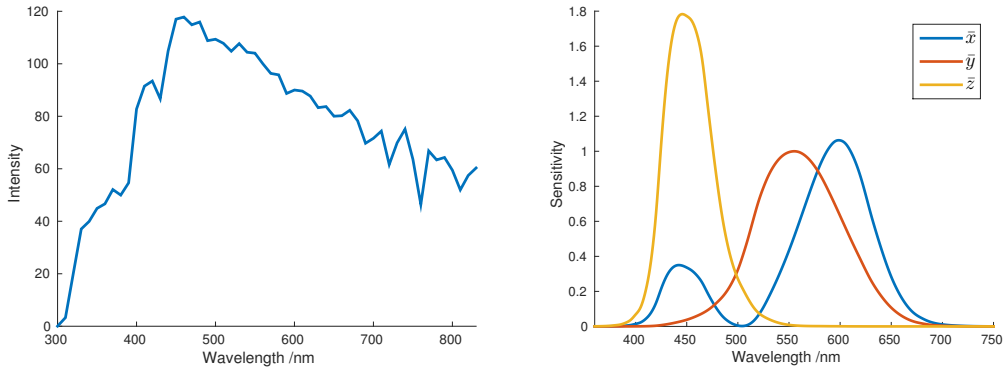

Figure 7.9: D65 Illuminant and $\bar{x}, \bar{y}, \bar{z}$ sensitivities: Left: Spectral power distribution of D65 illuminant. Right: $\bar{x}, \bar{y}, \bar{z}$ spectra, used in the calculation of XYZ tristimulus values from reflectance in equation 7.12.

$$\begin{bmatrix} X \\ Y \\ Z \end{bmatrix} = \begin{bmatrix} 0.4124564 & 0.3575761 & 0.1804375 \\ 0.2126729 & 0.7151522 & 0.0721750 \\ 0.0193339 & 0.1191920 & 0.9503041 \end{bmatrix} \begin{bmatrix} r \\ g \\ b \end{bmatrix} \tag{7.16}$$

Converting YXZ to L*a*b*

The XYZ tristimulus values can be converted to L*a*b* by the following scheme

$$L^* = 116 f_y - 16 \tag{7.17}$$

$$a^* = 500(f_x - f_y) \tag{7.18}$$

$$b^* = 200(f_y - f_z) \tag{7.19}$$

where, setting first the values $\kappa = 24389/27$ and $\varepsilon = 216/24389$

$$\begin{cases} f_x = \sqrt[3]{x_r} & | \quad x_r > \varepsilon \\ f_x = \frac{\kappa x_r + 16}{116} & | \quad x_r \leqslant \varepsilon \end{cases} \begin{cases} f_y = \sqrt[3]{y_r} & | \quad y_r > \varepsilon \\ f_y = \frac{\kappa y_r + 16}{116} & | \quad y_r \leqslant \varepsilon \end{cases} \begin{cases} f_z = \sqrt[3]{z_r} & | \quad z_r > \varepsilon \\ f_z = \frac{\kappa z_r + 16}{116} & | \quad z_r \leqslant \varepsilon \end{cases} \tag{7.20}$$

and the normalised tristimulus values, where X_0, Y_0, Z_0 are tristimulus values for a reference white:

$$x_r = \frac{X}{X_0} \qquad y_r = \frac{Y}{Y_0} \qquad z_r = \frac{Z}{Z_0} \tag{7.21}$$

which concludes both transformations.

7.5 Principal Component Analysis

Principal component analysis (PCA) seeks to re-express a $m \times n$ *data matrix* $\mathbf{D}$ as the product of two sister matrices called the *scores* $\mathbf{S}$ (also $m \times n$) and *loadings* $\mathbf{C}$ ($n \times n$). The number of samples m should ideally exceed the number of observations n, though this is not necessary. The loadings (also called

the *principal components* of the data), are found by eigendecomposition[x] of the covariance matrix; $\mathbf{C} = \text{eig}(\text{cov}(\mathbf{D}))$. Matrix division then straightforwardly gives the scores matrix $\mathbf{S} = \frac{\mathbf{D}}{\mathbf{C}}$.

We therefore now imply or understand the following:

1. the PCs are linear combinations of the responses from all samples
2. each PC loading is a basis function of the data set that is uncorrelated with the other loadings
3. the scores are coefficients for determining how much of each loading is present in the sample the score represents
4. the number of PCs is equal to the number of observations
5. the PCs are not constrained to be positive, and thus the basis functions may not represent real, physically tenable system variables
6. the scores and loadings come in pairs per PC, and the variance accounted for by the total contribution of the first PC to the data, is always higher than the second and so on.
7. the matrix multiplication of the first q loadings with the first q scores, reconstructs the data with the contributions from the remaining basis functions subtracted
8. the quality of the analysis is contingent on the quality of the data

For a more complete summary of PCA, with worked examples, see [175, p. 215].

The immediate consequence of this representation is to reduce the dimensionality of the data, by allowing the latter PCs to be discarded or ignored. The cut-off is generally just after the point where, starting with the first PC, the cumulative sum of the variance accounted for by the PCs is >95%.

Application to Imaging

The proposed application of PCA is to take a set of multispectral images, and consider each band to be an observation and each pixel a sample region. In this way, the information about each sampled region is condensed into fewer images, and the images that provide the greatest overall contrast between areas of a MS, determines which set of scores is useful for separating the regions of the manuscript. This is an atypical application of PCA to image analysis; though it is not unheard of to use dimensionality reduction as a utility in multi- and hyper-spectral data sets, the most frequent use of PCA in imaging is compression, or image enhancement [174, p. 201, p.676].

The alternative to PCA is ratiometric imaging. Finding another function to apply to the images to highlight a particular sort of pigment, would be discovered or postulated presumptively on a pigment-by-pigment basis. Individual images can be useful diagnostics, for instance copper pigments have absorption bands in the NIR, and Egyptian Blue has a characteristic luminescent emission band in the NIR that can be imaged with a red LED and a NIR filter.

[x] In practice, programs such as MATLAB® employ the *single value decomposition* of cov(**D**) by default, though for symmetric square matrices such as cov(**D**), eigendecomposition and single value decomposition give the same result in theory, and the difference is purely semantic.

Pre-Treatment

A consideration in PCA is the effect of pre-treatment. There are three major options for pre-treatments to standardise data sets, before undergoing PCA. There is also ongoing research that seeks to improve PCA in order to increase cluster separation and make classification protocols more accurate and efficient.

Mean-centering subtracts the mean co-ordinate (centroid) of the data set, from all individual samples within the set; it sets the mean co-ordinate of the data set to zero, without changing the relative dimensions of the data space. The effect of mean-centring on the output for PCA is to also set the mean of the scores matrix to zero, and change the absolute and relative magnitudes of the loadings (but not their form).

Range-scaling sets the data to scale between zero and unity, either on a per-observation or per-sample basis. For a *k*-means analysis (*vide infra*), it is preferable to choose the option that produces the fewest extremal values for the data set, as to preserve the sphericality of the clusters. Range-scaling by sample, in the case of images, produces two extremals per sample, which distorts the data space to yield an *n*-cube of side 1 with most data at the edges (where *n* is the number of observations). Range-scaling by observation, normalises the data by scaling it to fit within a minimum-bounding *n*-cube of side 1. The effect of range-scaling on the output for PCA is to equivocate the importance of either the sample-wise variations or the observation-wise variations.

Decorrelation performs PCA and then applies a stretch to minimise the distance between the scores and the new axes, whilst preserving the mean and standard deviation. The data is then regenerated by matrix multiplication, with the correlation between the variables minimised.

7.6 Non-Negative Matrix Factorisation

Non-Negative Matrix Factorisation (NNMF) seeks to find an approximation of the *basis functions* matrix $\mathbf{B}$ of a data matrix $\mathbf{D}$, and the complementary weights $\mathbf{W}$ that result in $\mathbf{D} \approx \mathbf{W} \times \mathbf{B}$. The method is iterative, with minimisation of the root mean square residual as the objective function, and both $\mathbf{W}$ and $\mathbf{B}$ are constrained to positive or zero values only.

In spectral analysis, basis functions can relate to real additive components that construct a spectrum e.g. in a UV-VIS absorbance spectrum of a mixture of non-interacting dyes in solution - the form of the spectrum of each dye, might correspond to a basis function of the mixture.

It is important to note that basis functions from NNMF are *ad-hoc* based on variation in the parent data and contain noise, so the quality of the basis functions is dependent on the quality of the data.

Data Quality: a note on redundancy

Redundancy in data analysis refers to repetition of the same information in a way that doesn't produce useful variation. The term applies here for analytical methods such as NNMF and PCA, that rely on systematic variation in the data in order to function effectively. Repetitive spectral information is surplus to requirement. An invariant fiducial peak common to all spectra is an example of redundant information, even if it has other utility outside of the method. Data sets containing little variation, have high redundancy; judicious removal of the most redundant data may yield clearer analysis.

7.7 Clustering Algorithms

Clustering in large experimental data, is an apparent trend for similar samples to produce similar metrics and thus linger in proximity to one another in a data space, usually as applied to two or more dimensions. In unidimensional data, clustering from multiple behaviours presents as bimodal and higher distributions and is most intuitively displayed as a histogram; in higher dimensional data, this is more conveniently represented by scatter plots. For fundamentals of clustering, see [175, p. 220].

Clustering methods seek to divide a data population into multiple classes according to a chosen metric, which is minimised for the ideal solution. Each class is held as a distinct and separate subpopulation, the significance of which is dependent upon the data type. The application of clustering algorithms is common to cosmology, where it classifies photons by association with emitter locations, effecting the discovery and counting of new stars and galaxies. For imaging applications in manuscripts, a clustering algorithm will allow dynamic, non-arbitrary classification of pixels by the spectral behaviour of the scene. For clarity in this document, the term *class* will refer exclusively to the classification decision by an algorithm (whether during or after) whilst *cluster* will be used to refer to the phenomenon of an apparent aggregation within the data. Thus, the aim of clustering methods is to produce classifications that represent the clustering.

7.7.1 *k*-means Clustering

A k-means clustering algorithm, producing k classes within a population of size n in N-dimensions seeks to minimise the sum of the means of the Euclidean distances between each point comprising each class, and the centroid $(\bar{x}_j, \bar{y}_j, \ldots \bar{N}_j)$ of that class (mean co-ordinate):

$$\sigma_k = \sum_{j=1}^{k} \sum_{i=1}^{m_j} \sqrt{(x_i - \bar{x}_j)^2 + (y_i - \bar{y}_j)^2 + \ldots + (N_i - \bar{N}_j)^2} \tag{7.22}$$

where $m_j > 0$ is the population of class j, and $\sum_{j=1}^{k} m_j = n$. Solution is achieved by setting a random start set of clusters, and iteratively altering cluster membership until convergence on a local minimum. To check for a global minimum, the process is repeated and the solution with the lowest value of σ_k is selected. There thus exists no strict metric for exclusion from all clusters, as transfer of a datum to membership of the null cluster will *always* reduce σ_k, leading to the extreme case of $\sigma_k = 0$ when all class populations reach unity. As all points must therefore be given membership to a class (and no class can be empty), k-means does not deal effectively with noise or skew, performing best when well-defined and resolved spherically symmetrical clusters of equal population are presented, or when the classification is nominal and for convenience. As such, k-means is termed a *poor classifier*, as resultant classes tend to have similar populations, and poorly resolved clusters may prove problematic for meaningful boundary negotiation between classes.

The principal advantage of k-means is that it is computationally cheap even for large data sets, and when presented with any data will function reproducibly. Anticipated problems of k-means, are non-representative splitting of real clusters between classes, complications in boundary determination due to anomalous population density spikes[(xi)], and the problem of determining k, which is fixed at runtime.

[(xi)] a very small, dense cluster near the boundary between two classes will skew the boundary, potentially randomly as it may cause two close local minima. This cluster may be real data, or an artifact of coding

7.7.2 Density-Based Clustering

Density-Based Spatial Clustering of Applications with Noise (DBSCAN) is a well-cited algorithm which seeks to classify by finding all groups of data wherein each datum lies within a critical distance of a critical number of other data [176]. The remainder which do not classify, are considered meaningless interstices dispersed between real clusters, are classed as noise and discarded. The number of classes to use is determined by the algorithm, introducing a new class each time the algorithm fails to find a new datum in range to include within the current class.

The principal advantage of DBSCAN is that it possesses the capacity to define and exclude noise. It accommodates not only aspherical clustering, but can representatively classify broad and fluid data features, which are elongated, bent, flattened, striated, or branched. As such it can classify well, irrespectively of skews in data. The principal disadvantage of DBSCAN is that only the minimum population required to recognise a cluster and the critical distance are specified at runtime, which can lead to over- or under-characterisation of clusters, overallocation of classes among few clusters, or a class singularity (all data are allocated to a single class). As the processor time of DBSCAN can be considerable for large populations (at time of writing, 6 hours per run on a contemporary desktop for sample manuscript image data) it is unwieldy for a fast, facile in-field analysis as required for these purposes.

7.7.3 Linkage

Linkage-type algorithms are agglomerative hierarchial clustering methods, which begin with as many classes as data points, and agglomerate the points into larger classes according to a chosen metric that optimises the pair-wise agglomerations, usually one based on euclidean distance. The cost-benefit of subsequent agglomerations is tested and the result is a dendrogram, depicting the agglomeration process that produces the most beneficial agglomeration “moves" leading up the class hierarchy from p data points at the bottom to a single data class at the top, according to the chosen metric (which must increase for each agglomeration, and increase the most for the best agglomeration). The challenge is to choose an appropriate metric for the type of data distribution, and to then also find an appropriate cut-off within the hierarchy that produces the most representative classification. The computational demand and thus computation time is much longer than k-means, and this is especially pronounced with >100,000 data points.

7.7.4 Gaussian Mixtures

A Gaussian mixture model (GMM) seeks to express the relative distribution and density of a set of data points, as a sum of orthonormal Gaussian distributions in as many dimensions as the data. A GMM therefore makes the assumption that the distribution is essentially normal in all directions, and further then seeks to guess how many of those distributions exist and in what proportion relative to each other. GMMs share their principal advantages with Gaussian deconvolutions - they are computationally straightforward and differentiate discrete contributions to the form of the data.

A GMM, although in principle capable of distinguishing the presence of multiple clusters, is not a *classifier*. Without any information other than distribution in a space, a GMM is not capable of deciding which unresolved data belong to which cluster.

7.7.5 Support Vector Machines

Support vector machines (SVM) separate data in N dimensions into two portions, by defining a flat plane in N-1 dimensions that lies along a gap in the data. A training set of completely characterised, labelled data is split optimally by the SVM, assuming that a plane exists. Subsequent unlabelled data mapped into the space, is then labelled according to which side of the vector it lies on.

The principal advantage of a SVM is the use of training data to ensure the verity and identity of classes, and data within a given distance of the plane can be excluded. The principal disadvantages are the necessity of using a labelled data set (supervised learning), the assumption that a plane exists and the need to be able to map data accurately into the same space.

7.8 Discussion & Conclusion

We have defined two broad objectives; the spectroscopic analysis of the pigments used in ancient manuscripts, and the development of an imaging system capable of separating portions of a manuscript on merit of spectral behaviour alone.

For the analysis of ancient manuscripts, Raman spectroscopy is the core method of choice; it offers unambiguous, in-situ, non-contact identification of materials, and such capability already exists at Durham. Diffuse reflectance spectroscopy provides complementary spectra, for materials that fluoresce significantly or give poor Raman signal. It is a fast, facile, portable method that lends itself to the use of fibre-optics. It does not require any filter systems, only a white standard and a steady broadband light source whose emissions cover the visible and NIR wavelength range (400-1100 nm).

Both of these methods' data (in the form of the remission function in the case of DRS) can undergo non-negative matrix factorisation to yield useful basis functions. Materials that occur in mixture can be separated spectrally, if they have inhomogeneities that can be detected. This is achieved by acquiring multiple spectra, that capture different compositional cross sections of the material. The 'pure' components can be analysed and interpreted, and compared to real standard spectra, even if they are difficult to obtain in purity.

The projection of data from a camera, into eigen- or colour-spaces, should be a good basis for separating discrete pigments. The subsequent classification by k-means separation or thresholded ratiometrics is the most straightforward option to try, to get camera-based identification methods working. Although thresholding methods in imaging are well-known and automatable, it makes less sense to use ratiometrics to identify pigments, as this puts exquisite importance on a single type of information and it is far more labour intensive to find useful combinations. An example of ratiometrics is determination of green vegetation coverage using the infra-red:red ratio in satellite images, but the thresholding is itself manual.

The utility of support vector machines can only be determined, once the condition of the acquired data is understood. A SVM isn't ideal, because one has no reason to assume that separation planes will exist in the data natively and reproducibly, and any attempts at kernel methods (higher-dimensional weighting of data) are both presumptive and derivative.

Although description of the data by a Gaussian mixture model is possible, its procedural utility is questionable. Even if some clusters in the data fail to resolve, this is going to become apparent anyway once the clustering analysis is complete. The number of clusters in the model is also as presumptive as a k-means separation, so it requires a routine to determine the goodness of fit, so that peaks and

troughs in the goodness of fit as a function of k can be interpreted. This is costly with respect to time and ultimately won't help the determination of the optimal value of k for separation.

Projection into the a*b* plane, is independent of illumination intensity, provided that the camera is responding linearly. In modern cameras there is (and has been for some years) a feature called auto white-balance. This re-scales the values of the red, green and blue channels of an RGB image, to correct their sensitivity so that a white diffuse reflector under the presumed illuminant will appear white. Auto white-balance should be set as close to the D65 illuminant as possible whilst using an illuminant equivalent to the D65. If a different illuminant is used, different auto-white settings are required, and a different XYZ transformation matrix is required also. Analyses to be compared, should be conducted with the same camera on identical settings with identical illuminants.

Regarding PCA, the dimensionality reduction is not only useful because it makes routines for k-means computationally cheaper (which will be increasingly welcome as more images are added in future), but also because it could make many clusters within the data less elongated. The majority of the data in a multispectral image, given that the background on which the pigment is painted is close in behaviour to a diffuse white reflector, will be near the equivalence line $x = y = z = \ldots$. As a result, the first PC (the principal axis of the eigenspace) might lie along or near this line, especially if there are variations in reflected intensity due to deviation from flatness, or there is a near-perfect black absorber within the image also, as with carbon black.

The normalisation of the variables merely changes the overall scale of the data to fit within a minimum-bounding hypercube, without altering the presence or separation of the clusters. Though it removes redundant information, it doesn't effect change on the entropy of the image (as zero-valued bins in the histogram for each image don't count toward entropy) and thus offers neither information nor unwanted interference. PCA will project the largest possible linear contribution to variance from all possible images, into the first PC, which means altogether that regardless of normalisation, in the absence of a perfectly diffuse illuminator, the first PC is most prone to variance that originates from non-ideal illumination geometry. This must be assessed individually as a matter of course, so it is recommended that the analytical procedure should be stepwise and modular.

The caveat of k-means is that it is *ad-hoc*, based on the individual data set on which it is run and does not benefit from training data. As each data set is projected into its eigenspace by PCA, the cluster centroids (and the clusters) might be compared by projection back into the original data space (by *retro-projection*) in which classification performance is expected to be poor. However, the hypothetical absence of an effective standard white and black in a fieldwork setting, means that some data spaces aren't going to be comparable because the magnitude of the pixel values will be scaled according to a variable maximum and minimum. In any case, standard black and white standards don't permit the maximisation of entropy within each image.

All other things being ideal, accumulated dirt and other discolourations will still cause clusters to distort or shift co-ordinates in the data space. It is therefore unlikely that any prototype analysis will be capable of explicit identification, therefore this should not be an immediate goal or priority. Ultimately however, no separation procedure will be capable of classifying pixels based on information that is absent, so separation into clusters by the collected spectral information must be intrinsically good[(xii)] in order to proceed.

In conclusion, one identifies the following basic protocol for imaging[(xiii)]:

[(xii)] Clustering must be clear and present within the data, rather than unresolvable

[(xiii)] Step 4-6 also applies to a cropped RGB image.

1. Illuminate a manuscript with a chosen illuminant covering all possible wavelengths for the filter(s) in use
2. For all filters, have the camera be in a fixed position, maximise contrast by varying exposure time and take a grey-scale photograph that is focussed
3. Stack the images digitally, crop to the region of interest and normalise the values
4. Perform PCA and inspect all scores images, in particular the first PC image which might have illumination artefacts
5. Deduce the optimal value of k for k-means classification
6. Classify

We identify the following basic protocol for spectroscopic investigation of ancient manuscripts:

1. Determine folios of interest ahead of time by consultation with academic staff, to acquire spectra of multiple instances of all colours in manuscript if possible (Prof. Richard Gameson, Department of History, Durham University)
2. Calibrate Raman spectrometer, applying any corrections. Periodically validate calibration, noting any linear shifts or deviations due to non-ideal conditions.
3. For each folio, acquire Raman spectra of all different coloured pigments on folio, and a reference white light spectrum.
4. If time permits, acquire DRS spectra of all different coloured pigments on folio, especially where no useful Raman signal can be obtained.
5. Treat all spectra as appropriate to their condition; reduce the effects of fluorescence backgrounds and interference where possible, apply NNMF to remission spectra.
6. Compare spectra and basis functions to those of standard materials in the literature, or in-house standard spectra where available.

In this way, both Raman and DRS will identify pigments, whilst imaging might provide further information as to their distribution on a folio.

Chapter 8

Experiment & Analysis

Abstract

The preparation of images and pigments is described, as is collection of diffuse reflectance (DRS) spectra and the setup of the camera system. Multi-spectral imaging (MSI) is described, and the pre-treatments of images justified. The overall process of MSI analysis is described, as is that for colour-space segmentation. The experimental details of the Raman spectroscopy is described.

The MSI workup for classification procedures is described in detail, including the theory of silhouettes and entropy as markers of goodness of classification. The results of PCA are presented graphically, and an optimal value of k for k-means classification is derived. Comments are made on clustering. Some Raman and DRS spectra are presented as examples of analysis, and comments on the findings on a manuscript-by-manuscript basis. The problems of red lead contamination are made clear using a modern sample, and the non-negative matrix factorisation (NNMF) basis functions of an analysis of red lead are presented.

The clustering in spaces is compared and contrasted, and the utility of the determination of an optimal value of k is evaluated. Density appraisal is addressed, and the effect of the number of channels in an MSI image is treated with respect to the geometry of the original feature space. Near infra-red (NIR) imaging and ratiometrics for finding copper pigments are briefly addressed, and the straightforward contrast provided through PCA is shown in false colour imaging.

Raman meta-analysis is performed through connectivity graphs, demonstrating the effect of information redundancy. Overall the Insular palette includes red lead with massicot impurities, orpiment, vergaut, copper green, indigo, orcein, and iron gall ink. The post-1066 pigments transition sharply to copper green, lapis lazuli, vermilion, red ochre, white lead and pure red lead. It is concluded that the availability of technology and resources after the Norman invasion changes the face of manuscript creation. Also, although Raman analysis is laborious and specialist, imaging techniques and DRS are complementary rather than the sole future of the field.

—

8.1 Introduction

Chapter 1 addressed the history, practical and theoretical considerations of imaging and spectroscopic systems. In this chapter the experimental conditions and the results are described, and the data analysed. Analysis primarily takes the form of qualitative determination of pigment materials.

Identifier	Cornelissen	Kremer	Aldrich	Made in Durham
Azurite	2003-1c	10200, 102005		
Malachite	2013-1c	10300, 103601		✓
Verdigris	2009-1c			✓
Lazurite	2000-1c, 2012-1c	10510		
Orpiment	2010-1c			
Realgar	2011-1c			
Indigo			229296	
Orcein			O7380	
Tyrian Purple				✓
Red Lead	1205-1c			
White Lead	1800-4h			
Vermilion	1218-1d			
Litharge	1114-3f			
Red Ochre	1606-3f			
Mars Red	1602-3f			
Yellow Ochre	1607-1c			

Table 8.1: Pigment Standard Suppliers: Pigments and their suppliers as used. Cornelissen refers to L. Cornelissen & Son, 105A Great Russell St, London WC1B. Kremer refers to Kremer Pigmente GmbH & Co. KG. The alphanumeric entries in the table are product codes; a tick in the last column indicates that this pigment has been synthesised at Durham (§8.2.1).

8.2 Experimental

8.2.1 Pigments, & Preparation of Test Images

Standard pigments have been acquired from sources as shown in Table 8.1. Some pigments indicated in Table 8.1 were synthesised at Durham, using the following protocols:

Malachite 0.1 M aqueous copper sulfate was prepared from the pentahydrate in distilled water. 25 ml of an aqueous solution of 0.1 M sodium hydrogen carbonate, made to pH 8 with concentrated sodium hydroxide, was added dropwise to 50 ml of the copper sulfate, with stirring. The clouded solution was filtered under suction, washed with three lots of 10 ml deionised water and one 10 ml acetone, allowed to dry under suction and stand overnight. The dry green-blue solid is hence referred to as *synthetic malachite*.

Verdigris Copper sulfate pentahydrate (3.32 g 0.013 mol) was dissolved in 30 ml deionised water, and added to a solution of sodium hydroxide (1.06 g 0.026 mol) in 30 ml deionised water. The resultant precipitate was filtered off under suction and rinsed three times with 10 ml deionised water. The gelatinous blue solid was immediately ground to an homogenous paste with 1.70 g anhydrous copper carbonate in a pestle and mortar and allowed to dry overnight. The dried concreted mass was ground roughly. The dry blue-green solid is hence referred to as *synthetic verdigris*.

Tyrian Purple Tyrian purple was prepared in-situ according to the scheme in figure 8.1. A spatula-tip of **TP1** was dissolved in three drops of deionised water, and a drop of concentrated sodium hydroxide solution. The solution was agitated in an agate pestle and mortar until a deep purple suspension was produced. This solution was mixed directly with gum arabic solution for use as an ink, and was

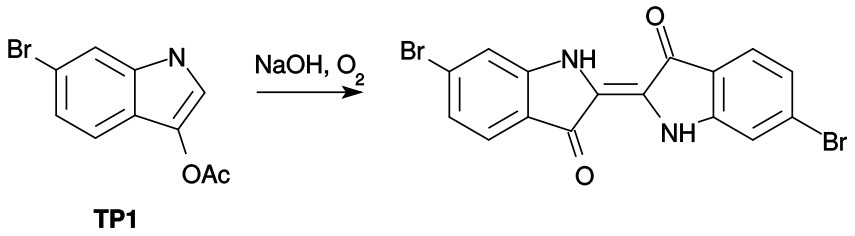

TP1

Figure 8.1: Synthesis of Tyrian purple from precursor: Synthesis of Tyrian purple from precursor **TP1**. **TP1** (6-bromoindoxyl acetate) was synthesised by Dr J. Sellars from Durham. It was kept in a freezer, and used as-provided at need.

ultimately close to pH 7 when used. Tyrian purple solid was provided by Dr J. Sellars for diffuse reflectance measurements.

Unless stated otherwise, pigments were used as-received. **Azurite** (Cornelissen & Son) and **malachite** (Cornelissen & Son) were manually relieved of large impurities, ground in a pestle and mortar, and levigated (separated into particle size fractions by washing the grind and decanting the cloudy supernatant) to produce coarse, dark powders before use.

Paint-making Paints of each pigment were prepared separately in an agate pestle and mortar, by grinding of <1 g of pigment with <5 drops of gum arabic solution (Winsor & Newton) to achieve a smooth, homogenous fluid. In the case of tyrian purple, the solid pigment was not used directly; the pigment was generated by condensation of the precursor monomer (6-bromoindoxyl acetate) in-situ using catalytic sodium hydroxide and aerial oxidation, followed by addition of gum arabic to the concentrated solution. Some orcein paint was made basic with a drop of saturated potassium carbonate solution. Insular imagery was traced onto 120 gsm paper, painted in with pigment paint and allowed to dry. Both were protected by laminating with 90 μm thick laminating wallets. The resultant artwork is shown in figure 8.2.

8.2.2 Diffuse Reflectance

Diffuse reflectance measurements were undertaken on pigment powder sample materials by oblique illumination of the sample, and collection of light orthogonally to the surface with a fibre-optic setup. Illumination was provided by a steady-output W-halogen lamp. An OceanOptics Maya2000Pro fibre-optic USB spectrometer was used to analyse the collected light. The standard spectrum of the illumi-

Figure 8.2: Original Test Artwork: Left: Image *lion*. Showing use of *carbon* (black), *orpiment* (yellow), *verdigris* (green), *basic orcein* (blue-violet) and *tyrian purple* (purple). Right: Image *bird*, showing also the use of (right) *carbon* (black), *orpiment* (yellow), *verdigris* (green), *orcein* (purple) and *red lead* (orange).

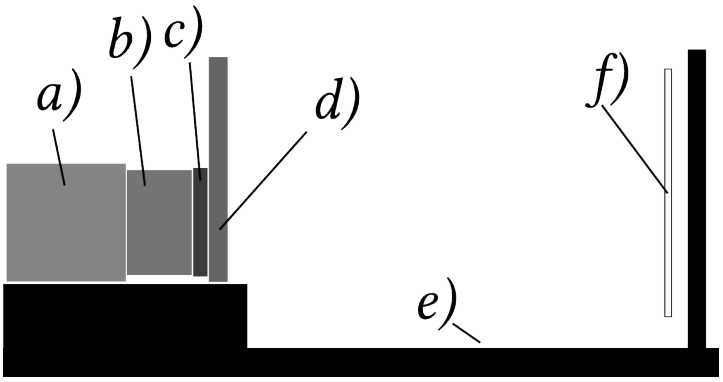

Figure 8.3: Diagram of the camera setup: *a)* camera module, *b)* aperture & focusing unit, *c)* rubber seal, *d)* filter wheel, *e)* steel block, *f)* sample.

nant was obtained from a clean Teflon substrate. The experimental reflectance is given by:

$$R(\lambda) = \frac{(I_a(\lambda) - d(\lambda))}{(I_0(\lambda) - d(\lambda))} \tag{8.1}$$

where $I(\lambda)$ is an unprocessed diffusely reflected light intensity profile, $d(\lambda)$ is accumulated electrical noise in $I(\lambda)$ unrelated to the real signal, $_{0,a}$ is signal from a reflectance standard and from the analyte/sample respectively. This information can be meaningfully interpreted in a manner analogous to absorbance, using the remission function (equation 7.8).

As the wavelength-dependent reflective contrast of a material is how it is later to be theoretically identified by imaging (rather than evaluating absolute reflectance), comparison of normalised profiles is therefore of greater import:

$$S(\lambda)_{norm} = \frac{S(\lambda)}{S(\lambda)_{max}} \tag{8.2}$$

where $S(\lambda)$ is the signal to be normalised, and the subscript $_{max}$ indicates the maximum signal within $S(\lambda)$. This treatment scales all signal maxima to unity.

8.2.3 Multi-Spectral Imaging

An Edmund Optics high dynamic range monochrome USB CCD camera was fitted to a focusing lens and aperture. The camera was attached via screws to a steel block mounted to an optical breadboard, and a 5-position filter-wheel was likewise attached. A rubber guard was affixed between the filter wheel and camera lens to block stray light. The filter positions were filled with nominally 20 nm FWHM interference filters with nominal centre wavelengths at 450, 500, 550, 600 and 850 nm - the transmission spectra are shown in figure 8.4. A diagram of the setup is presented in figure 8.3.

In this way it was possible to alter the observed spectral band without moving the camera or altering the scene. Illumination was provided by daylight. The test images from Section 8.2.1 were mounted on a firm backing wall as in Figure 8.3. For each filter, the camera lens and aperture were adjusted for focus and maximum contrast, and a 1280 × 1024 (1.3 Mp) bitmap image was captured.

Image Pre-Treatment

For code, refer to supplementary information.

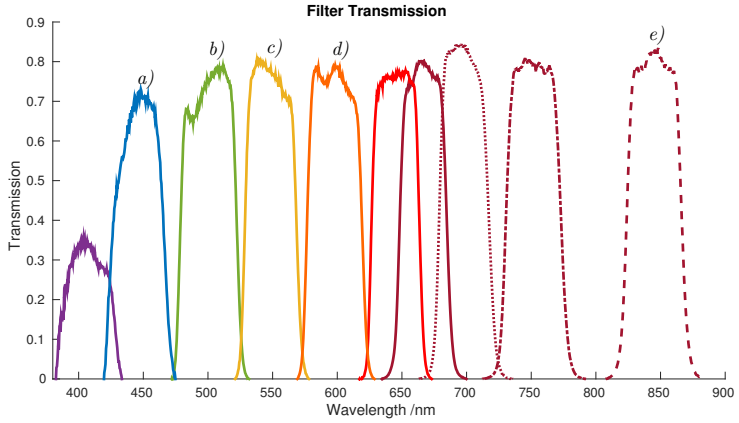

Figure 8.4: Transmission of Camera Filters: Transmission spectra of available filters for use in the camera. Spectra acquired by Emileigh Clifford MChem, and reproduced with permission. The filters used in the 5-filter setup are labelled *a)* 450 nm *b)* 500 nm *c)* 550 nm *d)* 600 nm *e)* 850 nm

Bitmap images were loaded into MATLAB® 2014a and partly cropped to exclude most of the peripheries, before multi-modally contrast registering and finally cropping to the desired region. Multi-modal registration accommodates for differing magnitude and direction of greyscale contrast. Images were first registered by translation to approximately align all features, then affine-registered (permitting translation, rotation, scaling and shear operations) to account for minor distortions of images. The accuracy of registration was checked, by superimposing the images. The effect of registration can be seen in figures 8.5 and 8.6.

The images were converted to a 3D matrix of single-precision numbers, and the matrix reshaped to 2D so that each column represented an image, and each row to a pixel. The images were standardised by scaling each column to values between 0 and 1, and optionally decorrelation-stretched.

The *decorrelation stretch* is a process described by MATLAB® as doing the following:

1. Removes a mean from each band.
2. Normalizes each band by its standard deviation (correlation-based method only).
3. Rotates the bands into the eigenspace of the correlation or covariance matrix
4. Applies a stretch in the eigenspace, leaving the image decorrelated and normalized in the eigenspace.
5. Rotates back to the original band-space, where the bands remain decorrelated and normalized
6. Rescales each band according to σ
7. Restores a mean in each band.

In broader terms, we perform PCA on the original data (*vide infra*), stretch the scores matrix, then multiply by the loadings matrix to restore the data back to its space. The resultant transformed data is already partly (if not wholly) orthogonalised within its space, and so the resultant PCA can be expected to be less effective overall by the metric of σ^2.

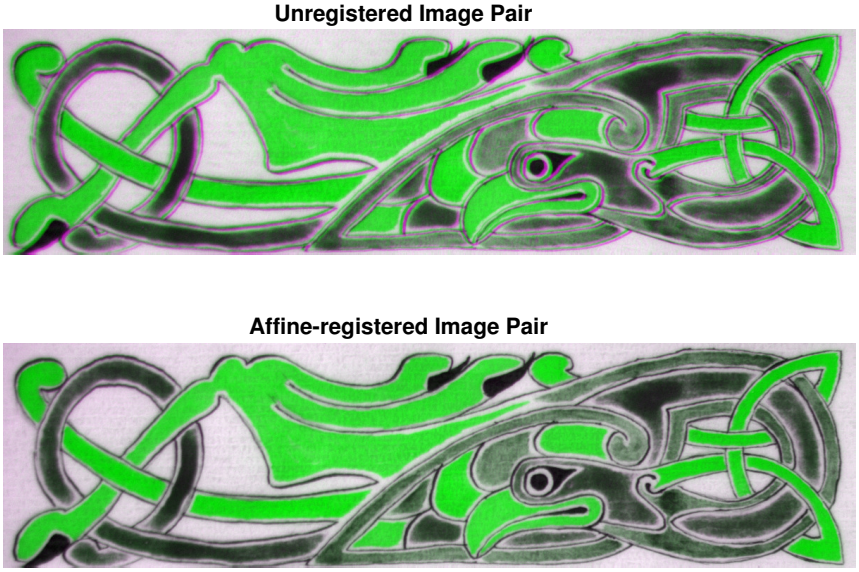

Figure 8.5: Spatial Effect of Image Registration: The spatial effect of image registration, is to align between two images, features that produce contrast within their own image. The haloes of pink in the top superimposed image, make the misregistration evident, which has been fixed in the bottom image.

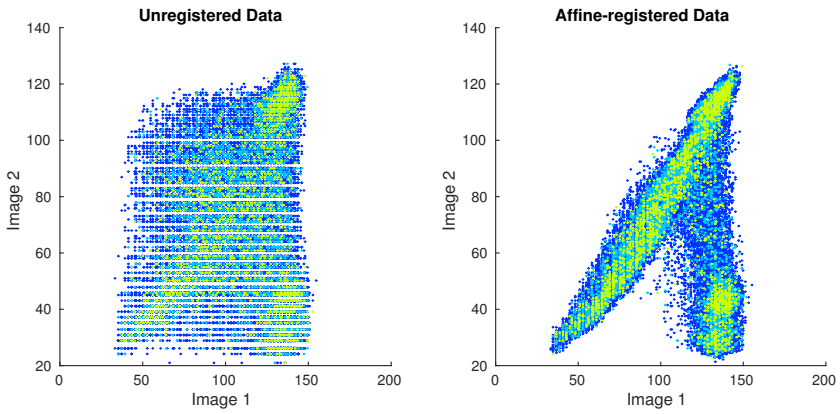

Figure 8.6: Value Effect of Image Registration: Digital image registration proceeds by changing the values of pixels according to an interpolation scheme in the spatial domain (see figure 8.5 for the corresponding images). As a direct result, image data that undergoes registration is shifted in the data spaces shown, and can take non-integer values. In this instance, as *image 1* is a reference image, it remains unchanged. In practical terms, overall the distribution of the data becomes less diffuse and more localised. Aggregations of cyan and green data points indicate regions of ever more densely packed data.

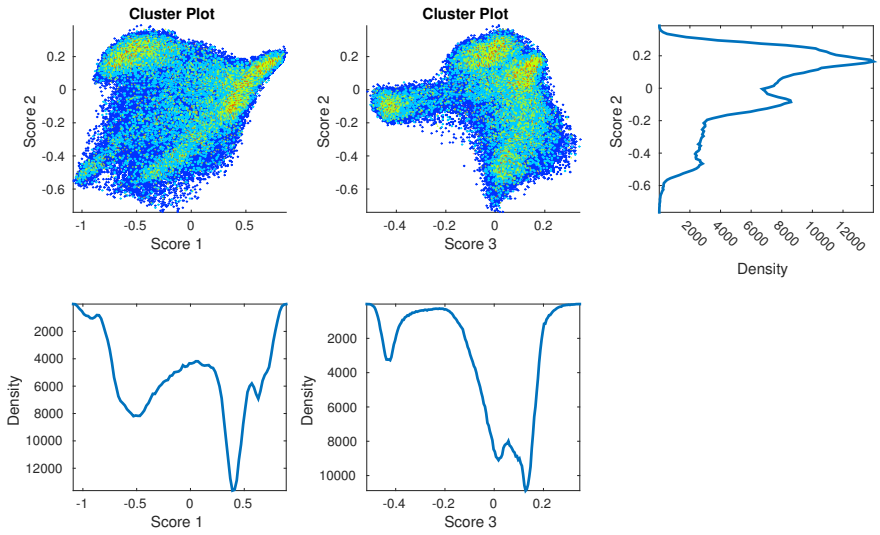

Figure 8.7: Plots of PCA Scores: The plots of PCA scores for the standard *lion*, demonstrate clustering both in the scatter plots and density traces. The corresponding data showing contrast in the spatial domain, are shown in figure 8.8. The traces and their scales are aligned as to correspond to the axes of the scatter plots in their row and/or column. Increasing density on the scatter plots, are indicated by aggregation of different colours: blue < cyan < green < orange.

PCA & *k*-means Clustering

The data matrix for Principal Components Analysis (PCA) was constructed from the pre-treated images, to give a tall thin matrix. The MATLAB® command `pca` performed PCA on the data matrix.

The scores matrix was reshaped to give a stack of 5 scores images of dimensions equal to the input images. The contrast between these images was appraised in a manner similar to the registration appraisal, as well as using plots to show the distribution of the values in each score. This is shown in figure 8.8 and 8.7, respectively.

The first three scores were used for *k*-means clustering analysis via `kmeans`, where the argument k is the number of probable discrete clusters. This produces a matrix `IDX`; a matrix of integers of dimensions $[m \times 1]$, indicating the numeric label of the cluster to which each sample pixel belongs. `reshape` reshapes `IDX` to the dimensions of the cropped images, and `mat2gray` then makes the image suitable for a greyscale display.

Cluster data for selected scores are separated into spectral behaviour cluster maps using logical operators on the reshaped `IDX` to generate logic matrices identifying the pixels in each cluster separately. The binary logic may then be displayed using custom colour-mapping.

Colour-space Segmentation

RGB colour images were acquired using a 5 Mp colour CCD camera on an Android smartphone. The resultant imported $[m \times n \times 3]$ matrix for each image was directly converted from the RGB to L*a*b* co-ordinate system using the `makecform` and `applycform` commands. The *k*-means protocol above was used to classify the image using the a* and b* components in place of PCA scores.

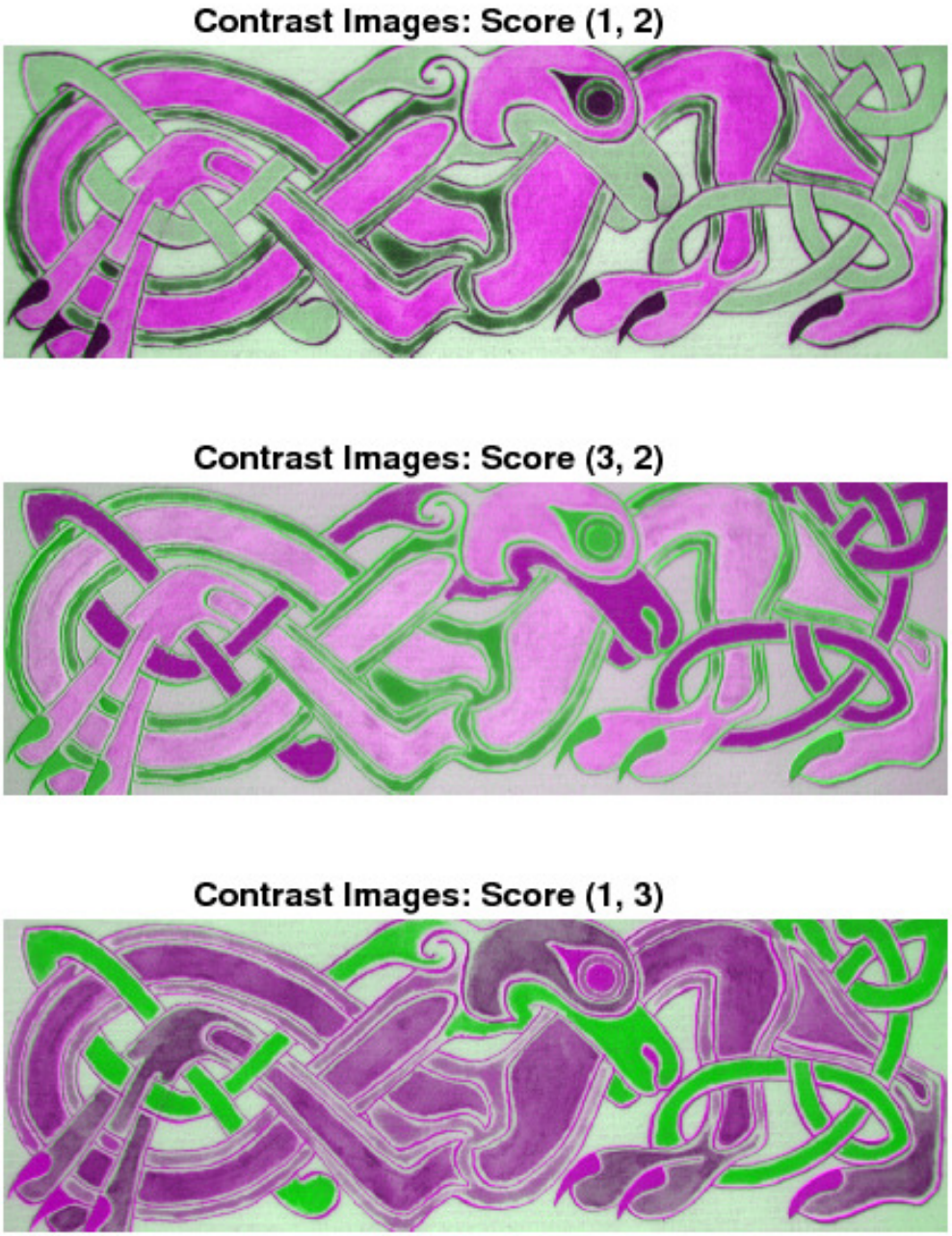

Figure 8.8: PCA Scores Contrast Images: The contrast between PCA scores for the standard image *lion*, are shown here in the spatial domain, by superimposition of individual reshaped scores vectors converted to the unsigned 8-bit data type. The first score of the pair provides green values, whilst the second provides magenta. The key quality in an ideal pair is vivid contrast between many pigments; similar colours will struggle to separate. In this set of enlarged images, the retention of image detail is easy to see, as are some very minor registration haloes.

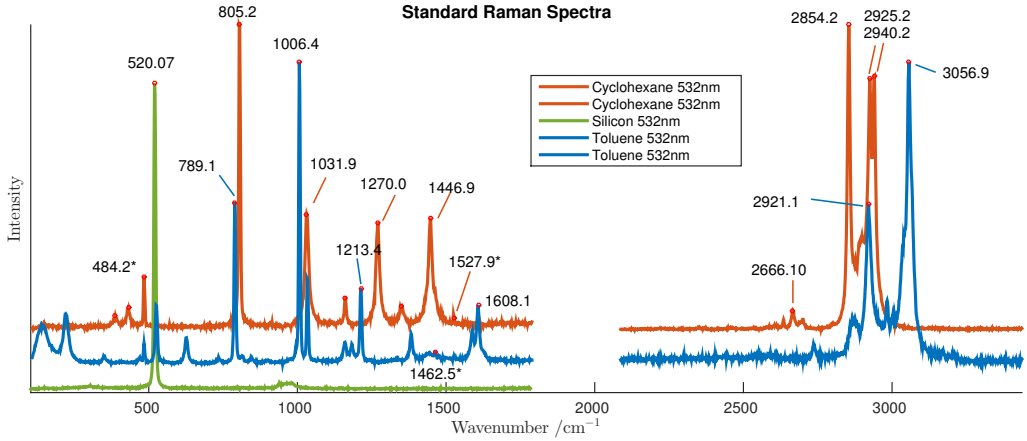

Figure 8.9: Standard Raman Spectra for Calibration: Standard spectra used for calibration of the instrument and wavenumber correction of sample spectra. Spectra given are for 532 nm laser line only. An asterisk (*) indicates an atomic emission line of mercury, that had been directed into the instrument.

Mercury Line /nm	He-Ne / cm^{-1}	Nd:YAG / cm^{-1}	Diode / cm^{-1}
546.0753		484.5	
567.5922		1178.7	
576.9598		1464.8	
579.0663		1527.8	
671.6429	888.7	3908.1	
690.7461	1300.5	4319.9	

Table 8.2: Emission lines of mercury: Emission lines of mercury, converted to Raman Stokes shift relative to the laser lines used in this study [32].

8.2.4 Raman Analysis

Raman spectra were collected using a Horiba JY LabRAM HR, equipped with a 632.81 nm He-Ne laser, a frequency-doubled Nd:YAG laser outputting at 532.0 nm, and a 785 nm NIR diode laser. The detector was a Peltier-cooled CCD array, and the gratings were 600 and 1800 grooves/mm. Samples were arranged either on a joystick-controlled xy-translation stage, or a manually-controlled translation stage constructed at Durham for supporting books. The objective lens was 50x magnification with numerical aperture 0.55. The microscope attachment provided z-control.

Standard Raman spectra for calibration checks were principally the 520.07 cm^{-1} band from crystalline silicon, though the mercury lines from fluorescent lighting were accepted (Figure 8.2), as were the spectra of cyclohexane and toluene (Figure 8.9).

The wavenumber calibration of the Raman spectrometer was carried out by Horiba technicians during the instalment of the instrument at Palace Green Library, and the instrument was confirmed as being “within specification". The validation of the Raman spectrometer was carried out by comparison of standard calibration spectra. Where the difference was <5 cm^{-1}, the x-axes of Raman spectra were linearly shifted in wavenumber, according to the difference required to set the peaks of a standard spectrum to their proper position. Where useful to the analysis (limited by background spectrum availability), spectra were divided element-wise by a background spectrum, to yield a new spectrum free of interference effects. Spectra received no further treatment save for shifting and scaling along

the y-axis for clarity.

8.3 Results & Analysis

The spectra this section is based upon, have been presented in their entirety in the supplementary information. The data have been summarised in table 8.3, on page 214.

8.3.1 Diffuse Reflectance Spectroscopy

The objective of DRS was two-fold; to assess the likelihood of being able to separate out a set of pigments given a set of filters, and to identify pigments as they are found. The pigments of three palettes are shown in Figure 8.10; an Insular palette, a general Norman palette, and the spectra for a series of pigmented semiconductor chalcogenides with closely-placed bandgaps.

Regarding Multi-Spectral Imaging

Based on the varied spectral features in Figure 8.10(top) on page 177, the placement of the five interference filters used for multispectral imaging (450, 550, 600, 650, 850 nm) might distinguish between all pigments shown. The potential exceptions if any, being tyrian purple & orcein, and carbon (not shown) & lead white. The justification for this being that the pattern of changes in the integrated F(R) at each observation band is not significantly different - i.e. the spectral form of each pigment pair is very similar when observed only by those wavelengths.

From the spectra in Figure 8.10(middle), it is hypothesised that it will be almost impossible to reliably distinguish red lead, red ochre and vermilion from one another, and also orpiment from yellow ochre. This is further explored in Figure 8.10(bottom); there are three distinct groups of pigments, where the differentiating factors in the spectra lie so closely together, that a series of narrow, yet overlapping observation bands may be required to generate enough uncorrelated variance to separate them successfully.

8.3.2 Multispectral Imaging, PCA & k-means

The PCA scores images of the regular and decorrelated images, are shown in contrast-pairs in figures 8.12 and 8.12, and their corresponding scores plots are shown in figures 8.13 and 8.14.

k-means

For a given k with data set $\mathbf{x}$, containing m data in n dimensions, the objective of k-means is to split m data into k discrete classes $\{c_1, c_i, \ \ldots \ , c_k\} \subset \mathbf{x}$. The function

$$\chi = \sum_{i=1}^{k} \sum_{c_i \subset \mathbf{x}} f(c_i, \mu_i) \tag{8.3}$$

uses the distance function $f(c_i, \mu_i)$ to assign each datum within the ith class c_i, a distance to the mean co-ordinate μ_i of that class. This function is usually the euclidean squared distance. This function is summed over all members of each class, and all classes summed to give χ. When exchange of data between classes causes negligible change in χ, a solution is found.

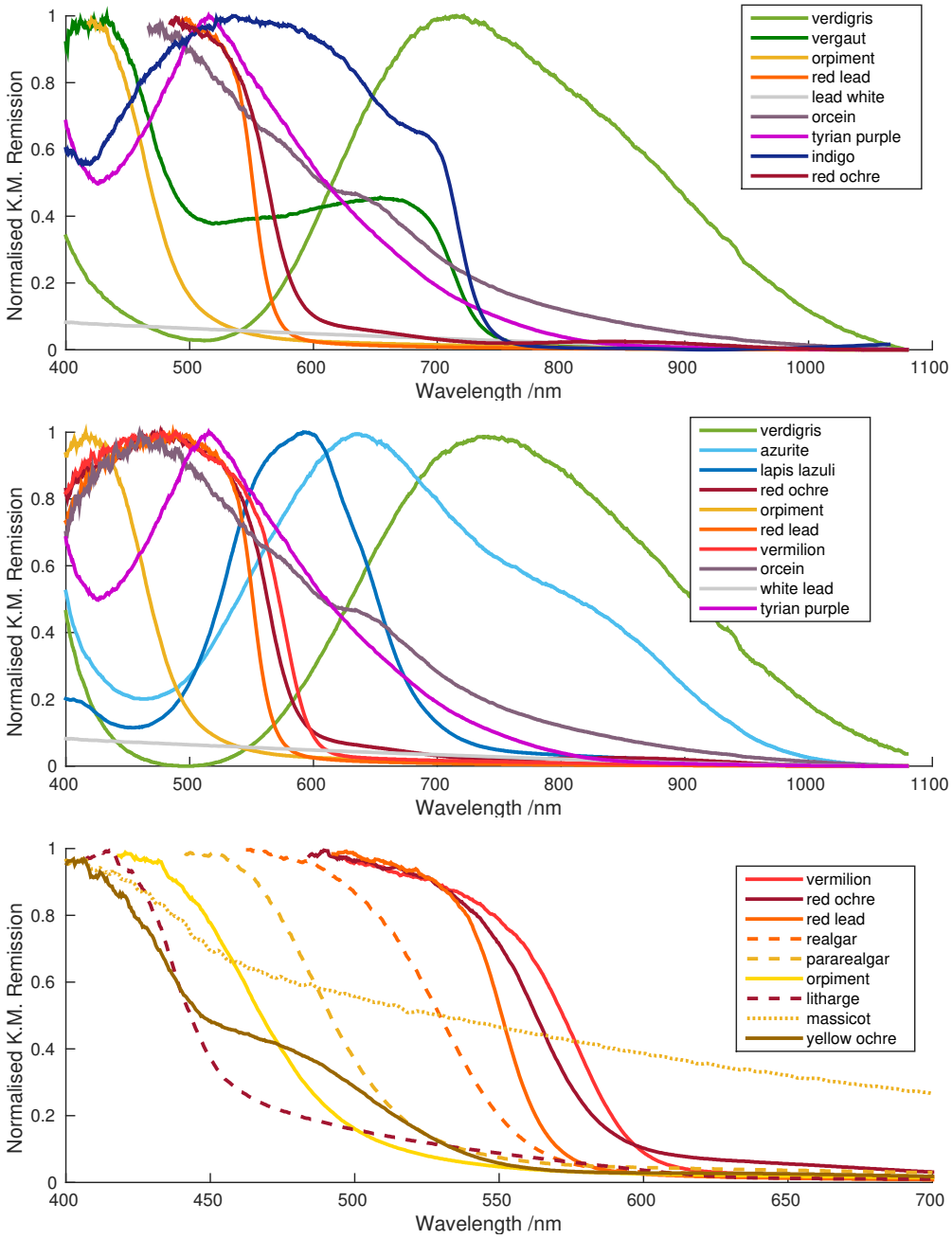

Figure 8.10: Palettes: F(R) of some representative palettes of pigments, in powdered form. This illustrates the variety and similarity of some spectral forms. These are described here as Top: Northumbrian Insular, Middle: Norman and Bottom: chalcogenides of arsenic, iron, lead and mercury. The typical colourants in the Northumbrian Insular palette possess largely distinguishable spectral forms across the visible and NIR spectrum (NB: normalisation of the lead white spectrum greatly exaggerates its slight deviation from spectral flatness, so it is re-scaled here). The palette *(b)* has a more even distribution of spectral features that allow a more arbitrary choice of filters, but the cluster of band-gap features for *red lead*, *red ochre* and *vermilion* would be more efficiently distinguished by a 570 nm filter. The chalcogenides of mercury, arsenic, lead, and iron in *(c)* show semiconductor band-gaps, and as in the *Norman* spectrum, to distinguish efficiently between a selection of these demands a series of filters chosen expressly for this purpose.

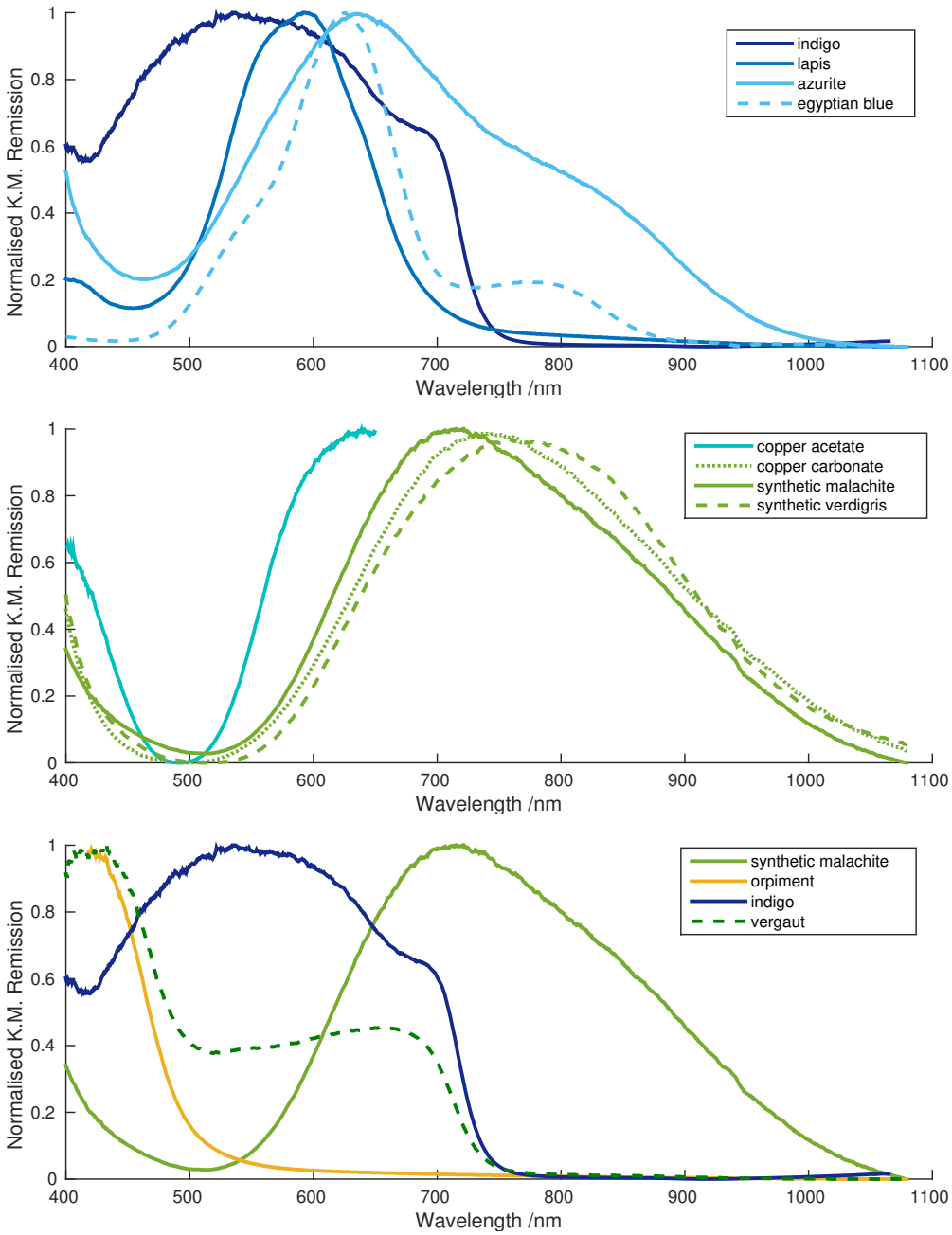

Figure 8.11: Spectral distinction between pigments of the same colour: F(R) of some groups of pigments with the same type of colour, in powdered form. This illustrates the variety and similarity of some spectral forms. These are described as Top: Blue Pigments, Middle: Copper Greens, Bottom: Vergaut vs. a Copper Green. The blue pigments all possess spectra that are distinguishable from one another using only one or two filters, though by contrast spectra of green copper compounds demonstrate that copper greens might be less straightforward to distinguish from one another. The main other type of green encountered, is a mixture of orpiment and indigo, named *vergaut*, the spectrum of which shows the spectral features of both parent compounds, and is straightforwardly distinguishable from a copper green using only a NIR filter.

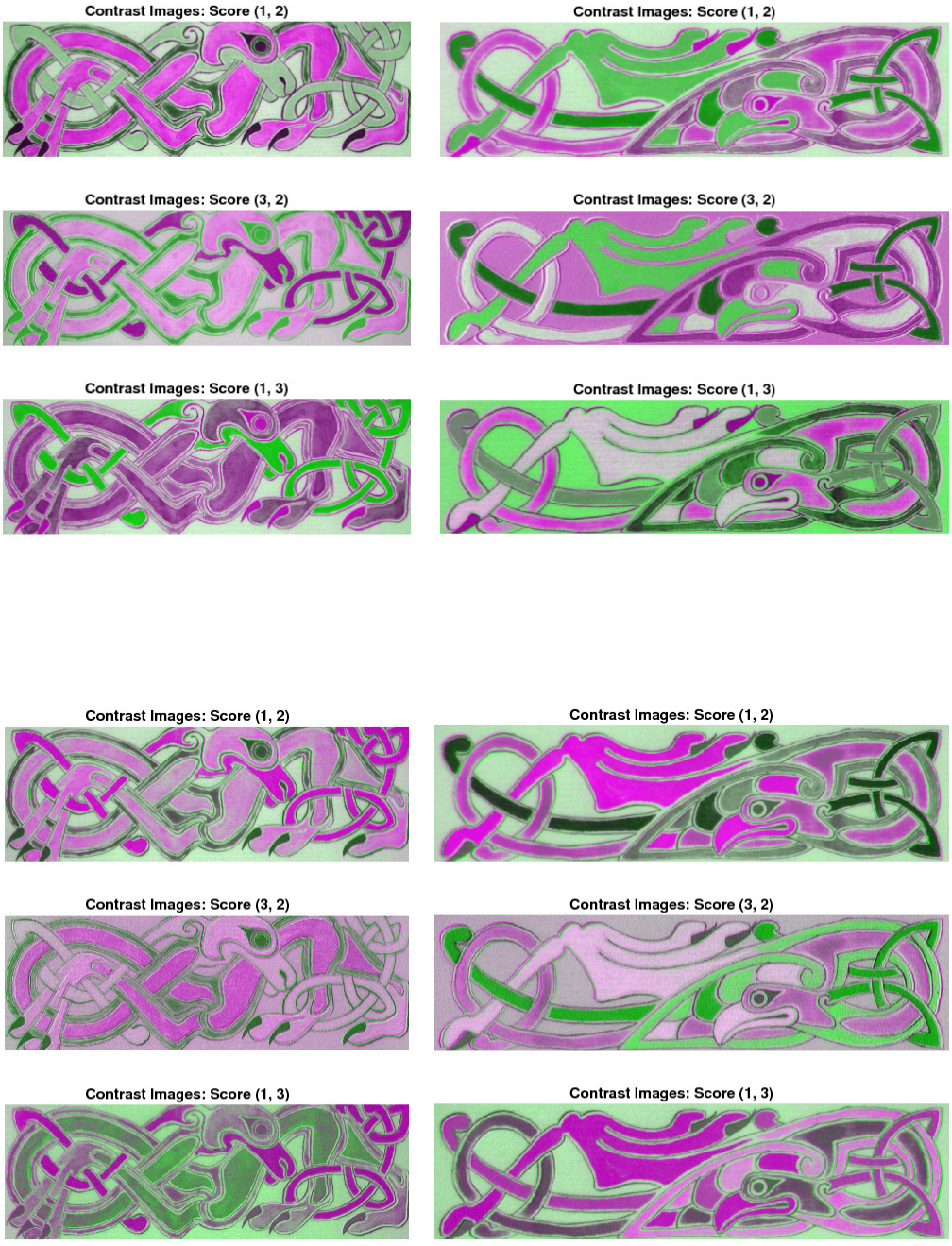

Figure 8.12: Lion & Bird: Contrast Images: Scores image pairs are shown in green-magenta contrast by allowing the first image of the pair to contribute magenta and the second, green. Top: Scores image pairs for raw data. Bottom: Scores image pairs for decorrelated data. The key quality in an ideal pair is vivid contrast; similar colours will struggle to separate.

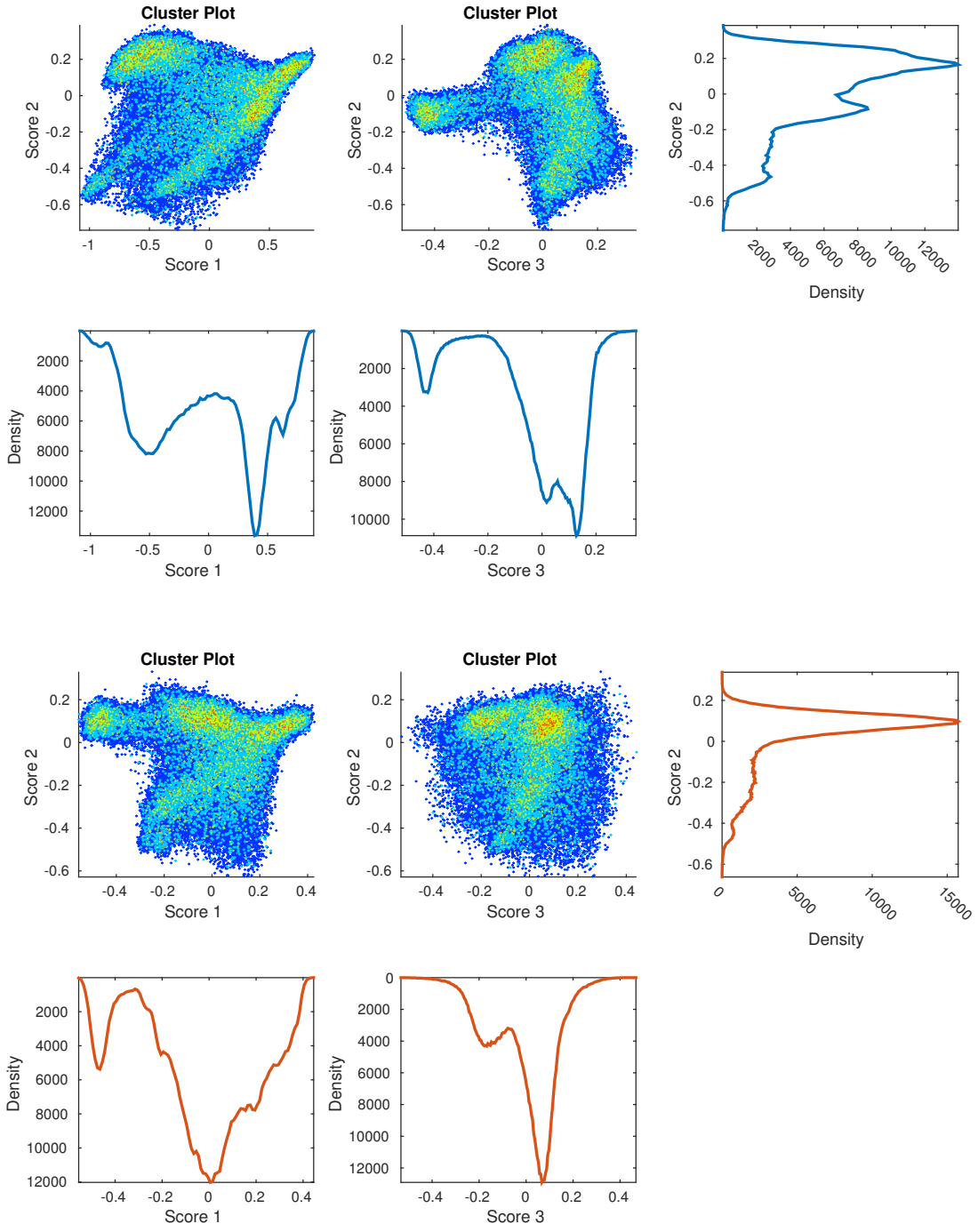

Figure 8.13: Lion: Scores Density Plots: PCA scores density plots for standard image *lion*. Top Set (Blue Traces): Non-decorrelated data. Bottom Set (Red Traces): Decorrelated data.

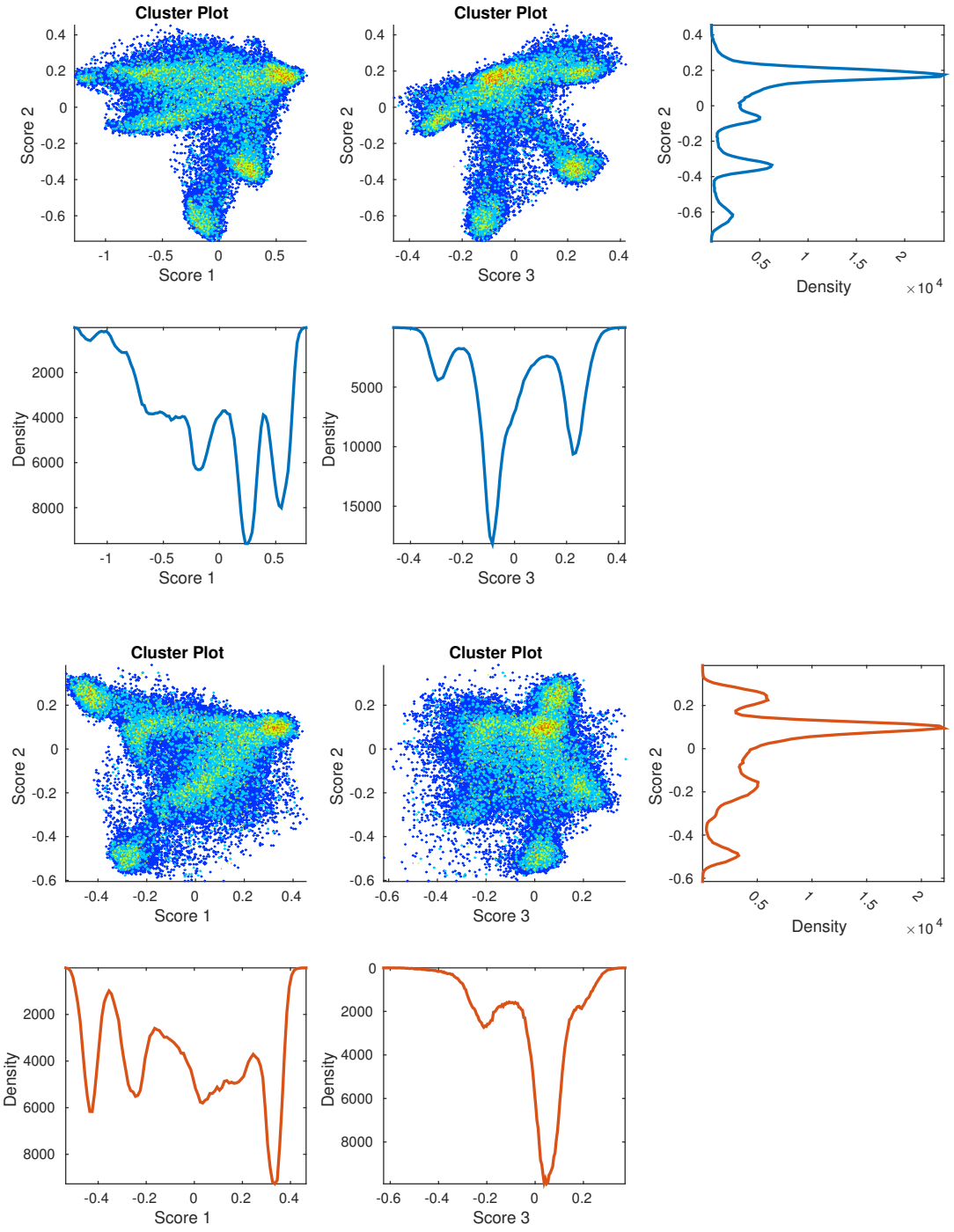

Figure 8.14: Bird: Scores Density Plots: PCA scores density plots for standard image *bird*. Top Set (Blue Traces): Non-decorrelated data. Bottom Set (Red Traces): Decorrelated data.

As the division into subsets is judged on χ alone, the membership boundaries are necessarily linear within the space, and not all memberships will be ideal or representative. The sum-of-distances method does not itself assess the fitness of its individual classes, nor does it normalise χ.

Silhouettes

Optimal classes are populated exclusively by data *which is less suited to a neighbouring class than the current class.* The best value of k therefore, is the one which gives the best classification according to this metric, and will be denoted $\hat{k}$. As above, for a given value of k, k-means provides the least-bad classification by sum-of-distances. Over a set of values of k, we assess the fitness of each least-bad classification using the silhouette function S of each datum, in order to objectively determine $\hat{k}$.

For the jth datum, let $a(j)$ be the dissimilarity of j to its own class, generally equivalent to $f(j, \mu_i)$. The dissimilarity of j to its nearest neighbour class shall be $b(j)$. Let the silhouette $S(j)$:

$$S(j) = \begin{cases} 1 - a(j)/b(j) & | \quad a(j) < b(j) \\ 0 & | \quad a(j) = b(j) \\ b(j)/a(j) - 1 & | \quad a(j) > b(j) \end{cases} \tag{8.4}$$

such that it is normalised to the range $-1 < S(j) < 1$. For $S(j) < 0$, j may be better in the neighbouring class, whilst $S(j) \to 1$ indicates that j is close to μ_i.

Both the average value $\bar{S}(j)$, and the proportion of positive values Q, explicitly indicate the *goodness* of a classification rather than its *badness*; the normalisation of its value to a meaningful range makes $S(j)$ a less arbitrary metric than χ.

Entropy

Entropy is a measure of the information content of an array of numbers. For an array of continuous real numbers binned into F value ranges of fixed width and normalised to an integral of unity, the proportion of members in the ith bin is the probability p_i of finding a number in the range represented by that bin. Excluding all zero-member bins to give a number of filled bins G, the entropy of the array is then:

$$H = -\sum_{i=1}^{G} p_i \log p_i \tag{8.5}$$

where $H_{max} = \log(G)$ is the maximum entropy of repetition, and $H' = H/H_{max}$ is a standardised entropy.

Entropy is notably used to measure and optimise the information content of greyscale images, and as a goodness-of-fit metric when applied to the residual of a curve-fitting procedure. In both cases the highest possible entropy is optimal. In images, $H \approx H_{max}$ signifies an even distribution of greyscale values across the image, such that the significance of each pixel is nearly maximised and approximately equal to all others. A χ-square residual of maximised entropy has the most even distribution of values, and represents pure noise. Low entropy signifies that the distribution of values is uneven, and if data fits into a single bin, $H = 0$.

The indices produced by a k-means separation to label the data according to class, are randomised on each repeat *even if the resultant grouping into subsets of data points is otherwise identical.* This is an artefact of the random placement of starting centroids. As a result, for a classification of m data into

k classes, repeated n times, we find that each original datum is represented as an array of n integers with k^n possible unique combinations. The pigeonhole theorem however, limits this number to a maximum m. If each n-integer combination can be represented as a unique integer in the range 1-m, the standardised entropy of the resultant $m \times 1$ matrix is then inversely proportional to the reproducibility of the separation on a scale of 0-1, and is termed the *entropy of repetition*, H_R. By contrast, H_S is the entropy of the silhouette function itself.

Ab-initio deduction of $\hat{k}$

Classification of a hyperspectral image cannot progress with an arbitrary number of classes, when the number of clusters is an unknown quantity. The number of clusters and the optimal number of classes are deduced using three separate methods:

1. **Evaluation of Histograms.** Scores plots with density traces, give a visual indication of the presence of clustering. Traces reduce ambiguity in the case of poorly resolved clusters, whilst the plot itself is used to manually count.

2. **Silhouette Values & Entropy.** Over a range of values of k, the k-means classification is performed on a randomised subset of the data; the entire process is repeated a number of times with a new subset for each repeat. The calculated mean silhouette and entropies of the result are tabulated.

3. **Standard Deviations.** For an indicative peak, the corresponding relative standard deviation for silhouette, iteration time and entropy should ideally be low compared to its neighbouring values.

We deduce from figures 8.15 and 8.16, that the evaluation of $\bar{S}$ and H_S is more useful than H_R, as H_R possesses no distinct features save for its general curve. Nevertheless, we define an adjusted silhouette $\dot{S}(k)$ to give some indication as to the magnitude of each of the following terms:

$$\begin{aligned} \zeta(k) &= \frac{\bar{S}(k) - \sigma_S(k)}{\bar{H}_S(k)} \\ \dot{S}(k) &= \frac{\zeta(k)}{\zeta_{max}(k)} \end{aligned} \tag{8.6}$$

where $\bar{S}(k)$ is the mean silhouette, $\sigma_S(k)$ is the standard deviation of the mean silhouette, and $\bar{H}_S(k)$ is the mean entropy of the silhouette. This simply gives more importance to values of k that yield silhouettes that are consistently high both between and within k-means separations.

Classification

The classifications of the test images according to $\hat{k}$ are shown in figures 8.17 and 8.18.

Lion For the first image in figure 8.17, the silhouette plot demonstrates that of class 1 and 4, neither show ideal pure behaviours (they are slanted) and both contain improperly classified data points (negative values of S). The class plot shows that these clusters are adjacent, and class 5 is bimodal. We see from the map and foreknowledge of the composition of the image, that classes 1 and 4 encompass

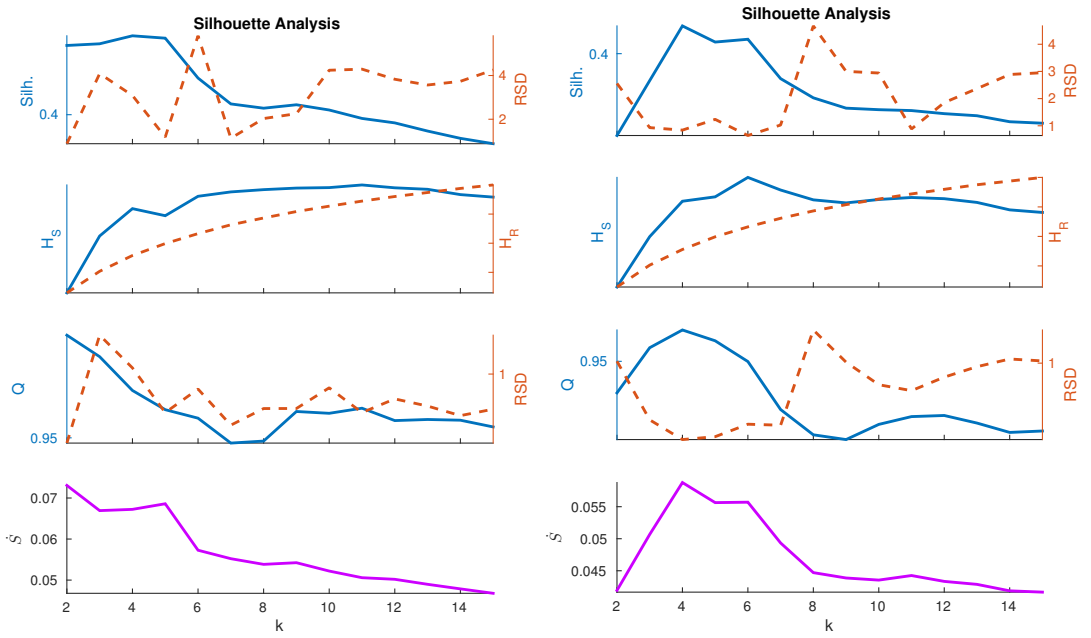

Figure 8.15: Analytics for Lion Test Image: Left: Statistics for non-decorrelated data as a function of k. Right: Statistics for decorrelated data as a function of k. Profiles indicate $\hat{k} = 5$ and $\hat{k} = \{4, 6\}$, respectively

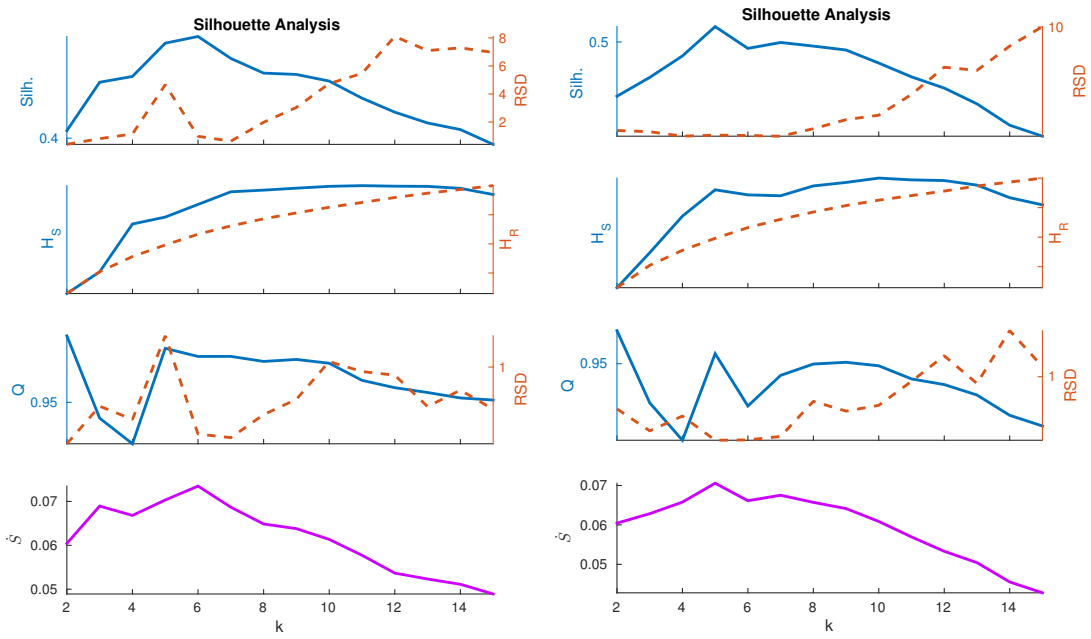

Figure 8.16: Analytics for Bird Test Image: Left: Statistics for non-decorrelated data as a function of k. Right: Statistics for decorrelated data as a function of k. Profiles indicate $\hat{k} = 6$ and $\hat{k} = \{5, 7\}$, respectively.

carbon and verdigris between them, and class 5 encompasses tyrian purple and orcein. Class 1 is properly carbon, though it extends into class 4 which is verdigris.

The decorrelated scores split into 4 classes, are largely well-classified. Carbon has not separated from verdigris in class 4, whilst tyrian purple and orcein are in class 1. The decorrelated scores split into 6 classes, incompletely separates all 6 pigments. Classes 4, 5 and 6 by silhouette are the least well classified and adjacent to one another in the class plot, representing on the map carbon-verdigris, tyrian purple and verdigris respectively. On the map, it is evident that the boundary between tyrian purple and orcein is imperfectly defined.

Bird For the first image in figure 8.18, the classification into 6 clusters does not classify fully into 6 separate pigments. Classes 1 and 6 encompass carbon and verdigris together; the majority of both are in class 1, and class 6 is a diffuse class comprising edge regions within the map. The shape and magnitude of the silhouettes of those classes represent that class 6 is the poorest class, and that class 1 has a possible secondary behaviour represented by a shoulder on the silhouette.

Scores for decorrelated data split by 5 clusters, yields a very clean separation with slight crossover between classes 4 and 5. Class 4 is carbon-verdigris, whilst class 5 is orcein with a slight presence of carbon. Split instead by 7 clusters, it appears that class 3 is then sacrificial; it covers an interstitial diffuse region populated by data that classifies poorly in the previous classification. The value of $\bar{S}$ is lower than for $k = 5$, but the overall consistency of the silhouette is improved, as reflected in H_S. The poor boundary negotiation between classes 3 and 4, and the apparent necessity of class 3, can be explained by the diffuse nature of the data and the failure to completely resolve the information in the original data space.

8.3.3 Clustering in Colour-Space

In figure 8.19, we can see that the image *lion* has a clear feature at $k = 5$ in $\bar{S}(k)$, $\bar{H}_S(k)$ and $\bar{Q}(k)$ for an a*b* separation; there is no clear value of $\hat{k}$ for an L*a*b* separation of the same image. On the basis of the spike in $\bar{\sigma}_S(k)$, a nominal value of $\hat{k} = 4$ is chosen for the L*a*b* separation.

For the image *bird*, the common feature for a*b* is present clearly at $k = 4$, though a secondary feature exists at $k = \{6, 7\}$. The main feature is less clear for L*a*b* insofar that favourable features are spread across $k = \{5, 6, 7\}$, though the standard deviations of $\bar{S}(k)$ and $\bar{Q}(k)$ both have minima at $k = 6$. The form of $\bar{H}_S(k)$ is interesting, as there are two troughs at $k \approx \{4 - 5, 7\}$, indicating that these separations are more consistent in their value of silhouette than they otherwise might be expected to be.

MSI Field-Test, Bodley Douce 319 *f.* 8r: *le livre du Trésor: Mappa Mundi*

The Bodleian Library's own record, dates this Italian MS to the early 14th century. The author of the original work, Brunetto Latini, wrote the original in France and died in 1294. This makes this MS a later copy of his original encyclopædic work, which was a collated review of the philosophy and science of the ancient Greeks, rendered in Old French (13th century langue d'oïl).

The result of the MSI classification procedure with decorrelation, applied to *f.* 8r, is shown in false colour beside the respective colour photograph in figure 8.21. Original colour photograph is courtesy of the Bodleian Library in Oxford. The two shades of green have separated well, and the parchment separated mostly from all other clusters. The black pigment was lost among the cluster associated

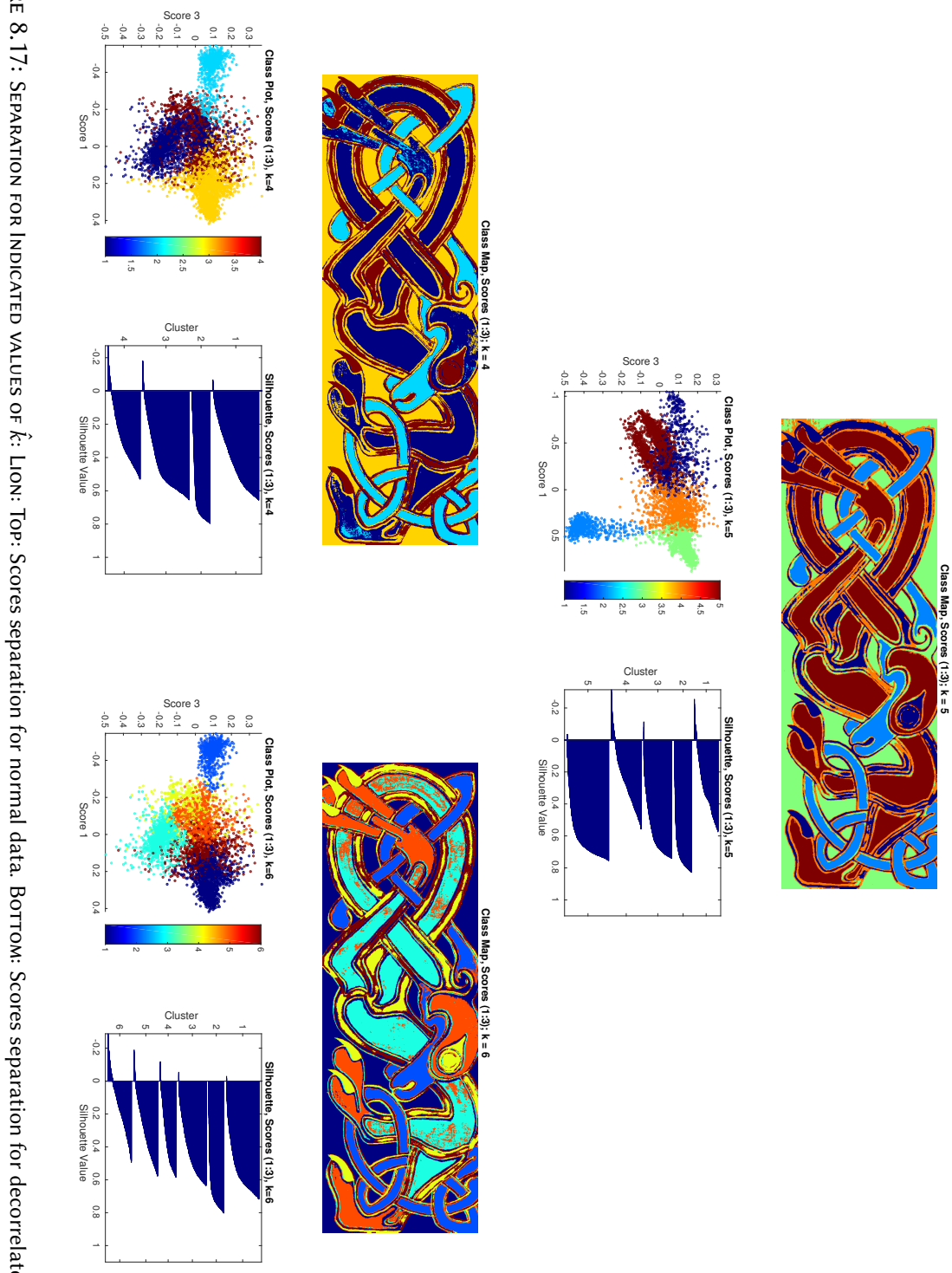

Figure 8.17: Separation for Indicated values of $\hat{k}$: Lion: Top: Scores separation for normal data. Bottom: Scores separation for decorrelated data.

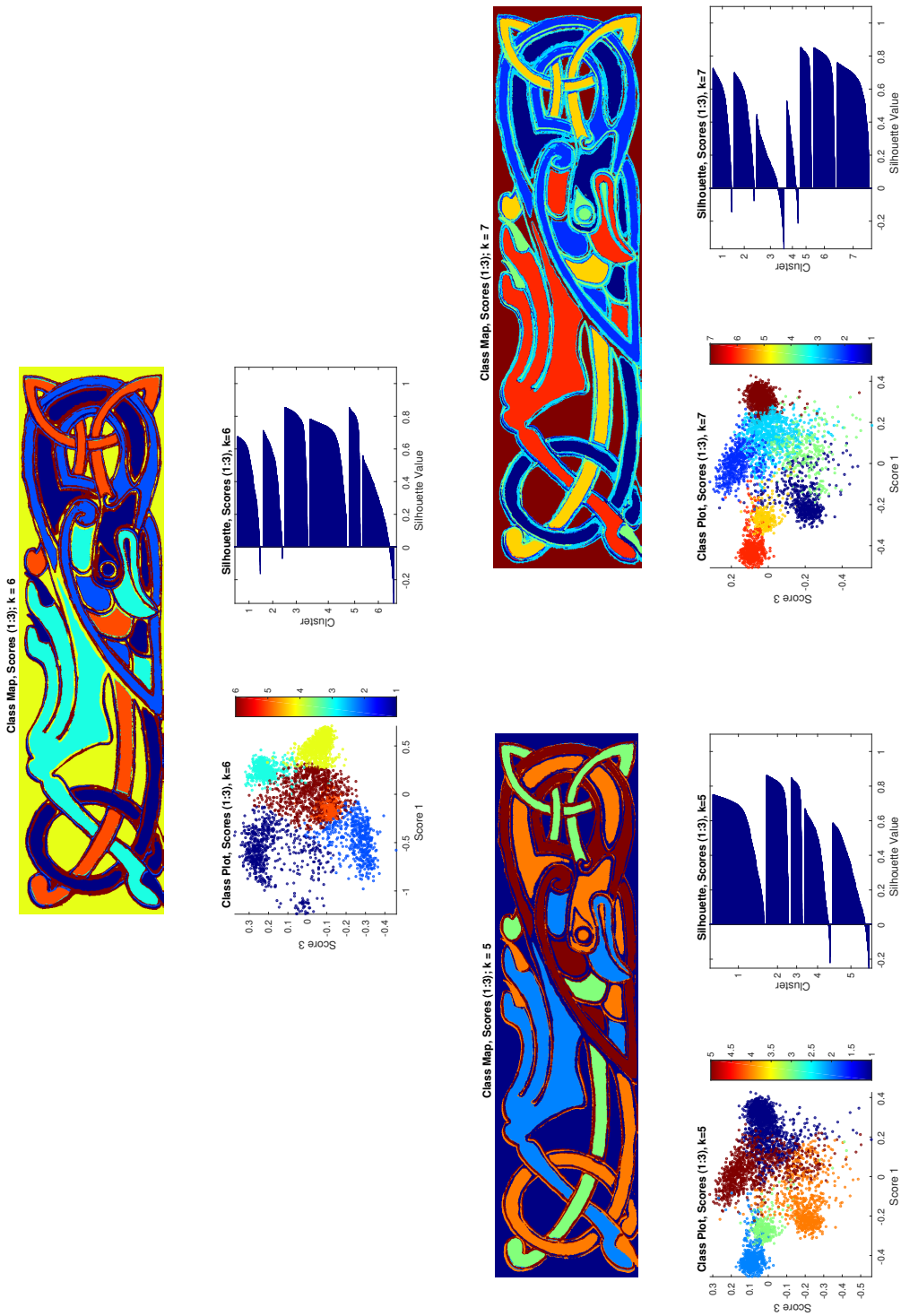

Figure 8.18: Separation for Indicated values of $\hat{k}$: Bird: Top: Scores separation for normal data. Bottom: Scores separation for decorrelated data.

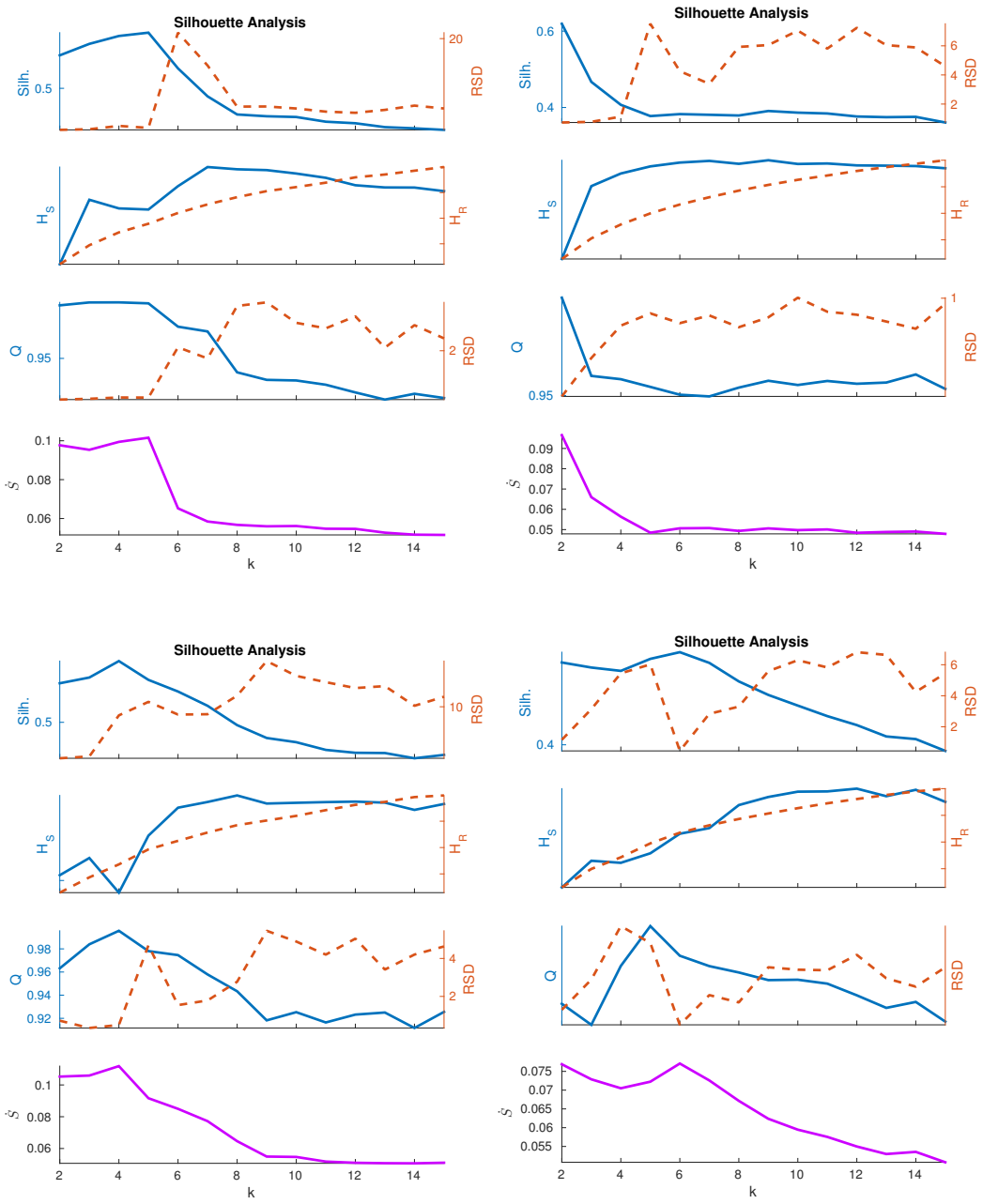

Figure 8.19: Colour-Space Separation: Determining $\hat{k}$: Top-Left: lion, a*b* separation, $\hat{k} = 5$. Top-Right: lion, L*a*b* separation, $\hat{k}$ unknown. Bottom-Left: bird, a*b* separation, $\hat{k} = 4$. Bottom-Right: bird, L*a*b* separation, $\hat{k} = 6$.

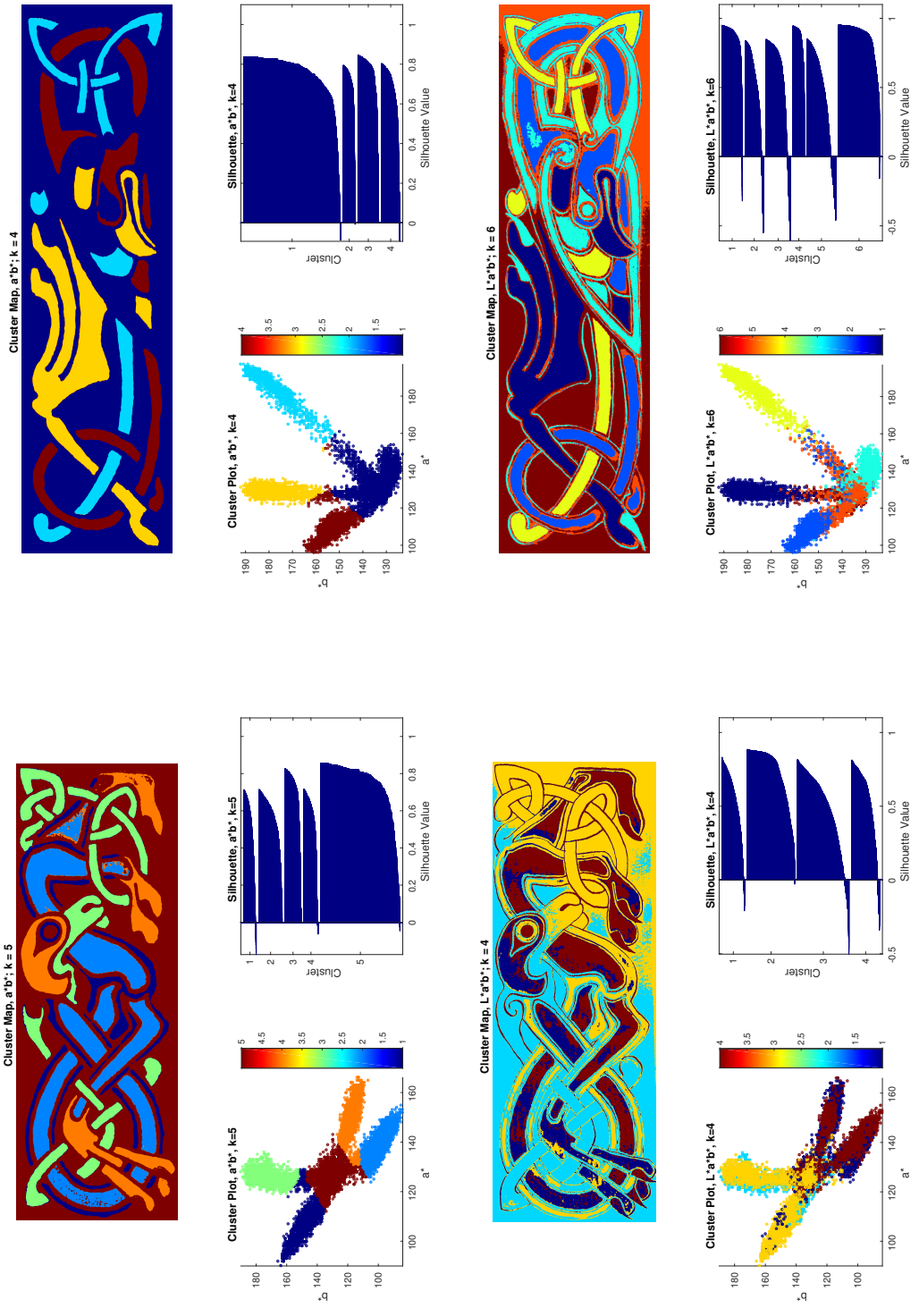

Figure 8.20: Colour-Space Separation: Classification: Top-Left: lion, a*b* separation, $\hat{k} = 5$. Top-Right: bird, a*b* separation, $\hat{k} = 4$. Bottom-Left: lion, L*a*b* separation, $\hat{k} = 4$. Bottom-Right: bird, L*a*b* separation, $\hat{k} = 6$

.

with rivers, which also failed to completely resolve from the cluster associated with the oceans. The red pigment is shown in sharp relief here, and does not show well in the digitised manuscript.

8.3.4 Raman & DRS of Manuscripts

The convention in the legends of presented spectra is to give the shelfmark, folio or pagination, and a spectrum number as an identifier of the original spectrum. Spectra are presented with their original numberings. If the spectrum is stated as having been corrected, a suitable background was used to achieve this by normalisation, and the spectra are then scaled to unity. Some spectra have been vertically shifted and scaled for clarity, but no further treatment e.g. background subtraction, has been performed. As the collection of Raman spectra was spread across two campaigns, pages may have been revisited at a later date; when this is the case, a separate pictorial record of sample regions (if any) may be given. Spectra collected during the original campaign are prefixed with a zero, whilst those of the second campaign (the “first re-visit campaign") are prefixed with unity. Repeat visits to a page within the same campaign, are suffixed by a lower case letter.

The convention in the mapping of sample regions, is to use a spot to indicate the region and a number to indicate the spectrum. The colour of the spot indicates the following:

Red: Excitation 633 nm laser

Green: Excitation 532 nm laser

Black: DRS spectrum

White: No useful Raman spectra acquired

Maccabees: *DCL B.IV.6 f. 169*

This folio did not yield any Raman spectra.

Four diffuse reflectance spectra were acquired from Maccabees, shown in figure 8.22. Three inked regions 001-003, and one of a representative section of parchment 000. NNMF of the remission spectra yielded two basis functions B_1 and B_2. B_1 is interpreted as the remission of a theoretical clean parchment substrate. B_2 is interpreted as a composite of the dirt and ink on the surface of the parchment. The residuals plot demonstrates, that the approximation is good within the visible spectrum. To further separate the spectral contributions, requires significantly more DRS spectra.

The ink is orange/brown, yields no measurable Raman response, and B_2 is not a flat spectrum; it is unlikely that the ink in this folio is carbon. A more likely assignment would be a degraded iron gall ink, as both complexed and uncomplexed iron centres in gall inks eventually form Fe^{3+} in air.

Gospel Book: *DCL A.II.17 ff. 103-111*

Folios 106r (figure 8.23) and 111r were analysed by DRS. The text is that of a gospel, though the folia contain marginalia, added at Chester-le-Street by an unskilled hand. The ink of the marginalia is identifed as being the same type of ink of the text, which is iron gall. Comparing to Maccabees, the absorption feature is flatter across the 400-700 nm region, though the parchment basis function B_1 for the current manuscript, exhibits an apparent non-ideal dip near 720 nm. This is explained by the raised baselines of remissions 005 and 007 - the NNMF algorithm is compensating for this, therefore the rest of the analysis can likely be trusted.

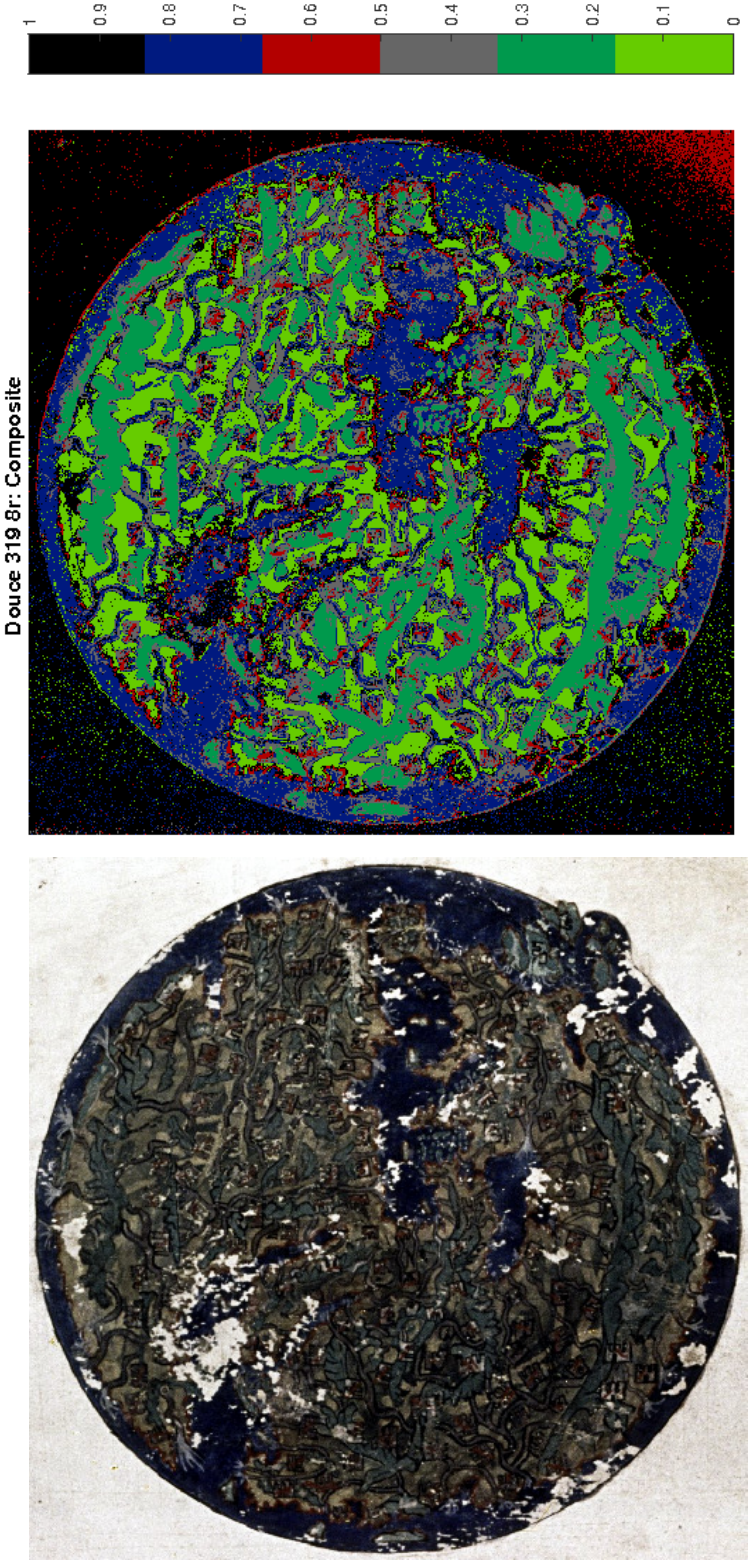

Figure 8.21: Mappa Mundi Case Study Result: For $\hat{k} = 6$, the resultant mapping of this complex scene is largely satisfactory. A false-colour classification map indicates why. Thanks to Prof. Andy Beeby for providing the multispectral images of this page for analysis.

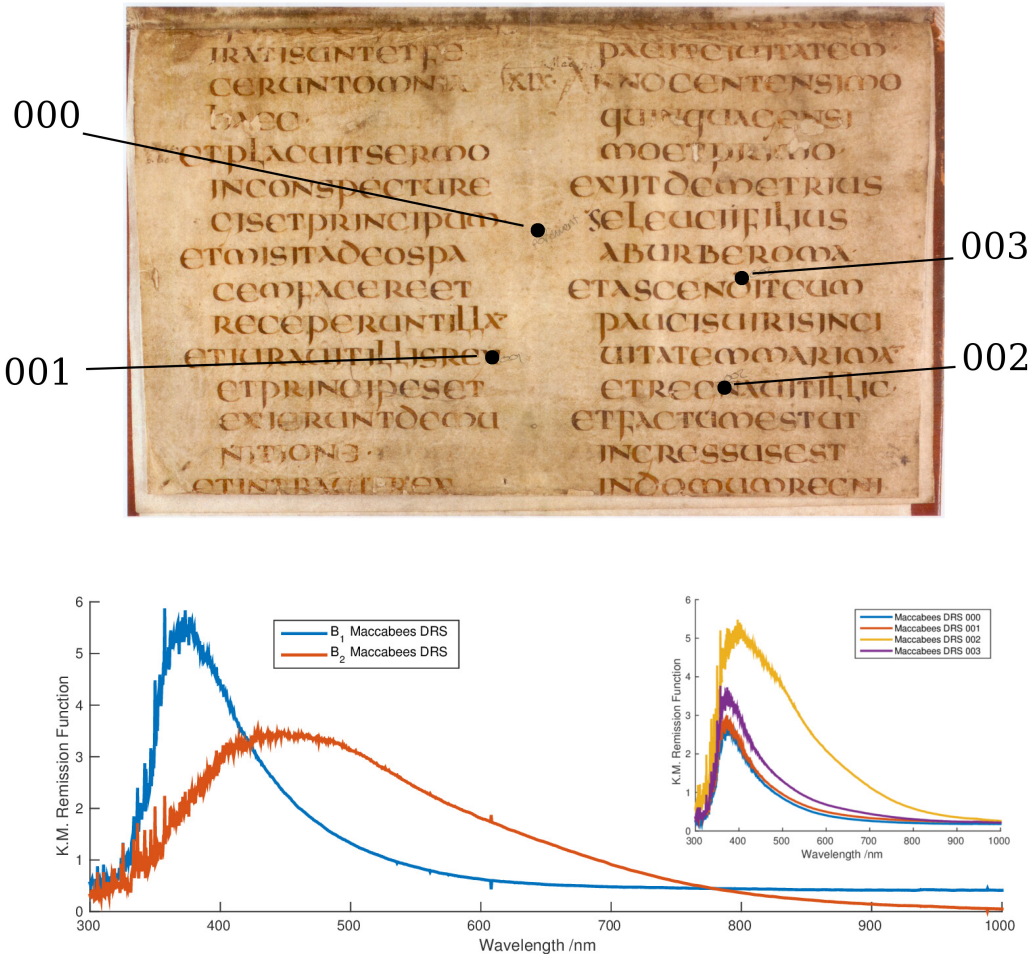

Figure 8.22: DCL B.IV.16 *f.* 169 Maccabees. Top: *f.* 169 and DRS spectra locations. Bottom: NNMF basis functions of the F(R) spectra. Bottom Inset: F(R) spectra.

The eusebian markings at 002 and 009, and the doodle at 011, are dominated by a broad, featureless shift of the baseline; a) they do not contain notable features in their remission spectra aside from baseline variations and parchment background and b) this is in any event indistinguishable from the flat spectral behaviour of carbon blacks [177] on parchment substrate. They were excluded from the NNMF analysis of the other regions for these reasons. No assignment is offered for these sample regions at this time.

Gospel or New Testament: *DCL A.II.10 ff. 2-6*

The frontispages of this manuscript that were analysed, comprised *ff.* 2r-3r (figures 8.25 and 8.24). The earliest decorated Northumbrian incipit line on 2r, uses four pigments: orpiment, indigo, red lead and vergaut. This usage continues into 2v, "the DDD page", where all four pigments are again in use. Throughout, orpiment and red lead are in use for infills that indicate the eusebian sectioning.

These pages, having been recycled as protective flyleaves for another manuscript, are understandably worse for wear. 1v, not depicted in this thesis, shows imprints where pigmented regions on 2r have lost pigment, possibly due to water damage or lack of binder. The orange regions in particular have suffered. It becomes clear on close physical inspection, in Raman by absence of the white lead signal, and in DRS features of the red lead regions, that the "pale" portions are exposed (and relatively clean) parchment, rather than formation somehow of e.g. lead carbonate. NNMF analysis of the remission functions, yields a red lead spectrum and an underlying spectrum that resembles parchment. These can be seen in figure 8.24. As the DRS of vergaut is due to the combined absorption of indigo and orpiment, the remission spectra of orpiment, indigo and vergaut together decompose into just two basis functions.

Durham Gospels: *DCL A.II.17 ff. 2-102*

The Durham Gospels have been analysed across *ff.* 1r, 1v, 2v, 3r, 38(3)v, 38(4)r, 39r, 68v & 69r (figure 8.26). This manuscript shows frequent use of skilfully decorated initials, words, and infills, and incorporates an early depiction of the crucifixion. The pigment use is consistent throughout, and those identified by both Raman spectroscopy and DRS are orpiment, red lead, and a copper green. There exists a purple pigment; though its identity remains enigmatic, it is not tyrian purple - it is either folium or orcein, reasonably the latter. The purple regions yield no Raman spectrum, but according to the DRS spectral features shown in [163] could feasibly be either orchil or folium. It is certainly not tyrian purple (figure 8.10). The twin peaks on the DRS spectra of the purple regions 019 and 020, show the twin peaks at 587 and 545 nm which would be characteristic of orchil [179], but the trough at 460 nm is more characteristic of folium in [163]. As this latter feature could feasibly be due to parchment or the choice of white standard, the assignment of orcein is made on the basis of the sharper features.

The vagueness of the term *copper green* is intentional; the Raman spectra of the green regions indicated in figure 8.26 are of bands in the C-H stretching region. Although an arguably ubiquitous vibrational band in samples containing biological sources of carbon, it is nevertheless absent from the spectra of all other pigments and materials within this study, including (in practice) the bare parchment and regions that should contain binder. It is known [180] that copper green pigments such as the basic copper carbonates of any stoichiometry, and copper acetate, all possess this band, and further [181] that it is this band that is of particular interest in the distinction *between* copper greens. Copper resinates, copper-protein and copper-amino acid complexes, and copper oleates that form by reaction

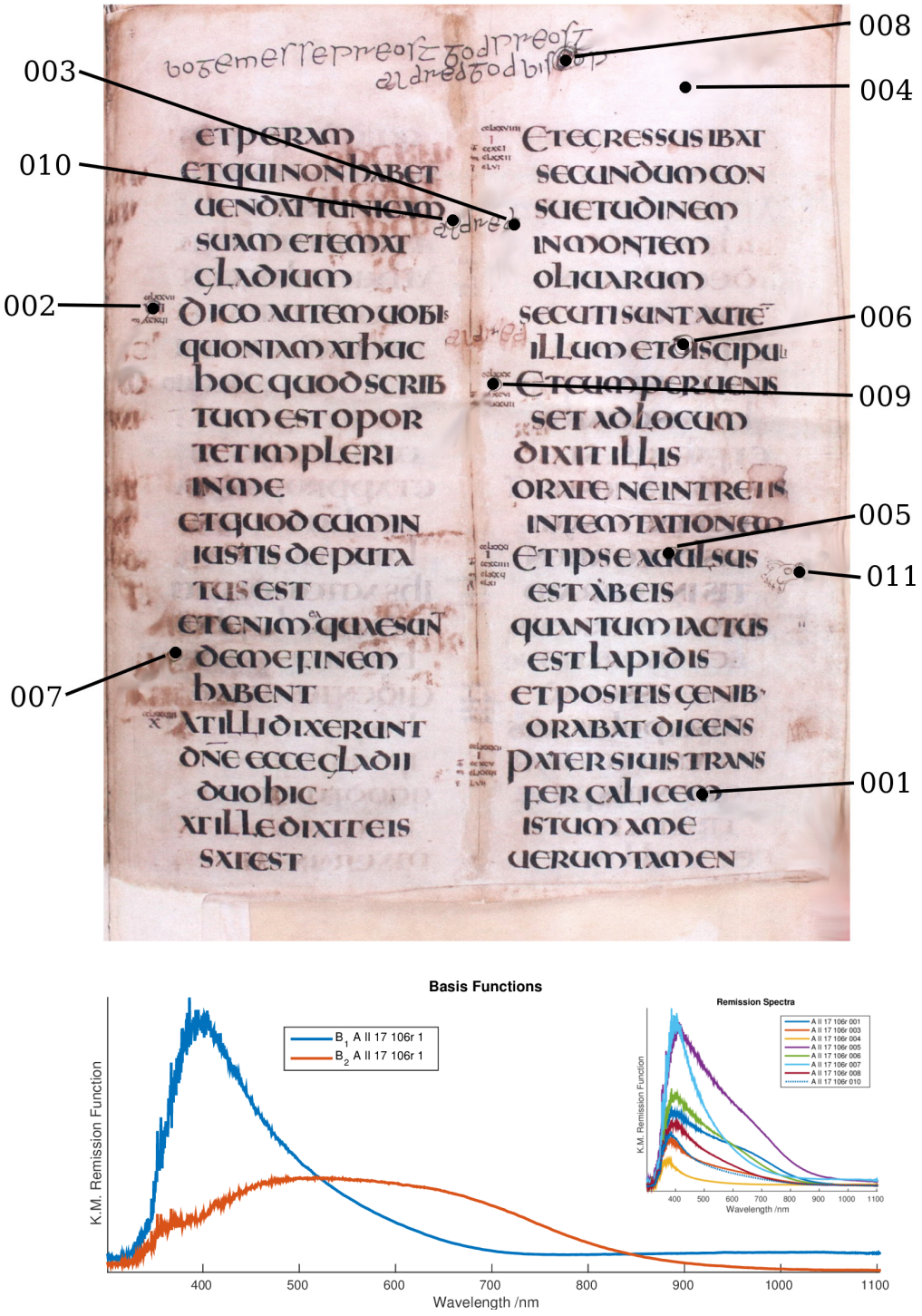

Figure 8.23: DCL A.II.17 *f.* 106r. Top: Locations of numbered DRS spectra. The marginalia in an unskilled hand was added at Chester-le-Street. Bottom: *f.* 106r. remission spectra. These spectra show that the main content of the ink on this page, basis function B_1 here, is consistent with the ink found on maccabees (figure 8.22), with a broader absorption feature. The additions at Chester-le-street are consistent with this ink type, as well.

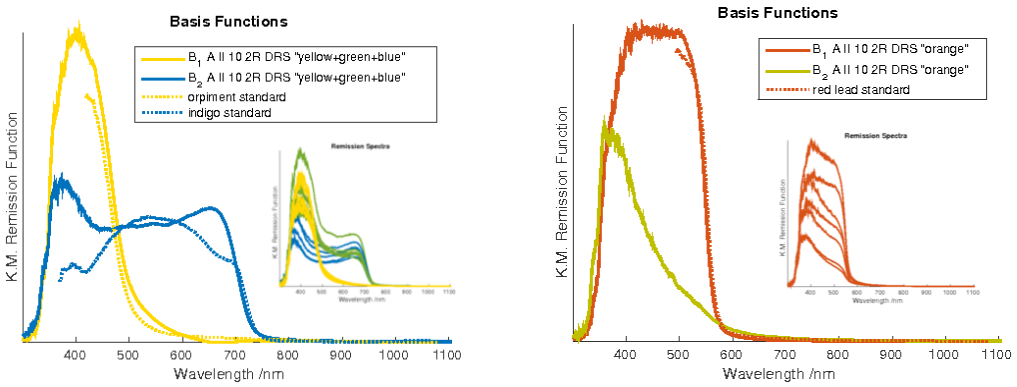

Figure 8.24: DCL A.II.10 *f.* 2r. The NNMF method of spectral decomposition can separate out pure spectral components, lessening the uncertainty of assignment in the absence of Raman spectroscopy. Left: green, yellow and blue regions (comparable to those in figure 8.25) together produce two basis functions that resemble orpiment (B_1, confirmed by Raman) and indigo (B_2, confirmed by Raman). Right: orange regions produce two basis functions that resemble red lead (B_1) and parchment (B_2). Insets: Parent data.

with binder materials, should in principle all possess this band in their Raman spectra. The Raman C-H stretching bands of the green pigment were absent from test regions used to check the origin of the band, including bare parchment, and purple pigment which fluoresced. This rules out binder as a source of this band.

In combination with the NIR absorption band of the pigment, which is visualised also in figure 8.26, the C-H band now makes assignment to a copper-based pigment quite straightforward. The uniqueness of the NIR band makes it a characteristic among the current palette; thus, the Raman spectrum in the fingerprint region not being facile, copper green will in future cases be assigned based on DRS and imaging.

The DRS ink spectra produce the most open-ended analysis. By conjecture, the broad feature at 700 nm on DRS spectrum 030 in figure 8.26 might leads us to assign iron gall; the absence of a Raman spectrum for carbon might also point to this, but the general lack of evidence for either option means that there is no assignment to be had - the NNMF analysis is inconclusive due to the redundancy of the data.

The Durham Cassiodorus: *DCL B.II.30*

Across *ff.* 81v, 169v, 212v & 214v, the only identifiable pigments by Raman were red lead and copper green, which was corroborated by DRS. The purple and yellow pigments did not produce Raman spectra as much as simply fluoresce, possibly indicating an organic yellow such as weld [147, p.33], and again orcein is suspected for purple. The red lead content is contaminated with PbO.

Gospel Book: *DCL A.II.16*

Being only sparsely decorated, this book is almost exclusively penned in black. The regular in-fills, dot-work and occasional note or mark consist of orpiment and red lead. An emergent pattern in the insular books, seems to be to use orpiment as an in-fill for the beginning of a eusebian section, and reserve red lead for the fine marginal notes that label them. Any *silhouetting* (decorative pointillism that suggests an outline) surrounding the first few letters of a section, is exclusively red lead.

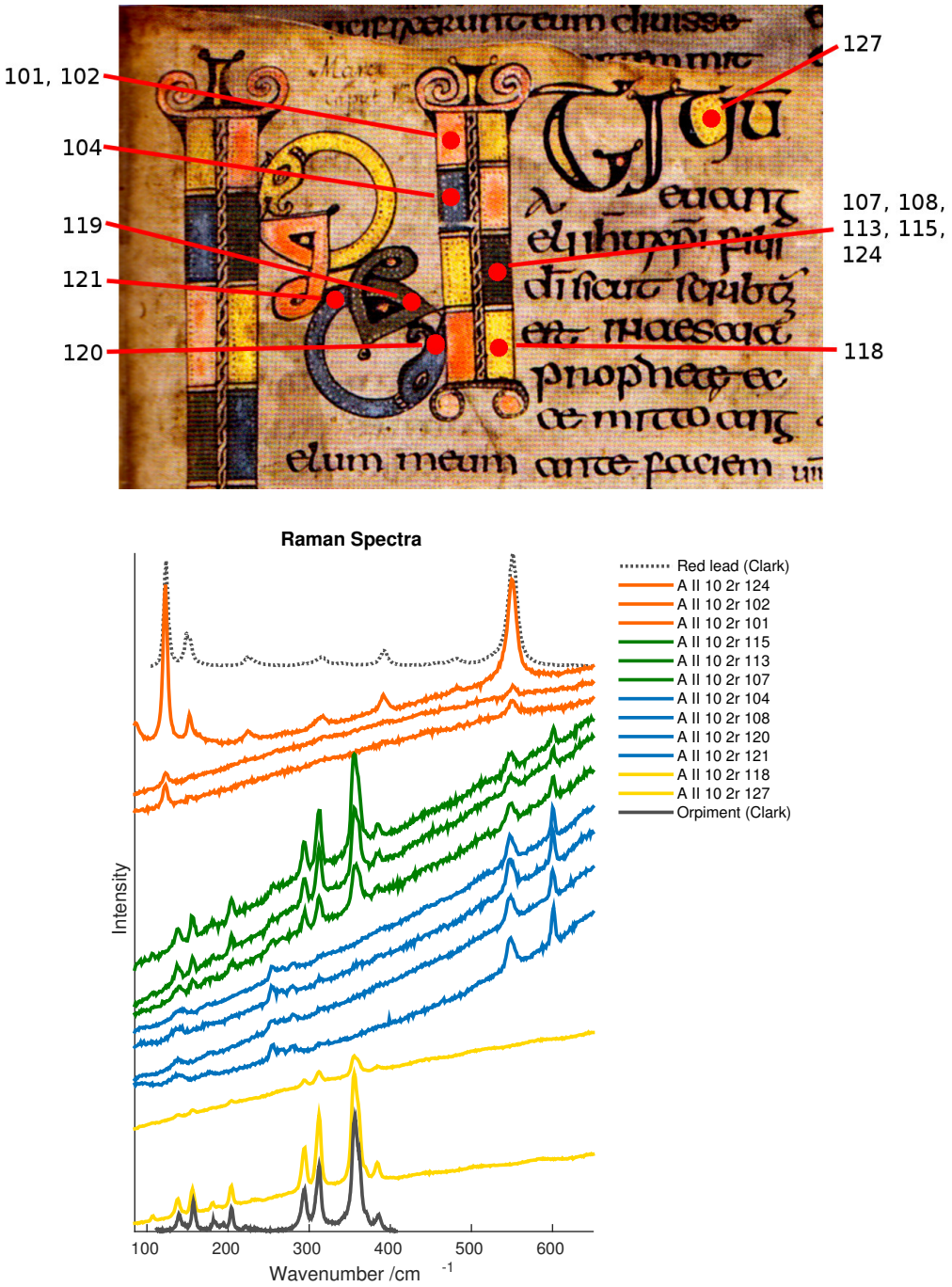

Figure 8.25: DCL A.II.10 *f.* 2R. Raman. The spectra stack in the order shown in the legend. The Raman spectral analysis reveals the use of orpiment yellow, red lead orange, indigo blue, and vergaut green (a mixture of indigo and orpiment). The resolution of the objective allows spectrum 124, to spatially resolve the red lead dots, used as decoration on the contrasting green. The spectrum *Orpiment (Clark 633 nm)* reproduced from [139] has been shifted along the *x*-axis, as to correspond to the vibrational band positions observed in [178]; the band positions for orpiment in [139] do not correspond to other literature.

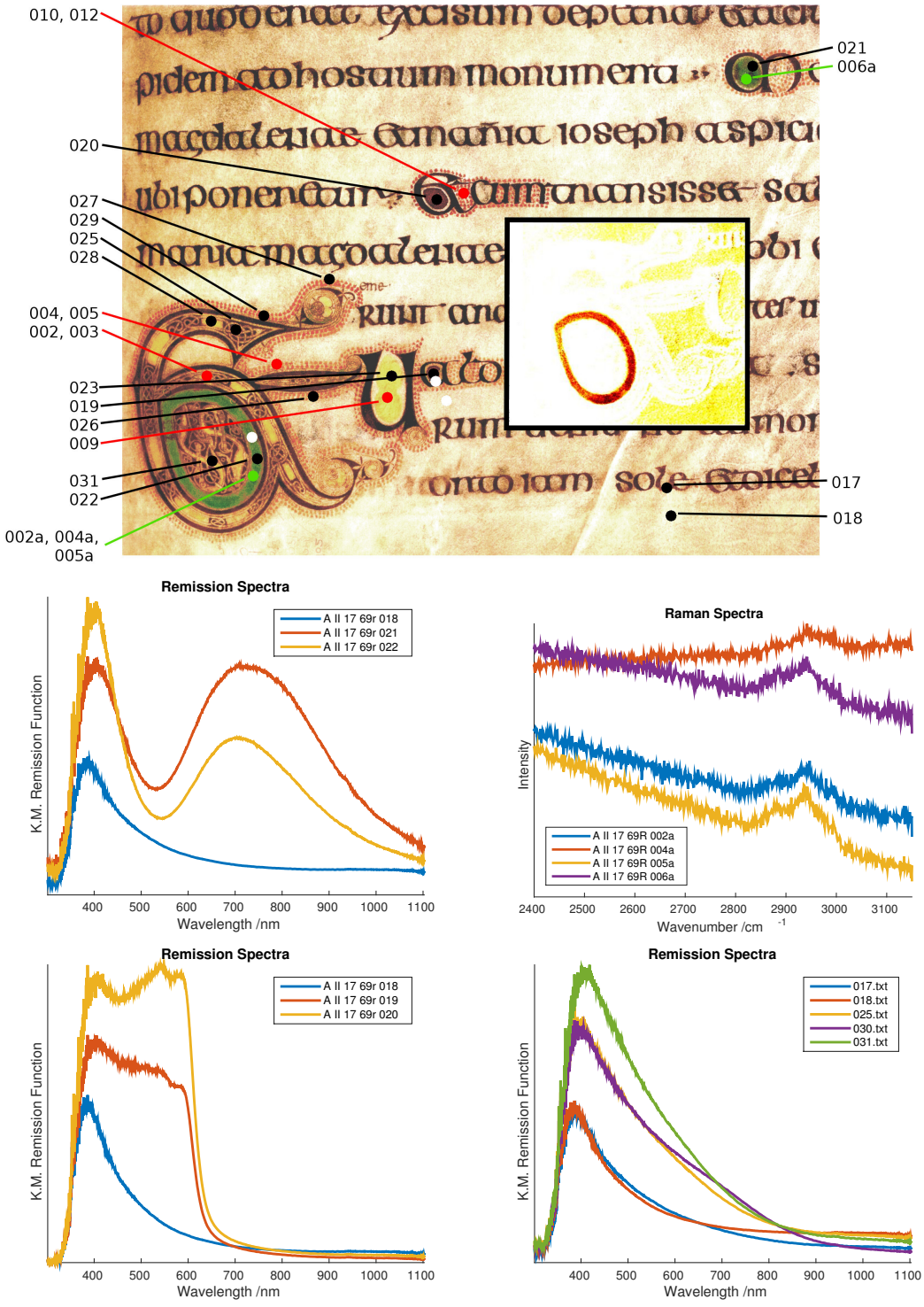

Figure 8.26: DCL A.II.17 *f.* 69r: Top: Spectra locations. Top Inset: Thresholded NIR image, showing the intense absorption by the green region, characteristic of copper pigments, but not vergaut. Middle: DRS and Raman Spectra of green regions. Bottom Left: DRS Spectra of purple. Bottom Right: DRS Spectra of ink.

This is the second book in the chronological order, to have PbO as a contaminant in its red lead content. The separate styles of writing and decoration from the three scribes that wrote this [168, p.38], are mirrored in the separate quality of the red lead; the scribe of 37r uses $Pb_3O_4 + PbO$, though in other portions credited to other scribes, the red lead is Pb_3O_4.

The Raman analysis of laboratory samples of lead oxides is presented in figure 8.27. By NNMF, this has yielded "pure" component spectra as basis functions of the parent data. This is comparable to [139], but is of a much improved resolution. The NNMF method is inappropriate for direct application to the Raman spectra of manuscripts, as the baselines of those spectra are often variable. However, the ability to deconvolve spectral responses in this manner is important in applications where pure standard spectra are difficult to acquire, such as this case of contaminated red lead.

Gospel Book: *CCCC 183*

This book is not so heavily decorated as e.g. A.II.17, possessing a few decorated initials and an opening illustration on *f.* 1v. Indigo, orpiment and $Pb_3O_4 + PbO$ were found across *ff.* 2r, 72r and 92v by Raman spectroscopy. Red lead is used throughout the book for various ends such as illustration, illumination and as an ink in its own right for letters of significance or to draw the eye, but is often found heavily degraded. The most extreme example of degradation is on *f.* 95v, where the galena obscures almost all of the red orange colouration and the DRS spectra do include some odd features that may or may not be galena. No Raman peaks for galena were found. DRS spectra support the assignments for red lead, indigo and even an instance of orcein, but no conclusive individual spectra exist for orpiment. This is owing to the red-shifted parchment absorption, and the translucent nature of the wash, which is not lain so thickly as for the insular books so the parchment dominates the DRS spectra of yellows. The black ink of this book was not investigated.

The degradation of red lead in this book helps indicate the possible spectral hallmarks of degradation, though in the illustration on *f.* 1v, the bluish patches that by eye might appear to be PbS show features of multiple pigments - red lead, indigo and an unknown infra-red absorber. More data is required for NNMF to separate these features.

Cambridge-London Gospels: *CCCC 197b*

This manuscript is heavily decorated; *ff.* 1r, 2r, 2v, 6v and 9r were investigated by Raman spectroscopy. Copper green, red lead and orpiment are the core complement of colours. Purple appears again in this manuscript; it is fluorescent and provides no useful Raman features, but no DRS spectra were taken. A Raman spectrum of yellow dots layered on purple, confirms orpiment.

Collectar: *DCL A.IV.19*

The collectar exhibits two non-ink colours. The inter-linear gloss is red, and some decorations appear yellow. Across *ff.* 1v, 28v, 32v and 56v, all identifiable spectral components by Raman are red ochre, though the endleaves show iron gall ink by DRS-NNMF.

There is no conclusive evidence that the yellow pigment is yellow ochre or orpiment - though the absence of any spectra for orpiment by Raman (which has otherwise proven capable of yielding signal from microscopic flecks of orpiment during this study), might indicate that it is not orpiment, the absence of evidence is not evidence of absence. DRS fails to prove that the pigment is orpiment or yellow ochre, though one might speculate that the use of red ochre pigment (sourced from iron

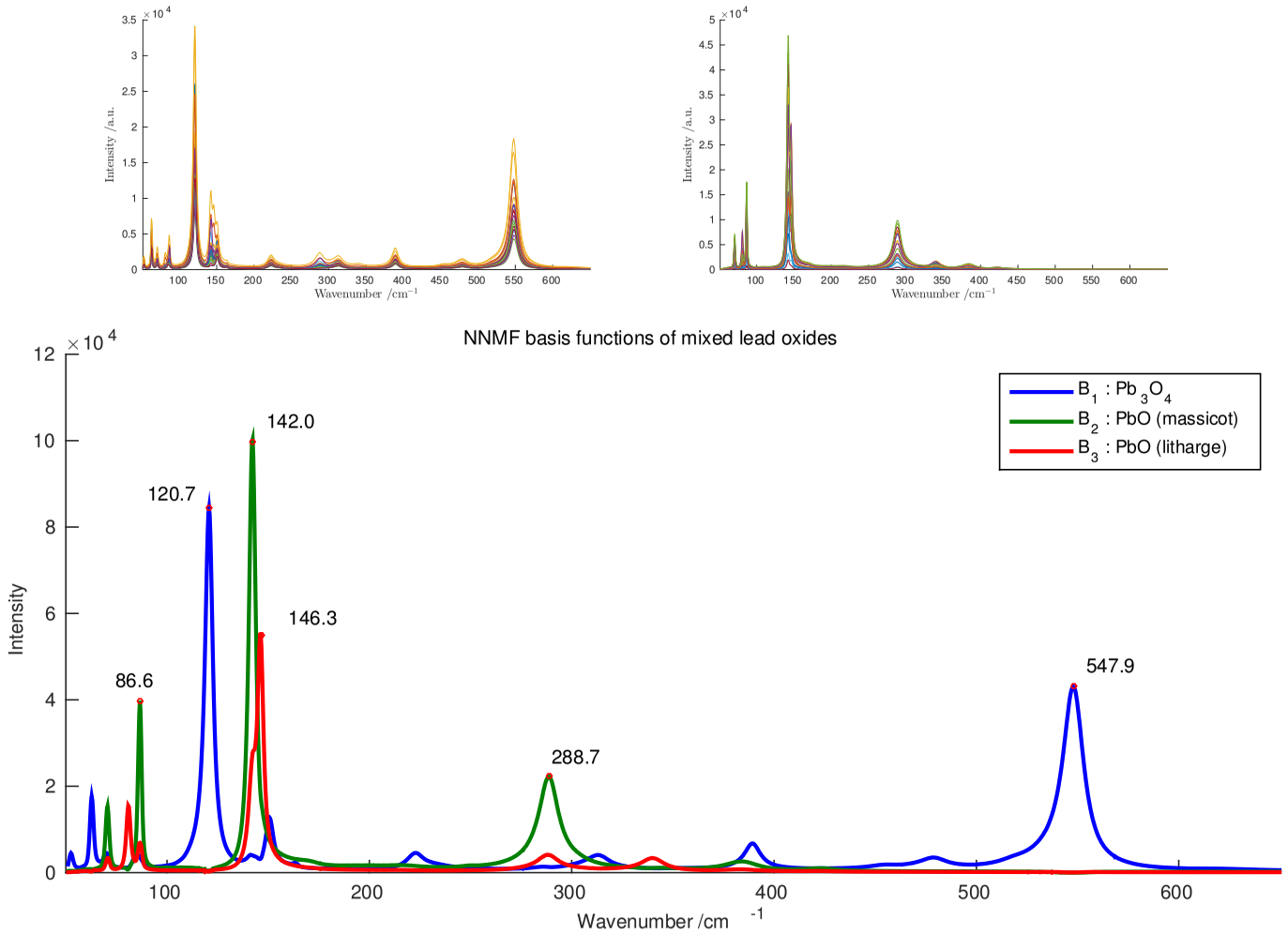

Figure 8.27: Litharge/Massicot Contamination of Red Lead. Top: Overlain Raman spectra of red lead (Cornelissen, left) and litharge (Cornelissen, right), collected using 1800-grating and HeNe laser. Bottom: NNMF analysis of complete set; basis functions approximate spectra of the three pure substances. As the resolution of the instrument is <1 cm^{-1}, the resultant spectra produce a better basis for comparison of the strongest diagnostic peaks.

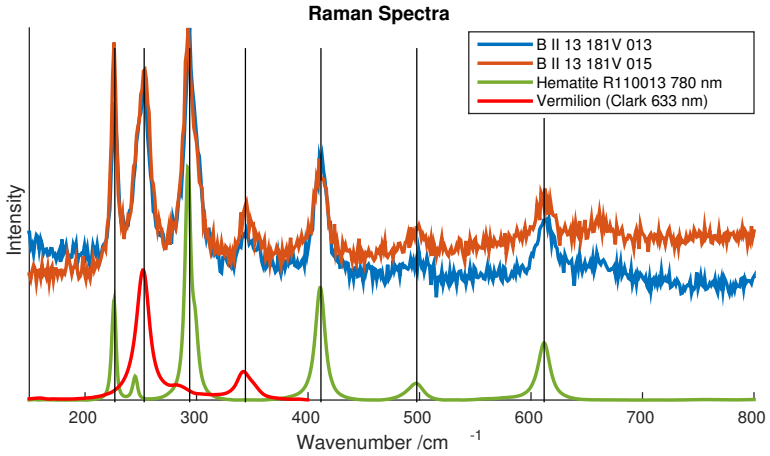

Figure 8.28: DCL B.II.13 *f. 181v* corrected spectra of black particles interdispersed in vermilion. The non-vermilion peaks exhibit the peak pattern and position observed in [182], confirming α-Fe_2O_3. Shown also for demonstration, spectrum of haematite sample R110013 from [184], and vermilion from [139].

clay-type materials) might also support the use of yellow ochre in future studies as it is from a similar source.

Benedictine Gradual: *Cosin V.v.6*

Raman spectroscopy on *ff.* 13r, 30r, 69v, 79r, 124v reveals copper green, vermilion red, lapis, red lead and orpiment. This manuscript is interesting, as the artist has layered orpiment on vermilion. Excepting the illustration in CCCC 183 and the orpiment dots atop purple in CCCC 197b, until this point in the time-line, pigment has been reserved for block colour, text, or the occasional flourish or indicator dot.

Purple pigments yielded no Raman spectra. No DRS spectra were obtained.

Augustine: *DCL B.II.13*

The pigments vermilion, lapis lazuli, and a copper green have been found across *ff.* 68r, 72v, 102r and 181v. Black particles were found microscopically interdispersed in the vermilion, which is shown to be haematite [182] in figure 8.28. The presence of haematite in a manuscript of this period is consistent with the account of Cennini regarding adulterants (p. 142), especially as the identity of what Cennini calls *brick dust* is vague. Uddin [183] gives the iron oxide content of red bricks at around 8% by mass, most of the rest of which being silica, which gives a weak Raman response. It is also reasonable, given its deep red appearance in powdered form and utility as a pigment in its own right, that *brick dust* may simply refer to ground haematite.

Symeon of Durham: *Cosin MS V.II.6*

Of this complex manuscript, *ff.* 6r, 77v and 195v were analysed by Raman and DRS. The artist has used layering on 77v to effect complex colouration, some of which has degraded. Orpiment is not used in such great quantity in this manuscript as for insular manuscripts, though it is still present. On the degraded regions, the darkened appearance of red-orange reveals vermilion and red lead mixtures, though the Raman signal of galena is absent. Darkened blue regions reveal use of orpiment and lapis

lazuli together by Raman, though whether this is degradation or a result of paint mixing on the page or being worn away, cannot be discerned.

DRS spectra from across this manuscript are consistent with the Raman assignments. The core pigment complement is lapis, copper green and vermilion. No evidence of azurite is found among the blue by DRS, though the remission of some laboratory mixtures of azurite and lapis lazuli on vellum are shown alongside. Even small amounts of azurite (10% by mass, Appendix A.2 spectrum AL009) included in lapis lazuli results in a marked increase in NIR absorption.

Laurence of Durham: *Cosin V.III.1*

A sparsely decorated manuscript; *ff.* 22v, 23r, 90v and 106v show mostly pigmented initials in the form of vermilion, copper green and lapis lazuli by Raman. Only *ff.* 22v and 23r were investigated by DRS, resulting in the same assignments as for Raman.

Psalter: *Bamburgh Select 6*

This small tome contains complex use of colour. Across *ff.* 8v and 9r, layering of pigments and illumination with gold can be seen. Worn and scratched portions of gold leaf reveal a substrate that is red ochre and red lead by Raman analysis. Green is copper-based. White lead is present as a highlight colour layered on top of other pigments.

Contemporary manuscripts contain orpiment, but none was seen in this manuscript; yellow colouration was absent save for gold itself.

8.4 Discussion

8.4.1 Imaging

Colour-spaces are addressed here first, as the nature of RGB imaging is such that (barring chromatic aberration) perfect (sub-pixel) image registration is guaranteed from the outset.

Clustering in Colour-Space

The projection into the a*b* plane yields colour information that straddles distinct regions where clusters reside. The main body of a cluster does not appear as a discrete entity; rather, fringe data is distributed between clusters where there is a spatial transition (fringe) between the corresponding pigments depicted in the image.

This is a direct result of the inability of a digital image to resolve features, and further for the pigmented regions themselves to make a spatially sharp transition; colours that are not completely opaque (such as wash colours), or which sediment into layers of different particle size, produce internal variation within a block of colour and may transition gradually into other pigments. A perfect step function between two perfectly uniform behaviours in the scene, would still produce diffuse inter-cluster regions in the resultant data space.

The effect of RGB-decorrelation on visible hue is quite small (see figure 8.29), producing little notable change in a recombinant L*-neutral image. This should be expected, as the point of the RGB decorrelation stretch is to enhance the saturation of colour in RGB space, rather than simply shift its hue. Regardless, any shift in hue due to a decorrelation stretch should *intuitively* make clusters in the

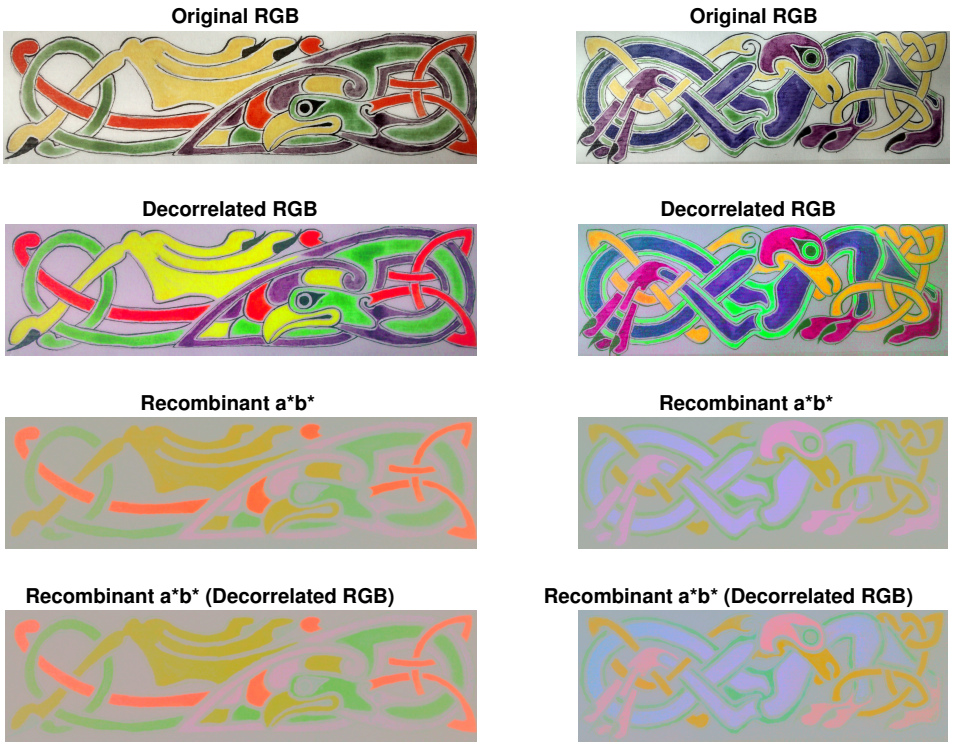

Figure 8.29: Effect of decorrelation on hue: The effect of a decorrelation in sRGB space, on the outcome of an L*-neutral regeneration of RGB images. Both the two top images have been converted to L*a*b*, the L* values for all pixels set to a single scalar, and the process reversed to produce the bottom two images. The resultant *recombinant* image has constant luminance, and therefore provides precisely zero brightness-based contrast.

a*b*-plane more, not less, separable. Careful inspection of the two recombinant images reveals slight shifts in hue. The non-uniformity of saturation (due to increased contribution of background) is visible as desaturated patches. Hue non-uniformity due to the stretch is visible on both the RGB and a*b* images on the left hand side; this is possibly due to variation in the illumination across the image.

However, the principal downside to decorrelation, is that unevenness in hue is also exaggerated, which can make for classifications that split the data inappropriately. Even if clusters *are* made more distinct from the equivalence line in RGB space, the internal distribution of data in the clusters must be made more disperse. It is also plausible due to the nature of the sRGB-L*a*b* transformation that, despite the effect in RGB space, more complex transformed data is improved much less in the a*b* plane. The overall effect is to simply move data further from both the equivalence line $R = G = B$ and the other data, and thus further from the grey-point in the a*b* projection. As shown in figures 7.7 and especially 7.8, an apparent convergence of parts of distinct clusters is now not only plausible, but depending on the complexity of data may be quite likely, especially as the grey-point is not located precisely along $R = G = B$, and the tail of one cluster may intersect with the main body of another.

It is shown in figure 8.30, that the effect of decorrelation on the a*b* projection is data-dependent and also dependent on when the transformation occurs; they are all, however, very similar. L*a*b* and

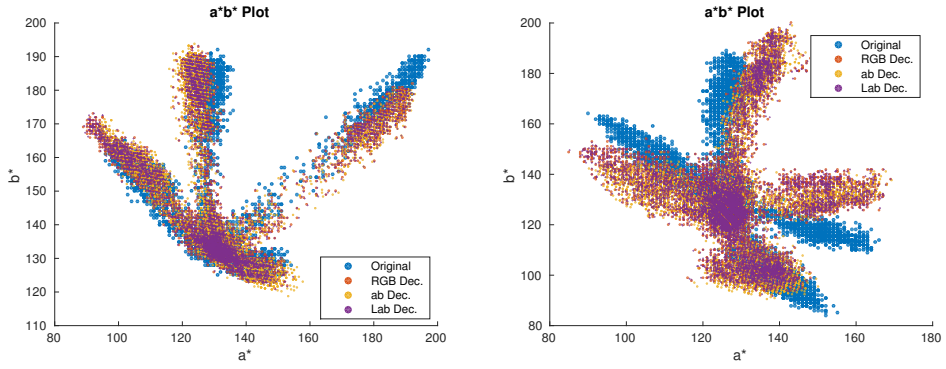

Figure 8.30: Effects of decorrelation on a*b* projection: Effect of decorrelation on a*b* projections of Left: *bird* data, Right: *lion* data. The data has been projected after decorrelation at different stages. *Original*) not at all, *RGB Dec.*) before projection, *ab Dec.*) in the a*b*-plane, *Lab Dec*) in the L*a*b* space. The grey-point is (127.5,127.5) and the maximal value is scaled to 255.

a*b* decorrelations have not been considered useful until now, primarily because ad-hoc transformation of the data must hamper any future colorimetric identification of pigments and in principle make clusters more diffuse. As shown (in figure 8.30 but particularly in figure 8.31), the similarity of cluster positions for the same pigment in the original data may be worth noting: orpiment around (130, 180), red lead (190, 185), verdigris (110, 150), paper and carbon very near the grey-point, basic orcein (140, 100), orcein (145, 125) and tyrian purple (150, 120), therefore corresponding to constant hue angles. The identification of purple pigments, especially in differentiation of multiple purples, might on this small basis be supported by colorimetric imaging methods without having to remove books from preserving conditions.

In figure 8.31, images *bird* and *lion* were aged for 12 months, demonstrating the tendency for the hue of verdigris to shift over time [144]. Due to their proximity to the achromatic point, tyrian purple, basic orcein, indigo and prussian blue have diminished populations from thresholding in the figure, but are still represented by hue angle.

Further to this, comparing the lion and bird data to that of a swatch of many pigments acquired under the same conditions, we find that a population analysis of hue angle is more clear than the series of scatter graphs used to represent clustering. In the middle row of figure 8.31, we compare the projections for both images and find that the data for pigments common to both images (verdigris and orpiment) overlap. In the bottom of that figure, the hue angles about the achromatic point are calculated by subtracting the achromatic co-ordinate, removing data within a distance of the origin (±0.5 scale: 0.05, ±127.5 scale: 6.375) and calculating the four-quadrant $\arctan(b^*/a^*)$. Thresholding removes the noise and artefacts due to the presence of white background and black pigment distributed about the achromatic point, but preserves most pigment data. The results were binned at intervals of 2°. For comparison, the full data on a scatter graph is presented in the top of that figure; it is clear from that however, that chroma (magnitude of the colour vector) possibly plays a large part in the differentiation of pigment. Though both lighter and darker regions do exist within pigments, it is not necessarily the case that either variation will have systematically lower chroma than any other.

It appears, by comparison of 2D and 3D separations in L*a*b* space, that the inclusion of L* data is specifically problematic, and that its removal improves the overall condition of the separation. In the case of both *bird* and *lion*, inclusion of L* effects no difficulty in separating into further clusters, and

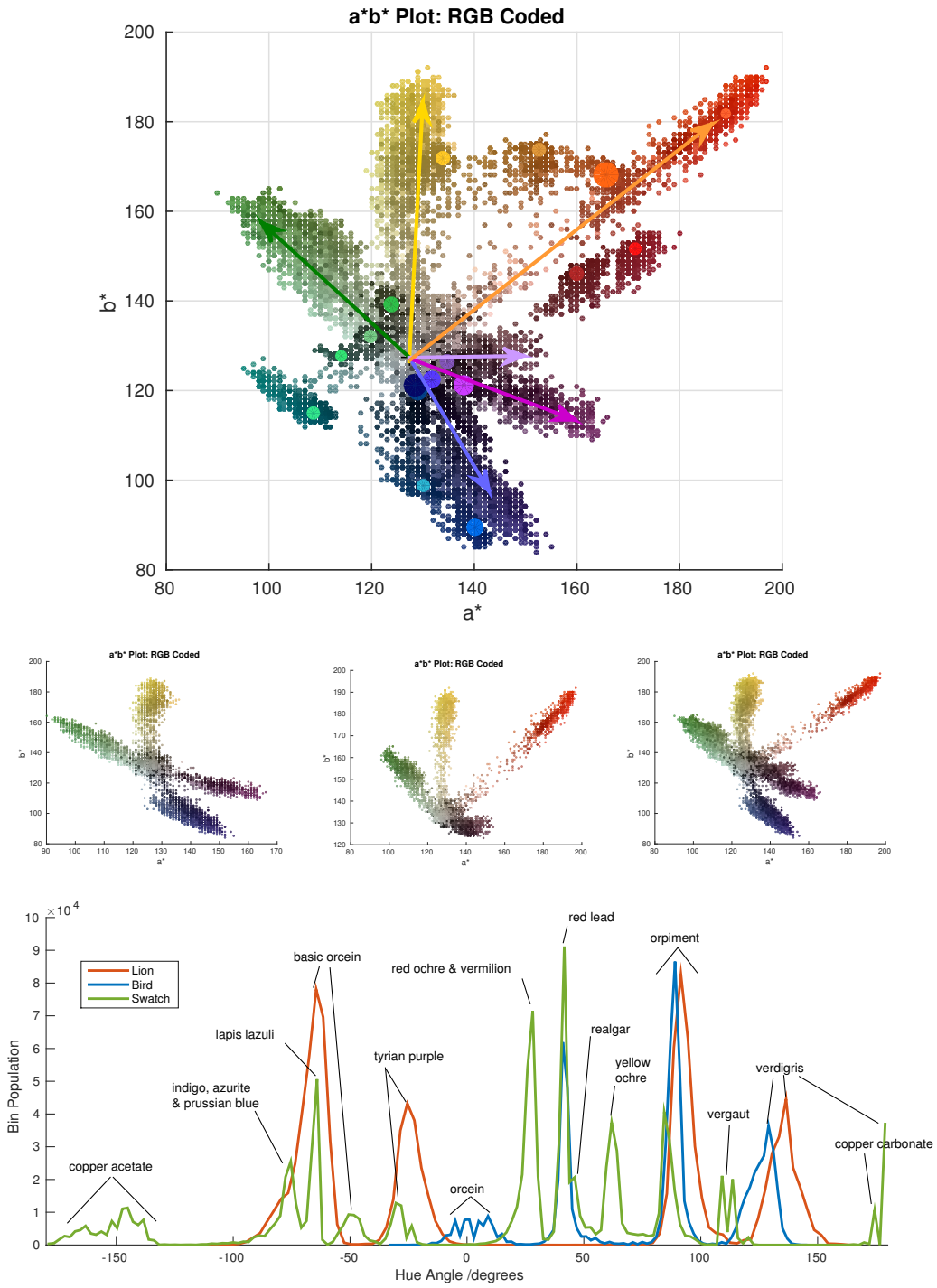

Figure 8.31: L*a*b* analyses: Scatter Graphs: Top: Scatter graph of all data for bird, lion and swatch together. Illustrative vectors for the bird and lion images are drawn, whilst the centroids of the swatch data are shown as circles - the radius directly represents the average standard deviation of the a* and b* directions. RGB values of pixels have been used for colour coding. Middle: Lion and bird data respectively, plotted separately then together. Bottom: Population as a function of hue angle about the achromatic point, relative to the positive direction of a* for bird, lion and the pigment swatch. Peaks are labelled with the pigment they represent.

certainly per $\hat{k}$ determination for *bird*, it promotes the use of more clusters. The separation however, is far less "clean" and this is reflected especially well in *lion*; despite conveying the ability to separate e.g. orcein and carbon from a paper background, it does not enable further separation between e.g. orcein and carbon at the determined value of $\hat{k}$. Any unevenness in illumination, makes itself known *via* L*.

The inconstancy of hue angle between separate preparations of pigment is potentially a camera issue, but as the batches of paint were different for each of the test samples, it is possible that they have different particle sizes. The yellow-red pigments are inherently more separable due to the number of hues represented in that part of the plane, but again the chroma plays a factor in identification - red lead has a consistent hue angle AND a strong chroma when fresh.

Clustering in Eigenspaces

From what we have gained in discussion of colour-spaces and sRGB images, we can immediately refer back to the PCA scores plots on pages 180 and 181. The scores are already quite disperse; the effect of decorrelation on the data in both cases is ultimately to make it internally moreso (less resolved, this is reflected in the separation quality), despite the fact that the mean and standard deviation of the transformed data are intentionally restored to it (§8.2.3, p 170).

However, a secondary effect seems to be to make the clusters more spherical, and for new clusters to become apparent. For instance, for *lion* in the non-decorrelated data on page 180 in the negative regions of scores 1 and 2, there exist at least two elongated clusters against a diffuse background. These are either not present in the equivalent plot for decorrelated data, or might be present as the two small clusters near (-0.25, -0.45). Regardless, it is more straightforward to demonstrate these in the decorrelated data (both scatter plot and traces).

Given the very diffuse nature of the *lion* scores from the outset, the problem and importance of registration is made clear. Examination of the scores images themselves reveals, that although the affine transform produces good registration with the reference image, good registration between the other images is not guaranteed. The multimodal nature of the transform, accommodates for different types of contrast between images, and causes the algorithm to seek to align common features within that contrast. Poorly-focused images can ultimately still converge without producing a computing error, despite having missing or diminished contrast features. These features then fail to align with one another in the same way that they aligned with the reference image, or even remain poorly registered, which altogether creates its own latent noise centred on those regions.

The affine transform was chosen, because translation alone proved insufficient when comparing to the reference image. It was assumed, that two images of the same scene in registration with a third such image, must also be in comparable registration with one another. This has proven not to be the case, and so a new registration routine (possibly iterative) must be designed in order to improve the accuracy of separation.

Silhouette analysis is for the most part straightforward and useful. Figures 8.17 (p. 186) and 8.18 (p. 187)[(i)] show the silhouette functions of the separations alongside the relevant colour-matched maps and plots. Clusters with the least-certain classifications, that show the most deviation from complete representativity, also display silhouette profiles with larger variation and proportion of negative values. These can be rationalised by examining first the corresponding plot, and then the map. Figure 8.18 demonstrates for both normal and decorrelated data, that carbon and verdigris do not separate easily;

[(i)] See Figure 8.20 (p. 189) for the L*a*b* counterparts

the efficient absorption of light by these pigments across three out of five filters makes them very similar, and the L* component of an RGB image shows that copper greens are not very reflective overall. If there were more carbon in the image, the cluster for carbon would be better-populated and it would show up more clearly; its pixels in class 1 of the normal data are the small cluster along the axis of score 1 (the principal axis), which as predicted (§7.8) lies near an extreme of the equivalence line.

A similar problem of separation occurs in figure 8.17, where not only do carbon and verdigris struggle to separate, but orcein and tyrian purple appear to poorly distinguish. Inspection of the raw image data makes it clear why this is so; the two purple pigments vary in a way that almost completely correlates. Not shown in this figure, is that if class 5 in the normal lion data is *forcibly split* by passing it through a k-means separation with $k = 2$, the two plainly visible subclusters (which do not separate simply by adding more classes to the original separation problem), are tyrian purple and orcein. The fact that these two clusters are very close to one another and are more spherical together than apart, likely prevents k-means from defining it a minimum. Likewise, the two behaviours aren't evident by the silhouette, which highlights a major downfall of silhouette analysis: closely packed data that one might expect to split neatly but along an axis or plane, are not necessarily recognised in principle or in practice by the metrics of k-means and silhouette. If they are classed together, the resultant placement of the centroid near or in the cleft between clusters makes both clusters approximately equal in terms of goodness of membership. Loss of either to a separate class is unfavourable, making such membership a deep local (or perhaps a global) minimum. The class plots shown in the figures are also sparsely populated (around 1% of the data is sampled) for clarity; the two clusters do not in fact resolve as well as they appear to, though the majority of their populations are separate. This failure to resolve is illustrated in the decorrelated data with $k = 6$.

It is not intuitively clear, given the distribution of data in the class plot, exactly why the normal data in this figure splits classes 1 and 4 the way it does. It is known that the euclidean distance metric favours sphericality of classes and therefore allows distortions mostly for sparsely populated boundaries. On that basis, as the carbon cluster is fairly small, it makes sense that it is nevertheless diffuse enough to have trouble classifying discretely; as it is fairly distinct due to its position, it classifies in its own class but borrows from other clusters. The presence of a resolved cluster is evident in the silhouette for class 1: a bundle of points that classify well, and a secondary lot that classify less and less well. The crossover between 1 and 4, with 1 borrowing from 4 is hypothesised by silhouette, supported by plot, and confirmed by map.

The problem of verdigris *vs* carbon for normal lion data is the same as above in figure 8.18: the small carbon cluster is at an extreme of the equivalence line in the data, which is situated near the principal axis of the eigenspace (and paper is at the other end). Thus, at least one expected trend is confirmed: overall lighter and darker regions are separated along the principal axis for the normal data, at the very least when a black and a white region are both present in the images. Decorrelation doesn't improve prospects for these two pigments, but it does effect an overall cleaner separation. There is nothing in the silhouette to truly suggest that there ought to be another class, save perhaps a suspicion based on the form of classes 4 and 5, which both contain improperly classified data that might classify better in a diffuse, interstitial class. The increase of k fully realizes this by providing not one but two interstitials, one of which is noisy artefacts and the other of which is carbon.

Again in figure 8.18, class 6 in the normal data is the poorest of all, and appears to be a diffuse standalone cluster that encompasses multiple pigments. This is plausibly an issue of registration, resolution or both, given the locations of the regions. This corresponds well to the above noisy artefacts.

Returning finally to figure 8.17, there is a suggestion in the decorrelated silhouette for $k = 6$ similar to that seen in the decorrelated data for image *bird*. An interstitial cluster might serve the separation well, especially as the silhouette entropy spike in figure 8.15 indicates that $k = 6$ is somewhat less ideal than its neighbours with respect to evenness of silhouette, but at the same time the sharp drop in the mean silhouette itself for $k = 7$ is not a positive indication that the separation is much better.

Overall there is no positive indication, that darkness/lightness is still associated with the principal axis for decorrelated data. In fact the principal axis lies along the line between orpiment and paper, for both images.

Determining $\hat{k}$

The analysis of statistics as a function of k, gives a set of charts derived from some randomised subsets of the data. The computational load of the separation is high; the separation is typically using the first 3 scores or the a* and b* components, and the number of pixels is to the order of $10^5 - 10^6$. The process initially used the whole data set while the routine was being tested, but it was found by testing random samples of varying size, that for both test images the statistical output became comparable to the result from the full data set (within 5%), once more than 1,000 pixels of data were used. A random subset of the data (1% of the pixels) was randomly indexed and, for a range of k, classified five times. This sampling process was repeated five to ten times. Each sampling had its own mean for each statistic except H_R, which is calculable only once per sampling. The presented means and standard deviations of those means are *between* samplings. No sampling contained fewer than 1,500 pixels. The mean silhouette $\bar{S}(k)$ is often seen as sufficient analysis for the determination of $\hat{k}$ in methods in the literature. Repeat analysis gives the benefit of the standard deviation $\sigma_S(k)$, which frequently peaks just before or after an optimum in $\bar{S}(k)$.

The mean entropy of the silhouette H_S further characterises the silhouette by giving a better idea of the distribution of the values, so lower entropy is more favourable. The increase in the number of classes naturally evens out the distribution of values by introducing more boundaries, therefore H_S is non-linearly proportional to k. The exact form of the curve is not known or suggested, but the logarithmic curve of H_R (essentially constant in form) is used as a reference. In e.g. figure 8.15 (p. 184), H_S has a trough at $k = 5$ for normal data, and a peak at $k = 6$ for decorrelated data. This is reflected in the quality of the silhouettes in figure 8.17 (p. 186) as already discussed (*vide supra*).

The positive silhouette quotient $\bar{Q}(k)$ and its standard deviation reflect the general condition of $\bar{S}(k)$, and both pairs of functions generally (but not always) possess similar features. This otherwise contains no distinct features but gives an indication which values of k give the most bad classifications of pixels. Though it is not analytically intuitive to know when or if $\bar{Q}(k)$ should ever take precedence over $\bar{S}(k)$, it might indicate nearby secondary $\hat{k}$ when it is necessary to distinguish between similar values of $\bar{S}(k)$. Of course, it may be more straightforward to use $\bar{Q}(k)$ as a threshold to narrow down ranges of acceptable solutions.

None but $\bar{S}(k)$ and $\sigma_S(k)$ have produced telling features and maxima at most sampling sizes; the other metrics corroborate these features in some general sense though not always explicitly. The function $\dot{S}(k)$ is of very little use compared to the complete trio; the information it contains is already available in other charts and those can (and should) be evaluated on their own merit.

In the absence of a kernel method, the effective weighting of pixels for k-means favours dense regions over less-dense regions. The immediate downside to this is that regions in the data space which are sparsely populated do not get classified on their own. In such cases, it may be beneficial

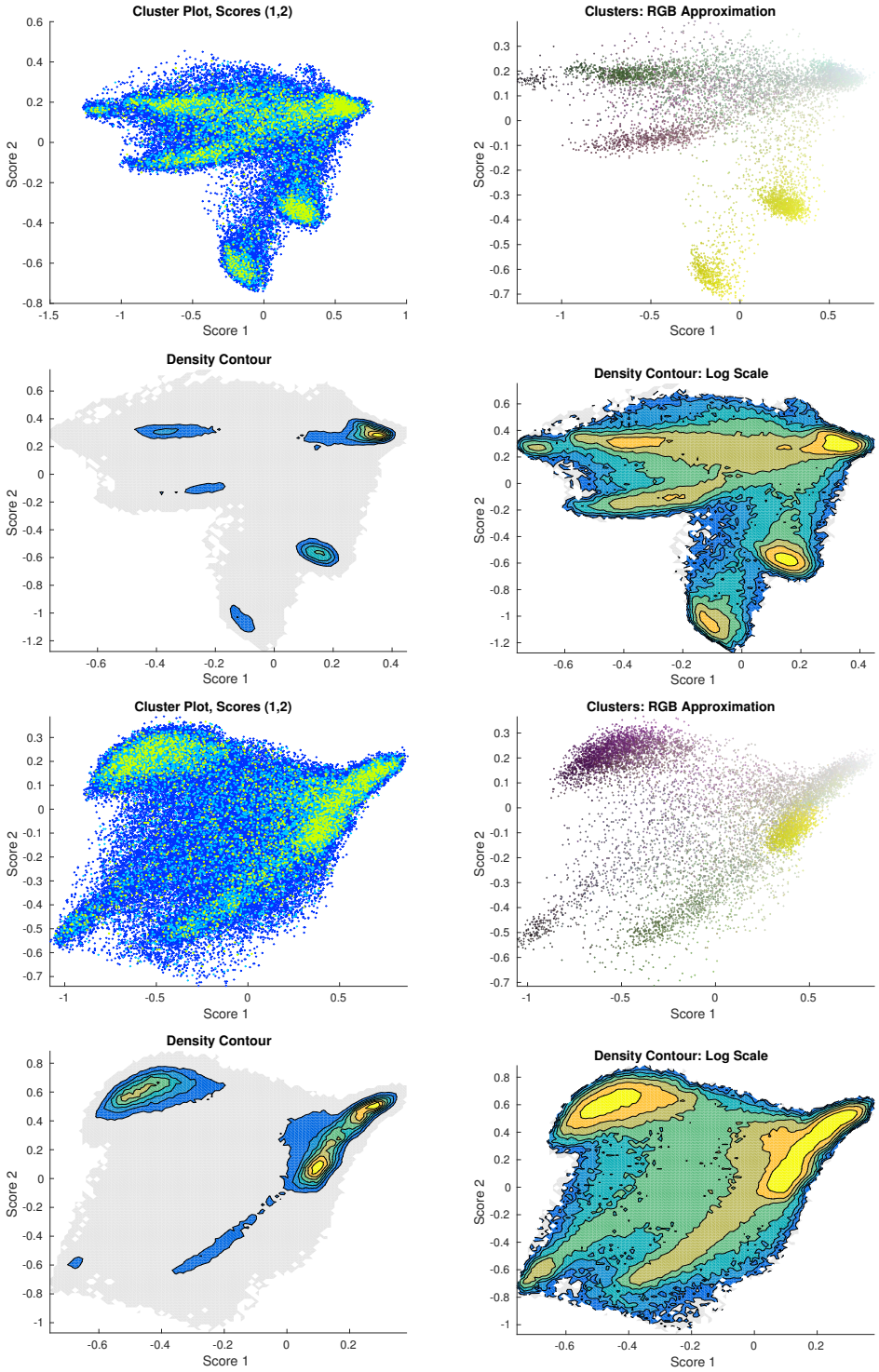

Figure 8.32: Comparison of Density Plots: Examples of the use of scatter plot vs contour plot for deducing the presence of clusters, including the incorporation of colour information (see text). Top Four: bird data. Bottom Four: lion data.

to either define a “drill-core" through the plane of the data that selects data based on proximity to a chosen co-ordinate, or otherwise have the ability to forcibly split a cluster into sub-clusters based on the presence of multiple behaviours. In either case, the cluster itself has to be evident *ab-initio*.

It is possible in more recent releases of MATLAB® to present true density plots for sets of coordinates such as that in figure 8.32 via the output from `hist3()`, which are a little more helpful than the presented scatter plots for deducing cluster centres. The inclusion of colour information in the *RGB Approximation* scatter plots, is achieved by using the data from the 600, 550 and 450 nm filters for red, green and blue colour data, respectively. This gives some sense of relation back to the original manuscript, as well as showing whether clusters managed to properly separate within the current projection.

Colour-Space vs. Eigenspace

Colour spaces excel at characterising and separating pigments when the majority of the distinguishing spectral information lies in the visible range. Hue angle analysis is extremely straightforward to perform on any image in practice, but the data quality and comparability is reliant on standard cameras and illuminants in a way that simply has not been explored in-depth experimentally in this thesis. Colour spaces could be used in education about manuscript studies, or where the resources to train, build and use MSI is limited.

The data reduction by PCA is as useful as the data it represents, but scores clustering is hampered by the orthogonality constraint. Absence of information is problematic and could be supplemented by more images under variable lighting. However, clustering in eigenspaces suffers from the potential for the following paradox of information density, in which additional bands can make the clusters in the initial data space more diffuse, not less. This can be understood as being analogous to signal and noise. Noise causes data within a cluster to spread, as it enhances the differences (dirt, tonal quality, regular image noise) between pixels that nominally represent the same pigment. Signal causes clusters to separate, by providing information that significantly differentiates between pigments (*via* reflectance *differences* between the materials). The benefit of adding a new channel is maximised when its between-pigment information is fully resolved and it is not correlated with any information from other channels (zero redundancy). In a data space bounded by n-cube of side 1, the diagonal of the space is of length $\sqrt{n}$, which is then the maximum length of the principal axis. Addition of new channels increases n, and therefore the maximum benefit of adding a new channel (increase in the dimensions of the data-reduced projection of scores) decreases with increasing n (see figure 8.33, and superfluous channels will detract from separation if the addition of noise outstrips the real-terms benefit of the information.

In an n-space, the only requirement for a displacement vector to point from the centre of the co-ordinate system to the corner of a bounding virtual n-cube of edge a that shares its centre-point with the system, is that each component of the vector is $\pm a/2$, and the dihedral angle between two such vectors is constant. Therefore in the simplest case we use the inner product to generalise that the

acute angle between any two diagonals of an n-cube is given (for $a = 2$) by:

$$\begin{aligned} \text{let:} \quad \vec{a} &= [1, 1, \ldots, 1] \quad \text{and} \quad \vec{b} = [-1, 1, \ldots, 1] \\ |\vec{a} \cdot \vec{b}| &= |\vec{a}||\vec{b}| \cos\theta \\ \text{so as:} \quad |\vec{a} \cdot \vec{b}| &\equiv n - 2 \\ \text{and:} \quad |\vec{a}||\vec{b}| &\equiv \sqrt{n}\sqrt{n} = n \\ \theta &\equiv \arccos((n-2)/n) \end{aligned} \tag{8.7}$$

As $\theta \neq 90°(n \neq 2)$ and tends to 0 with increasing n, we know that even (or especially) when many channels are used, if many channels then contribute to the differences between clusters (as is ideal), the 2D projections will become distorted and the orthogonality constraint prevents the other PC axes from representing other diagonals well unless θ is approximately a factor of 90. Further, as the vertices of the original data space would represent data that is as far removed from other data as possible, we prove what might have been intuitively guessed: the dimensionality reduction is a compromise between euclidean separation and the ability to represent the data with less redundancy and complexity.

It is not possible to add a new channel without introducing noise, and it is also not possible to optimise channels for a manuscript without already possessing the knowledge we seek to gain; although the data reduction might *appear* to remove noise, adding in extra noise only to remove dimensions from the eigenspace with the least information is not the same thing as simply removing the channel with the least information. A channel that clearly distinguishes only one pigment from the others is less information-rich for our purposes than an image which separates a few pigments on a scale or separates the pigments into two extreme ends of a scale. As each PC score is a linear combination of each channel in the MSI stack, each channel contributes the same proportion of both its noise and its signal to a PC, according to its loading for that PC. As these contributions are all orthogonal in the data space, $\sqrt{n}$ still applies and the addition of a new band cannot tighten clusters unless it itself provides the maximum separation benefit (and thus is a major determining factor of the principal axis, the gain to which is shown in figure 8.33) and also has the least noise. As noise is as much a problem of the manuscript's condition as the image collection process, it is not realistic to expect that such a revolutionary band can ever be introduced, and so judicious choice of a limited number of bands remains important.

From figure 8.34 we can determine for the case even of fully-separated clusters, the projection into reduced dimensions can yield clusters that nevertheless don't separate. This doesn't take into account the fact that most clusters aren't ideally spaced in the original feature space.

Therefore it is concluded that for the separation of clusters in reduced dimensions using eigenspaces, there are several competing influences, not all of which are beneficial. Although more information is always gained in the original data/feature space by adding channels, the real-terms cost-benefit of adding more noise to the projections needs to be addressed in the future.

Although an RGB camera does possess only 3 channels, the sensitivity profiles of those channels are complex, overlapping, and span the entire visible spectrum without gaps. So far it has been presumed that an abundance of channels, in providing only explicitly resolved spectral information, would have superior separation capacity because of the "spectroscopic element" which, in a noise-less scenario, would have been ideal. However, the fact remains that information is lost for a multispectral camera when it doesn't possess a full complement of filters across the entire range of wavelengths. The

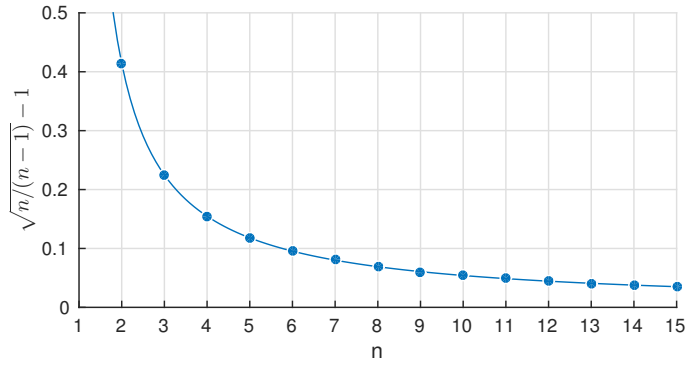

Figure 8.33: Maximum Increase in Principal Axis Length: The maximum increase in principal axis caused by increasing to n dimensions from $n-1$ dimensions, is given by $\sqrt{n/(n-1)}-1$. Although there will never be a zero benefit whilst n is finite, the principal gain is to the principal axis (see text) and the remaining axes lose direct resolving capacity.

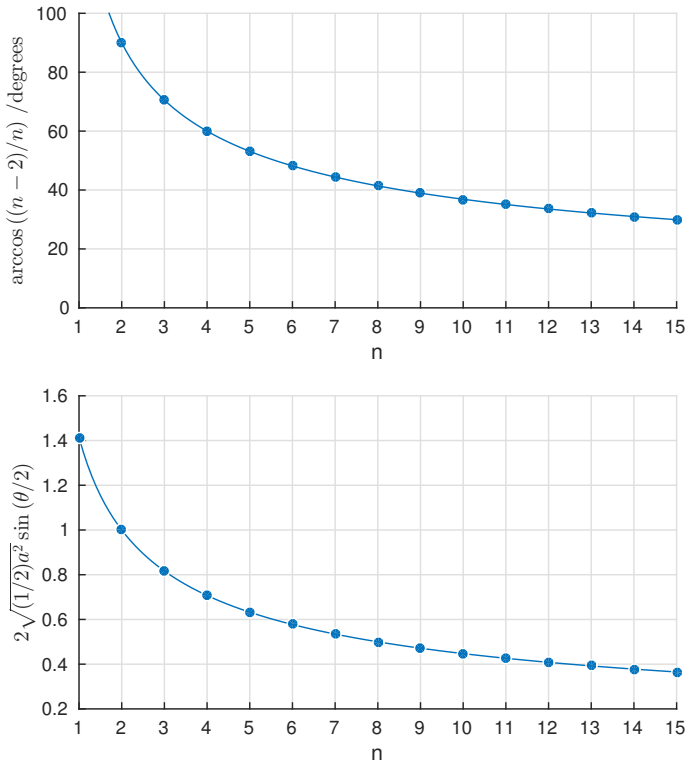

Figure 8.34: Maximum Angular Separability of Ideal Clusters: Top: The vertex-origin-vertex angle (equation (8.7)) between the vertices of an n-cube represent the maximum angular separation that can be achieved by ideally separated adjacent points in a principal plane (see text). Bottom: A simple limiting case of the separation of vertices in plane-projection leads to maximum inter-vertex distances for adjacent vertices, of which there are $(2^n-2)/(n-1)$ in range of a given reference vertex in the feature space ($a=1$). A cluster centroid never reaches a vertex - the data range along the principal axis is 0.89 of maximum, and we define cluster resolution as centroid separation of approximately $3\bar{\sigma}$. From the most ideal cluster we obtain $3\sigma/0.89 \approx 0.44$, giving a limiting optimistic-realism case of $n_{max} = 10$.

advantage of the RGB camera therefore, is the interrelatedness of its bands and the maximisation of information content in only 3 bands at the expense of explicit spectral resolution. The $\sqrt{n}$ problem is largely avoided, though the addition of a NIR and UV channel would be useful for some pigments.

The nominal separation by k-means has nevertheless been shown to work in a near-ideal case. The benefit of decorrelation stretching is dubious or zero on its own, as it defeats the object of PCA. However, clusters that separate poorly in the eigenspace of the unstretched data, can separate well in that of the stretched data, and so it is useful to do both and compare. Furthermore it should now be possible to use `customclust` (see appendices) or similar to do bespoke classification based on the judgement of the operator regarding the density distributions.

8.4.2 NIR Absorption Images and Ratiometrics

Copper pigments absorb NIR light at least as intensely as black iron gall ink. It is this feature which easily distinguishes them from vergaut, therefore we can see in figure 8.35 that this absorption is easily spotted. Further to this, as green pigments must reflect green light well, the ratio of NIR:green light in registered image stacks shows these pigments up especially well, whilst the same cannot be said for most other pigments. In the insular pigments, the only other green (vergaut) is reflective in the NIR.

Using the scores images, false colour stacks (Set each score to represent RGB values) show contrast between pigments without having to perform a classification, as shown in the figure 8.36. This level of contrast is not possible to achieve with the original data and contains spectral information not contained in RGB images.

8.4.3 DRS & Raman Spectroscopy

The analysis of ancient manuscripts is summarised in table 8.3. The data in table 8.3 is meta-analysed in figures 8.39 and 8.40 as graphical representations.

Identification of Pigments

The analysis by NNMF produces either a straightforward basis set or one which is evidently dubious, though the latter cases arise more due to the choice and quality of data. This is most often when there is high redundancy or little data to begin with. In the single and dual-pigment cases presented in this thesis, it removes contributions from parchment substrate without having to acquire a spectrum of parchment itself.

Most identifications by Raman spectroscopy were straightforward, presenting appropriate spectral features for positive confirmation of pigment. However copper green, azurite, black inks and orcein were problematic in that they rarely if ever provided any spectra. Copper greens include several samples of malachite in crushed and solid form obtained from the Department of Geology at Durham University. With incremental power under the LWD objectives used for books, all of these samples produced spectra with either 633 or 532 nm lasers before they were destroyed by the laser. A crystal of azurite provided by Dr Kate Nicholson did not yield a Raman spectrum except under a 100× objective at unacceptably high power density for manuscripts work. The spectra for laboratory chemicals and the green patinas on coins, are shown in figure 8.37. The coins did not yield spectra in the grooves where oils might accumulate, but the spectra presented were taken from the green layer. The difficulty of confirming inorganic green and blue copper is illustrated in the use of high incident power by Clark; it was only by dredging the gutter between the pages of the Lindisfarne Gospels, that a sample

Figure 8.35: NIR absorption by copper green. CCCC 197b, visualised with NIR:green ratiometric imaging. The images on the left are from [185] for comparison. Top: *f.* 2r (p. 247) Bottom: *f.* 1r (p. 245). The dark regions on the right are copper green.

	carbon	*iron gall*	*orcein*	*red ochre*	*white lead*	*indigo*	*vergaut*	*orpiment*	*red lead*	*copper green*	*lapis lazuli*	*vermilion*	*vermilion + red lead*	*orpiment + vermilion*	*orpiment + lapis*	LAYERING
Bamburgh																
Select 6				✓	✓				✓	✓	✓	✓				✓
C.C.C.C.																
183			D			+		✓	+*							
197b								✓	✓*	✓						
D.C.L																
A.II.10						+	+	+	+							
A.II.16		D						+	+*							
A.II.17		D	D					+	+*	+						
A.IV.19				✓												
B.II.13									✓	✓	✓	✓	✓			
B.II.30									✓*	✓						
B.IV.6		D														
D.U.L Cosin																
V.II.6								✓	+	+	+	✓	✓		✓	✓
V.III.1										+	+	+				
V.V.6								✓	✓	✓	✓	✓		✓		✓

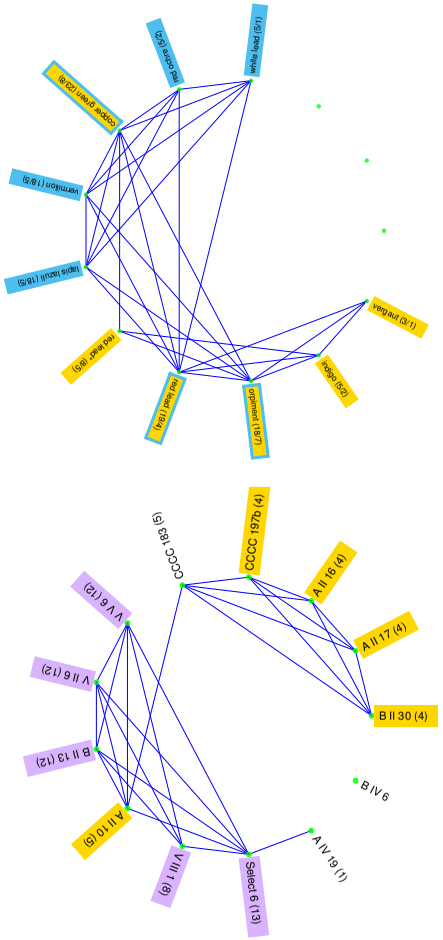

Table 8.3: Summary of Raman & DRS Analysis: Left: The pigment content of thirteen bound volumes, as demonstrated by Raman and DRS spectroscopy. The pigments in the column headers are described in §7.1.1. Where multiple pigments are indicated as per *vermilion + red lead*, this indicates that the named pigments were found in intimate contact. The manuscripts are in alphabetical rather than chronological order, organised by library. A.II.17 is *ff.* 2-102 (The Durham Gospels); the data for *ff.* 103-111 indicates exclusively iron gall. Right: Connectivity diagrams from figures 8.39 and figure 8.40 (*see text*).

Key: D: DRS assignment, +: Raman with a supporting DRS assignment, ✓: Raman assignment, *: PbO contamination.

Figure 8.36: False Colour Imaging with Maximised Contrast: The high contrast provided by PCA is ideal for false colour imaging using the maximum amount of information possible.

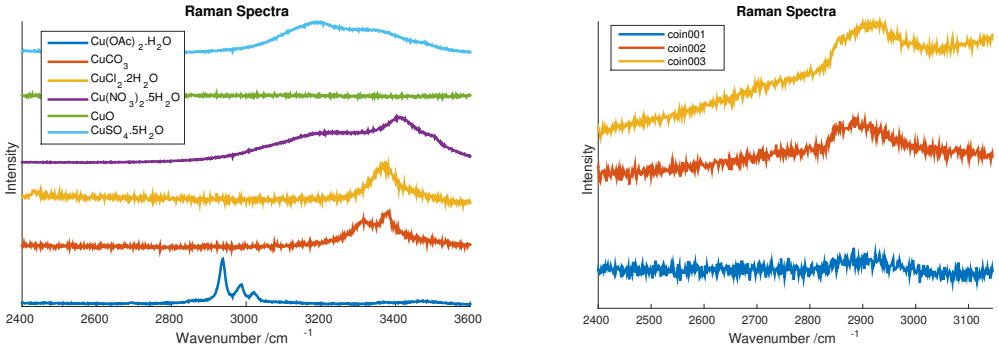

Figure 8.37: Raman Spectra of Copper Chemicals: The spectra shown here are of laboratory chemicals and the green patinas on copper coins. The $-CH_3$ stretches and proton stretches of water are plainly visible. The coins did not yield spectra in other parts of the coin.

of green pigment could be obtained "non-destructively" that was suitable for potentially destructive analysis [140, 186].

Black carbon inks produced in the laboratory from activated charcoal do easily yield Raman response, but can be destroyed by localised heating by the laser even at low incident power. An iron gall formed crudely in the laboratory from oak galls, red wine, gum arabic and ferrous sulfate, did not produce a Raman spectrum, but its DRS spectrum is presented in figure 8.38.

The Book of Kells (Trinity College Dublin MS 58, an early insular book from Ireland) uses both carbon and iron gall inks [187]. We might anticipate that any of the insular books analysed might contain one or both of these pigments due to the transfer of this technology through the Irish missionaries that ultimately produced them. The remission spectrum of carbon ink is essentially flat well into the infra-red [177], whilst that of iron gall inks is *lower* in the infra-red. The MSI technique (*vide supra*) is in principle capable of distinguishing between iron gall and carbon if it uses at least one filter far enough into the infra-red to make the difference noticeable. However, if we seek only to characterise or differentiate ink, the imaging technique referenced in [187] is certainly capable of doing so and is

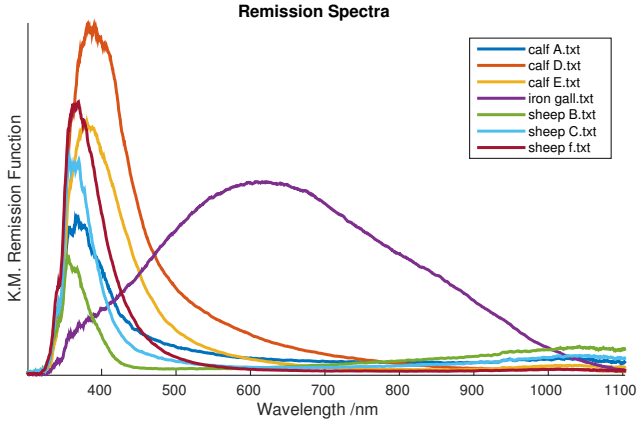

Figure 8.38: DRS of Iron Gall and Parchment: The DRS remission spectra of a lab-prepared iron gall, and several samples of parchment provided by Professor Richard Gameson. This demonstrates the native variability in the absorption maxima of parchment.

more straightforward.

Even in cases where carbon might be explicitly seen in a Raman spectrum, due to the effects of local heating on an unknown black it is plausible that pyrolysis of the pigment and of carbon-containing polymers in the surrounding matrix such as gums and resins, could yield carbon allotropes *in-situ*. Therefore care must be taken in acquiring Raman spectra of black inks, so that photo-destruction of the sample region cannot be confused for carbon. This is the case even for laser power that is known to be safe to other pigments on a page, as it is the high absorbtivity of a black pigment that makes it vulnerable. Therefore, a multi-spectral imaging technique capable of specifically visualising which pigments have high or low NIR reflectance, is desirable. It can be seen in all unambiguous DRS spectra of black and brown materials, that the ink is iron-based rather than carbon, but as in [187] it may not be visibly obvious *where* the scribe has made a transition between inks, if at all, and so an imaging technique is preferable to DRS in this case.

Meta-analysis of pigments

Using only the Raman data, a graph is constructed in figures 8.39 and 8.40. We exclude data for iron gall, carbon and orcein because not all purples and inks were confirmed, and so any connectivity due to these pigments is not wholly consistent with a palette; their nodes still exist in the diagrams, though they are empty to demonstrate their deliberate absence. A symmetric permutation of the underlying data places the nodes that have the least in common with one another far away, whilst those with the most in common are adjacent. By comparison, all other pigment colours were positively identified by Raman. The palettes can be divided into two major ones, insular and Norman. The insular palette is indigo, vergaut, orpiment, red lead (with PbO) and copper green. The Norman palette is red lead (pure), copper green, lapis lazuli, vermilion, red ochre and white lead. Figure 8.39 also effectively excludes the data from the Collectar DCL A.IV.19, because it contains only one pigment that was positively identified.

The books split generally into two categories: insular and Norman influence, using the respective palettes (though CCCC 183 is not insular itself). The split between the palettes is a demonstration of both knowledge/technology and availability. On one hand, the difference between the qualities of

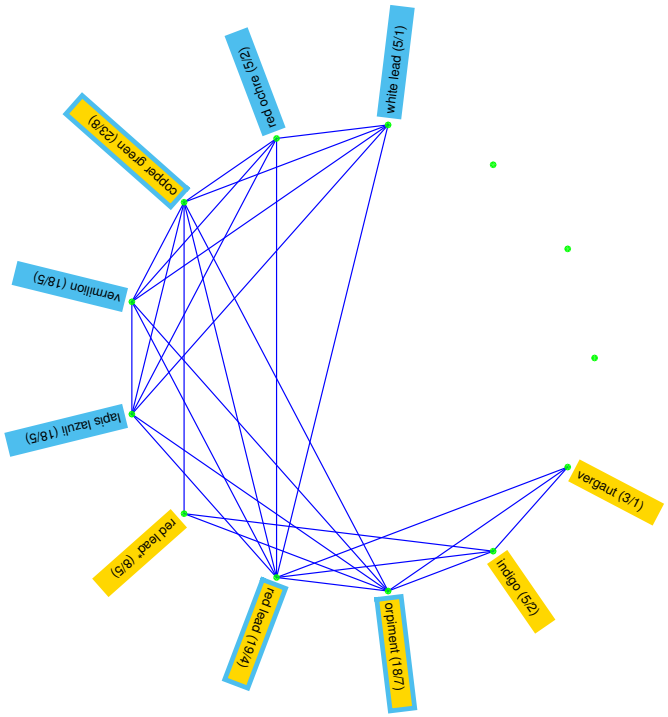

Figure 8.39: Raman Pigment Connectivity: This is a re-representation of the data in table 8.3, with respect to common use of pigments. Pigments are shown as labelled nodes. Nodes with at least one book in common with one another are joined by an arc. The labels have been colour-coded so that insular pigments are in yellow, non-insular are in blue, and those spanning both are yellow with a blue border. As the arcs could not be shown with variable weight for repeat co-occurrence, numbers in parentheses represent the total weight of all arcs between that pigment and any other pigments, and the number of manuscripts in which they occur. Carbon, iron gall and orcein stand as empty nodes, as none produced any Raman signal.

red lead almost divides the books into pre- and post-1066, the exception being The Gospel Book DCL A.II.10. Though absence of evidence is not evidence of absence, the general finding is that $Pb_3O_4 + PbO$ is not uncommon or difficult to get a spectrum of, and in one instance a pure massicot spectrum is observed in a red lead patch in A.II.17 *f.* 38(4)r. On the other hand, the pigments lapis lazuli and vermilion are used exclusively post-1066. It is shown in figure 8.40, that removal of the more ubiquitous pigment data leaves only strong correlations between use of vermilion and lapis, and pure or impure red lead to leave two islands of book types, bridged by the use of indigo. Further, figure 8.39 shows that, ignoring the red lead, copper green and orpiment data, two 'islands' of pigments are found.

This is consistent with the findings of Brown in [188]. English manuscripts post-1066 have a richness of palette based on mineral pigments, that comes from better trade in both skills and luxuries with the continent. The connectivity graphs demonstrate intuitively what is perhaps harder to show in a table: pigments split into groups based on book commonalities, and books split into groups based on pigment commonalities. This is still evident when most of the information is retained and select redundant information is discarded.

The the truly insular manuscripts here (even though they sometimes contain multiple types of green and the identity of the purples has not been confirmed for all of them), they never contain purple and blue *together*. The Lindisfarne Gospels use both [186].

The Lindisfarne Gospels and the Book of Kells use both vergaut and copper greens [186, 187]; there is otherwise no specific or definitive pattern regarding the availability of orpiment and indigo and the use of vergaut, though in the manuscripts here, they are always used separately.

Speculative Considerations

The knowledge and availability of woad and orchil may be responsible for the blue/purple issue. Orchil makes an intense blue-violet colour in base, though it can be speculated that the action of carbon dioxide and atmospheric moisture over time could shift the hue closer to the neutral purple. It is however generally assumed that orcein was intended to be used as a cheaper substitute for tyrian purple (§7.1.1). Woad on the other hand, demands specialist knowledge and effort to extract indigo. In the event of a catastrophic loss of an apprentice-less master scribe [189] or a crop of woad (or simply running out of a stock of pigment in the absence of both), a scriptorium might be starved of an indigo supply indefinitely until a replacement could be found. This being the case, orcein *might* have been seen as an attractive alternative pigment which, although not blue, still fills a gap in the spectrum of hues.

It is not clear exactly where orpiment came from in the British isles. Short of import from known sources in mainland Europe, there is no reason why arsenic sulfides couldn't at some point have been sourced from small accumulations in hydrothermally active regions such as the Lake District [190]. Any volcanic waters might in principle contain or deposit arsenic, but as arsenic is monoisotopic it is unlikely that this problem will ever be solved. It is certainly the case that insular scribes had access to it, and that they used it frequently, whilst later and continental sources used it less frequently. Whether this is simply a difference in practices or insular scribes had unprecedented access to orpiment, is not clear.

White lead roasting to form red lead is a specialist skill [148]. It is straightforward to obtain a pigment of the right general red-orange hue, but complete roasting to obtain pure Pb_3O_4, requires either intimate understanding of how to work a furnace, a method that produces it coincidentally, or a

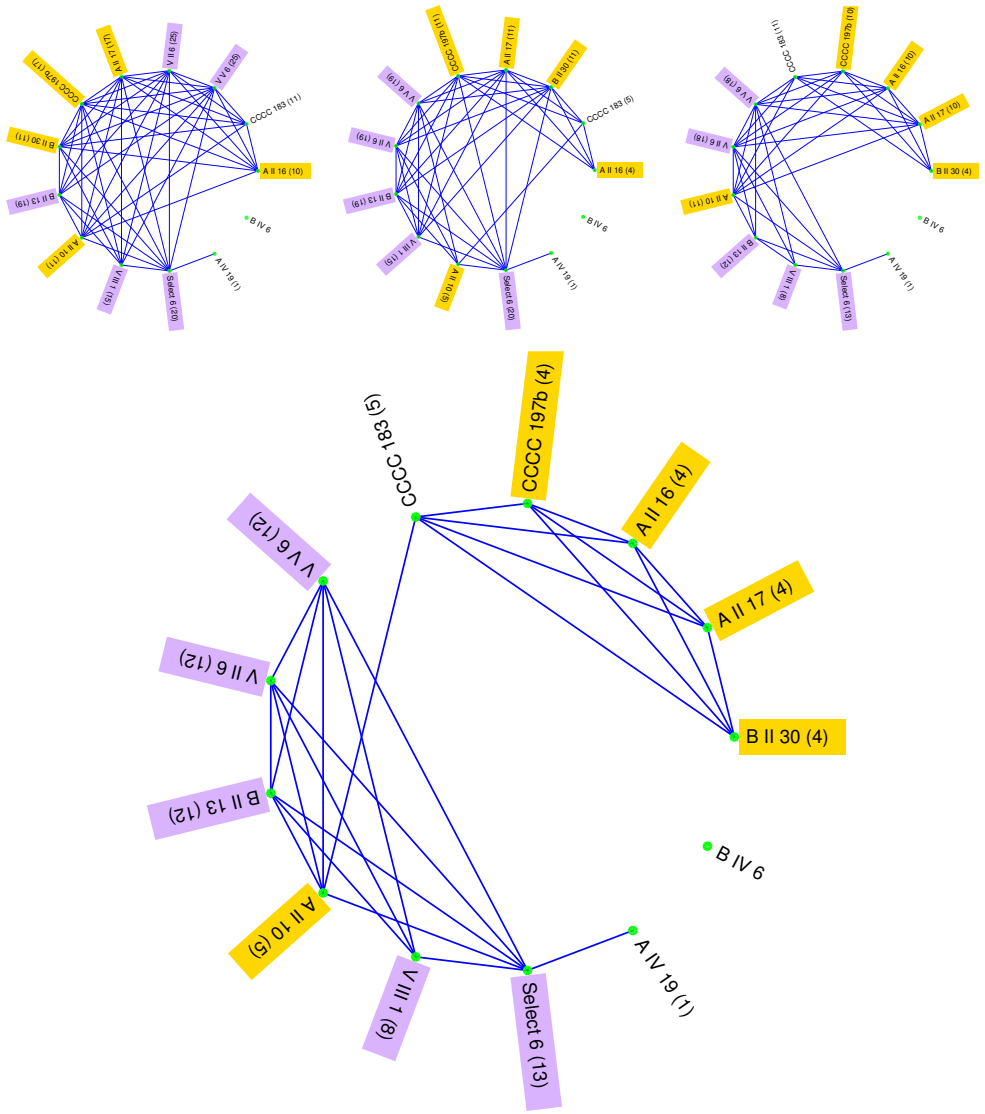

Figure 8.40: Raman Book Connectivity: This is a re-representation of the data in table 8.3, with respect to common use of pigments between books. Books are shown as labelled nodes. Nodes with at least one pigment in common with one another are joined by an arc. The labels have been colour-coded so that the five insular manuscripts are in yellow, whilst the books that use lapis lazuli and vermilion are in lilac. As the arcs could not be shown with variable weight for repeat co-occurrence of pigments, numbers in parentheses represent the total weight of all arcs between that book and any other books. In Reading Order: Red lead data have been split into pure and impure in all cases. First all pigments are included that are present in at least two books. Second, orpiment data is then omitted. Thirdly, copper green data is omitted and orpiment data reintroduced. Finally, neither orpiment nor copper green data are included. B IV 6 stands alone as an empty node, as no Raman spectra could be acquired.

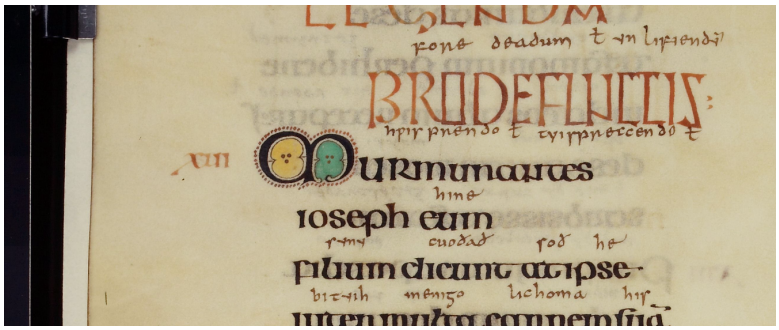

Figure 8.41: Cotton Nero D IV: Dots on Orpiment: The Lindisfarne Gospels Cotton Nero D IV, showing dots atop orpiment on *f.* 205v. Image accessed 1st February 2017, courtesy of The British Library Digitised Manuscripts collection at http://www.bl.uk/. This image is in the Public Domain.

precise temperature controller. If it is instead produced from litharge, there would be no reason for the manufacturer to know to remove the lead (II) oxide impurities by washing with aqueous hydroxide. It could be that the impure form is produced and used by insular scribes with inferior technology or a different method, and another by the continental and southern English. Given the presumed abundance of lead metal from mining, lead white by environmental exposure of lead metal (and lead oxides by extension), it might never be entirely clear why this divide exists. The isotopic distribution and half lives of lead are not useful for determination of British vs continental provenance, as the half-lives of the natural isotopes of lead are either very long (>50,000 years) or very short (<50 years), and mass spectrometry requires destructive sampling.

Pigment Mixing

Red lead was never seen used in direct contact with orpiment. Insular scribes (certainly after A.II.10) leave bare parchment borders about their pigment blocks, and they certainly do not layer pigment as a matter of course. The exception to this can be seen in the digitised Lindisfarne Gospels (figure 8.41), where red pigment dots are layered on top of orpiment infills for purposes unknown. It is speculated that this is either red lead or red ochre. Later manuscripts don't combine sulfides with lead pigments save for vermilion and red lead, due to well-known darkening of pigment. In the historiated initial on Symeon *f.* 77v, this mixture results in darkening of red lead and vermilion without totally obscuring the artwork. Simple experiments in the laboratory reveal, that a 1:1 by weight mixture of loose powdered orpiment and either white or red lead ground to a homogeneous powder begins as a pale lemon yellow, but discolours within three days and turns completely grey within a matter of weeks; vermilion and red lead mixtures produce no visible change during the same time frame. Both white and red lead darken intensely in a matter of seconds in the effluent stream of a simple $H_2S_{(g)}$ generator ($Fe_2S_{3(s)} + 6\,HCl_{(aq)} \longrightarrow 3\,H_2S_{(g)} + 2\,FeCl_{3(aq)}$), but are stable enough to traces of $HCl_{(g)}$ and water vapour to produce no colour change prior to introduction of Fe_2S_3 to the generator reaction vessel. It is therefore reasonable to say that insular scribes either knew to keep nearly all of their base colour palette separate from one another, or they developed an artistic style that didn't require much mixing and vergaut was simply an exception.

Copper Green

The wavelength of minimum green remission of the copper green, varied between 500-540 nm, which is more consistent with an aged basic verdigris in egg tempera, but less consistent with neutral verdigris, or either in gum arabic [144, p. 136]. This would suggest the presence of copper proteinate and oleate complexes, which would in turn explain the relative abundance of $-CH_3$ vibrational stretching modes in the Raman spectrum of green compounds.

8.5 Conclusion & Further Work

In conclusion, this part of the thesis has established original contributions to knowledge in two forms. Firstly, the palettes of the earliest Northumbrian and related manuscripts in the lead-up to and immediately following the Battle of Hastings. Secondly, methods to apply MSI-PCA and colourimetry with an ordinary RGB camera for separation of pigments in a manuscript by imaging.

The establishment of the palettes is essentially complete with regard to the pigments, but not the ink. The ink was itself not a focus except when pigment was sparse or absent, but has otherwise proven to be iron gall where proof exists.

There is no evidence of tyrian purple in these manuscripts whatsoever, though a campaign of reflectance spectroscopy would be useful in order to compare and contrast the uses of purple in these manuscripts. Where it can be identified, the purple pigment is always orcein.

Red lead has varying quality and is often prone to degradation in manuscripts. However, the confirmation of PbO in red lead for manuscripts with known provenance, is of greater interest as a forensic measure. As red lead can be formed by roasting white lead or PbO, but PbO has been historically formed by simply heating molten lead metal in air [148, pp. 100–103], it would be a more primitive and straightforward method to produce red lead directly as a by- or end-product of simply smelting lead ores. White lead roasting creates a pure Pb_3O_4 at temperatures not exceeding 300° C, but PbO starting material leaves impurities, therefore PbO always implies either primitive methods, unskilled labourers, or both.

The limitations of NNMF in determining pigment content might be overcome in the future by using larger data sets that optimise for the method. Also, as NNMF for spectral analysis so far discards the other information comparable to scores, these data could be used in future to map relative spectral contributions, though the utility of this information is low for spatially unresolved data. NNMF has been applied to the spectral imaging of fluorescence, in order to use this information to image the locations of known independent fluorescers in a solution. A similar technique would be useful to develop for reflectance imaging, which would if successful characterise each pixel according to the amount of e.g. dirt and the contribution of each pigment spectrum, which effects a map of effective pigment concentration rather than requiring any laborious classification method in a hyperspace. This would require however a considerable amount of virtual memory, though this could soon become available in portable form.

In the analysis of manuscripts by laser for μ-Raman it is essential that the flux does not exceed a level that is considered safe, such that heating of the sample voxel does not result in damage. The real limit of non-destruction is defined as much by the sample absorptivity as by the instrument, though as the freedom to experiment with this on real manuscripts should be considered unavailable, it is sensible to observe safe operating limits used by earlier researchers.

If we begin by defining flux in a 2D cross-section of a beam as $\rho = W/A$, where W is area integrated power at the sample in Watts, and A is cross-sectional area in m^2, then the limiting power in the cross section W_{lim} is given as the product of a limiting flux ρ_{lim} and the area of the laser spot. We define the size of a confocal spot in a microscope system as the Airy disk, which as previously mentioned has an effective diameter:

$$d_A = \frac{1.22\lambda_0}{2 \cdot \mathrm{NA}}$$

where NA is the numerical aperture of the objective, and λ_0 is the vacuum wavelength of the laser. It is then straightforward to convert this to a disk area, $\pi(d_A/2)^2$. In [191, Chapter 1], the limiting factors are a power of 4 mW, and 3 μm diameter spot, constituting $\rho_{lim} = 5.66 \times 10^8$ W m^{-2} , giving the following expression:

$$W_{lim} = \frac{5.66 \times 10^8 \pi}{10.74} \left(\frac{\lambda_0}{\mathrm{NA}}\right)^2 \tag{8.8}$$

where 10.74 is a dimensionless constant equal to $(4/1.22)^2$, so that this expression further reduces with a useful unit conversion (10^{-15} mW m^{-2} W^{-1} nm^{-2}) to:

$$W_{lim} \approx 1.636 \times 10^{-7} \mathrm{mW\ nm^{-2}} \left(\frac{\lambda_0}{\mathrm{NA}}\right)^2 \tag{8.9}$$

giving now W_{lim} in mW. Higher NA has lower tolerance for incident power, but also lower power requirements to achieve high power densities. For this reason it is more efficient to use higher NA when examining manuscripts, and also the scattered light is more easily collected. Of course, with the necessity of LWD objectives this becomes limited.

In practical terms, it is now straightforward to use equation 8.9 to calculate the limiting power for any μ-Raman system and select appropriate filters by direct measurement of power exiting the objective. If the proposed limiting power is reconsidered, even perhaps substituting for a value calculated from e.g. a remission or reflectance function, one may recalculate easily from equation 8.8. A review of destructive power and experimental work would be useful future work in this regard, especially with respect to pigments with high attenuation of excitation wavelengths such as black pigments.

Christian [192] describes an illumination system for imaging that uses diffuse, oblique LED lighting instead of filters, using a reference white to normalise values to be comparable to reflectance, and a machine-learning algorithm to differentiate iron gall inks. The wavelength ranges covered by that system are not continuous, though the lighting is always ideal. In any case, Christian uses the images individually as diagnostics as well as using laboratory samples for direct comparison with machine learning. An LED array in a dedicated manuscripts cradle, although not specific with regard to bandpass into the camera, is nevertheless ideal for facile automated capture with an absence of mechanical parts. The camera needs to be focused only once, and if the lens is achromatic the images will never require registration.

Although the separation of pigments using multispectral data was not a misguided effort per se, it remains to be seen whether introducing many bands to the data will in actuality hamper or aid a classification procedure. The classification as it currently stands is unsatisfactory but could easily be improved. If the principal axis can be constrained to a diagonal and the data appropriately centered, a cosine separation will separate data into segments in a 2D projection. This should work for a*b* without further adaptation, and the hue-angle spectrum might prove useful in a similar manner as

infra-red correlation tables.

Mean shift segmentation uses the co-ordinates in a data space alongside the spatial information in the image, to overcome problems of resolution in the data space whilst simultaneously providing classification. It is explained completely with working example code in [174, Chapter 6], that can be modified for use with many channels. This can take a considerable amount of time to complete, though Freedman has developed a procedure that achieves this end very speedily [193].

The use of an infra-red sensitive camera and a simple filter can be used to find distributions of copper-based pigments on manuscripts, and with two filters the copper green can be differentiated from iron gall inks. Supplementing the R channel of an RGB image with data from a registered NIR image can skew the colour of iron gall inks, but not carbon, and the combination of MSI channels for false-colour representation (in the form of ratiometrics and false-colour RGB stacks) is a reasonably potent demonstration technique in both the case of extreme differences of reflectance within a pigment patch (ratiometrics) and comparatively small differences between pigments. Contrast between scores images themselves, or using scores images as RGB false colour channels, highlights differences between pigments without having to undertake explicit classifications.

In conclusion, although classification techniques are useful and interesting for comparatively facile mapping of pigments, the manual analysis of MSI data on its own merit, is nevertheless still useful. Development of unsupervised classification for manuscript studies using imaging is a step that would be useful to take for the purposes of education and dissemination, and as a tool to supplement portabilised techniques such as Raman spectroscopy, but it is not entirely straightforward to develop. Raman spectroscopy, despite its shortcomings, remains a sensitive and effective (though comparatively laborious and specialist) non-contact tool for the analysis of pigments, the portabilisation of which should remain a focus for research alongside imaging and DRS.

Appendix A

Digital Content: Disc

The following digital content is available on the supplied compact disc:

A.1 Part I

This folder contains the fluorescence excitation-emission and lifetime analyses of dyes. It also contains the LabVIEW virtual instruments written to control the monochromator.

A.2 Part II

There is no easy way to distinguish which Raman and DRS spectra from Part II were taken by myself, Prof. Andy Beeby, Prof. Tony Parker or Dr Kate Nicholson, and so I acknowledge here that an unspecifiable proportion of that data has in fact been freely shared in the interest of scholarship.

This folder contains the DRS & Raman spectra, and MATLAB® suite of programs written to analyse image data.

References

[1] A. Gilbert and J. Baggott. *Essentials of Molecular Photochemistry*, (Blackwell Science1990).

[2] C. E. Wayne and R. P. Wayne. *Photochemistry*, (Oxford University Press1996), 1st edition.

[3] J. D. Coyle. *Introduction to Organic Photochemistry*, (Wiley1986), 1st edition.

[4] "Supplement Volume IV: Fluorescent Whitening Agents". In F. Coulston (Ed.), "EQS: Environmental Quality and Safety", , (Georg Thieme1975).

[5] K. Hunger (Ed.). *Industrial Dyes*, (Wiley2003), 1st edition.

[6] R. A. Watson. "Laundry Detergent Formulations". In M. S. Showell (Ed.), "Handbook of Detergents Part D: Formulation", chapter 3, (CRC Press2009).

[7] D. Barton and H. Davidson. "Fluorescent Brighteners". *Rev. Prog. Coloration* (1974) **5**:3–11.

[8] B. Hapke. *Theory of Reflectance and Emittance Spectroscopy*, volume 3 of *Topics in Remote Sensing*, (Cambridge University Press2005), 1st edition.

[9] R. M. Christie. *Colour Chemistry*, (RRC Publishing2015), 2nd edition.

[10] T. Shakespeare and J. Shakespeare. "A fluorescent extension to the Kubelka-Munk model". *Color Res. Appl.* (2003) **28**:4–14.

[11] P. N. Euan Magennis. Unpublished data in a private communication (2013).

[12] C. D. Byrne. *Angle-Resolved Evanescent Wave Induced Fluorescence Spectroscopy: A Tool for Quantitative Interfacial Analysis.* Ph.D. thesis, Imperial College of Science, Technology and Medicine (2000).

[13] G. Rumbles, A. J. Brown, D. Philips, and D. Bloor. "Surface-induced chromism and enhanced fluorescence of the soluble polydiacetylene, poly(4-butoxycarbonylmethylurethane), at a solid/-solution interface: an evanescent wave induced fluorescence study". *J Chem. Soc. Faraday Trans.* (1992) **88**:3313–3318.

[14] D. Ausserre, H. Hervet, and F. Rondelez. "Concentration dependence of the interfacial depletion layer thickness for polymer solutions in contact with nonadsorbing walls". *Macromolecules* (1986) **19**:85–88.

[15] J. Edwards, D. Ausserre, H. Hervet, and F. Rondelez. "Quantitative studies of evanescent wave intensity profiles using optical fluorescence". *Applied Optics* (1989) **28**:1881–1884.

[16] C. A. Scholes. *Conformational Aspects of Macromolecular Adsorption through Evanescent Wave Induced Spectroscopy*. Ph.D. thesis, University of Melbourne (2007).

[17] M. L. Gee, L. Lensun, and T. A. Smith. "Time-resolved evanescent wave-induced fluorescence anisotropy for the determination of molecular conformational changes of proteins at an interface". *Eur. Biophys. J.* (2004) **33**:130–139.

[18] H. Masuhara, S. Tazuke, N. Tamai, and I. Yamazaki. "Time-resolved total internal reflection fluorescence spectroscopy for surface studies". *J. Phys. Chem.* (1986) **90**:5830–5835.

[19] G. Rumbles, A. J. Brown, and D. Philips. "Time-resolved evanescent wave induced fluorescence spectroscopy". *J. Chem. Soc. Faraday Trans.* (1991) **87**:825–830.

[20] J. R. Lakowicz. *Principles of Fluorescence Spectroscopy*, (Kluwer Academic/Plenum Publishers1999), 2nd edition.

[21] N. J. Harrick. *Internal Reflection Spectroscopy*, (Wiley Interscience1967), 1st edition.

[22] B. P. Straughan and S. Walker. *Spectroscopy*, volume 2, (Chapman and Hall1976).

[23] V. May and O. Kühn. *Charge and Energy Transfer Dynamics in Molecular Systems*, (Wiley2004), 2nd edition.

[24] https://chem.libretexts.org/Core/Physical_and_Theoretical_Chemistry/Fundamentals/Fluorescence_Resonance_Energy_Transfer. Accessed: 2017.

[25] A. McNaught and A. Wilkinson (Eds.). *Compendium of Chemical Terminology*, (Blackwell1997), 2nd edition.

[26] https://chem.libretexts.org/Core/Physical_and_Theoretical_Chemistry/Fundamentals/Dexter_Energy_Transfer. Accessed: 2017.

[27] E. Hecht. *Optics*, (Addison-Wesley2001), 4th edition.

[28] W. N. Hansen. "Expanded formulas for attenuated total reflection and the derivation of absorption rules for single and multiple ATR spectrometer cells". *Spectrochim. Acta* (1965) **21**:815–833.

[29] A. T. R. Williams and S. A. W. J. N. Miller. "Relative fluorescence quantum yields using a computer-controlled luminescence spectrometer". *Analyst* (1983) **108**:1067–1071.

[30] W. Becker. *Advanced Time-Correlated Single Photon Counting Techniques*, (Springer2005), 1st edition.

[31] P. Soleillet. "Sur les parametres caractérisant la polarisation partielle de la lumière dans les phénomènes de fluorescence". *Ann. Phys. Biol. Med.* (1929) pp. 23–97.

[32] D. R. Lide (Ed.). *Handbook of Chemistry and Physics*, (CRC Press1990), 71st edition.

[33] A. J. deMello, B. Crystall, and G. Rumbles. "Evanescent wave spectroscopic studies of surface enhanced fluorescence quantum efficiencies". *J. Colloid Int. Sci.* (1995) **169**.

[34] P. Wong-Wah-Chung, G. Mailhot, and M. Bolte. "4,4'-diaminostilbene-2,2'-disulfonate (DSD) behaviour: under irradiation in water. Decrease of its activity as a fluorescent whitening agent." *J. Photochem. Photobiol. A* (2001) **138**:275–280.

[35] J. M. Dyer, C. D. Cornellison, S. D. Bringans, G. Maurdev, and K. R. Millington. "The photoyellowing of stilbene-derived fluorescent whitening agents - mass spectrometric characterization of yellow photoproducts". *Photochem. Photobiol.* (2008) pp. 145–153.

[36] K. R. Millington and G. Maurdev. "The generation of superoxide and hydrogen peroxide by exposure of fluorescent whitening agents to UVA radiation and its relevance to the rapid photoyellowing of whitened wool". *J. Photochem. Photobiol. A* (2004) **165**:177–185.

[37] A. Pappas, S. Johnsen, J.-C. Liu, and M. Eisinger. "Sebum analysis of individuals with and without acne". *Dermatoendocrinol.* (2009) **1**:157–161.

[38] R. M. B. Mackenna, V. R. Wheatley, and A. Wormall. "The composition of the surface skin fat ('Sebum') from the human forearm". *J. Invest. Dermatol.* (1950) **15**:33–47.

[39] M. Picardo, M. Ottaviani, E. Camera, and A. Mastrofrancesco. "Sebaceous gland lipids". *Dermatoendocrinol.* (2009) **1**:68–71.

[40] Y. Nishiyama, H. Chanzy, and P. Langan. "Crystal structure and hydrogen-bonding system in cellulose 1(beta), from synchrotron X-ray and neutron fiber diffraction". *J. Am. Chem. Soc.* (2002) **124**:9074–9082.

[41] Y. Nishiyama, J. Sugiyama, H. Chanzy, and P. Langan. "Crystal structure and hydrogen bonding system in cellulose 1(alpha), from synchrotron X-ray and neutron fiber diffraction". *J. Am. Chem. Soc.* (2003) **125**:14300–14306.

[42] T. F. Cooke, J. H. Dusenbury, R. H. Kienle, and E. E. Lineken. "Mechanism of imparting wrinkle recovery to cellulosic fabrics". *Text. Res. J.* (1954) **24**:1015–1036.

[43] "Cotton Morphology and Chemistry". http://www.cottoninc.com/product/NonWovens/Nonwoven-Technical-Guide/Cotton-Morphology-And-Chemistry/. Accessed: Nov 2015.

[44] L. E. Hessler and R. E. Power. "The use of iodine adsorption as a measure of cellulose fiber crystallinity". *Text. Res. J.* (1954) **24**:822–827.

[45] P. J. W. et al. *Cotton Fiber Chemistry and Technology*, (CRC Press2007), 3rd edition.

[46] G. K. Cooper, K. R. Sandberg, and J. F. Hinck. "Trimethylsilyl cellulose as a precursor to regenerated cellulose fiber". *J. App. Polym. Sci.* (1981) **26**:3827–3836.

[47] "Tencel at Courtaulds: From Genesis to Exodus and Beyond". http://www.lyocell-development.com/p/introducing-tencel.html. Accessed: June 2017.

[48] W. Schempp, T. Krause, T. Seifried, and A. Koura. "Production of highly substituted trimethylsilyl cellulose in the system dimethylacetamide/lithium chloride". *Das Papier* (1984) **38**:607–610.

[49] K. Saalwächter and W. Burchard. “Cellulose Solutions in Water Containing Metal Complexes”. *Macromol.* (2000) **33**:4094–4107.

[50] K. Ruel, Y. Nishiyama, and J.-P. Joseleau. “Crystalline and amorphous cellulose in the secondary walls of Arabidopsis”. *Plant Science* (2012) pp. 48–61.

[51] S. D. Zhu, Y. X. Wu, Q. M. Chen, Z. N. Yu, C. W. Wang, S. W. Jin, T. G. Ding, and G. Wu. “Dissolution of cellulose with ionic liquids and its application: a mini-review”. *Green Chem.* (2006) **8**:325–327.

[52] H. Zhang, J. Wu, J. Zhang, and J. S. He. “1-Allyl-3-methylimidazolium chloride room temperature ionic liquid: A new and powerful nonderivatizing solvent for cellulose”. *Macromol.* (2005) **38**:8272–8277.

[53] R. P. Swatloski, S. K. Spear, J. D. Holbrey, and R. D. Rogers. “Dissolution of cellose [sp.] with ionic liquids”. *J. Am. Chem. Soc.* (2002) **18**:4974–4975. Spelling error in article title, should be “cellulose".

[54] C. Zhang, R. Liu, J. Xiang, H. Kang, Z. Liu, and Y. Huang. “Dissolution Mechanism of Cellulose in N,N-Dimethylacetamide/ Lithium Chloride: Revisiting through Molecular Interaction”. *J. Phys. Chem. B* (2014) **118**:9507–9514.

[55] T. Tammelin, T. Saarinen, M. Österberg, and J. Laine. “Preparation of Langmuir/Blodgett-cellulose surfaces by using horizontal dipping procedure. Application for polyelectrolyte adsorption studies using QCM-D”. *Cellulose* (2006) **13**:519–535.

[56] E. Kontturi, P. C. Thune, and J. W. Niemantsverdriet. “Novel method for preparing cellulose model surfaces by spin coating”. *Polymer* (2003) **44**:3621–3625.

[57] E. Kontturi, P. C. Thune, and J. W. Niemantsverdriet. “Cellulose model surfaces-simplified preparation by spin coating and characterization by X-ray photoelectron spectroscopy, infrared spectroscopy, and atomic force microscopy”. *Langmuir* (2003) **19**:5735–5741.

[58] W. Mormann and M. Wezstein. “Trimethylsilylation of cellulose in ionic liquids”. *Macromol. Biosci.* (2009) **9**:369–375.

[59] K. Petzold, A. Koschella, D. Klemm, and B. Heublein. “Silylation of cellulose and starch - selectivity, structure analysis and subsequent reactions”. *Cellulose* (2003) **10**:251–269.

[60] F. Dourado, F. M. Gama, E. Chibowski, and M. Mota. “Characterization of cellulose surface free energy”. *J. Adhesion Sci. Technol.* (1998) **12**:1081–1090.

[61] P. Luner and M. Sandell. “The wetting of cellulose and wood hemicelluloses”. *J. Polymer Sci.* (1969) **28**:115–142.

[62] J. M. Hazendonk, J. C. van der Putten, J. T. F. Keurentjes, and A. Prins. “A simple experimental method for the measurement of the surface tension of cellulosic fibres and its relation with chemical composition”. *Colloid Surface A* (1993) **81**:251–261.

[63] E. M. Baba, C. E. Cansoy, and E. O. Zayim. “Optical and wettability properties of polymers with varying surface energies”. *App. Surface Sci.* (2015) **350**:115–120.

[64] "Critical Surface Tension, Surface Free Energy, Contact Angles with Water, and Hansen Solubility Parameters for Various Polymers". https://www.accudynetest.com/polytable_01.html. Accessed: January 2017.

[65] "Surface Free Energy Components by Polar/Dispersion and Acid–Base Analyses; and Hansen Solubility Parameters for Various Polymers". https://www.accudynetest.com/polytable_02.html. Accessed: January 2017.

[66] "Solid surface energy data (SFE) for common polymers". http://www.surface-tension.de/solid-surface-energy.htm. Accessed: May 2014.

[67] J. R. Overton and H. L. B. Jr. "Size Exclusion Chromatography". In T. Provder (Ed.), "ACS Symposium Series No. 245", , (American Chemical Society1984).

[68] E. E. Paschke, B. A. Bidlingmeyer, and J. G. Bergmann. "New solvent system for gel-permeation chromatography of poly(ethylene terephthalate)". *J. Polym. Sci. A* (1977) **15**:983–989.

[69] M. M. Sang, N. N. Jin, and E. F. Jiang. "Determination of the molecular-weight distribution of polyethylene terephthalate by gel-permeation chromatography". *J. Liq. Chrom.* (1982) **5**:1665–1678.

[70] S. A. Jabarin and D. C. Balduff. "Gel-permeation chromatography of polyethylene terephthalate". *J. Liq. Chrom.* (1982) **5**:1825–1845.

[71] L. E. Amborski and D. W. Flierl. "Physical properties of polyethylene terephthalate films". *J. Ind. Eng. Chem.* (1953) **45**:2290–2295.

[72] D. E. Bornside, C. W. Macosko, and L. E. Scriven. "Spin coating - one-dimensional model". *J. Appl. Phys.* (1989) **66**:5185–5193.

[73] J. A. Moriarty, L. W. Schwartz, and E. O. Tuck. "Unsteady spreading of thin liquid films with small surface tension". *Phys. Fluids A* (1991) **3**:733–742.

[74] A. Münch, C. P. Please, and B. Wagner. "Spin coating of an evaporating polymer solution". *Phys. Fluids* (2011) **23**:102101.

[75] A. Acrivos, M. J. Shah, and E. E. Petersen. "On the flow of a non-Newtonian liquid on a rotating disk". *J. Appl. Phys.* (1960) **31**:963–968.

[76] L. W. Schwartz and R. V. Roy. "Theoretical and numerical results for spin coating of viscous liquids". *Phys. Fluids* (2004) **16**:569–584.

[77] R. Tadmor. "Line energy and the relation between advancing, receding and young contact angles". *Langmuir* (2004) **20**:7659–7664.

[78] C. J. VanOss, M. K. Chaudhury, and R. J. Good. "Monopolar Surfaces". *Adv. Colloid Interface Sci.* (1987) **28**:35–64.

[79] C. J. VanOss, M. K. Chaudhury, and R. J. Good. "Interfacial Lifshitz-van der Waals and polar interactions in macroscopic systems". *Chem. Rev.* (1988) **88**:927–941.

[80] E. Chibowski. "Surface free energy of a solid from contact angle hysteresis". *Adv. Colloid Interface Sci.* (2003) **103**:149–172.

[81] E. Chibowski and K. Terpilowski. "Surface free energy of sulfur–Revisited. I. Yellow and orange samples solidified against glass surface". *J. Colloid Interface Sci.* (2008) **319**:505–513.

[82] S. Yu and M. Dekker. *Polymer Interface and Adhesion*, (New York1982).

[83] W. A. Zisman. "Relation of the Equilibrium Contact Angle to Liquid and Solid Constitution". In R. F. Gould (Ed.), "Advances in Chemistry 43: Contact Angle, Wettability, and Adhesion", chapter 1, pp. 1–51, (American Chemical Society1964).

[84] M. J. Kamlet and R. W. Taft. "The solvatochromic comparison method. I. The β-scale of solvent hydrogen bond acceptor (HBA) basicities". *J. Am. Chem. Soc.* (1975) **98**:377–383.

[85] M. J. Kamlet and R. W. Taft. "The solvatochromic comparison method. 2. The α-scale of solvent hydrogen bond donor (HBD) acidities". *J. Am. Chem. Soc.* (1976) **98**:2886–2894.

[86] M. J. Kamlet, E. G. Kayser, M. E. Jones, J. L. Abboud, J. W. Eastes, and R. W. Taft. "The solvatochromic comparison method. 4. Dilution studies". *J. Am. Chem. Soc.* (1978) **82**:2477–2483.

[87] R. R. Minesinger, M. E. Jones, R. W. Taft, and M. J. Kamlet. "the solvatochromic comparison method. 5. Spectral effects and relative strengths of the first and second hydrogen bonds by 40-nitroaniline to hydrogen bond acceptor solvents". *J. Org. Chem.* (1977) **42**:1929–1934.

[88] M. J. Kamlet, J. L. Abboud, and R. W. Taft. "The solvatochromic comparison method. 6. The π^* scale of solvent polarities". *J. Am. Chem. Soc.* (1977) **99**:6027–6038.

[89] C. M. Hansen. *Hansen Solubility Parameters: A User's Handbook*, (CRC Press2007), 2nd edition.

[90] J. P. Cerón-Carrasco, D. Jacquemin, C. Laurence, A. P. C. Reichardt, and K. Sraïdi. "Solvent polarity scales: determination of new $E_T(30)$ values for 84 organic solvents". *J. Phys. Org. Chem.* (2012) **27**:512–518.

[91] G. M. Kontogeorgis and S. Kiil. *Introduction to Applied Colloid and Surface Chemistry*, (Wiley2016).

[92] D. A. Olsen and A. J. Osteraas. "The Critical Surface Tension of Glass". *J. Phys. Chem.* (1964) **68**:2730–2732.

[93] V. Chechik, R. M. Crooks, and C. J. M. Stirling. "Reactions and reactivity in self-assembled monolayers". *Adv. Mater.* (2000) **12**:1161–1171.

[94] J. A. Creighton, C. G. Blatchford, and M. G. Albrecht. "Plasma resonance enhancement of Raman scattering by pyridine adsorbed on silver or gold sol particles of size comparable to the excitation wavelength". *J. Chem. Soc., Faraday Trans. 2* (1979) **75**:790–798.

[95] M. Hohenwarter. *GeoGebra: Ein Softwaresystem für dynamische Geometrie und Algebra der Ebene.* Master's thesis, Paris Lodron University, Salzburg, Austria (2002). (In German.).

[96] M. Hohenwarter, M. Borcherds, G. Ancsin, B. Bencze, M. Blossier, A. Delobelle, C. Denizet, J. Éliás, A. Fekete, L. Gál, Z. Konečný, Z. Kovács, S. Lizelfelner, B. Parisse, and G. Sturr. "GeoGebra 4.0" (2013). http://www.geogebra.org.

[97] H. E. Ramsey. *"Whiter than white": interactions between optical brighteners and surfactants in detergents.* Ph.D. thesis, University of Durham (2016).

[98] P. Atkins and J. de Paula. *Atkins' Physical Chemistry*, (Oxford University Press2006), 8th edition.

[99] T. Kondo and C. Sawatari. "A Fourier transform infra-red spectroscopic analysis of the character of hydrogen bonds in amorphous cellulose". *Polymer* (1996) **37**:393–399.

[100] J. H. Lai. "An investigation of spin coating of electron resists". *Polym. Eng. Sci.* (1979) **19**:1117–1121.

[101] J. H. Wiley and R. H. Atalla. "Band assignments in the Raman spectra of celluloses". *Carbohyd. Res.* (1987) **160**:113–129.

[102] M. Holmberg, J. Berg, S. Stemme, L. Odberg, J. Rasmusson, and P. Claesson. "Surface force studies of Langmuir-Blodgett cellulose films". *J. Colloid Int. Sci.* (1997) **186**:369–381.

[103] V. Buchholz, P. Adler, M. Bäcker, W. Hölle, A. Simon, and G. Wegner. "Regeneration and Hydroxyl Accessibility of Cellulose in Ultrathin Films". *Langmuir* (1997) **13**:3206–3209.

[104] "Surface tension values of some common test liquids for surface energy analysis". http://www.surface-tension.de/index.htm. Accessed: May 2014.

[105] J. Clayden, N. Greeves, S. Warren, and P. Wothers. *Organic chemistry*, (Oxford University Press2007).

[106] D. W. J. McCallien, P. L. Burn, and H. L. Anderson. "Chelation of diamine ligands to zinc porphyrin monolayers amide-linked to glass". *J. Chem. Soc., Perkin Trans.* (1997) **1**:2581–2586.

[107] D. F. S. Petri, G. Wenz, P. Schunk, and T. Schimmel. "An improved method for the assembly of amino-terminated monolayers on SiO_2 and the vapor deposition of gold layers". *Langmuir* (1999) **15**:4520–4523.

[108] M. Hussain, R. Shamey, D. Hinks, A. El-Shafei, and S. I. Ali. "Synthesis of novel stilbene-alkoxysilane fluorescent brighteners, and their performance on coton fiber as fluorescent brightening and ultraviolet absorbing agents". *Dyes and Pigments* (2012) **92**:1231–1240.

[109] S. P. A. Fodor, J. L. Read, M. C. Pirrung, L. Stryer, A. T. Lu, and D. Solas. "Light-directed, spatially addressable parallel chemical synthesis". *Science* (1991) **251**:767–773.

[110] F. Caprassse, D. Leroy, L. Martinot, S. Lambert, J. P. Pirard, J. Guillaume, and C. Jérôme. "New silica based polymeric systems designed for the solid-liquid extraction of uranyl ions". *J. Mater. Chem.* (2002) **12**:137–142.

[111] J.-C. Broudic, O. Conocar, J. J. E. Moreau, D. Meyer, and M. W. C. Man. "New hybrid silica based materials for the solid-liquid extraction of actinides". *J. Mater. Chem.* (1999) **9**:2283–2285.

[112] K. M. R. Kallury, W. E. Lee, and M. Thompson. "Enhanced stability of urease immobilized onto phospholipid covalently bound to silica, tungsten and fluoropolymer surfaces". *Anal. Chem.* (1993) **65**:2459–2467.

[113] M. Thompson and L. M. Furtado. "High density oligonucleotide and DNA probe arrays for the analysis of target DNA". *Analyst* (1999) **124**:1133–1136.

[114] J. Jennane, T. Boutros, and R. Giasson. "Photolithography of self-assembled monolayers: optimization of protecting groups by an electroanalytical method". *Can. J. Chem.* (1995) **74**:2509–2517.

[115] S. Flink, F. C. J. M. van Veggel, and D. N. Reinhoudt. "Functionalization of self-assembled monolayers on glass and oxidized silicon wafers by surface reactions". *J. Phys. Org. Chem.* (2001) **41**:407–415.

[116] "Kamlet-Taft solvent parameters". http://www.stenutz.eu/chem/solv26.php. Accessed: Sept 2015.

[117] M. Reischl, K. Stana-Kleinshchek, and V. Ribitsch. "Electrokinetic investigations of oriented cellulose polymers". *Macromol. Symp.* (2006) **244**:31–47.

[118] M. Mackley. "Stretching polymer chains". *Rheol. Acta* (2010) **49**:443–458.

[119] R. Clemens and T. Graham. *Introduction to Manuscript Studies*, (Cornell University Press2007).

[120] R. J. H. Clark and M. L. Curri. "The identification by Raman microscopy and X-ray diffraction of iron-oxide pigments and of the red pigments found on Italian pottery fragments". *J. Mol. Struct.* (1998) **440**:105–111.

[121] R. J. H. Clark and C. J. Cooksey. "Monobromoindigos: a new general synthesis, the characterization of all four isomers and an investigation into the purple colour of 6,6'-dibromoindigo". *New J. Chem.* (1999) pp. 323–328.

[122] R. J. H. Clark. "Pigment identification by spectroscopic means: an arts/science interface". *C. R. Chimie* (2002) pp. 7–20.

[123] R. J. H. Clark and J. van der Weerd. "Identification of pigments and gemstones on the Tours Gospel: the early 9th century Carolingian palette". *J. Raman Spectrosc.* (2004) **35**:279–283.

[124] R. J. H. Clark. "Applications of Raman Spectroscopy to the Identification and Conservation of Pigments on Art Objects". *Handbook of Vibrational Spectroscopy* (2006) **1**.

[125] R. J. H. Clark. "Raman microscopy as a structural and analytical tool in the fields of art and archaeology". *J. Molec. Struct.* (2007) **834-836**:74–80.

[126] R. J. H. Clark. "The scientific investigation of artwork and archaeological artefacts: Raman microscopy as a structural, analytical and forensic tool". *Appl. Phys. A* (2007) **89**:833–840.

[127] R. J. H. Clark. "Far-infrared spectroscopy, the wavenumbers of metal-ligand vibrations and the characterisation of inorganic pigments". *J. Raman Spectrosc.* (2010) **41**:361–362.

[128] R. J. H. Clark, R. R. Hark, N. Salvado, S. Buti, and T. Pradell. "Spectroscopy study of mural paintings from the Pyrenean Church of Saint Eulàlia of Unha". *J. Raman Spectrosc.* (2010) **41**:1418–1424.

[129] L. Burgio, K. Melassanaki, M. Doulgeridis, R. J. H. Clark, and D. Anglos. "Pigment identification in paintings employing laser induced breakdown spectroscopy and Raman microscopy". *Spec. Acta B* (2001) pp. 905–913.

[130] L. Burgio, R. J. H. Clark, and K. Theodoraki. "Raman microscopy of Greek icons: identification of unusual pigments". *Spec. Acta A* (2003) **59**:2371–2389.

[131] L. Burgio, R. J. H. Clark, and M. Rosser-Owen. "Raman analysis of ninth-century Iraqi stuccoes from Samarra". *J. Archaeol. Sci.* (2007) **34**:756–762.

[132] L. Burgio, R. J. H. Clark, V. S. F. Muralha, and T. Stanley. "Pigment analysis by Raman microscopy of the non-figurative illumination in 16th- to 18th-century Islamic manuscripts". *J. Raman Spectrosc.* (2008) **39**:1482–1493.

[133] L. Burgio, R. J. H. Clark, and R. R. Hark. "Spectroscopic investigation ofmodern pigments on purportedly medieval miniatures by the 'Spanish Forger'". *J. Raman Spectrosc.* (2009) **40**:2031–2036.

[134] L. Burgio, R. J. H. Clark, and R. R. Hark. "Raman microscopy and x-ray fluorescence analysis of pigments on medieval and Renaissance Italian manuscript cuttings". *PNAS* (2010) **107**(13):5726–5731.

[135] G. Adami, A. Gorasssini, and E. Prenesti. "Micro-XRF and FT-IR/ATR analyses of an optically degraded ancient document of the Trieste (Italy) cadastral system (1893): A novel and surprising iron gall ink protective action". *Microchemical Journal* (2016) **124**:96–103.

[136] A. Duran, M. L. Franquelo, and M. A. Ceteno. "Forgery detection on an Arabic illuminated manuscript by micro-Raman and X-ray fluorescence spectroscopy". *J. Raman Spectrosc.* (2011) **42**(1):48–55.

[137] J. K. Delaney, P. Ricciardi, and L. D. Glinsman. "Use of imaging spectroscopy, fiber optic reflectance spectroscopy, and X-ray fluorescence to map and identify pigments in illuminated manuscripts". *Studies in Conservation* (2014) **59**(2):91–101.

[138] I. Nastova, O. Grupce, and B. Minceva-Sukarova. "Micro-Raman spectroscopic analysis of inks and pigments in illuminated medieval old-Slavonic manuscripts". *J. Raman Spectrosc.* (2012) **43**(11):1729–1736.

[139] I. M. Bell, R. J. H. Clark, and P. J. Gibbs. "Raman spectroscopic library of natural and synthetic pigments (pre- approximately 1850 AD)." *Spectrochim. Acta A Mol Biomol. Spectrosc.* (1997) **53A**(12):2159–2179.

[140] R. J. H. Clark and L. Burgio. "Library of FT-Raman spectra of pigments, minerals, pigment media and varnishes, and supplement to existing library of Raman spectra of pigments with visible excitation." *Spectrochim. Acta A Mol Biomol Spectrosc.* (2001) **57**(7):1491–1521.

[141] M. Aceto, A. Agostino, and E. Boccaleri. "Evidence for the degradation of an alloy pigment on an ancient Italian manuscript". *J. Raman Spectrosc.* (2006) **37**(10):1160–1170.

[142] S. Mosca, T. Frizzi, and M. Pontone. "Identification of pigments in different layers of illuminated manuscripts by X-ray fluorescence mapping and Raman spectroscopy". *Microchemical Journal* (2016) **124**:775–784.

[143] R. L. Feller and A. Roy (Eds.). *Artists' Pigments, A Handbook of their History and Characteristics*, volume 1, (National Gallery of Art, Washington1987).

[144] A. Roy (Ed.). *Artists' Pigments, A Handbook of their History and Characteristics*, volume 2, (National Gallery of Art, Washington1997).

[145] E. W. Fitzhugh (Ed.). *Artists' Pigments, A Handbook of their History and Characteristics*, volume 3, (National Gallery of Art, Washington1998).

[146] N. Eastaugh, V. Walsh, T. Chaplin, and R. Siddall (Eds.). *Pigment Compendium: A Dictionary and Optical Microscopy of Historical Pigments*, (Butterworth-Heinemann2008).

[147] J. N. Liles. *The Art and Craft of Natural Dyeing: Traditional Recipes for Modern Use*, (University of Tennessee Press2006), 6th edition.

[148] J. H. Parry and E. J. Coste. *The Chemistry of Pigments*, (Scott, Greenwood and Co.1902).

[149] D. Goltz, J. McClelland, A. Schellenberg, M. Attas, E. Cloutis, and C. Collins. "Spectroscopic studies on the darkening of lead white". *Appl. Spectrosc.* (2003) **57**:1393–1398.

[150] N. Purinton and M. Watters. "A study of the materials used by medieval persian painters". *Spec. Acta A Mol. Biomol. Spec.* (2015) **142**:159–168.

[151] F. G. Ullman. "Raman spectrum of $CuSO_4 \cdot 5\,H_2O$ single crystal". *J. Raman Spectrosc.* (1991) **22**:525–528.

[152] X. Fu, G. Yang, J. Sun, and J. Zhou. "Vibrational Spectra of Copper Sulfate Hydrates Investigated with Low-Temperature Raman Spectroscopy and Terahertz Time Domain Spectroscopy". *J. Phys. Chem. A* (2012) **116**:7314–7318.

[153] A. Perisamy, S. Muruganand, and M. Palaniswamy. "Vibrational studies of Na_2SO_4, K_2SO_4, $NaHSO_4$ and $KHSO_4$ crystals". *Rasayan J. Chem.* (2009) **2**:981–989.

[154] M. de Veij, P. Vandenabeele, T. D. Beer, J. P. Remon, and L. Moens. "Reference database of Raman spectra of pharmaceutical excipients". *J. Raman Spectrosc.* (2009) **40**:279–307.

[155] P. Atkins, T. Overton, J. Rourke, M. Weller, and F. Armstrong. *Inorganic Chemistry*, (Oxford University Press2006), fourth edition.

[156] D. L. Douglas and C. Shing. "The light-induced alteration of realgar to pararealgar". *Am. Mineral.* (1992) **77**:1266–1274.

[157] J. Martin-Gil, F. J. Martin-Gil, G. D. de Castro, P. Zapatero-Magdaleno, and F. J. Sarabia-Herrero. "The first known use of vermilion". *Experientia* (1995) **51**:759–761.

[158] P. Ball. *Bright Earth: Art and the Invention of Colour*, (University of Chicago Press2003).

[159] C. D. Cennini. *Il Libro dell' Arte (The Craftsman's Handbook)*, (Yale University Press1933).

[160] D. V. Thompson. *The Materials and Techniques of Medieval Painting*, (Dover2003).

[161] K. Eremin, J. Stenger, and J. F. Huang. "Examination of pigments on Thai manuscripts: the first identification of copper citrate". *J. Raman Spectrosc.* (2008) **39**(8):1057–1065.

[162] H. Beecken, E. M. Gottschalk, U. V. Gizycki, H. Kr amer, D. Maassen, H. G. Matthies, H. Musso, C. Rathjen, and U. I. Záhorsky. "Orcein und Lackmus". *Angew. Chem. Int. Edit.* (1961) pp. 665–673.

[163] M. Aceto, A. Arrais, F. Marsano, A. Agostino, G. Fenoglio, A. Idone, and M. Gulmini. "A diagnostic study on folium and orchil dyes with non-invasive and micro-destructive methods". *Spec. Acta A Mol. Biomol. Spec.* (2015) **142**:159–168.

[164] F. Rosi, C. Clementi, M. Paolantoni, A. Romani, R. Pellegrino, B. G. Brunetti, W. Nowik, and C. Miliani. "Study of Raman scattering and luminescence properties of orchil dye for its nondestructive identiiňĄcation on artworks". *J. Raman Spectrosc.* (2012) pp. 1451–1456.

[165] T. Jawahari, A. Roid, and J. Casado. "Raman spectroscopic characterization of some commercially available carbon black materials". *Carbon* (1995) **33**:1561–1565.

[166] M. Pawlyta, J.-N. Rouzaud, and S. Duber. "Raman microspectroscopy characterization of carbon blacks: Spectral analysis and structural information". *Carbon* (2014) **84**:479–490.

[167] A. Ponce, L. B. Brostoff, and S. K. Gibbons. "Elucidation of the Fe(III) Gallate Structure in Historical Iron Gall Ink". *Analytical Chemistry* (2016) **88**(10):5152–5158.

[168] R. Gameson. *Manuscript Treasures of Durham Cathedral*, (Third Millennium2010), 1st edition.

[169] A. Beeby, A. R. Duckworth, R. G. Gameson, and C. E. Nicholson. "Pigments of the Earliest Northumbrian Manuscripts". *Scriptorium* (2015) **69**:33–59, P1. 10–15.

[170] I. Wood (Ed.). *Church and Chronicle in the Middle Ages: Essays Presented to John Taylor*, (A & C Black1991).

[171] R. Gameson (Ed.). *Treasures of Durham University Library*, (Third Millennium2007), 1st edition.

[172] A. Filippidis, L. C. Jain, and N. Martin. "Multisensor data fusion for surface land-mine detection". *IEEE T. Syst. Man Cy. C* (2000) **30**:145–150.

[173] S. Montan. "Multispectral system for medical fluorescence imaging". *IEEE J. Quantum Elect.* (1987) **23**:1798–1805.

[174] M. Petrou and C. Petrou. *Image Processing: The Fundamentals*, (Wiley2010), 1st edition.

[175] J. N. Miller and J. C. Miller. *Statistics and Chemometrics for Analytical Chemistry*, (Pearson2005), 5th edition.

[176] M. Ester, H. peter Kriegel, J. Sander, and X. Xu. "A density-based algorithm for discovering clusters in large spatial databases with noise", (AAAI Press1996) pp. 226–231.

[177] A. Consetino. "FORS Spectral Database of Historical Pigments in Different Binders". *e-conservation Journal* (2014) **2**:53–65.

[178] R. Forneris. "The infrared and Raman spectra of realgar and orpiment". *The American Mineralogist* (1969) **54**:1062–1074.

[179] M. Aceto, E. Cala, A. Agostino, G. Fenoglio, A. Idone, C. Porter, and M. Gulmini. "On the identification of folium and orchil on illuminated manuscripts". *Spec. Acta A Mol. Biomol. Spec.* (2017) **171**:461–469.

[180] T. D. Chaplin, R. J. H. Clark, and D. A. Scott. "Study by Raman microscopy of nine variants of the green-blue pigment verdigris". *J. Raman Spectrosc.* (2006) **37**:223–229.

[181] B. Gilbert, S. Denoel, G. Weber, and D. Allart. "Analysis of green copper pigments in illuminated manuscripts by micro-Raman spectroscopy". *Analyst* (2003) **128**:1213–1217.

[182] D. L. A. de Faria, S. V. Silva, and M. T. de Oliviera. "Raman Microspectroscopy of Some Iron Oxides and Oxyhydroxides". *J. Raman Spectrosc.* (1997) **28**:873–878.

[183] M. K. Uddin. "Use of brick dust in concrete as mineral admixture and partial replacement of cement". *J. Civil Eng.* (2004) **32**:69–78.

[184] B. Lafuente, R. T. Downs, H. Yang, and N. Stone. "The power of databases: the RRUFF project. In: Highlights in Mineralogical Crystallography". http://rruff.info (2015).

[185] S. University. "Cambridge, Corpus Christi College, Parker Library, CCCC MS 197B". http://http://dms.stanford.edu/catalog/CCC197B_keywords. [Online; accessed 07-07-2017].

[186] K. L. Brown and R. J. H. Clark. "The Lindisfarne Gospels and two other 8th century Anglo-Saxon/Insular manuscripts: pigment identification by Raman microscopy". *J. Raman Spectrosc.* (2004) **35**:4–12.

[187] S. Bioletti, R. Leahy, J. Fields, B. Meehan, and W. Blau. "The examination of the Book of Kells using micro-Raman spectroscopy". *J. Raman Spectrosc.* (2009) **40**:1043–1049.

[188] K. L. Brown and R. J. H. Clark. "Three English manuscripts post-1066 AD: pigment identification and palette comparisons by Raman microscopy". *J. Raman Spectrosc.* (2004) **35**:217–223.

[189] Private conversation with Prof. Richard Gameson.

[190] E-mail communication with David Oxlade, Geospatial Research Ltd.

[191] K. L. Brown. *Raman spectrosccopic and computational studies of artists' pigments and other inorganic compounds.* Ph.D. thesis, University of London (2002).

[192] G. Christian. *Applications of multispectral imaging and reflection spectroscopy in the field of palaeography.* Master's thesis, University of Manchester (2014).

[193] D. Freedman and P. Kisilev. "Fast Mean Shift by Compact Density Representation". In "Computer Vision and Pattern Recognition", , (IEEE2009) pp. 1818–1825.